

Khashan, Lamia M.A. (2015) Dispersion analysis of two-dimensional unstructured transmission line modelling (UTLM). PhD thesis, University of Nottingham.

Access from the University of Nottingham repository:

http://eprints.nottingham.ac.uk/28509/1/Lamia_Khashan_thesis.pdf

Copyright and reuse:

The Nottingham ePrints service makes this work by researchers of the University of Nottingham available open access under the following conditions.

This article is made available under the University of Nottingham End User licence and may be reused according to the conditions of the licence. For more details see:
http://eprints.nottingham.ac.uk/end_user_agreement.pdf

A note on versions:

The version presented here may differ from the published version or from the version of record. If you wish to cite this item you are advised to consult the publisher's version. Please see the repository url above for details on accessing the published version and note that access may require a subscription.

For more information, please contact eprints@nottingham.ac.uk



The University of
Nottingham

UNITED KINGDOM • CHINA • MALAYSIA

THE UNIVERSITY OF NOTTINGHAM

SCHOOL OF ELECTRICAL AND ELECTRONICS ENGINEERING

**Dispersion Analysis of Two-Dimensional Unstructured
Transmission Line Modelling (UTLM)**

By:
Lamia M A Khashan (BSc, MSc)

**Thesis submitted to the University of Nottingham
for the degree of Doctor of Philosophy
December 2014**

To the spirits of my parents

ABSTRACT

Numerical simulation techniques play an important role due to their flexibility in dealing with a broad range of complex geometries and material responses. This flexibility requires substantial computational time and memory. Most numerical methods use structured grid for graphical discretization, although this approach is straightforward it is not ideal for smoothly curved boundaries.

In this thesis the two-dimensional Transmission Line Modelling (TLM) method based on unstructured meshes is adopted. TLM is an established numerical simulation technique that has been employed in a variety of applications area. Using unstructured meshes to discretize the problem domain permits smooth boundary presentation which provides significant enhancement in the flexibility and accuracy of the TLM simulations. An algorithm is developed to implement Unstructured Transmission Line Modelling (UTLM) which is carefully designed for simplicity and scalability of model size. Several examples are employed to test the accuracy and efficiency of the UTLM simulations.

Delaunay meshes, as a type of unstructured meshes, provide good quality triangles but have the disadvantage of providing close to zero transmission line length which has impact on the maximum permissible time step for stable operation. In this thesis, a simple perturbation method for relaxing the minimum link length and clustering triangles in pairs is presented, which permits substantial increase in time step and hence computational runtime to be made without compromising the simulation stability or accuracy. Also, a new model for relaxing the short link lines that fall on the boundaries is presented.

UTLM method is based on temporal and spatial sampling of electromagnetic fields which results in dispersion. In this thesis, dispersion characteristics of the unstructured TLM mesh are investigated and compared against structured TLM results for different mesh sizes and shapes. Unlike the structured TLM mesh, the unstructured mesh gives rise to spatial mode coupling. Intermodal coupling behaviour is investigated in a statistical manner upon the change of the mesh local characteristics.

PUBLICATIONS

1. Lamia Khashan, Ana Vukovic, Phillip Sewell, Trevor M.Benson, “Assessment of Accuracy and Runtime Trade-offs in Unstructured TLM Meshes for Electromagnetic Simulations”, 2013 Loughborough Antennas & Propagation Conference, 11-12 November 2013, Loughborough, UK.
2. Lamia Khashan, Ana Vukovic, Phillip Sewell, Trevor M.Benson, “Dispersion in the 2D Unstructured Transmission Line Modelling (UTLM) Method”, 2015 IEEE International Conference on Electromagnetic Computability, 2-5 February, Hong Kong, Hong Kong SAR.
3. Lamia Khashan, Ana Vukovic, Phillip Sewell, Trevor M.Benson, “Assessment of Dispersion and intermodal coupling in the Unstructured Transmission Line Modelling (UTLM) Method”, in preparation for Microwave and Optical Technology Letters.

ACKNOWLEDGEMENTS

First I would like to thank my supervisor, Prof. Phillip Sewell, his invaluable suggestions made this work successful. I would like also to thank my supervisor, Dr. Ana Vukovic for the constant guidance, support and patience throughout the PhD. She was thoughtful, kind and a sincere supervisor and friend.

My sincere thanks go to Dr. Ashraf Abdelraouf for helping me understand Object-Oriented Programming and for providing me his valuable insights on system implementation. He also provided his time and advice throughout the whole PhD path.

I would like to thank all my friends and colleagues in my university, Misr International University (MIU). I am thankful to the head of administrative affairs, Mr. Hassan ElRashidy and special thanks to the head of the department Assoc. Prof. Dr. Alemam Ragab.

I am very grateful to Prof. Hoda Hosni for being my rock, and for providing a role model in every aspect of life. I wish someday I can be a beautiful and successful person like her.

Sincere thanks to my brother Eng. Ahmed Khashan and my uncle Eng. Adel Kabil for the support and the prayers.

I thank my husband Dr. Tarek Nasser for his patience, for encouraging me to pursue my studies and for being of a great support in all the struggles and frustrations in my PhD.

And finally, I am deeply and forever indebted to my mentor and my father Prof. Mahmoud Khashan, who believed in me and saw the potential that I didn't realize that I have. He pushed me to pursue my PhD in the University of Nottingham in a very rough time, but life didn't give him the chance to accompany me along that long road. Dad, I owe you everything I learnt and every success I achieved in my life. God rest your soul.

TABLE OF CONTENTS

Abstract	i
Publications	ii
Acknowledgements	iii
Table of Contents	iv
List of Symbols	vii
List of Acronym	ix
Chapter 1. Introduction	1
1.1 Background	2
1.2 Organization of the thesis	10
Chapter 2. A review of unstructured numerical techniques	12
2.1 Introduction	12
2.2 Maxwell's equations and wave equation.....	12
2.3 Transverse modes	14
2.4 General plane wave equation	15
2.5 Boundary conditions.....	19
2.6 Numerical techniques for electromagnetic problems	20
2.6.1 Finite Element Method (FEM).....	21
2.6.2 Finite Difference Time Domain (FDTD).....	26
2.6.3 Transmission Line Modelling (TLM)	32
2.6.4 Errors in numerical methods	45
2.7 Unstructured meshing techniques.....	46
2.8 Summary	51
Chapter 3. Two-Dimensional Unstructured Transmission Line Modelling	52
3.1 Introduction	52
3.2 Unstructured meshes and Delaunay triangulation.....	53
3.2.1 Delaunay properties	53
3.2.2 Delaunay triangle circumcentre	57
3.2.3 Voronoi mesh	58
3.3 2D UTLM node	60
3.4 Circuit analysis of shunt TLM node.....	68
3.4.1 Stub model of inductor and capacitor	68
3.4.2 Thevenin equivalent circuit.....	71
3.4.3 Scatter and connect processes	74
3.5 Implementation of 2D unstructured TLM.....	77

3.5.1	Mesh geometry.....	77
3.5.2	Software Design.....	80
3.6	General unstructured TLM algorithm.....	82
3.6.1	Pre-processing.....	84
3.6.2	Main process.....	87
3.7	Results.....	89
3.7.1	Effect of number and type of meshes on an air-filled cylindrical PEC Resonator.....	89
3.7.2	Effect of number and type of meshes on dielectric-filled cylindrical resonator.....	99
3.7.3	Effect of number and type of meshes on an air-filled rectangular resonator.....	106
3.8	Summary.....	114
Chapter 4.	Triangle Pair Model for 2D Unstructured TLM.....	116
4.1	Introduction.....	116
4.2	Triangle pair model.....	119
4.3	Short link line on the boundary plane.....	124
4.3.1	Short-circuit boundary.....	124
4.3.2	Open-circuit boundary.....	126
4.3.3	Impedance boundary.....	127
4.4	Pair model implementation.....	128
4.5	Results.....	130
4.5.1	Air filled cylindrical PEC resonator.....	130
4.5.2	Dielectrically loaded cylindrical resonator.....	136
4.6	Summary.....	140
Chapter 5.	Dispersion and intermodal coupling in 2D UTLM.....	141
5.1	Introduction.....	141
5.2	Mesh quality.....	142
5.3	Plane wave propagation.....	143
5.4	Problem description.....	148
5.5	Study of plane wave dispersion.....	151
5.6	Study of inter-modal coupling.....	164
5.6.1	Mode coupling in structured meshes.....	165
5.6.2	Mode coupling in unstructured meshes.....	167
5.7	Summary.....	187
Chapter 6.	Conclusions and Future work.....	188
6.1	Conclusions.....	188
6.2	Future work.....	193

Appendix: Unstructured TLM simulator	194
References	200

LIST OF SYMBOLS

E	Electric field intensity [V/m]
H	Magnetic field intensity [A/m]
Z	Impedance [Ω]
Y	Admittance [S]
L	Inductance [H]
C	Capacitance [F]
ϵ_0, ϵ_r	Free space and medium relative permittivity [F/m]
μ_0, μ_r	Free space and medium relative permeability [H/m]
Δl	Spatial segment [m]
$\Delta x, \Delta y, \Delta z$	Spatial segment in x, y and z directions [m]
Δ_i	Link length of segment I [m]
Δ_{\min}	Minimum link length [m]
Δt	Time step [s]
k	Time index
λ	Wavelength [m]
c	Free space velocity [m/s]
u_{TL}	Signal velocity on transmission line [m/s]
Z_{Lm}	Impedance of link line m [Ω]
Y_{Lm}	Admittance of link line m [S]

Y_{Sm}	Admittance of stub m [S]
${}_kV_L^i$	Incident voltage on link L at time k [V]
${}_kV_L^r$	Reflected voltage on link L at time k [V]
S_i	Triangle side length i [m]
E	Edge
N	Neighbour
ω	Angular frequency [rad/s]
f_a	Analytical resonance frequency [Hz]
f_{TLM}	TLM resonance frequency [Hz]
Δ_{Thres}	Threshold length [m]
k_0	Free space wave number [rad]
v_p	Phase velocity [m/s]
k_x, k_y	Wave number in x and z directions [rad]
d	Parallel plate waveguide width [m]
L	Parallel plate waveguide length [m]
A_{av}	Average mesh area [m ²]
Q	Mesh quality factor

LIST OF ACRONYM

2D	Two-Dimensional
3D	Three-Dimensional
ABC	Absorbing Boundary Conditions
AFT	Advancing Front Technique
BVP	Boundary Value Problems
CC	Circumcentre
CEM	Computational Electromagnetic
EM	Electromagnetic
EMC	Electromagnetic compatibility
FDTD	Finite Difference Time Domain
FEM	Finite Element Method
FFT	Fast Fourier Transform
MoM	Method of Moments
PEC	Perfect Electric Conductor
PML	Perfectly Matched Layer
STLM	Structured Transmission Line modelling
TLM	Transmission Line Modelling
TM _{mn}	Transverse Magnetic mode of order mn
UTLM	Unstructured Transmission Line modelling

Chapter 1.

Introduction

Electromagnetic (EM) fields are present everywhere in our environment. Man-made sources of electromagnetic fields that form a major part of industrialized life such as microwaves, radio frequency and electrical systems are characterized by frequency and its corresponding wavelength, where fields with different frequencies interact with bodies in different ways. Electromagnetic simulation is a common activity in many branches of science and technology where different methods can be applied for simulating the interaction of electromagnetic fields with physical objects and/or environment.

A variety of methods are available to solve EM equations but real-world electromagnetic problems are in general not analytically soluble which demands the use of numerical techniques to approximate the solution of EM equations. Numerical solution of electromagnetic problems started mid-sixties due to the increase of computer capabilities, and since then it played an important role in solving EM problems due to their flexibility in dealing with a broad range of complex geometries and material responses. However, this flexibility requires substantial computational time and memory. Consequently, both the complexity and scale of the problems have to be compromised limiting the accuracy of the simulations produced, which is severely hampering systematic progress in many technological areas. It is becoming more apparent that relying on rapidly increasing computer power is not a sustainable strategy for overcoming the limitations of large scale simulations. Therefore, it is important that the computational resources available are used in the most effective manner possible and that the new and improved algorithms are constantly under development.

The field of numerically solving the field equations is known as the Computational Electromagnetics (CEM). CEM is a fast growing area that is concerned with

development of numerical techniques for modelling of general problems [1-4]. This makes CEM valuable to design or model waveguides, antennas, satellite, radar and varieties of communication systems through computationally efficient approximations.

1.1 Background

Electromagnetic behaviour is governed by Maxwell's equation, which best describe the relationship between the electric and magnetic fields that form the electromagnetic wave. These fields are time-dependent and can be expressed spatially in different coordinate systems. Maxwell's equations can be expressed in either differential or integral forms and are solved through analytical or numerical methods to extract the electric and magnetic fields components.

There are several popular numerical techniques that are used for solving electromagnetic problems. Choosing the correct method that suits the intended problem is of great importance in order to obtain the correct results and through the most effective use of the computational resources. CEM can be generally divided into time-domain or frequency-domain methods and depending on the operator domain methods can be classified into differential or integral equation methods [5].

Time-domain numerical methods are best suiting problems involving transient response, nonlinear or time-dependent parameters. Alternatively, problems requiring steady-state response or with frequency-dependent parameters are better solved using frequency domain methods.

Differential numerical methods discretize the differential form of Maxwell's equations over the problem space. In differential methods physical laws are applied on number of discretization elements N occupying the modelled region. The resultant is large but sparse system of linear algebraic equations, which requires a CPU time and memory of the order $O(N)$ when solved iteratively [3]. They are best used in modelling inhomogeneous or non-linear problems, but then requires special treatment of open boundary problems [1]. Such methods are Finite Difference Time Domain (FDTD) [6], Transmission Line Modelling (TLM) [7] and Finite Element Method (FEM) [8].

These methods are represented by a sparse matrix solution where each sample couples to few others such as the exchange of data between nearest neighbours; this results in a matrix with sufficient number of zeros. Sparse matrices are solved iteratively in a very efficient way and can compress easily for huge matrix since it is mostly zero, also, they often parallelise very well. On the other side, in order to get the required accuracy more and smaller discretization elements are required. FEM, FDTD and TLM are among the most popular and successful numerical methods in solving electromagnetic problems. The overview of FE, FDTD and TLM methods will be discussed in detail in Chapter 2.

Integral equation methods use the integral form of Maxwell's equations, and they require discretization of only the source of electromagnetic field such as the surface charge density. Integral methods result in dense linear system. The dense system requires a CPU time and memory of the order $O(N^2)$ if solved iteratively, which consequently would be intensive for large-scale problems [3]. Integral methods work best with open-boundary problems but are not suitable for inhomogeneous problems [9]. The Method of Moment (MoM) [10] is one example of integral equation method, where only the surfaces are discretized so fewer points are present and each entry is stored in a dense matrix. Dense matrices are small matrices but they are not as efficient as sparse matrices to solve and they are not amenable to parallelization.

Both differential and integral methods require problem discretization in which general rule of thumb is that the discretisation length is equal to or less than one-tenth the wavelength [1].

In general, solving a complex problem using numerical methods incurs high computational costs in computer-memory and simulation-time. There are three unavoidable sources of errors in numerical solutions; modelling error, truncation error and roundoff error [4]. Modelling error is presented due to several assumptions made in the mathematical model such as the assumptions of linearity or homogeneity, etc. Truncation error is due to the numerical analysis that requires the usage of finite number of terms in some expansions. This error can be reduced by using more terms in an expansion or reducing the discretization length and the time increment. And finally the roundoff error is due to the limited size of the computational memory and

this error can be minimized by the use of double-precision arithmetic. In addition to these errors, a numerical error or dispersion error occurs due to discretizing the problem into finite mesh resolution. Using fine meshes can minimize the numerical dispersion but significantly impacts the computational resources.

Meshes are categorized as structured and unstructured. A structured mesh is a regular array of quadrilateral (squares or rectangles) in 2D problems as shown in Figure 1.1(a) and hexahedron (cubes or rectangular parallelepiped) in 3D problems to discretize the problem space. Unstructured mesh is irregular pattern of triangles in 2D problems as shown in Figure 1.1(b) and tetrahedral in 3D problems [11, 12].

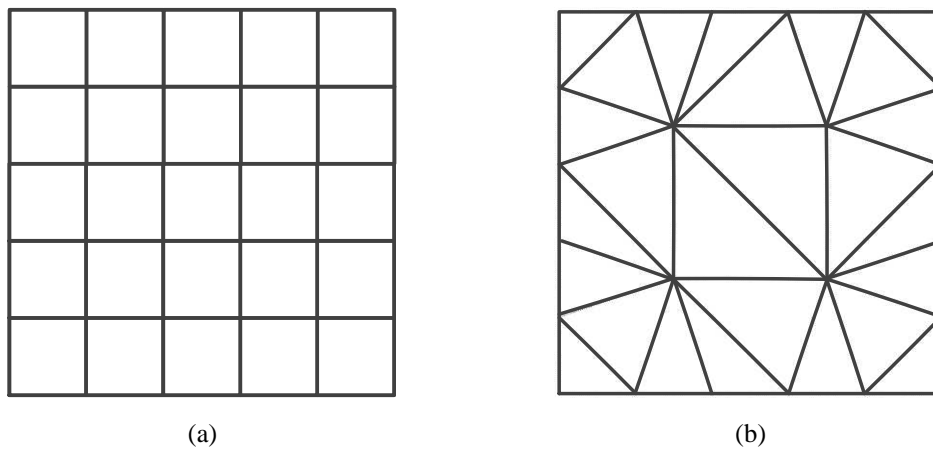


Figure 1.1: Rectangular space discretized using (a) structured and (b) unstructured meshes.

A structured mesh provides straightforward implementation of the numerical methods; this also involves simple indexing of cells and reasonable value of run time since the discretization length is manageable. On the other hand, some problems feature curved domains such as circular resonators which are more difficult to discretize using structured cells. Structured mesh introduces quantization error due to staircase approximation of the curved boundaries as shown in Figure 1.2.

The staircasing error also introduces numerical noise in simulations. These errors can be minimized by reducing the mesh size which in return increases the total run time.

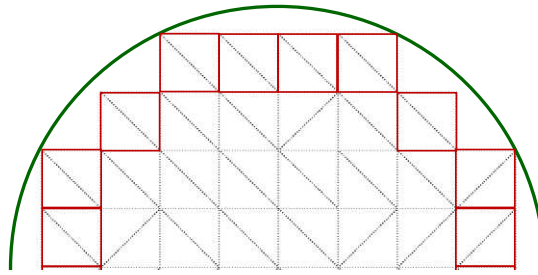


Figure 1.2: Curved boundary modelled by structured meshes, where staircase approximation of the curved boundary causes quantization error.

To use the simplicity of the structured mesh but also be able to accurately model curved geometries and fine features two different types of conformable surface models are used; namely, locally distorted grid models in which the basic Cartesian grid is preserved except those adjacent to the structure surface [13] as shown in Figure 1.3(a), globally distorted grid models (body fitted) in which mesh follows structured non-Cartesian grids that conform to the surface [14-16] as shown in Figure 1.3(b). Multigridding is another meshing technique that uses structured mesh of different resolutions to different areas of the same problem [17-20] as shown in Figure 1.3(c). Both multigridding and variable mesh techniques are used to increase the spatial resolution around small features in the problem. In a variable mesh different sizes of structured mesh are employed to model specifications of the problem space as shown in Figure 1.4(a). As for the multigridding scheme shown in Figure 1.4(b), regions of uniform coarse and uniform fine meshes are employed wherever it is appropriate.

The computational complexity and the multiscale nature of modern problems demands that structured meshes are replaced by unstructured meshes [21-24]. Unstructured meshes use triangles and tetrahedral in 2D and 3D problems, respectively. The benefit of using unstructured meshes is that it is used to discretise geometries that do not fit into rectangular Cartesian coordinates, for example curved waveguides, bends and directional coupler. It proved its efficiency in modelling thin wire embedded in large homogeneous region [25], and modelling optoelectronics devices [26] and micro-resonators [27, 28]. Also, unstructured mesh can be used at the interface between coarse and fine structured meshes in multigridding schemes [23].

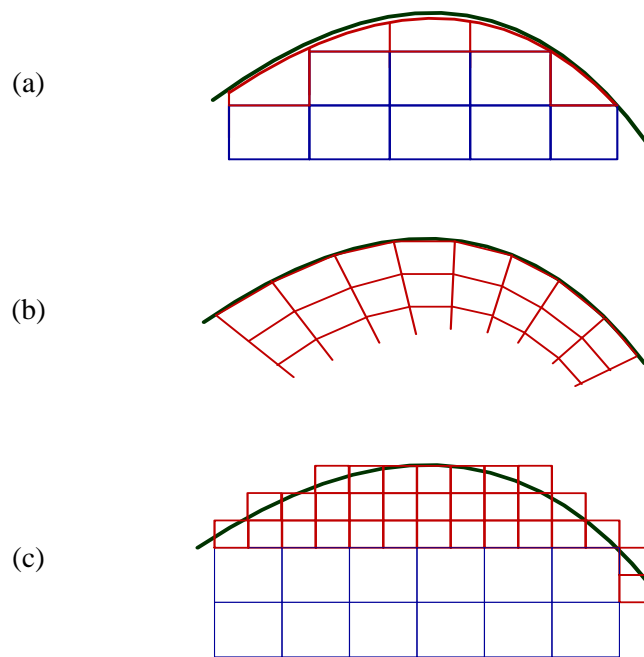


Figure 1.3: Structured modelling of curved surfaces by (a) locally distorted grid, (b) globally distorted grid and (c) multigridding

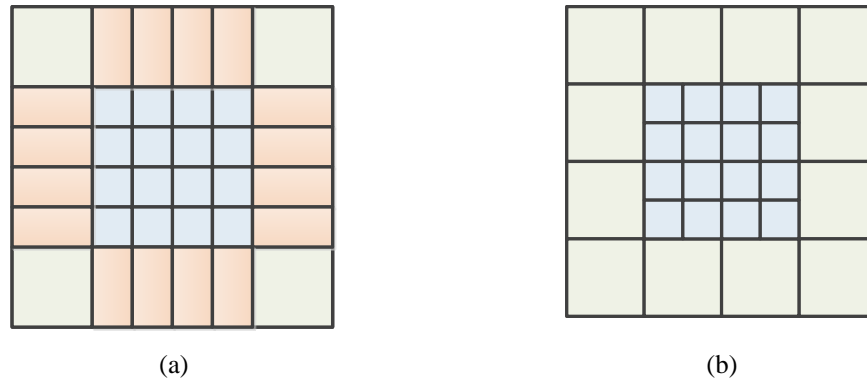


Figure 1.4: (a) variable mesh and (b) multigridding schemes

Unstructured mesh models curved lines using piecewise linear elements as shown in Figure 1.5 in which the curved boundary is discretized by polygon approximation [23, 24, 29]. Unstructured meshes can overall reduce the number of mesh cells and they provide greater freedom in providing fine resolution to one region and coarse resolution to others [30]. However, as each cell has an increased set of attributes to define connectivity and position compared to the structured mesh, unstructured meshes typically involve more complicated algorithms, larger amount of memory and longer pre-processing time to determine the cells relative positions and cells inter-

connectivity; which all together adds to the overall computational runtime. Also, the timestep can be very small in unstructured mesh as well due to the smallest geometry in the problem [23, 31] which leads to long run time.

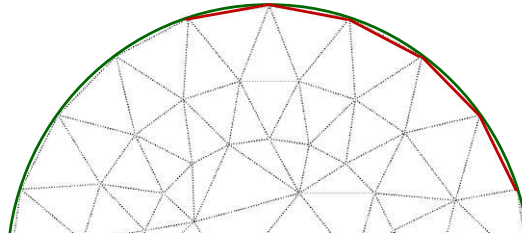


Figure 1.5: curved boundary modelled by unstructured meshes. Triangles offers very low quantization error to the curved boundary.

Different techniques are adopted for unstructured mesh generation; some of the most used techniques are Advancing Front mesh (AFT) and Delaunay mesh [12]. In the first approach the element creation propagates from the boundaries of the domain so points are placed inside the domain while creating the element of the meshed region, whilst Delaunay triangulation refers to particular connectivity for a given set of points [30]. Advancing front mesh provides high quality 2D meshes but not necessarily good at the centre of the domain, and it is suitable for meshing boundary layers but it is not efficient for meshing 3D problems [12]. Delaunay triangulations are also robust and efficient and have the advantage of maximizing the minimum angle.

One of the widely used unstructured models is Delaunay triangulations [30, 32]. Delaunay meshes are well-known set of triangulation of an arbitrary set of points. It has the advantage of maximizing the minimum angle and avoiding skinny triangles which consequently provide good quality triangles [32]. They also provide minimum error for field approximation over a domain [23]. These characteristics have important implications in practice, and stability in numerical computations. In some methods it is better to represent the Delaunay mesh by its dual mesh known as Voronoi [33, 34]. Voronoi mesh [35] is formed by connecting the circumcentres of the Delaunay triangles so each segment in the Voronoi mesh is orthogonal to the original Delaunay mesh as shown in Figure 1.6. More detail on Delaunay triangulations is given in Section 3.2.

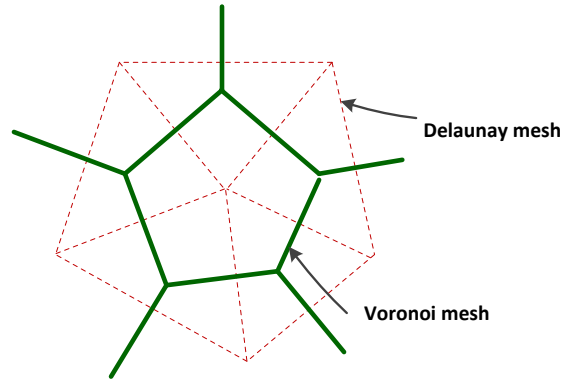


Figure 1.6: Delaunay mesh and corresponding Voronoi mesh

As using the unstructured mesh is computationally expensive it is only used when necessary, however, one of the very useful usage of triangular nodes is that it can be used to stitch together different mesh areas of coarse and fine structured meshes [19] as shown in Figure 1.7.

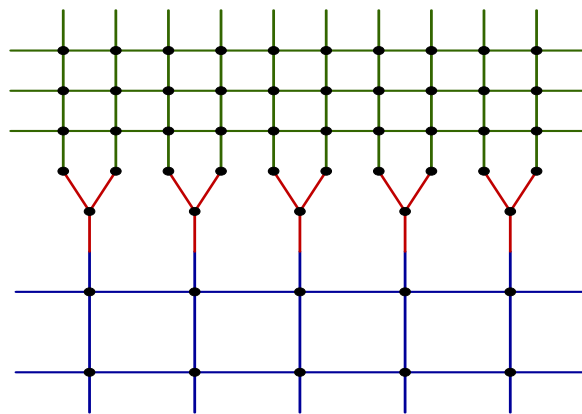


Figure 1.7: Unstructured mesh (red) used at the interface between coarse (blue) and fine (green) structured meshes

The TLM method based upon triangular mesh for two-dimensional (2D) problems [23] and tetrahedral mesh for three-dimensional (3D) problems [24] both have been reported as a general tool and as a special case of multigriding [19, 23, 24, 36]. Both 2D and 3D TLM unstructured meshes are based on Delaunay mesh. The analysis and implementation of two-dimensional TLM based on Delaunay meshes will be displayed in detail in Chapter 3.

Readily available software for 2D and 3D Delaunay-based triangulations [37, 38] discretize the problem domain by the insertion of points that define the problem space.

Then the required mesh quality and mesh density are requested from the mesh generation software, which in return insert additional vertices within the problem space to achieve such demands. Although the criteria of meshing is quite clear in many documents, but obtaining a mesh of good quality is far from being simple.

An important issue that arises in Delaunay triangulation is that the circumcentre of the Delaunay triangle can lay outside the triangle which affects the distance between the two adjacent circumcentres. This distance can be very small or even equal zero. The time step for the TLM is calculated upon the shortest distance between triangle circumcentres [7, 23]. Having a very small or zero distance will lead to infinitesimally small time step which has big impact on the computational resources. In such scenario it is required to investigate approaches that will maximise the minimum distance between triangles circumcentres as will be discussed in Chapter 4.

The dispersion of TLM and FDTD with structured meshes has been investigated and documented in [7, 39-44]. Analytical relations and formulas for dispersion for condensed TLM nodes are reported in [41]. Two-dimensional TLM and FDTD have identical propagation characteristics [39], and both TLM nodes and FDTD mesh are isotropic (or dispersionless) at low frequencies [42]. Three dimensional TLM and FDTD scheme do not have the same propagation characteristics where the FDTD offers better dispersion characteristics [39]. It is proved that numerical dispersion depends on the direction of propagation as have been reported in [7] for 2D structured TLM, where zero dispersion is experienced for waves propagating at 45° through the mesh and the maximum dispersion for waves propagating at 0° angle. Characterization of dispersion error is a critical enabler to allow confident selection of parameters by user and it is never been studied or reported to date for unstructured TLM. Therefore, it is important that the user has reference benchmarks in order to permit them to manage dispersion errors and in most cases these are expressed in terms of known results for simple geometrical scenarios such as free space. A complete study of dispersion error for 2D unstructured TLM is reported in Chapter 5.

1.2 Organization of the thesis

This thesis focuses on the two-dimensional TLM method based on unstructured Delaunay mesh.

Chapter 2 overviews fundamental EM theory including Maxwell's equations, wave equation and boundary conditions. It presents an overview of different types of meshes. Also, it provides an overview of the most used numerical techniques working on structured and unstructured meshes. And finally, it highlights and considers a survey study of common features between TLM and its competitors.

Chapter 3 presents the mathematical derivation of the 2D UTLM technique together with the algorithm of how the author has practically implemented it in the course of this work. It also presents the concept of Delaunay triangulations and its associated parameters. The first contribution of this research develops a simulator that works with both unstructured and structured meshes. The simulator incorporates all the advanced TLM concepts and procedures described in [7, 23] using the object-oriented programming paradigm. Chapter 3 also analyses the accuracy and efficiency of the developed UTLM numerical code on several examples of resonant cavities and captured it to the equivalent structured mesh.

Chapter 4 describes a method for increasing the time step in the 2D UTLM. Since the time step in UTLM is determined by the shortest distance between triangles circumcentres in the meshed problem, all pairs of triangles that share a circumcentres distance shorter than a given threshold are merged together and processed implicitly in the algorithm. Furthermore, a new model for isolating triangles with short link lines located on boundaries is derived. The impact of isolating triangles with short links or merging pair of triangles on the accuracy and run time is investigated for an air-filled PEC circular resonator and a dielectrically loaded PEC circular resonator.

Chapter 5 presents a study of the dispersion and intermodal coupling of the UTLM mesh for 2D unstructured problems. Dispersion of a plane wave is analysed on a rectangular space with an open boundary condition on top and bottom to simulate open space. Dispersion introduced by unstructured meshes is analysed and compared with the results obtained using the structured mesh. Furthermore, the impact of the mesh

quality and size is investigated by monitoring the mode coupling between the excited spatial mode and other spatial modes.

Chapter 6 summarises the main conclusions of the thesis and gives suggestions for future work.

Chapter 2.

A review of unstructured numerical techniques

2.1 Introduction

This chapter will outline the fundamental concepts of electromagnetics including Maxwell's equations, wave equation, boundary conditions and plane wave solution. Widely used differential numerical methods including Finite Element Method (FEM), Finite Difference Time Domain (FDTD) and Transmission Line Modelling (TLM) will be overviewed with special attention to conventional TLM. Different types of meshing techniques are also discussed.

2.2 Maxwell's equations and wave equation

Maxwell's equation describe the relationship between the electric and magnetic fields that form the electromagnetic wave. The differential form of time varying Maxwell's equations can be expressed in differential form as [45],

$$\nabla \times \bar{E} = -\mu \frac{\partial \bar{H}}{\partial t}, \quad (2.1.a)$$

$$\nabla \times \bar{H} = \bar{J} + \varepsilon \frac{\partial \bar{E}}{\partial t}, \quad (2.1.b)$$

$$\nabla \cdot \varepsilon \bar{E} = \rho_v, \quad (2.1.c)$$

$$\nabla \cdot \mu \bar{H} = 0. \quad (2.1.d)$$

where \bar{E} is the electric field vector [V/m], \bar{H} is the magnetic field vector [A/m], ρ_v is the electric charge density [coul/m³], the current density $\bar{J} = \sigma \bar{E}$ where σ medium conductivity, $\varepsilon = \varepsilon_0 \varepsilon_r$, $\mu = \mu_0 \mu_r$ are the medium permittivity and permeability, respectively. Note than ε_0 is the free space permittivity and has the value 8.854×10^{-12}

F/m and μ_0 is the free space permeability of value $4\pi \times 10^{-7}$ H/m, ϵ_r and μ_r are the medium relative permittivity and permeability, respectively.

The source of the electromagnetic fields is the electric charge and the electric current, which are expressed by local densities known as charge density ρ_v and current density \vec{J} .

Maxwell's equations can also be given in the integral form as,

$$\oint_L \vec{E} \cdot d\vec{l} = -\frac{\partial}{\partial t} \int_S \mu \vec{H} \cdot d\vec{S}, \quad (2.2.a)$$

$$\oint_C \vec{H} \cdot d\vec{l} = \int_S (\sigma \vec{E} + \epsilon \frac{\partial \vec{E}}{\partial t}) \cdot d\vec{S}, \quad (2.2.b)$$

$$\oint_S \epsilon \vec{E} \cdot d\vec{S} = \int_{vol} \rho_v dv, \quad (2.2.c)$$

$$\oint_S \mu \vec{H} \cdot d\vec{S} = 0. \quad (2.2.d)$$

where L, C, S and vol denote line, contour, surface and volume, respectively.

Taking the curl of Equation (2.1.a) and then substituting with Equation (2.1.b) gives

$$\nabla \times \nabla \times \vec{E} = -\mu \frac{\partial}{\partial t} (\nabla \times \vec{H}) = -\mu \epsilon \frac{\partial^2 \vec{E}}{\partial t^2}, \quad (2.3)$$

Using the identity $\nabla \times \nabla \times \vec{E} = \nabla(\nabla \cdot \vec{E}) - \nabla^2 \vec{E}$, results in the electric field wave equation or Helmholtz equation expressed as

$$\nabla^2 \vec{E} - \mu \epsilon \frac{\partial^2 \vec{E}}{\partial t^2} = 0. \quad (2.4)$$

The magnetic field wave equation is derived similarly and is given by,

$$\nabla^2 \bar{H} - \mu\epsilon \frac{\partial^2 \bar{H}}{\partial t^2} = 0. \quad (2.5)$$

Equations (2.4) and (2.5) are the equations of motion of the electromagnetic waves in the medium under consideration. Solving either of these two equations and using Maxwell's relationship between electric and magnetic field will produce full set of field components.

2.3 Transverse modes

Unguided waves in free space can be expressed by the superposition of plane waves. For waveguides where boundaries are imposed by the presence of metal walls or dielectric material propagation is expressed by transverse modes. These modes are classified into transverse electric TE and transverse magnetic TM modes.

Expanding the curl in equations (2.1.a) and (2.1.b) leads to the following set of equations,

$$\frac{\partial E_z}{\partial y} - \frac{\partial E_y}{\partial z} = -j\omega\mu H_x, \quad (2.6.a)$$

$$\frac{\partial E_z}{\partial x} - \frac{\partial E_x}{\partial z} = j\omega\mu H_y, \quad (2.6.b)$$

$$\frac{\partial E_y}{\partial x} - \frac{\partial E_x}{\partial y} = -j\omega\mu H_z, \quad (2.6.c)$$

$$\frac{\partial H_z}{\partial y} - \frac{\partial H_y}{\partial z} = j\omega\mu E_x, \quad (2.6.d)$$

$$\frac{\partial H_z}{\partial x} - \frac{\partial H_x}{\partial z} = -j\omega\mu E_y, \quad (2.6.e)$$

$$\frac{\partial H_y}{\partial x} - \frac{\partial H_x}{\partial y} = j\omega\mu E_z, \quad (2.6.f)$$

Transverse electric (TE) waves are characterized by $E_z=0$ and $H_z \neq 0$, and Equations (2.6) reduce to,

$$\frac{\partial E_y}{\partial x} - \frac{\partial E_x}{\partial y} = -\mu \frac{\partial H_z}{\partial t}, \quad (2.7.a)$$

$$\frac{\partial H_z}{\partial y} = \varepsilon \frac{\partial E_x}{\partial t}, \quad (2.7.b)$$

$$\frac{\partial H_z}{\partial x} = -\varepsilon \frac{\partial E_y}{\partial t}. \quad (2.7.c)$$

Transverse magnetic (TM) waves are characterized by $H_z=0$ and $E_z \neq 0$, for which Equations (2.6) reduce to,

$$\frac{\partial E_z}{\partial y} = -\mu \frac{\partial H_x}{\partial t}, \quad (2.8.a)$$

$$\frac{\partial E_z}{\partial x} = \mu \frac{\partial H_y}{\partial t}, \quad (2.8.b)$$

$$\frac{\partial H_y}{\partial x} - \frac{\partial H_x}{\partial y} = \varepsilon \frac{\partial E_z}{\partial t}. \quad (2.8.c)$$

2.4 General plane wave equation

The wave equation for electric field (Equation (2.4)) expanded in 3D system becomes,

$$\frac{\partial^2 \bar{E}}{\partial x^2} + \frac{\partial^2 \bar{E}}{\partial y^2} + \frac{\partial^2 \bar{E}}{\partial z^2} - \frac{1}{u^2} \frac{\partial^2 \bar{E}}{\partial t^2} = 0, \quad (2.9)$$

where \bar{E} is the electric field vector and u is the wave velocity which is expressed as,

$$u = \frac{1}{\sqrt{\mu\varepsilon}} \quad (2.10)$$

The wave velocity u is equal to $c = \frac{1}{\sqrt{\mu_0 \varepsilon_0}}$ (m/s) if the wave is propagating in free space.

The vector wave equation (2.9) can be expressed for x , y and z directions by the scalar wave equations,

$$\frac{\partial^2 E_x}{\partial x^2} + \frac{\partial^2 E_x}{\partial y^2} + \frac{\partial^2 E_x}{\partial z^2} - \frac{1}{u^2} \frac{\partial^2 E_x}{\partial t^2} = 0, \quad (2.11.a)$$

$$\frac{\partial^2 E_y}{\partial x^2} + \frac{\partial^2 E_y}{\partial y^2} + \frac{\partial^2 E_y}{\partial z^2} - \frac{1}{u^2} \frac{\partial^2 E_y}{\partial t^2} = 0, \quad (2.11.b)$$

$$\frac{\partial^2 E_z}{\partial x^2} + \frac{\partial^2 E_z}{\partial y^2} + \frac{\partial^2 E_z}{\partial z^2} - \frac{1}{u^2} \frac{\partial^2 E_z}{\partial t^2} = 0. \quad (2.11.c)$$

The scalar wave equation is used to analyse bodies illuminated by a normally incident field such as the propagation of plane waves, TE and TM modes in waveguides and weakly guiding optical fibres [46]. On the other hand, vector wave equations are used for analysing bodies illuminated by obliquely incident excitation, scattering problems or propagation in anisotropic, inhomogeneous or dispersive materials [47].

Assuming a time dependent field in source-free, linear, isotropic and homogeneous region, the time derivative can be replaced by $j\omega$. If the field has only x-component, Equation (2.9) is then expressed by scalar wave equation,

$$\frac{\partial^2 E_x}{\partial x^2} + \frac{\partial^2 E_x}{\partial y^2} + \frac{\partial^2 E_x}{\partial z^2} + k^2 E_x = 0. \quad (2.12)$$

where $k = \omega\sqrt{\mu\varepsilon}$ is the medium wave number. Note that by setting $k=0$ in Equation (2.12), a solution of the electrostatic problem can be achieved.

To find a solution for plane wave propagation, Equation (2.12) is solved by the method of separation in which the electric field function is assumed to constitute three functions of each coordinate [45],

$$E_x(x, y, z) = f(x)g(y)h(z). \quad (2.13)$$

Substituting Equation (2.13) into Equation (2.12) and dividing by $f(x)g(y)h(z)$ gives

$$\frac{f''(x)}{f(x)} + \frac{g''(y)}{g(y)} + \frac{h''(z)}{h(z)} + k^2 = 0. \quad (2.14)$$

where “ ∇^2 ” denotes the second derivative. Each term of Equation (2.14) must equal a constant since functions $f(x)$, $g(y)$ and $h(z)$ are independent of each other. Constants are defined as follows [45]

$$\frac{f''(x)}{f(x)} = -k_x^2, \quad \frac{g''(y)}{g(y)} = -k_y^2, \quad \frac{h''(z)}{h(z)} = -k_z^2, \quad (2.15)$$

reducing Equation (2.14) to

$$k_x^2 + k_y^2 + k_z^2 = k^2. \quad (2.16)$$

Then Equation (2.12) can be separated into three independent ordinary differential equations [45]

$$\begin{aligned} \frac{\partial^2 f(x)}{\partial x^2} + k_x^2 f(x) &= 0, \\ \frac{\partial^2 g(y)}{\partial y^2} + k_y^2 g(y) &= 0, \\ \frac{\partial^2 h(z)}{\partial z^2} + k_z^2 h(z) &= 0, \end{aligned} \quad (2.17)$$

The solution of these three equations are of the form $e^{\mp k_x x}$, $e^{\mp k_y y}$ and $e^{\mp k_z z}$, respectively, where (-) and (+) signs refer to forward and backward propagating waves, respectively.

Then, the complete solution for the forward propagating field component of E_x can be written as,

$$E_x(x, y, z) = A e^{-j(k_x x + k_y y + k_z z)}. \quad (2.18)$$

where A is the signal amplitude.

For an arbitrary direction of propagation, the wave number \bar{k} is a vector defined generally as [45],

$$\bar{k} = k_x \hat{x} + k_y \hat{y} + k_z \hat{z} = k \hat{n}. \quad (2.19)$$

where \hat{n} is the unit vector in the direction of propagation.

In the case of arbitrary direction of propagation, each field component assumes the form of Equation (2.18) as,

$$\begin{aligned} E_x(x, y, z) &= A e^{-j\bar{k} \cdot \bar{r}}, \\ E_y(x, y, z) &= B e^{-j\bar{k} \cdot \bar{r}}, \\ E_z(x, y, z) &= C e^{-j\bar{k} \cdot \bar{r}}, \end{aligned} \quad (2.20)$$

where $\bar{r} = x\hat{x} + y\hat{y} + z\hat{z}$ is the vector position.

The divergence theorem in general is expressed as,

$$\nabla \cdot \bar{E} = \frac{\partial E_x}{\partial x} + \frac{\partial E_y}{\partial y} + \frac{\partial E_z}{\partial z} = 0. \quad (2.21)$$

This equation must also be applied to satisfy Maxwell's equations which implies that E_x , E_y and E_z must each have the same variation in x , y and z consequently k_x , k_y and k_z are the same [45].

The general electric field vector is expressed as,

$$\bar{E}(x, y, z) = \bar{E}_o e^{-j\bar{k} \cdot \bar{r}}, \quad (2.22)$$

where $\bar{E}_o = A\hat{x} + B\hat{y} + C\hat{z}$.

The solution in Equation (2.22) represents a plane wave of amplitude \bar{E}_o propagating in the direction \bar{k} .

The time-domain expression of Equation (2.22) is given as,

$$\bar{E}(x, y, z) = \bar{E}_o \cos(\bar{k} \cdot \bar{r} - \omega t). \quad (2.23)$$

The magnetic field can be found from Maxwell's curl equation as,

$$\begin{aligned}\bar{H} &= \frac{j}{\omega\mu} \nabla_x \bar{E}, \\ \bar{H} &= \frac{1}{\eta} \hat{n}_x \bar{E}.\end{aligned}\tag{2.24}$$

where $\eta = \frac{\omega\mu}{k}$ is the medium intrinsic impedance ($=\frac{1}{\sqrt{\epsilon_0\mu_0}}$ (Ω) for free space).

For an x-component electric field propagating in the z-direction and uniform in the x and y directions (i.e. $\partial/\partial x = \partial/\partial y = 0$), the scalar wave Equation (2.12) reduces to,

$$\frac{\partial^2 E_x}{\partial z^2} + k^2 E_x = 0.\tag{2.25}$$

which has the general solution

$$E_x(z) = E_o^+ e^{-jkz} + E_o^- e^{+jkz}.\tag{2.26}$$

The solution in time-domain for forward propagation is expressed as,

$$E_x(z) = E_o^+ \cos(kz - \omega t).\tag{2.27}$$

and the general form of the plane wave solution is,

$$\bar{E}(z) = \hat{x}A \cos(kz - \omega t).\tag{2.28}$$

2.5 Boundary conditions

When electromagnetic fields exist in material media, the field vectors are related to each other by the constitutive relations known as boundary conditions. The unknown amplitude coefficients A, B and C in the general solution of the wave equation (Equation (2.20)) are found by applying appropriate boundary conditions for the problem under investigation.

Many problems involve boundaries with good conductors such as waveguide metal walls. The boundary conditions on the perfect metal boundary are [45],

$$\begin{aligned}
\hat{n} \cdot \varepsilon \bar{E} &= \rho_s, \\
\hat{n} \times \bar{E} &= 0, \\
\hat{n} \cdot \mu \bar{H} &= 0, \\
\hat{n} \times \bar{H} &= \bar{J}_s.
\end{aligned} \tag{2.29}$$

where \hat{n} is the unit vector normal to the conductor, ρ_s and J_s are the electric surface charge density and surface current density, respectively.

The boundary conditions at the interface between two media characterized by dielectric permittivity ε_r and magnetic permeability μ_r are expressed by [45],

$$\begin{aligned}
\hat{n} \cdot \varepsilon_{r1} \bar{E}_1 &= \hat{n} \cdot \varepsilon_{r2} \bar{E}_2, \\
\hat{n} \times \bar{E}_1 &= \hat{n} \times \bar{E}_2, \\
\hat{n} \cdot \mu_{r1} \bar{H}_1 &= \hat{n} \cdot \mu_{r2} \bar{H}_2, \\
\hat{n} \times \bar{H}_1 &= \hat{n} \times \bar{H}_2.
\end{aligned} \tag{2.30}$$

where medium 1 is characterized by $(\varepsilon_{r1}, \mu_{r1})$ and medium 2 by $(\varepsilon_{r2}, \mu_{r2})$, \bar{E}_1, \bar{H}_1 are the electric and magnetic fields in medium 1, respectively, \bar{E}_2, \bar{H}_2 are the electric and magnetic fields in medium 2, respectively and \hat{n} is the unit vector normal to the interface between the two media.

2.6 Numerical techniques for electromagnetic problems

Not all problems in electromagnetics can be solved exactly analytically; this requires finding an approximate solution where analytical methods fail to solve a problem. It is required to find an approximate solution for Maxwell's equations subject to boundary conditions.

In solving EM wave propagation, the target is to approximate relevant equations in a numerically stable way. Stability means that errors in the input and intermediate calculations do not accumulate and lead to meaningless output. There are many ways of doing this, all with its own advantages and disadvantages. The most popular

methods used to solve Maxwell's differential equations are Finite Element method (FEM), Finite Difference Time Domain (FDTD) and Transmission Line Modelling method (TLM). Several papers intended to provide some case studies for the sake of determining the point of strengths of these methods and to prove the exchangeability of FE, FDTD and TLM [48-54].

2.6.1 Finite Element Method (FEM)

The Finite Element Method (FEM) [4, 8, 55, 56] is a mature and powerful numerical tools for modelling complex geometries and inhomogeneous media that has a history dating back to the 1960s. It can also be applied to all Boundary Value Problems (BVP). FEM has been introduced in electromagnetic applications since 1968 and it has been employed to diverse areas such as waveguides, microstrip, and absorption of EM radiation in biological bodies [57-61]. The FEM proved its flexibility and versatility due to its ability of using adaptive meshes [1] (where a solution is achieved with coarse mesh then meshes are getting refined at the places where the field changes rapidly, the simulation is re-run and meshes are refined till the solution converges). FEM does not model unbounded radiation problems as effectively as other techniques. Also, for different applications FEM approximations are specific to each problem and the resulting equations are difficult to solve. Time stepping FE is not computationally efficient; one either has to solve a linear equation problem every time step, or approximate the relevant sparse matrix to a diagonal one in what is called "mass lumping" approach which introduces errors [4].

The FEM involves four basic steps which begins by discretising the problem domain into subdomains known as elements, then deriving governing equations for each element followed by assembling element equations into the solution region and finally solving the system of equation derived [4].

The FEM uses unstructured meshes since the beginning of implementation. The problem domain is discretized into non-overlapping elements, normally triangles, but other shapes can be used such as quadrilateral and rectangles for 2D problems as shown in Figure 2.1(a), and tetrahedron and hexahedron for 3D problems as shown in Figure 2.1(b) [4, 62, 63].

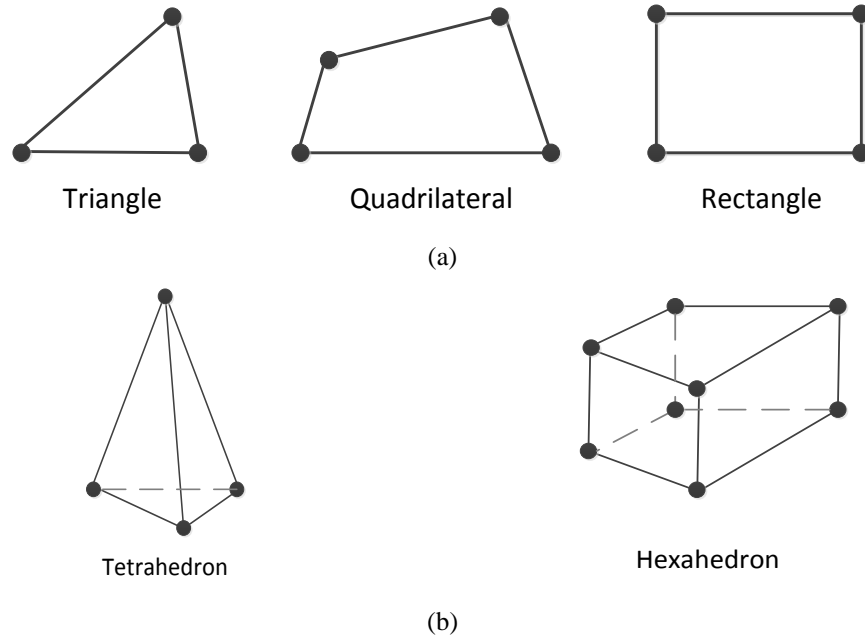


Figure 2.1: Different types of meshes used to discretise (a) 2D and (b) 3D problems

Consider the scalar inhomogeneous Helmholtz's wave equation,

$$\nabla^2 \Phi + k^2 \Phi = g. \quad (2.31)$$

where Φ is the field quantity that equals to E_z for TM mode or H_z for TE mode, $k = \omega\sqrt{\mu\epsilon}$ is the medium wavenumber and g is the source function. This scalar wave equation can be used in electromagnetics to analyse propagation of plane wave in geometries that does not change dramatically. For scattering problems vector wave equations are solved by FEM in [47, 65].

Variational methods [64] work on finding a functional $\Phi(X)$ that satisfies the same boundary conditions as X . This functional are obtained by a trial and error approach. Variational methods reduce the differential or integral forms of Maxwell's equations to the equivalent variational problem. The principle of the variational approach can be explained by defining an eignvalue problem of the form,

$$LX = \lambda X. \quad (2.32)$$

where L is the operator, X is the eigenvector and λ is the eigenvalue.

The FEM solve Equation (2.31) by minimization of a corresponding functional given by [46],

$$I(\Phi) = \frac{1}{2} \iint_S [|\nabla\Phi|^2 - k^2\Phi^2 + 2\Phi g] dS. \quad (2.33)$$

where S is the area of the discretized domain such as the waveguide cross sectional area.

The problem space is discretized into small elements such as triangles. We seek an approximation for the field within an element e and then to interrelate the field distribution in different elements such that the field is continuous across adjacent elements boundaries. The function Φ_e at a point of coordinates (x,y) inside the element can be approximated as [45],

$$\Phi_e = a + bx + cy + dx^2 + fy^2 + gxy. \quad (2.34)$$

where a, b, c, d, f and g are unknown coefficients.

For simplicity, Equation (2.34) is reduced to the linear term as [45],

$$\Phi_e = a + bx + cy. \quad (2.35)$$

Consider the triangle shown in Figure 2.2, the linear approximation of Equation (2.35) is applied at each vertex as following,

$$\begin{aligned} \Phi_{e1} &= a + bx_1 + cy_1, \\ \Phi_{e2} &= a + bx_2 + cy_2, \\ \Phi_{e3} &= a + bx_3 + cy_3. \end{aligned} \quad (2.36)$$

where (x_1, y_1) , (x_2, y_2) and (x_3, y_3) are the coordinates of triangle vertices.

The potential Φ and source function g is expressed in terms of the shape function α_i over a triangular element as [4],

$$\Phi_e(x, y) = \sum_{i=1}^3 \alpha_i \Phi_{ei}, \quad (2.37)$$

$$g_e(x, y) = \sum_{i=1}^3 \alpha_i g_{ei} \quad (2.38)$$

where e indicates the triangular element, i is the index of nodal point of such element and $\alpha_i = a_i + b_i x + c_i y$ is known as the shape function over a triangular element and Φ_{ei} is the value of Φ_e at the nodal point i of element [4, 45].

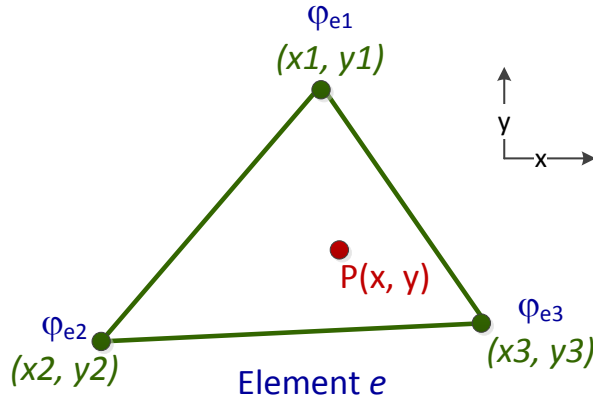


Figure 2.2: A first order triangle element

Substituting Equations (2.37) and (2.38) into Equation (2.33) leads to [4],

$$I(\Phi_e) = \frac{1}{2} \sum_{i=1}^3 \sum_{j=1}^3 \Phi_{ei} \Phi_{ej} \iint \nabla \alpha_i \cdot \nabla \alpha_j dS - \frac{k^2}{2} \sum_{i=1}^3 \sum_{j=1}^3 \Phi_{ei} \Phi_{ej} \iint \alpha_i \alpha_j dS + \sum_{i=1}^3 \sum_{j=1}^3 \Phi_{ei} \Phi_{ej} \iint \alpha_i \alpha_j dS. \quad (2.39)$$

or in a more compact form,

$$I(\Phi_e) = \frac{1}{2} [\Phi_e]^t [C^{(e)}] [\Phi_e] - \frac{k^2}{2} [\Phi_e]^t [T^{(e)}] [\Phi_e] + [\Phi_e]^t [T^{(e)}] [G_e]. \quad (2.40)$$

where $[\Phi_e]^t = [\Phi_{e1} \quad \Phi_{e2} \quad \Phi_{e3}]^t$, $[G_e] = [g_{e1} \quad g_{e2} \quad g_{e3}]$, $[C^{(e)}]$ is the element coefficient matrix. The element $C_{ij}^{(e)}$ of the matrix represents the coupling between nodes i and j such as $C_{12}^{(e)}$, $C_{23}^{(e)}$ and $C_{13}^{(e)}$, for example $C_{12}^{(e)}$ is expressed as,

$$\begin{aligned}
C_{12}^{(e)} &= \int \nabla \alpha_1 \cdot \nabla \alpha_2 dS \\
&= \frac{1}{4A^2} [(y_2 - y_3)(y_3 - y_1) + (x_3 - x_2)(x_1 - x_3)] \int dS \\
&\quad - \frac{1}{4A} [(y_2 - y_3)(y_3 - y_1) + (x_3 - x_2)(x_1 - x_3)] \int dS \quad (2.41)
\end{aligned}$$

where (x_1, y_1) , (x_2, y_2) and (x_3, y_3) are the coordinates of triangle vertices. The self coupling in the same element is expressed by $C_{ii}^{(e)}$ (i.e. for a triangle, we have $C_{11}^{(e)}$, $C_{22}^{(e)}$ and $C_{33}^{(e)}$) For example $C_{11}^{(e)}$ is expressed by,

$$C_{11}^{(e)} = \frac{1}{4A} [(y_2 - y_3)^2 + (x_3 - x_2)^2]. \quad (2.42)$$

And finally the matrix element of $[T^{(e)}]$ is expressed by,

$$T_{ij}^{(e)} = \int \alpha_i \alpha_j dS. \quad (2.43)$$

For triangular element, Equation (2.43) is expressed as

$$T_{ij}^{(e)} = \begin{cases} A/12, & i \neq j \\ A/6 & i = j \end{cases} \quad (2.44)$$

Equation (2.40) can be then applied for all triangles in the meshed domain, then the integration in Equation (2.33) can be expressed in the discrete form,

$$I(\Phi) = \sum_{e=1}^N I(\Phi_e) = \frac{1}{2} [\Phi]^t [C] [\Phi] - \frac{k^2}{2} [\Phi]^t [T] [\Phi] + [\Phi]^t [T] [G]. \quad (2.45)$$

where $[\Phi]$, $[G]$, $[C]$ and $[T]$ are known as the global matrices that comprises of the local matrices $[\Phi_e]$, $[G_e]$, $[C^{(e)}]$ and $[T^{(e)}]$.

Consider the special case of no source function in the problem space $g=0$ the last term in Equation (2.45) will vanish. And if the free nodes are numbered before the prescribed nodes, then Equation (2.45) will be in the form,

$$I = \frac{1}{2} [\Phi_f \quad \Phi_p] \begin{bmatrix} C_{ff} & C_{fp} \\ C_{pf} & C_{pp} \end{bmatrix} \begin{bmatrix} \Phi_f \\ \Phi_p \end{bmatrix} - \frac{k^2}{2} [\Phi_f \quad \Phi_p] \begin{bmatrix} T_{ff} & T_{fp} \\ T_{pf} & T_{pp} \end{bmatrix} \begin{bmatrix} \Phi_f \\ \Phi_p \end{bmatrix}. \quad (2.46)$$

Then,

$$\frac{\partial I}{\partial \Phi_f} = 0 = [C_{ff} \quad C_{fp}] \begin{bmatrix} \Phi_f \\ \Phi_p \end{bmatrix} - \frac{k^2}{2} [T_{ff} \quad T_{fp}] \begin{bmatrix} \Phi_f \\ \Phi_p \end{bmatrix}. \quad (2.47)$$

And for TM modes $\Phi_p=0$ and Equation (2.47) becomes,

$$[C_{ff} - k^2 T_{ff}] \Phi_f = 0. \quad (2.48)$$

Multiplying Equation (2.48) by T_{ff}^{-1} gives,

$$[T_{ff}^{-1} C_{ff} - k^2 I] \Phi_f = 0. \quad (2.49)$$

where I is the unit matrix. Equation (2.49) is in the form of $(A - \lambda I)X = 0$; the typical eigenproblem equation which can be solved for the eigenvalues λ and eigenvectors X of Helmholtz's equation.

2.6.2 Finite Difference Time Domain (FDTD)

The FDTD [2, 4, 6, 66, 67] technique is a time-domain differential numerical method. It calculates the electric and magnetic fields everywhere in the computational domain as they evolve in time. FDTD is robust, efficient, versatile and adaptable to complex geometries. It is easy to understand and easy to implement method [4]. FDTD can be implemented in general algorithm that can be applied to any problem. It allows modelling of complex inhomogeneous configurations and performs better modelling of unbounded problems than FE method [1]. FDTD provides direct solution to Maxwell's equations, which means that analyst can examine the radiation, propagation, and scattering of electric and magnetic fields as the computations proceed and the field distribution within the problem space can be monitored at any time step [68-74]. FDTD is used for a variety of applications such as microstrip [75-77], waveguides [78-80], antennas [77, 81], optoelectronics devices [82] and biological interactions [83, 84]. However, it exhibits problem of slow convergence for resonance problems and requires large memory requirements for inhomogeneous waveguide structures [4]. Standard FDTD has the inability to handle curved boundaries which led to the development of the method over non-orthogonal and unstructured meshes [85-

95]. The FDTD includes more complicated approach to terminate the problem space by introducing artificial termination conditions including PML to absorb incident and scattered fields. Care must be taken to minimize the error associated with such boundaries which dictate the accuracy of the FDTD [4]. Also, far-field calculations force the computational domain to be excessively large and requires extended amount of pre-processing [96].

The FDTD method is directly derived from discretizing the differential form of the Maxwell's equations. Maxwell's equations are solved by using the central difference technique to express the derivative over a spatial grid known as Yee cell [6, 68, 69]. The region being modeled is represented by two interleaved grids of discrete points. One grid contains the points at which the magnetic field is evaluated and the second grid contains the points at which the electric field is evaluated as shown in Figure 2.3 [6]. Note that i, j and k are integers in the x, y and z directions, respectively. The electric (E_x, E_y, E_z) and magnetic (H_x, H_y, H_z) field vectors are assigned to each grid cell. Each facet of the Yee's cubic cell is defined by two electric field components tangential to the facet and a magnetic field component normal to the facet in the third direction.

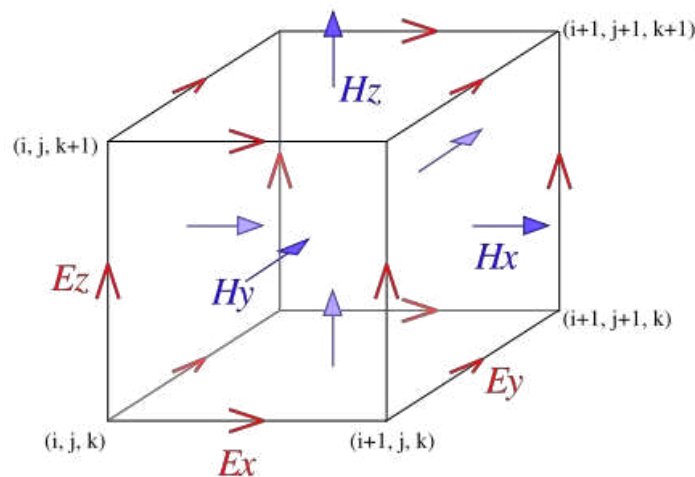


Figure 2.3: Yee cube [96]

The Yee algorithm [6] is based on finite difference approximations of the space derivatives and time derivatives. Consider any field component f as a function of space and time evaluated at a discrete point in the space lattice (x, y, z) and at a discrete point in time t , then u can be written as [69],

$$f(i\Delta x, j\Delta y, k\Delta z, n\Delta t) = f_{i,j,k}^n. \quad (2.50)$$

where the $i, j,$ and k indices represent the spatial positions and the n index represents time. $\Delta x, \Delta y$ and Δz are the spatial increments in x, y and z directions, respectively and Δt is the time increment.

Then Yee's expression for the first spatial derivative of f in the x -direction, evaluated at a fixed time is [6],

$$\frac{\partial}{\partial x} f(i\Delta x, j\Delta y, k\Delta z, n\Delta t) = \frac{f_{i+1/2,j,k}^n - f_{i-1/2,j,k}^n}{\Delta x} + O[(\Delta x)^2]. \quad (2.51)$$

with space finite difference over $\pm\Delta x/2$. $O[(\Delta x)^2]$ is the truncation error in Taylor series expansion, which is proportional to the squared spatial discretization.

The Yee's expression for the first time derivative of f , evaluated at the fixed space point (i,j,k) follows by analogy [6],

$$\frac{\partial}{\partial t} f(i\Delta x, j\Delta y, k\Delta z, n\Delta t) = \frac{f_{i,j,k}^{n+1/2} - f_{i,j,k}^{n-1/2}}{\Delta t} + O[(\Delta t)^2]. \quad (2.52)$$

For electromagnetic problems, Yee's algorithm is applied to the space and time derivative of Maxwell's equations.

TM modes are expressed by E_z, H_x and H_y field components as expressed in Equations (2.7). The field components are distributed in 2D Yee's Cell as shown in Figure 2.4, where H_x and H_y components are directed along the x and y direction, respectively, and E_z is normal to the x - y plane.

The derivative of Equations (2.7) can be expressed as,

$$\lim_{\Delta t \rightarrow 0} \frac{\Delta H_y}{\Delta t} = \frac{1}{\mu} \lim_{\Delta x \rightarrow 0} \frac{\Delta E_z}{\Delta x} \quad (2.53.a)$$

$$\lim_{\Delta t \rightarrow 0} \frac{\Delta H_x}{\Delta t} = -\frac{1}{\mu} \lim_{\Delta y \rightarrow 0} \frac{\Delta E_z}{\Delta y} \quad (2.53.b)$$

$$\lim_{\Delta t \rightarrow 0} \frac{\partial E_z}{\Delta t} = \frac{1}{\varepsilon} \left[\lim_{\Delta x \rightarrow 0} \frac{\partial H_y}{\Delta x} - \lim_{\Delta y \rightarrow 0} \frac{\partial H_x}{\Delta y} \right]. \quad (2.53.c)$$

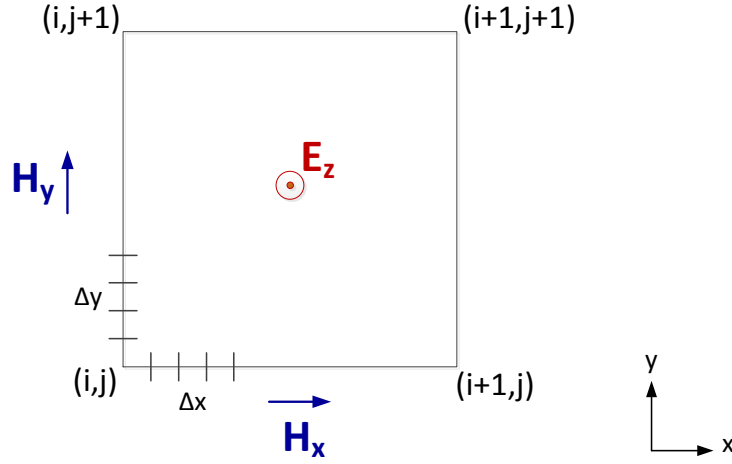


Figure 2.4: 2D Yee's cell formulation for TM mode

Discretizing space and time around a point (x,t) , then applying central differences to Equation (2.53.a) to relate the derivatives of the neighbouring discrete fields we get,

$$\frac{H_y \left(t_n + \frac{\Delta t}{2} \right) - H_y \left(t_n - \frac{\Delta t}{2} \right)}{\Delta t} = \frac{1}{\mu} \frac{E_z \left(x_i + \frac{\Delta x}{2} \right) - E_z \left(x_i - \frac{\Delta x}{2} \right)}{\Delta x}. \quad (2.54)$$

or in other terms,

$$\frac{H_y|_{i,j}^{n+1/2} - H_y|_{i,j}^{n-1/2}}{\Delta t} = \frac{1}{\mu} \frac{E_z|_{i+1/2,j}^n - E_z|_{i-1/2,j}^n}{\Delta x}. \quad (2.55)$$

The value of the H field at point x and at time $t+1/2$ is approximated by two E-field spatial values at $x+1/2$ and $x-1/2$ and depends on the previous H-field temporal value at $t-1/2$.

Similarly, applying the central difference for (2.53.b) leads to,

$$\frac{H_x|_{i,j}^{n+1/2} - H_x|_{i,j}^{n-1/2}}{\Delta t} = \frac{1}{\mu} \frac{E_z|_{i,j+1/2}^n - E_z|_{i,j-1/2}^n}{\Delta y}. \quad (2.56)$$

And finally, the central difference for Equation (2.53.c) leads to

$$\begin{aligned} \frac{E_z|_{i,j}^{n+1/2} - E_z|_{i,j}^n}{\Delta t} &= \frac{1}{\varepsilon} \left[\left(\frac{H_y|_{i+1/2,j}^{n+1/2} - H_y|_{i-1/2,j}^{n+1/2}}{\Delta x} \right) \right. \\ &\quad \left. - \left(\frac{H_x|_{i,j+1/2}^{n+1/2} - H_x|_{i,j-1/2}^{n+1/2}}{\Delta y} \right) \right]. \end{aligned} \quad (2.57)$$

The resolution of the grid is in practice determined by the dimensions of the smallest feature in the problem. In one time step, any point on the wave must not travel more than one cell to its nearest neighbours. The condition for numerical stability in one dimension is that [6]

$$\Delta t \leq \frac{\Delta x}{c}. \quad (2.58)$$

where c is the free space velocity and Δx is cell size over one direction. In 2D case and if the discretization length is the same in both directions, the condition becomes,

$$\Delta t \leq \frac{\Delta x}{c\sqrt{2}}. \quad (2.59)$$

To guarantee numerical stability in the general 3D case, Courant condition [6] must be satisfied,

$$\Delta t \leq \frac{1}{c \sqrt{\left(\frac{1}{\Delta x}\right)^2 + \left(\frac{1}{\Delta y}\right)^2 + \left(\frac{1}{\Delta z}\right)^2}}. \quad (2.60)$$

where Δx , Δy and Δz are the discretization length in x , y and z directions, respectively.

For open boundary problems, the problem is placed within an infinite free-space volume which is not practical to numerically discretise. The numerical problem must be truncated in such a way as to model open space and not introduce artificial reflections due to terminations. An artificial boundary conditions is applied to terminate the cells by absorbing the incident and scattered fields.

The first most widely used Absorbing Boundary Conditions (ABC) was devised by Mur in 1981 [97]. This boundary condition is derived from a one-way wave equation, which allows only outgoing waves as possible solutions. However, the attenuation of incident waves on the ABC boundary degrades as the incidence angle increases until at the grazing angle the boundary becomes perfectly reflecting.

In 1994, Berenger derived a new boundary condition referred to as a Perfectly Matched Layer (PML) which reduces reflections from boundaries [98]. The PML is placed around the boundaries of the FDTD domain. The presence of the PML ensures that a wave propagating in FDTD domain is fully absorbed once it hits the PML region at any incident angle, in other words the plane wave will be fully transmitted in the PML region without reflections back into the FDTD domain as shown in Figure 2.5.

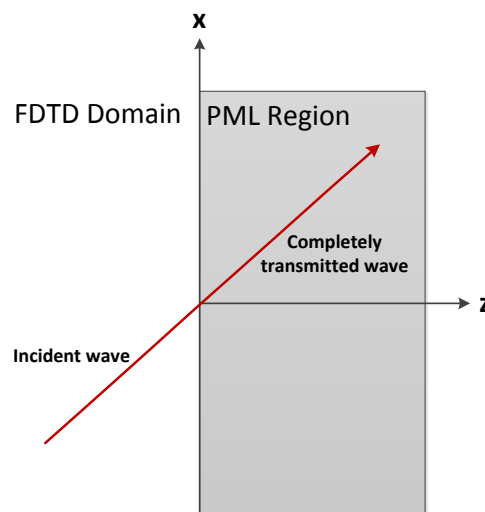


Figure 2.5: Perfectly matched layer (PML) terminating FDTD domain

PML uses a modified set of Maxwell's equations in which fields at the boundary layer interface are split into two components and an artificial anisotropic material is introduced to attenuate outgoing waves. The result is a PML wave impedance perfectly matched to the simulation space and independent of incidence angle. Incident waves are attenuated in the direction normal to the layers as they propagate through the artificial medium. Reflection coefficients as low as -80 dB have been demonstrated [99, 100] for both 2D and 3D FDTD simulations.

Although the PML technique provides an excellent boundary condition, its split field formulation requires a two-fold increase in computational memory and run-time in the regions containing the PML material relative to the conventional FDTD algorithm. To avoid this additional burden, a PML boundary condition based on a Maxwell formulation has been derived [101] and shown to be equivalent in effectiveness to the Berenger PML formulation. This alternate algorithm has the advantages of enhancing computational efficiency within the PML regions and eliminating the need for FDTD update equations modified for the split field formulation.

FDTD method that uses structured mesh, although a proven powerful numerical technique, has some limitations; one is involved with simulating problems with curved structures which need to be modelled using staircase approximations. In order to reduce the discretization error with staircasing, the mesh must be highly refined. This issue have motivated the development of new techniques based in unstructured meshes as discussed in Section 2.7.

2.6.3 Transmission Line Modelling (TLM)

The TLM method is well-established time-domain numerical method that is applied to different electromagnetic problems [7, 102-104]. It has great flexibility, versatility and stability in modelling complex geometries and suitable for nonlinear and inhomogeneous problems [105-116]. TLM involves mapping the electric field and magnetic field onto voltages and currents of the equivalent transmission line network. Unlike the FE and FDTD methods which use mathematical discretization of differential equations the TLM is a physical discretization in which a problem is replaced by a network of lumped elements. The TLM methodology involves two basic steps [4]; replacing the field problem by an electrical network and deriving the analogy between the field components and the network components, then solving the equivalent network by iterative method.

The computational space is discretized into cells, which is considered as a network of interconnected transmission lines. A TLM cell is formed of four transmission lines in the case of 2D TLM and 12 transmission lines in the case of the 3D TLM. A TLM node is the intersection of these transmission lines as shown in Figure 2.6. The TLM

method is based on Huygens's model of wave propagation in which electromagnetic field is modelled by waves propagating between adjacent cells and scattered within the cells.

If a pulse of value $1V$ is inserted at the centre of the TLM node Figure 2.7(a), part of the pulse will reflect back to the initial node in a process known by scatter as shown by the green arrow in Figure 2.7(b) and the rest will transmit to the adjacent nodes as known by connect process as shown by the black arrows in the same figure. Assume that each transmission line has a characteristic impedance Z , then the incident pulse sees three parallel similar transmission lines of equivalent impedance $Z/3$, then the reflection coefficient equals -0.5 and the transmission coefficient consequently equals to 0.5 . At the following time step the pulse will propagate further away from the initial node in which part of the new pulse will move outward and part will be reflected back to the new incident nodes as shown in Figure 2.7.c. and the scatter-connect process is repeated.

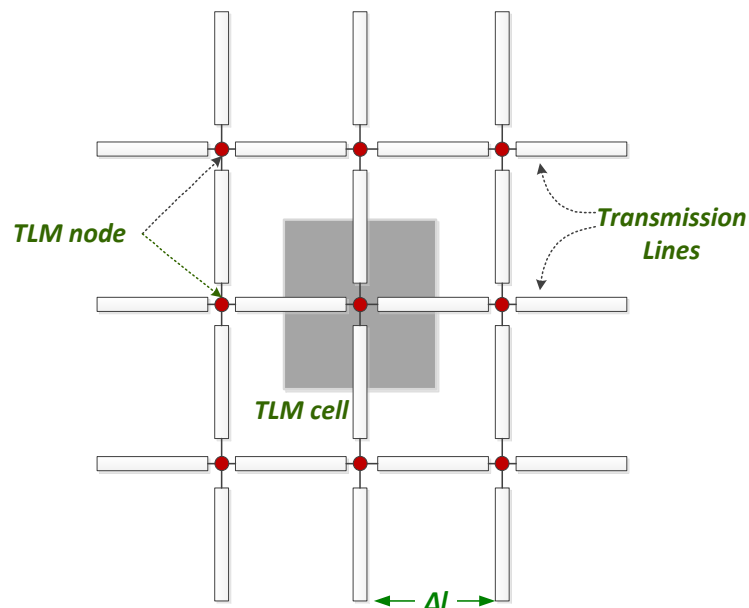


Figure 2.6: 2D TLM domain represented with a network of transmission lines

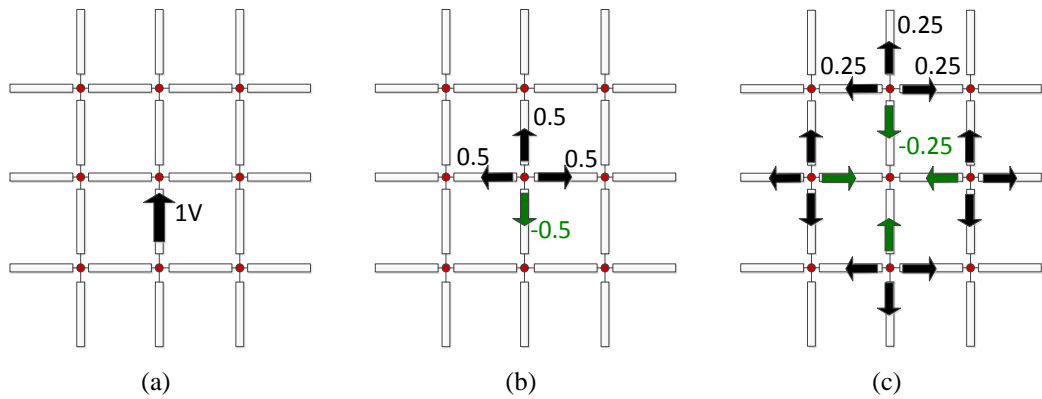


Figure 2.7: TLM pulse propagation; (a) Impulse excitation, (b) scattering in first time step, (c) scattering in second time step.

For 2D problem with no field change in the z direction, Maxwell’s equations are separated in two independent systems of partial differential equations; TE fields expressed by E_x , E_y and H_z and TM fields expressed by H_x , H_y and E_z . TE fields are represented by a circuit structure known as series node (Figure 2.8.a), while the TM fields are represented by a shunt node (Figure 2.8.b) [7].

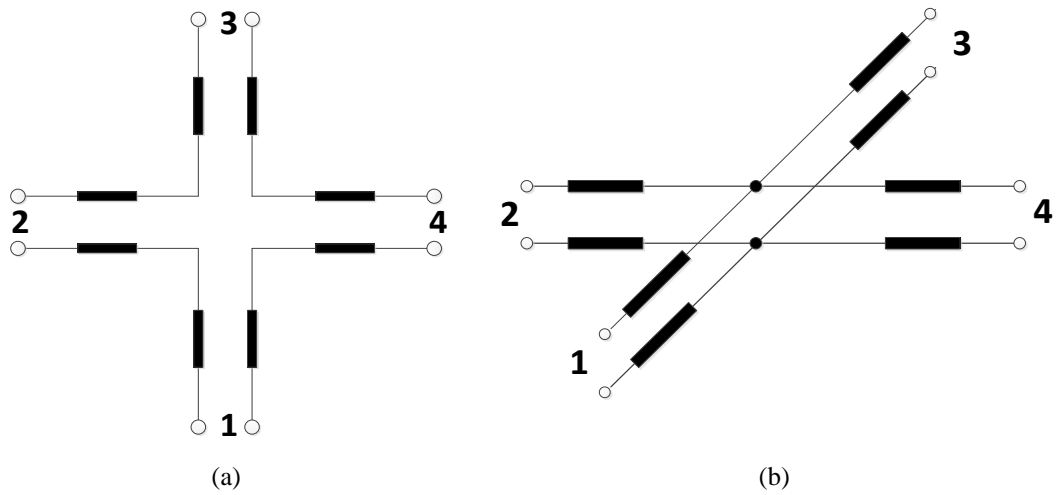


Figure 2.8: TLM (a) series node, (b) shunt node

2.6.3.1 TE polarization

For TE fields expressed in Equations (2.7), the wave equation is,

$$\frac{\partial^2 H_z}{\partial x^2} + \frac{\partial^2 H_z}{\partial y^2} = \mu\epsilon \frac{\partial^2 H_z}{\partial t^2}. \tag{2.61}$$

Equation (2.61) is expressed by the series node showed in Figure 2.8.a, which is a block of space of dimensions Δx , Δy and Δz and comprises four ports. The transmission line equivalence of the series node is shown in Figure 2.9. The mesh current I represents H_z and the x-directed and y-directed voltages are related to E_x and E_y . For analogy circuit analysis is carried on to find the relationship between field and circuit parameters.

Applying Kirchoff's voltage law around the loop in Figure 2.9 leads to [7],

$$V_{1x} + V_{4y} - V_{3x} - V_{2y} = 2L\Delta l \frac{\partial I}{\partial t}, \quad (2.62)$$

rearranging,

$$-(V_{3x} - V_{1x}) + (V_{4y} - V_{2y}) = 2L\Delta l \frac{\partial I}{\partial t}, \quad (2.63)$$

which can be expressed in terms of electric fields as,

$$\begin{aligned} -[E_y(x + \Delta x) - E_y(x)]\Delta y + [E_x(y + \Delta y) - E_x(y)]\Delta x \\ = 2L\Delta l \frac{\partial I}{\partial t}. \end{aligned} \quad (2.64)$$

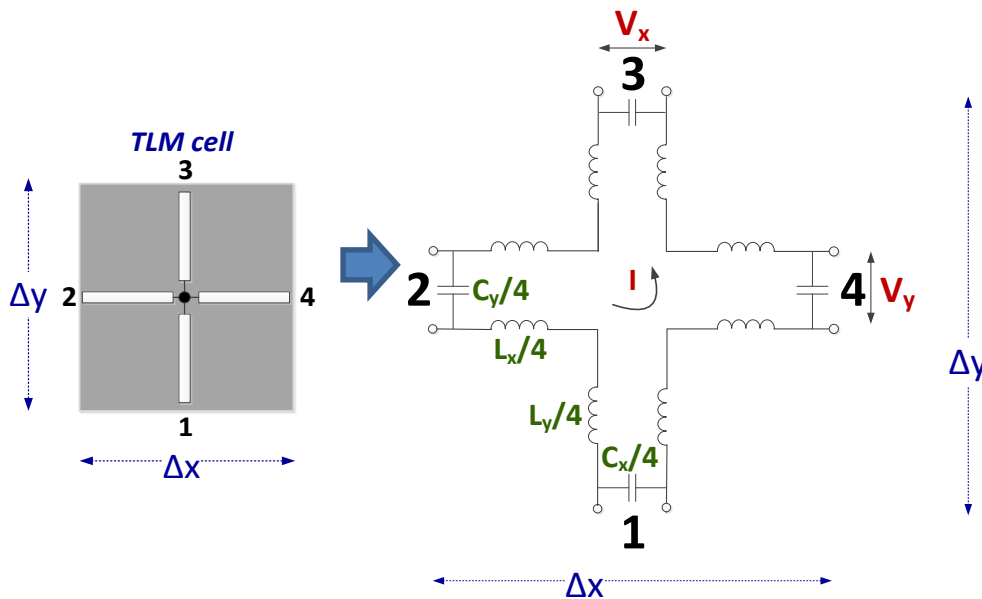


Figure 2.9: Circuit structure of the TLM series node

Dividing both sides by $\Delta x \Delta y$,

$$-\frac{E_y(x + \Delta x) - E_y(x)}{\Delta x} + \frac{E_x(y + \Delta y) - E_x(y)}{\Delta y} = 2L \frac{\Delta l}{\Delta x \Delta y} \frac{\partial I}{\partial t}. \quad (2.65)$$

For similar discretization length in all directions and substituting $I = H_z \Delta z$, Equation (2.65) becomes [7],

$$\frac{\Delta E_x}{\Delta y} - \frac{\Delta E_y}{\Delta x} = 2L \frac{\partial H_z}{\partial t}. \quad (2.66)$$

For two adjacent TLM nodes, Kirchhoff's current law can be applied where the two adjacent capacitors interconnected as shown in Figure 2.10 [7],

$$I_B - I_A = C \Delta x \frac{\partial V_C}{\partial t} \quad (2.67)$$

where C is the equivalent capacitance of the neighbouring capacitors and V_C is the voltage across the equivalent capacitance.

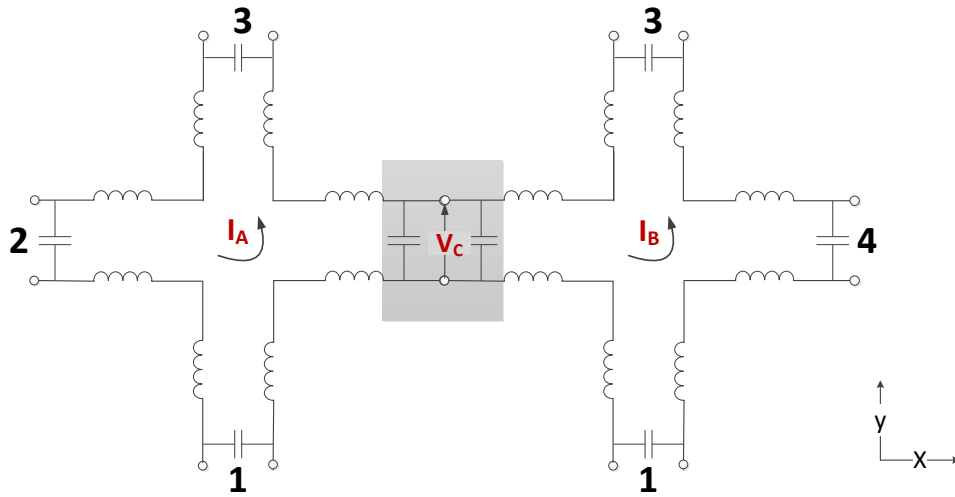


Figure 2.10: Adjacent TLM series nodes

Mapping the current and voltage into magnetic and electric fields yields to [7],

$$\frac{H_z(x + \Delta x) - H_z(x)}{\Delta x} \Delta z = C \frac{\Delta x \Delta y}{\Delta x} \frac{\partial E_y}{\partial t} \quad (2.68)$$

or

$$\frac{\partial H_z}{\partial x} = -C \frac{\partial E_y}{\partial t}. \quad (2.69)$$

The circuit parameters are related to the medium being modelled by [7],

$$C_x = \varepsilon \frac{\Delta y \Delta z}{\Delta x}, \quad (2.70.a)$$

$$C_y = \varepsilon \frac{\Delta x \Delta z}{\Delta y}, \quad (2.70.b)$$

$$L_x = \mu \frac{\Delta y \Delta x}{\Delta z}, \quad (2.70.c)$$

$$L_y = \mu \frac{\Delta y \Delta x}{\Delta z}, \quad (2.70.d)$$

For $\Delta x = \Delta y = \Delta z = \Delta l$, then,

$$L = \mu \Delta l, \quad (2.71.a)$$

$$C = \varepsilon \Delta l, \quad (2.71.b)$$

The equivalence between circuit and field quantities is established from Equations

(2.7), (2.66) and (2.69) lead to,

$$\frac{I}{\Delta z} \leftrightarrow H_z, \quad (2.72.a)$$

$$-\frac{V_y}{\Delta l} \leftrightarrow E_y, \quad (2.72.b)$$

$$-\frac{V_x}{\Delta l} \leftrightarrow E_x. \quad (2.72.c)$$

Equations (2.72) mean that the circuit model of series TLM node displays the TE modes in a medium of parameters ε and 2μ [7].

To calculate the voltages and currents, an equivalent Thevenin circuit is constructed as shown in Figure 2.11. Each transmission line is replaced by an equivalent source of double the incident voltage ($2 {}_k V_m^i$) due to the round trip, where i is used to indicate the incident signal, k indicates the current time, m is the index of the transmission line ($m=1, 2, 3, 4$). The Thevenin source is in series with impedance Z_{TL} . [7]

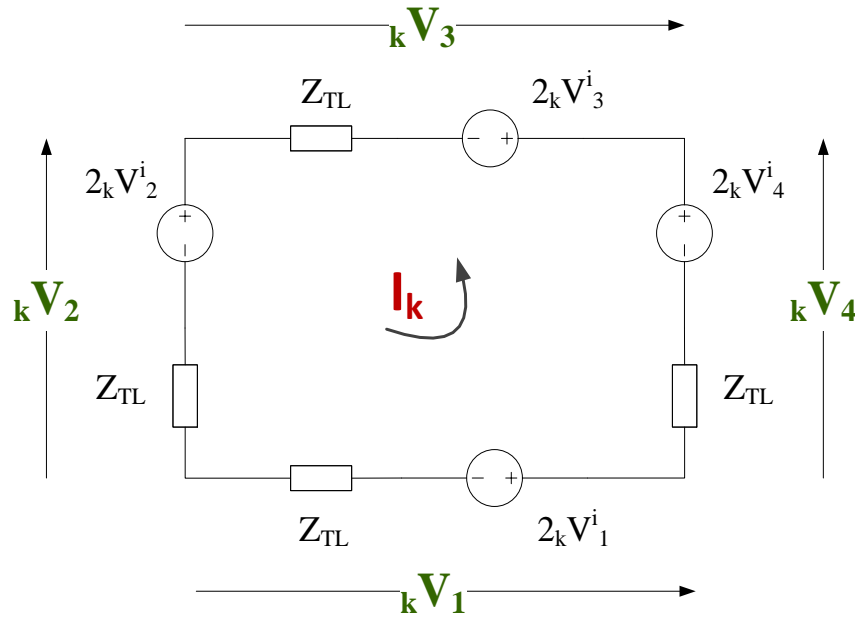


Figure 2.11: Thevenin equivalent circuit of the TLM series node

The loop current is calculated as,

$${}_k I = \frac{2 {}_k V_1^i - 2 {}_k V_2^i - 2 {}_k V_3^i + 2 {}_k V_4^i}{4Z_{TL}}. \quad (2.73)$$

Then the magnetic field is,

$${}_k H_z = \frac{I}{\Delta l} = \frac{{}_k V_1^i - {}_k V_2^i - {}_k V_3^i + {}_k V_4^i}{4\Delta l Z_{TL}}, \quad (2.74)$$

And the electric field components are calculated as,

$${}_k E_x = \frac{{}_k V_1^i + {}_k V_3^i}{\Delta l}, \quad (2.75)$$

$${}_kE_y = \frac{{}_kV_2^i + {}_kV_4^i}{\Delta l}. \quad (2.76)$$

The voltages at each port are reflected back to the original node in a process known as the scatter process. The reflected voltage is related to the incident voltage by,

$${}_kV^r = {}_kV - {}_kV^i. \quad (2.77)$$

Then the reflected voltage at port 1 can be calculated as,

$$\begin{aligned} {}_kV_1^r &= {}_kV_1 - {}_kV_1^i = 2{}_kV_1^i - IZ_{TL} - {}_kV_1^i, \\ {}_kV_1^r &= 0.5({}_kV_1^i + {}_kV_2^i + {}_kV_3^i - {}_kV_4^i). \end{aligned} \quad (2.78)$$

The reflected voltages for the four transmission lines can be expressed by the scattering matrix,

$$\begin{bmatrix} {}_kV_1^r \\ {}_kV_2^r \\ {}_kV_3^r \\ {}_kV_4^r \end{bmatrix} = 0.5 \begin{bmatrix} 1 & 1 & 1 & -1 \\ 1 & 1 & -1 & 1 \\ 1 & -1 & 1 & 1 \\ -1 & 1 & 1 & 1 \end{bmatrix} \begin{bmatrix} {}_kV_1^i \\ {}_kV_2^i \\ {}_kV_3^i \\ {}_kV_4^i \end{bmatrix}. \quad (2.79)$$

Consider the TLM cell that is centred at node (x,y) and that is connected to four adjacent TLM cells as shown in Figure 2.12. The pulse incident to the TLM node (x,y) at time k+1 are those reflected back from the adjacent node at time step k. The connect process is expressed by the following set of equations:

$$\begin{aligned} {}_{k+1}V_1^r(x, y) &= {}_kV_3^i(x, y - 1), \\ {}_{k+1}V_2^r(x, y) &= {}_kV_4^i(x - 1, y), \\ {}_{k+1}V_3^r(x, y) &= {}_kV_1^i(x, y + 1), \\ {}_{k+1}V_4^r(x, y) &= {}_kV_2^i(x + 1, y). \end{aligned} \quad (2.80)$$

Finally, boundaries should be expressed to take into account the termination of the problem space. TLM boundaries are short circuit, open circuit and matching impedance.

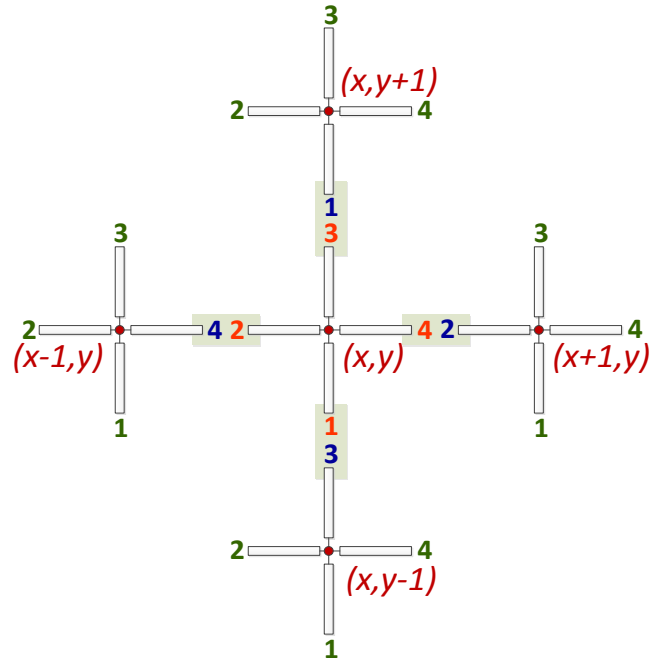


Figure 2.12: Connection of the TLM cells

If for example port 4 of the TLM node (x, y) in Figure 2.13(a) is short-circuited, the scattered voltage is reflected back completely into port 4, and then the incident voltage at time $k+1$ equals the reflected voltage of time k at the same port,

$${}_{k+1}V_4^i(x, y) = - {}_kV_4^r(x, y). \quad (2.81)$$

For open-circuit termination at port 4 of the TLM node (x, y) (Figure 2.13(b)), the incident voltage at time $k+1$ is expressed as [7],

$${}_{k+1}V_4^i(x, y) = {}_kV_4^r(x, y) = {}_kV_2^r(x+1, y). \quad (2.82)$$

And finally, a matching boundary is used to reduce the problem space to a finite size. For example, if port 4 of TLM node in Figure 2.13(c) is connected to a matching impedance Z_L to free space, Z_L value is chosen to be equal to free space impedance

$Z_o = \sqrt{\frac{\epsilon_o}{\mu_o}}$, and hence the reflection coefficient at port 4 is,

$$\Gamma = \frac{Z_L - Z}{Z_L + Z} \quad (2.83)$$

where Z is the transmission line impedance. Then the incident voltage at time $k+1$ is expressed as

$${}_{k+1}V_4^i(x, y) = \Gamma_k V_4^r(x, y). \quad (2.84)$$

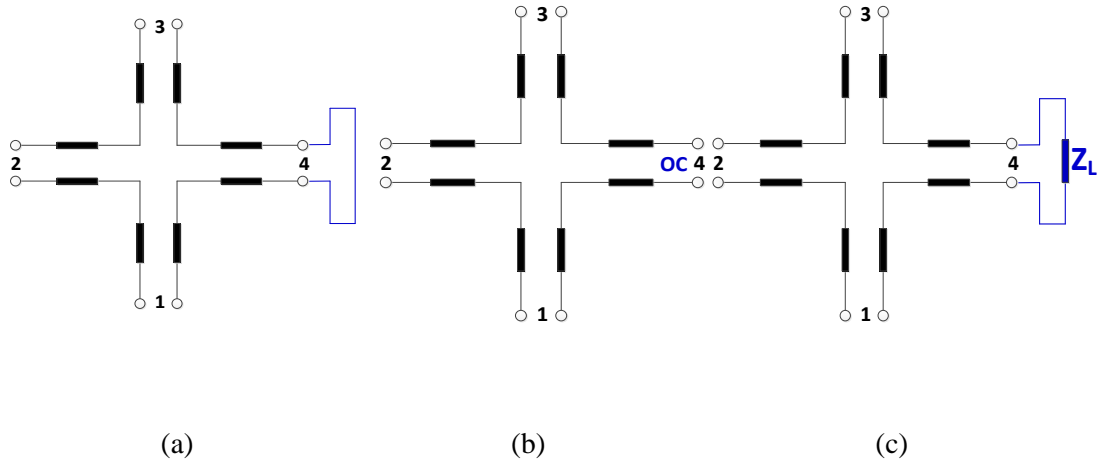


Figure 2.13: TLM series node terminated with (a) short-circuit, (b) open-circuit and (c) matching impedance

Time step Δt is the time the signal takes to travel from a TLM node to the adjacent node, thus it depends on the discretization length Δl ,

$$\Delta t = \frac{\Delta l}{u_{TL}}. \quad (2.85)$$

where u_{TL} is velocity of the signal over the transmission line and is calculated by,

$$u_{TL} = \frac{1}{\sqrt{LC}}. \quad (2.86)$$

where L and C are the transmission line equivalent inductance and capacitance, respectively.

2.6.3.2 TM polarization

For TM fields expressed in Equations (2.8) the wave equation is,

$$\frac{\partial^2 E_z}{\partial x^2} + \frac{\partial^2 E_z}{\partial y^2} = \mu\epsilon \frac{\partial^2 E_z}{\partial t^2}. \quad (2.87)$$

Equation (2.87) is expressed by the shunt node showed in Figure 2.8.b, which is a block of space of dimensions Δx , Δy and Δz . The voltage V_z is related to the electric field component E_z and the currents in the ports are mapped to the magnetic field components H_x and H_y . Consider the circuit structure shown in Figure 2.14.

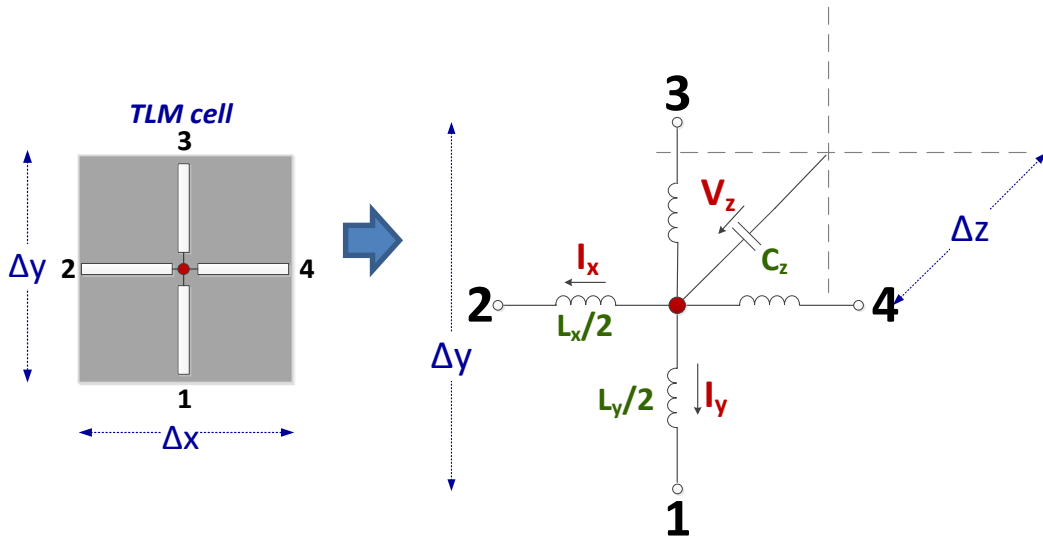


Figure 2.14: Circuit structure of the TLM shunt node

Applying Kirchhoff's law for the x-propagation transmission line [7],

$$L_x \frac{\partial I_x}{\partial t} = -\frac{\partial V_z}{\partial x} \Delta x, \quad (2.88)$$

$$C_z \frac{\partial V_z}{\partial t} = -\frac{\partial I_x}{\partial x} \Delta x. \quad (2.89)$$

Differentiating Equations (2.88) and (2.89) with respect to x and t , then combining the resulted equations leads to,

$$\frac{\partial^2 V_z}{\partial x^2} \frac{(\Delta x)^2}{L_x} = C_z \frac{\partial^2 V_z}{\partial t^2}. \quad (2.90)$$

Similarly for the y-propagation,

$$\frac{\partial^2 V_y (\Delta y)^2}{\partial y^2 L_y} = C_z \frac{\partial^2 V_z}{\partial t^2}. \quad (2.91)$$

Summing Equations (2.90) and (2.91) leads to

$$\frac{\partial^2 V_z (\Delta x)^2}{\partial x^2 L_x} + \frac{\partial^2 V_y (\Delta y)^2}{\partial y^2 L_y} = 2C_z \frac{\partial^2 V_z}{\partial t^2}. \quad (2.92)$$

The circuit parameters L_x , L_y and C_z are calculated from [7],

$$\begin{aligned} L_x &= \mu \frac{\Delta x \Delta z}{\Delta y}, \\ L_y &= \mu \frac{\Delta y \Delta z}{\Delta x}, \\ C_z &= \varepsilon \frac{\Delta x \Delta y}{\Delta z} \end{aligned} \quad (2.93)$$

Substitution of circuit parameters into Equation (2.92) leads to,

$$\frac{\partial^2}{\partial x^2} \left(\frac{V_z}{\Delta z} \right) + \frac{\partial^2}{\partial y^2} \left(\frac{V_z}{\Delta z} \right) = 2\varepsilon\mu \frac{\partial^2}{\partial t^2} \left(\frac{V_z}{\Delta z} \right). \quad (2.94)$$

Comparing the 2D wave equation (2.87) with Equation (2.94), the field to circuit analogy can be expressed as,

$$\begin{aligned} -\frac{V_z}{\Delta z} &\leftrightarrow E_z, \\ \frac{I_x}{\Delta y} &\leftrightarrow H_y, \\ -\frac{I_y}{\Delta x} &\leftrightarrow H_x. \end{aligned} \quad (2.95)$$

Thus, a shunt node can simulate a medium with parameters 2ε and μ . Then the Thevenin equivalent circuit is constructed to calculate the currents and voltages as shown in Figure 2.15.

The voltage V_z across the parallel transmission lines is calculated from,

$$V_z = 0.5(kV_1^i + kV_2^i + kV_3^i + kV_4^i), \quad (2.96)$$

and the currents I_x and I_y are calculated as,

$$I_x = \frac{kV_2^i - kV_4^i}{Z_{TL}}, \quad (2.97)$$

$$I_y = \frac{kV_3^i - kV_1^i}{Z_{TL}}. \quad (2.98)$$

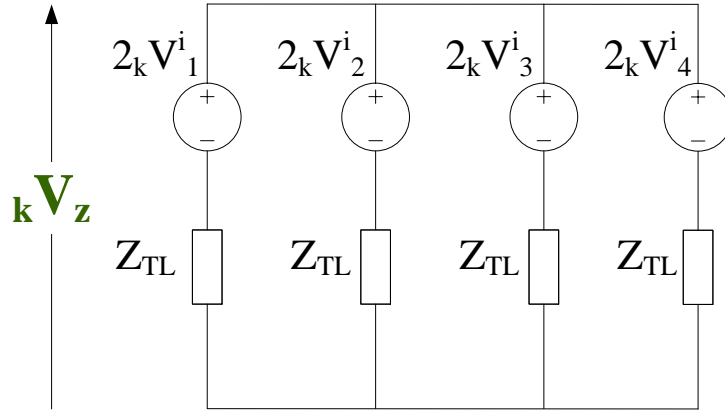


Figure 2.15: Thevenin equivalent circuit of the shunt TLM node

An incident pulse at certain port is partially transmitted to the other three ports, and the rest of the pulse is reflected back to same port. The reflected voltage kV_m^r at any port m can be obtained from,

$$kV_m^r = V_z - kV_m^i, \quad m=1,2,3,4 \quad (2.99)$$

For example, if a pulse is incident at port 1, the reflected pulse is calculated as,

$$kV_1^r = V_z - kV_1^i = 0.5(-kV_1^i + kV_2^i + kV_3^i + kV_4^i). \quad (2.100)$$

Applying the same approach to other ports, each incident pulse will be scattered and the reflected voltages at all ports can be given by the following matrix equation,

$$\begin{bmatrix} {}^kV_1^r \\ {}^kV_2^r \\ {}^kV_3^r \\ {}^kV_4^r \end{bmatrix} = 0.5 \begin{bmatrix} -1 & 1 & 1 & 1 \\ 1 & -1 & 1 & 1 \\ 1 & 1 & -1 & 1 \\ 1 & 1 & 1 & -1 \end{bmatrix} \begin{bmatrix} {}^kV_1^i \\ {}^kV_2^i \\ {}^kV_3^i \\ {}^kV_4^i \end{bmatrix}. \quad (2.101)$$

The reflected voltages at time step k are the incident voltages to the nodes at time step $k+1$. The connect process with adjacent TLM cells follows the same approach laid with the series TLM node (Equations (2.80)).

Finally, boundaries should be expressed to take into account the termination of the problem space. TLM boundaries are short circuit, open circuit or matching impedance as shown in Figure 2.16. Connection of TLM shunt node can be calculated using the same equations of the series node (Equations (2.81)-(2.83)).

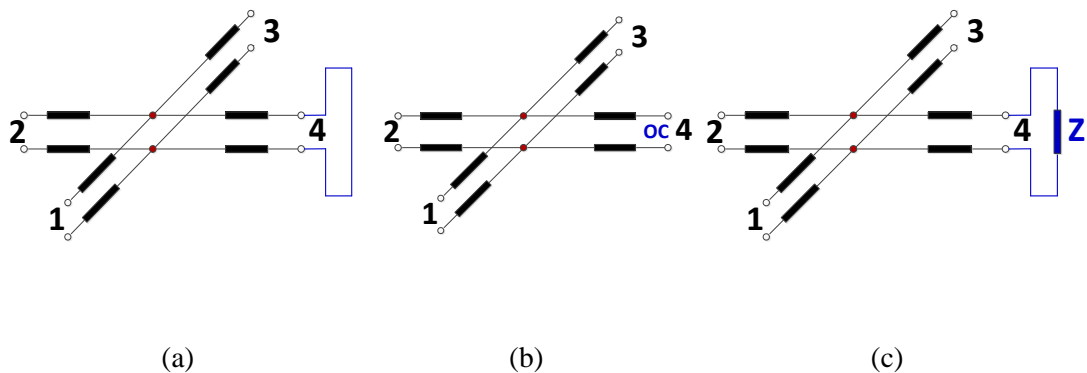


Figure 2.16: TLM shunt node terminated with (a) short-circuit, (b) open-circuit and (c) matching impedance

2.6.4 Errors in numerical methods

This section overviews three principal sources of error which can be identified [4] as:

The first error is the truncation error, which is due to the need to truncate the impulse response in time, such as setting finite number of iterations N . In frequency domain this error appears as a shift in the maxima for simulation of resonating structures, in other words, the frequencies are smeared out as with FFT data windowing. The maximum truncation error is given by [4]

$$e_T = \frac{3\lambda_c}{SN^2\pi^2\Delta l} \quad (2.102)$$

where λ_c is the free space wavelength between two neighbouring peaks, Δl is the discretisation length, S is the frequency separation expressed in terms of $\Delta l/\lambda_c$. The error can be minimized by increasing the number of iterations N and increasing S [4].

The first step in numerical simulation is the generation of a suitable mesh that discretize the problem space using either structured or unstructured meshes. The second source of error is the quantization error which is a result of sampling the problem into finite number of cells. To reduce such error it is required to choose the segment length Δl to be equal to or less than one-tenth of wavelength of interest [117],

$$\Delta l \leq \frac{\lambda}{10}. \quad (2.103)$$

The third error is the dispersion error, for example propagation velocity in the structured TLM is assumed to be the same in all directions and equal to $u_{TLM} = u/\sqrt{2}$, where u is the signal velocity in the medium. This condition is on the assumption that the TLM mesh wavelength λ_n is large as compared to the discretization length Δl [4]. Otherwise the propagation velocity depends on the propagation direction. The minimum error is achieved when the propagation angle is 45° and the maximum velocity error achieved with propagation angle 0° in the structured mesh [7]. The velocity error for unstructured meshes is investigated in Chapter 5.

2.7 Unstructured meshing techniques

Discretizing the problem space into finer meshes minimizes the time step and consequently increase the total run time. Therefore, it is an important problem on how to achieve high spatial resolution problems where fine details of the problem are present while keeping reasonable computer resources. Such problems are thin wire embedded in a large region [118-123], antennas [124, 125] and optoelectronics [27, 28].

Three different types of conformable surface models have been suggested; namely, locally distorted grid models [13, 17-19, 126, 127], globally distorted grid models (body fitted) [14] and unstructured models [23, 24, 29, 128].

Unstructured grid methods initially developed as an alternative to discretize complex geometries. The mesh involves elements of different size and shapes with irregular connectivity. These methods make use of triangular elements for 2D problems and tetrahedral for 3D problems [11, 30, 129].

In FDTD method, a generalized Yee's algorithm that is based on unstructured and irregular grids is presented [29, 128]. The unstructured grids are based on triangular pyramids, which provide second-order accuracy in condition that the interior angles of the triangular faces are less than 60° . The general Yee's algorithm is based on solving the integral form of Maxwell's equations with a closed 3D volume. For stability, the time step is chosen to be,

$$\Delta t \leq \frac{1}{c \left[\sum_{i=1}^3 \frac{1}{l_i^2} \right]}, \quad (2.104)$$

where c is the speed of light, l_i is the three edges in each cell sharing a common vertex.

There are different techniques for generating unstructured meshes, two of the most famous ones are Advancing-Front technique and Delaunay based approaches.

In unstructured mesh generation techniques, nodes are distributed in the domain prior the triangulation is carried on. Advancing front technique (AFT) create nodes wherever needed in a local procedure in the same time elements are generated. The elements created are triangles and the creation starts from the domain boundary. AFT involves propagating a layer from boundaries into domain. The method starts by discretizing the boundaries of the geometry (known as front) into edges. These edges form the initial front that will advance into the field. Starting with an edge the first triangle is created by joining the two ends of the edge to an existing point or to a point on the front. Then the current edge is removed from the front and the remaining two edges of the new triangle are assigned to the new front as shown in Figure 2.17.

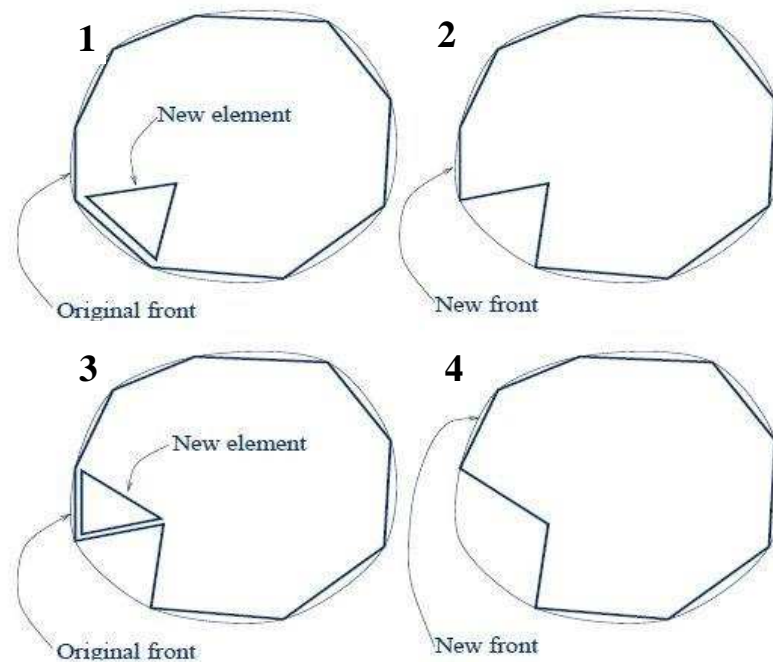


Figure 2.17: Advancing front technique (AFT) [130]

The procedure is iterative as it is repeated till all edges of the initial front are removed as shown in Figure 2.17. New points placed in the domain are chosen to form triangle of good shape and size, the position is determined by a prescribed field function. Advancing front method result smooth high quality triangulation in most regions of the domain but difficulties are encountered at the places where fronts collide, usually in the centre of the domain [129, 131].

Delaunay-based approaches start with random number of points, where triangles of Delaunay types are initially created. For arbitrary number of points there are many possible triangulations. Figure 2.18 shows two different Delaunay triangulations; the first one contains long triangles (bad triangles) and the second is for good quality (uniform) Delaunay triangles. The initial triangulation is formed by forming the maximum pairs of nodes without crossing any line. The first node is then added and connected to each vertex of the enclosing triangle, add the second node and if it falls into one of the triangles you already created then subdivide that triangle as shown in Figure 2.19. The process is then repeated until the last node is added and the whole domain is triangulated [32, 130] as shown in Figure 2.20. All triangles should obey the Delaunay condition that the circumcircle containing the triangle vertices should not

contain other points as shown in Figure 2.20. Delaunay triangles are mostly of good shape and it has the advantage of maximizing the minimum angle of all triangles, it does a better job of connecting nearby nodes rather than far points which avoid the formation of long triangles and produce more uniform shapes [130].

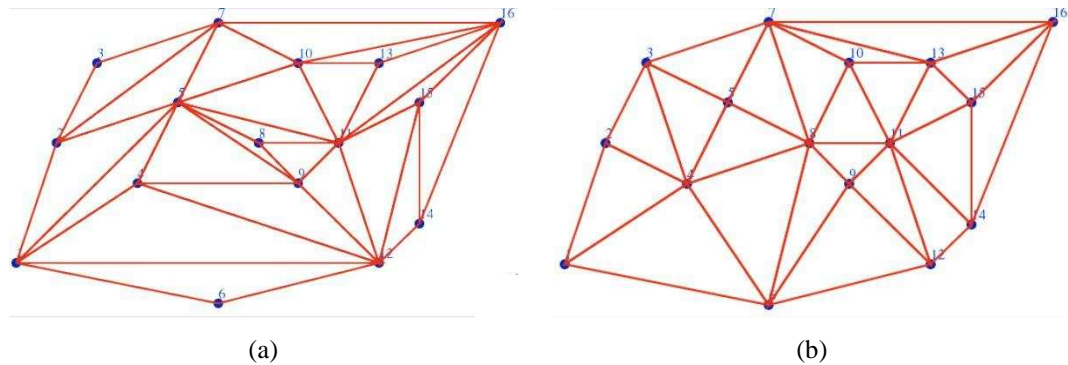


Figure 2.18: (a) Delaunay triangulation with long triangles, (b) Uniform Delaunay triangulation [132].

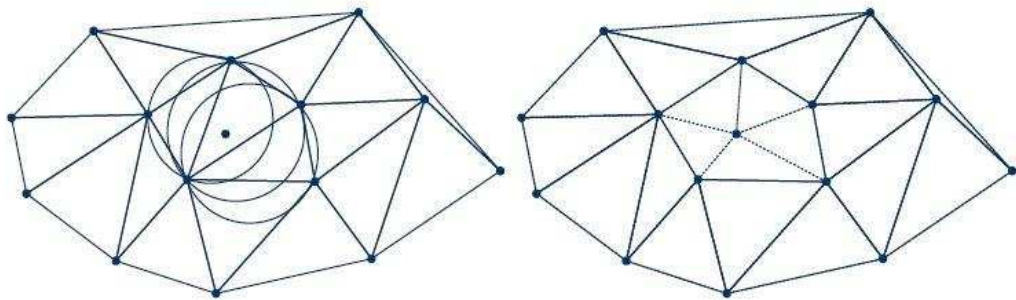


Figure 2.19: Transforming non-Delaunay triangle (left) into Delaunay type triangle (right) [12, 130].

Delaunay mesh can be expressed by its dual mesh known as the voronoi mesh which is formed by connecting the triangles circumcentres as shown in Figure 2.20. More details on Delaunay meshes are discussed in Chapter 3.

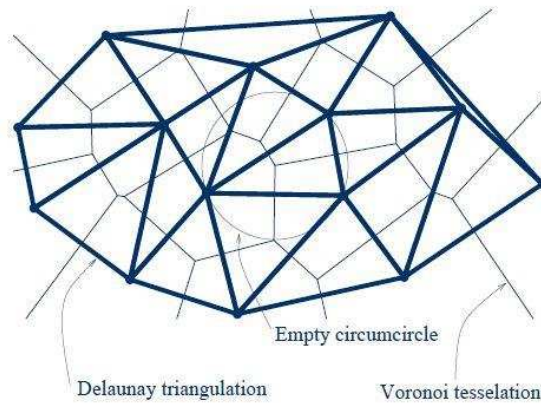


Figure 2.20: Delaunay mesh (light) and its dual mesh Voronoi tessellation (dark) [12, 130].

Unstructured mesh in the TLM is a meshing criteria that is adopted in [23, 24] to discretize problems with fine features and that of curved boundaries. Unstructured mesh is used to discretise the problem space into triangular shapes in 2D problem and tetrahedral in 3D problems that fulfil Delaunay condition. TLM node must coincide with the circumcentre of the Delaunay triangle. In 2D problems, each node combines three transmission lines that connect the TLM node to its neighbouring nodes. Since the triangles in the mesh are of different sizes, the maximum useable time step Δt_{max} is proportional to the length of shortest transmission line Δ_{min} in the entire problem [23],

$$\Delta t_{max} = \Delta_{min} \sqrt{2\varepsilon\mu}. \quad (2.105)$$

where ε and μ are the medium permittivity and permeability, respectively.

Stubs are inserted at the end of each transmission line to compensate for the discrepancy in transmission lines lengths, and to allow signal to travel with the same velocity between nodes. In Chapter 3, 2D unstructured TLM (2D UTLM) will be discussed in detail.

The most critical point that faces the UTLM is the optimization between the mesh size and the time step. In some Delaunay triangles, the circumcentre can lay outside the triangle which affects the distance between the two adjacent circumcentres. This distance can be very small or even equal zero, which lead to very small time step. A small time step has big impact on the computational resources, so a solution must be applied to maximise the time step. This point will be addressed and solved in Chapter

4. Unstructured mesh has better dispersion characteristics as compared to the structured mesh but has the disadvantage of intermodal coupling, in which any excited is coupled to other spatial modes. A complete dispersion and modal coupling study is discussed in Chapter 5.

2.8 Summary

In this chapter, a theoretical and mathematical background for solving Maxwell's equations and wave equations is summarized. First, Maxwell's equation, derivation of wave equation and the general solution of plane wave propagation and boundary conditions are discussed. Numerical methods that are used to solve Maxwell's equations and wave equations such as TLM, FDTD and FE are overviewed. Different meshing techniques are discussed paying attention to unstructured meshes.

The next chapter overviews the 2D Unstructured Transmission Line Modelling (2D UTLM) theory and implementation, and then the accuracy and efficiency of the 2D UTLM algorithm is validated and compared against the structured TLM method.

Chapter 3.

Two-Dimensional Unstructured Transmission Line Modelling

3.1 Introduction

In this chapter, Unstructured Transmission Line Modelling (UTLM) is presented for modelling two-dimensional (2D) problems, together with the algorithm of how it can be practically implemented in a computer program. A formulation of the 2D UTLM is presented starting with a general TLM node and followed by the mapping of the EM field onto the network of equivalent transmission lines. The accuracy of the UTLM method is validated on several canonical examples of cylindrical and square metal resonant cavities and results are compared with the structured TLM (STLM).

The main philosophy of the TLM method is that EM field is mapped onto the network of transmission lines along which voltages propagate. The transmission lines intersect at nodes which are placed at the centres of mesh cells (cells are of square or cuboidal shape for STLM and triangular or tetrahedral for UTLM). Transmission lines of neighbouring cells are connected at the cell boundaries which are defined as ports. The EM simulation begins by inserting an appropriate voltage excitation at an arbitrary node which then travels through the network of transmission lines. The voltages scatter at the nodes and the new reflected signals become the incident signals on neighbouring nodes in the next time step – process known as connect. These processes are repeated until a steady state is reached.

The UTLM requires that problem of interest is meshed using Delaunay triangulation. Delaunay triangles have the characteristics of well-shaped triangles in which it maximizes the internal angles of triangles and avoids the formation of skinny triangles. Delaunay triangle also minimizes the error in approximation of a function over a domain. The UTLM node should coincide with the circumcentre of the Delaunay

triangle for proper implementation of the Electromagnetic theory as will be discussed later. The network orthogonal to Delaunay is Voronoi which connects the triangles circumcentres. The Voronoi diagram corresponds to the network of transmission lines where the signal propagates.

3.2 Unstructured meshes and Delaunay triangulation

3.2.1 Delaunay properties

Delaunay triangulations are widely used in scientific computing in diverse applications. Delaunay meshes are well-known set of triangulation of an arbitrary set of points. It has the advantage of maximizing the minimum angle and avoiding skinny triangles which consequently provides good quality triangles [30, 32].

Delaunay triangulation provides unique triangulations which obey the empty circumcircle property; for which a set of 2D points a Delaunay triangulation of these points ensures the triangle circumcircle contains no other point in its interior. Thus, two-dimensional triangulation is often called the empty circumcircle criterion [32].

Figure 3.1 shows an example of Delaunay and Non-Delaunay triangles. In Figure 3.1(a) the triangle circumcircle contains only the triangle three vertices, whilst in Figure 3.1(b) the circumcircle includes another vertex from the adjacent triangle.

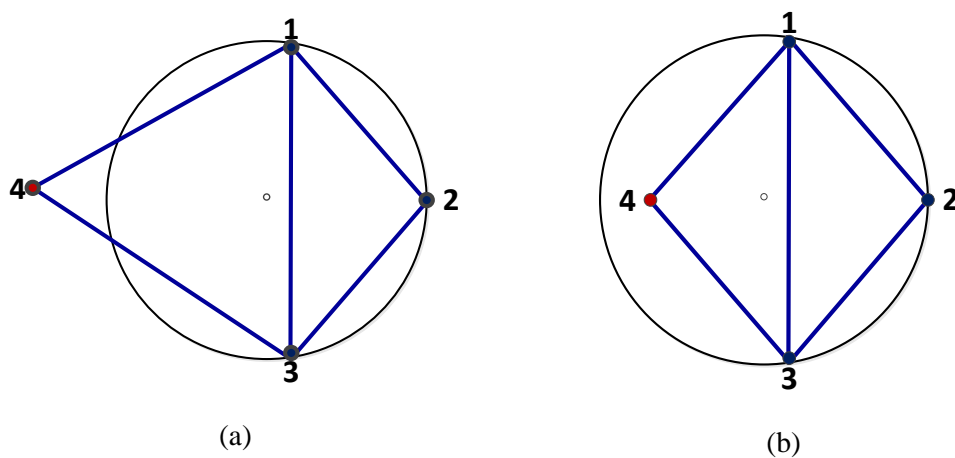


Figure 3.1: Set of four points forming (a) Delaunay triangles, (b) Non-Delaunay triangles

The Delaunay condition implies that for any two adjacent triangles in the triangulated area, the sum of the angles facing the same side should be less than or equal to 180° . This condition allows the use of the flip technique [133]. If the two triangles shown in Figure 3.2(a) do not fulfil the Delaunay condition where $\alpha + \beta > 180^\circ$ then the edge BD shared between the two triangles can be flipped to be AC as shown in Figure 3.2(b) and the resulting triangles will be of Delaunay type where $\gamma + \delta < 180^\circ$.

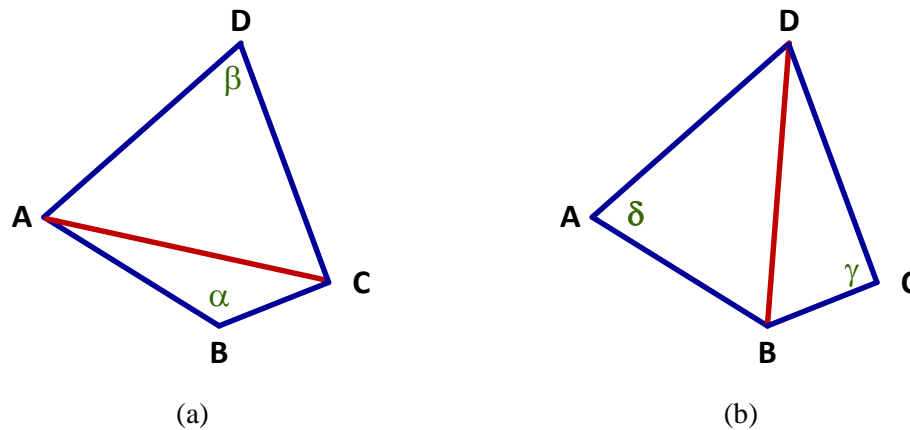


Figure 3.2: Flipping technique: (a) non-Delaunay triangles converted into (b) Delaunay triangles

Although Delaunay property is well defined but the topology of the triangulation is not unique if four points forming a square lies on the circumference of a circle, it ends to forming two similar non-unique right angled triangles which still obey the Delaunay condition as shown in Figure 3.3. The resulting triangles are referred as degenerate Delaunay triangles.

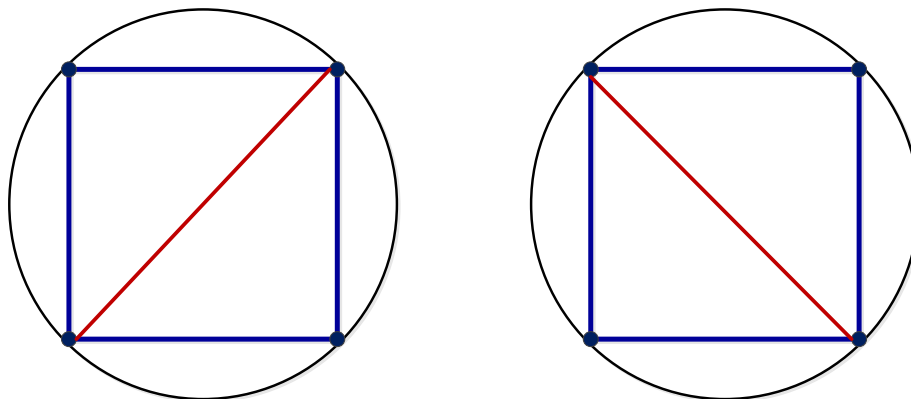


Figure 3.3: Degenerate Delaunay triangles

Delaunay triangulation is formed by defining the polygon points known as the mesh points from which initial triangulation is constructed. The mesh points are inserted sequentially into that initial triangulation using Bowyer-Watson algorithm [30]. Inserting the first point to the initial triangulation, then the empty circumcircle property is adopted in that locating and deleting all triangles whose circumcircle contains the inserted point. Then this point is connected to boundary vertices of the cavity created of the removal of non-fulfilling triangles. The second point is inserted and the Delaunay condition is applied and so on till the last point in list is inserted. Then, the resulting mesh contains triangles of Delaunay type.

Another type of Delaunay triangulation is known as Constrained Delaunay Triangulation that enforces specific segments into the triangulation. These segments may not satisfy Delaunay conditions, thus, some triangles might not be Delaunay [32].

Delaunay triangulation can be refined by inserting new vertices known as Steiner points to subdivide the segments into several edges to create smaller triangles whilst maintaining the Delaunay property of the mesh. Segments are subdivided in a way to prevent the creation of unnecessarily short edges. This is known as Conforming Delaunay Triangulation [32].

Unstructured mesh generation is an important step in the simulation, where the mesher should produce triangles that are of Delaunay type, but one must bear in mind that not all Delaunay type triangles are of good type. Quasi-equilateral triangles are considered to be the good Delaunay triangle due to the uniform structure, whilst sliver or skinny triangles are considered to be bad quality triangle. The mesher is required to avoid the production of skinny triangles (whose height h is much greater than its base b) shown in Figure 3.4 which decreases the quality and uniformity of the mesh in the simulation. Different approaches are adopted for optimal mesh triangulation [134-138].



Figure 3.4: Skinny triangle

A local measure of triangle quality is mesh quality factor Q which is the ratio between the circumcircle radius to the shortest link line in the triangle [32]. So, for equilateral triangle the Q value is $1/\sqrt{3}$ or 0.57735. Practically, it is expected that a mesh of good quality have Q equals to 1 or 2 [131]. The effect of mesh quality on the accuracy of the TLM simulation will be further investigated in Chapter 5.

An intended problem is defined by setting exterior boundaries that separate the meshed from the unmeshed areas which is known as polygon. Interior boundaries can be added to the polygon as shown in Figure 3.5(a,b) to separate different meshed regions and they are used to set some region constraints and attributes, such as the presence of holes as shown in Figure 3.5(c) or different media as shown in Figure 3.5(d). For 2D unstructured mesh generation a polygon is produced by creating a closed loop of straight edges.

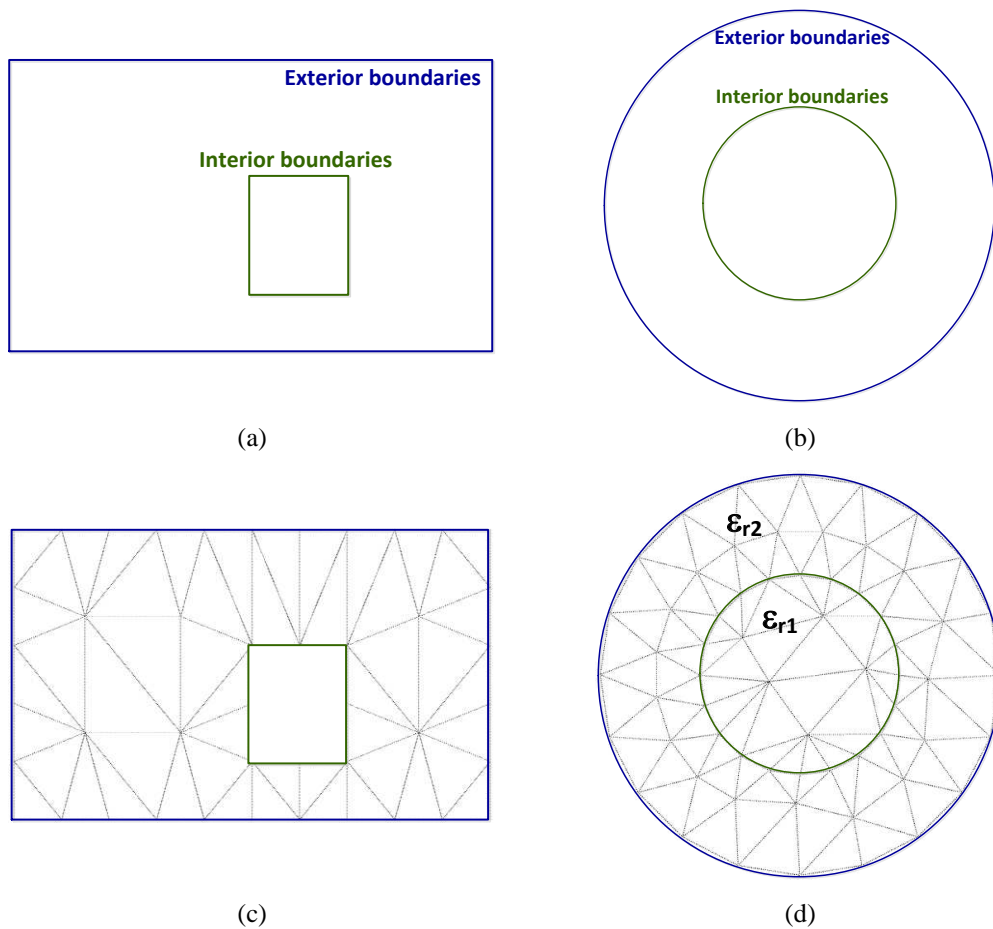


Figure 3.5: Generation of unstructured meshes: (a,b) creating a polygon (c,d) meshing the polygon with respect to the exterior and interior boundaries.

Upon mesh generation the first set of formulated triangles coincide with the vertices of the polygon, and then the mesh generator introduces additional vertices inside the polygon which are called Steiner points [32]. Those points are the vertices of inside triangles, and the produced meshes are called a Steiner triangulation of the polygon. For a set of points, there exist many possible triangulations of these points. Most Delaunay mesh generators create their worst elements near the domain boundary and their best elements in the interior.

Then Delaunay refinement can be applied to improve the produced Delaunay triangles by moving the node location. This can be achieved by iteratively moving nodes to average of neighbours, which is known as Laplacian smoothing [30].

$$x_i \rightarrow \frac{1}{n_i} \sum_{j=1}^{n_i} x_j. \quad (3.1)$$

where n_i is the number of nodes, x_i and x_j are the new and old node positions. Generally, extra random points can be placed within the problem domain to enforce quality mesh or to put size constraints such as an upper limit for the triangle area.

3.2.2 Delaunay triangle circumcentre

Triangle circumcentre is the intersection of the triangle normal bisectors. It is located inside an acute triangle, outside an obtuse triangle and located on centre of hypotenuse of the right-angled triangle as shown in [Figure 3.6](#).

The location of the circumcentre (CC_x, CC_y) depends on the triangle vertices. For a triangle of vertices $A(x_1, y_1)$, $B(x_2, y_2)$ and $C(x_3, y_3)$ the circumcentre coordinates can be calculated as follows [139]

$$\begin{aligned} CC_x &= \frac{S_x}{a}, \\ CC_y &= \frac{S_y}{a}. \end{aligned} \quad (3.2)$$

where

$$S_x = \frac{1}{2}[A(y_2 - y_3) - B(y_1 - y_3) + C(y_1 - y_2)], \quad (3.3)$$

$$S_y = \frac{1}{2}[x_1(B - C) - x_2(A - C) + x_3(A - B)], \quad (3.4)$$

$$a = x_1(y_2 - y_3) - x_2(y_1 - y_3) + x_3(y_1 - y_2). \quad (3.5)$$

and

$$\begin{aligned} A &= x_1^2 + y_1^2, \\ B &= x_2^2 + y_2^2, \\ C &= x_3^2 + y_3^2. \end{aligned} \quad (3.6)$$

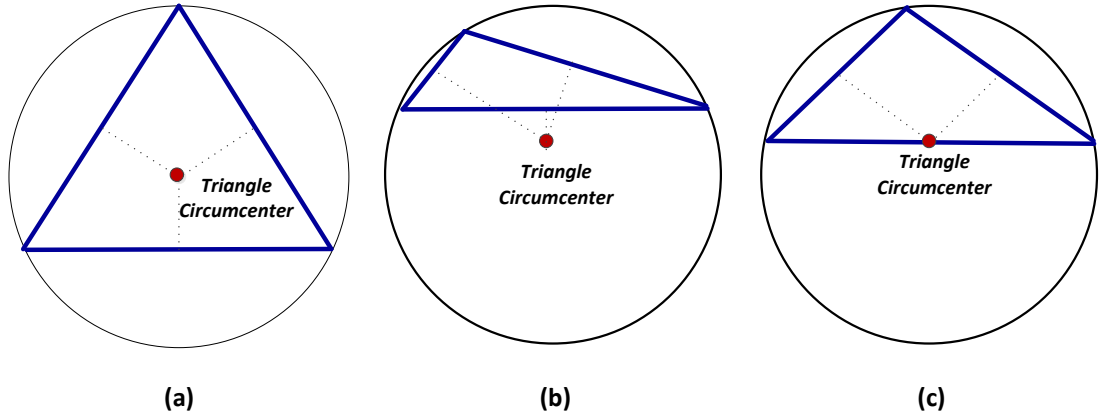


Figure 3.6: Location of circumcentre for (a) acute, (b) obtuse and (c) right-angled Delaunay triangle.

3.2.3 Voronoi mesh

A Voronoi diagram is a geometric structure that represents proximity information about a set of points or objects. It is a way for dividing a region into sub-regions. Voronoi diagram of random set of points is formed of segments that connect a point to the nearest points. Voronoi mesh is the dual mesh of Delaunay triangulation, in which each segment is normal to the original Delaunay mesh. In this thesis Voronoi mesh will refer to set of segments or link lines that connect each triangle circumcentre to the neighbour's circumcentres as shown in Figure 3.7.

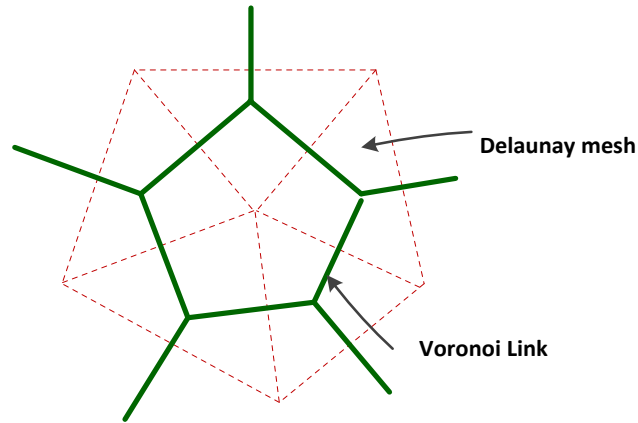


Figure 3.7: Delaunay (dotted red) and Voronoi (solid green) diagram

To create Voronoi mesh, link lines are identified. Link lines are either connecting a triangle circumcentre CC_1 to neighbour circumcentre CC_2 (Figure 3.8(a)), or connecting a triangle circumcentre to the port (side bisector) for triangles located on the outer boundaries as shown in Figure 3.8(b).

Link length is calculated using the distance formula. For two points $P1 (x_1, y_1)$ and $P2 (x_2, y_2)$, the distance between those points is calculated as

$$\text{Link line length} = \sqrt{(x_2 - x_1)^2 + (y_2 - y_1)^2}. \quad (3.7)$$

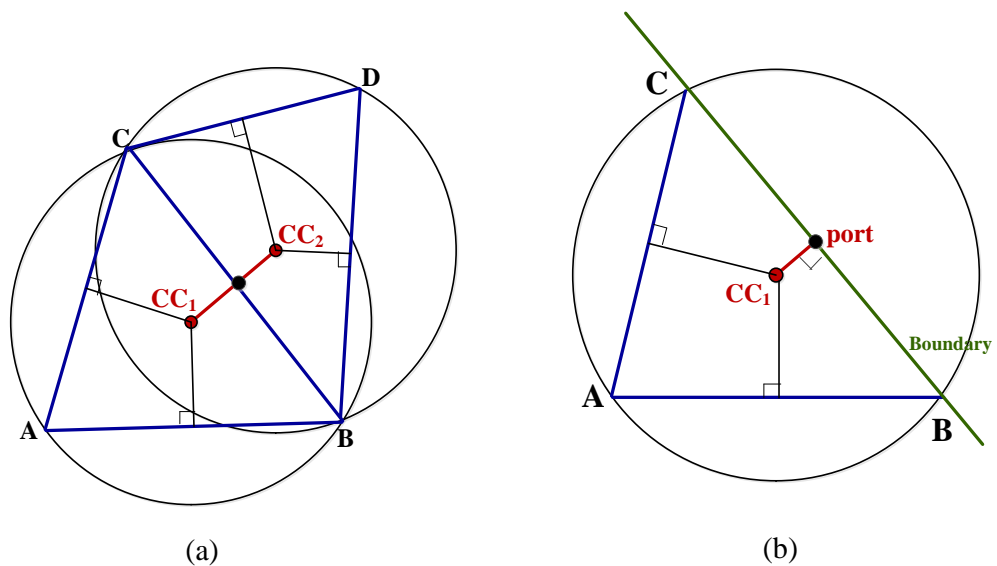


Figure 3.8: link line (a) between circumcentres ($CC_1 - CC_2$) and (b) from circumcentre to port ($CC_1 - \text{port}$)

Figure 3.9 shows the Delaunay and Voronoi meshes of the example shown previously in Figure 3.5.

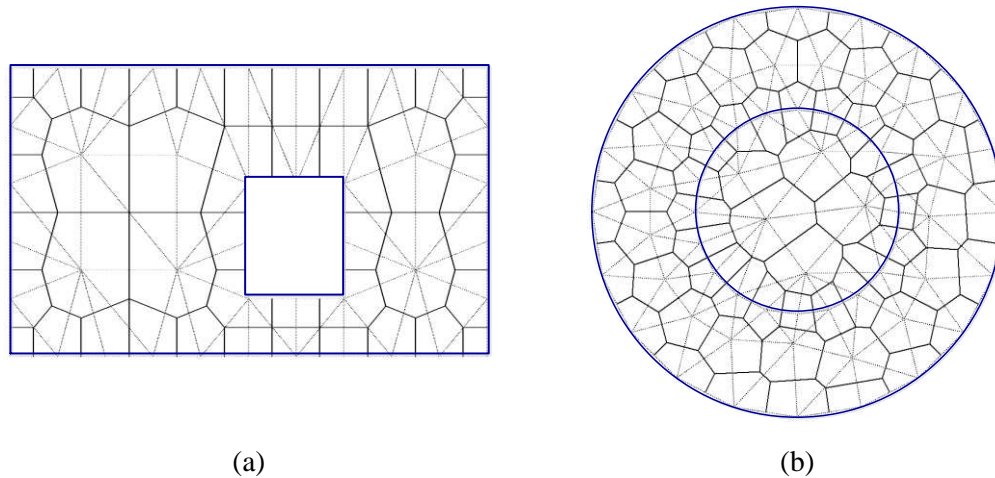


Figure 3.9: Delaunay (light) and Voronoi (dark) meshes of a polygon

Unstructured transmission line modelling (UTLM) is applied on Voronoi mesh where each transmission line is aligned on a Voronoi segment. Due to duality, the problem domain is first triangulated into Delaunay mesh then Voronoi mesh is created. UTLM requires that the TLM node coincides on the Delaunay circumcentre and Voronoi mesh comprises segments linking adjacent triangles circumcentres, then UTLM still hold true working on Voronoi diagram..

3.3 2D UTLM node

In 2D UTLM, each node combines three transmission lines where each transmission line is connected to the neighbour transmission line via a port. The EM fields are sampled on the node boundaries.

An arbitrary UTLM node is shown in Figure 3.10 and is comprised of three transmission lines of lengths Δ_0 , Δ_1 and Δ_2 are the lengths of the transmission lines at which the voltage propagate. The node centre is defined at the intersection of the transmission lines. Three ports are defined which connect node to its neighbours. Each port is located at a distance Δ from the node centre, and an angle φ defines the angle between transmission lines.

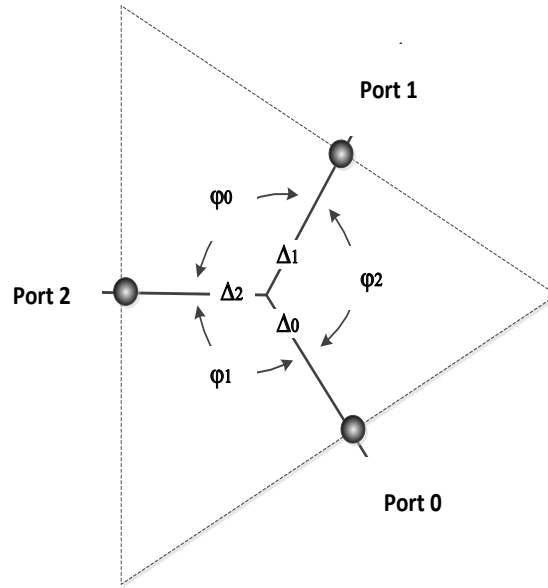


Figure 3.10: The basic structure of the 2D UTLM node.

The node presented in Figure 3.10 is the shunt TLM node which is appropriate for modelling Transverse Magnetic (TM) field propagation with the electric field E_z polarized perpendicular to the plane of the node.

The full set of Maxwell's equations in the cylindrical coordinate system is [45]

$$\left(\frac{\partial E_z}{r \partial \varphi} - \frac{\partial E_\varphi}{\partial z} \right) = -\mu \frac{\partial H_r}{\partial t}, \quad (3.8)$$

$$\left(\frac{\partial E_r}{\partial z} - \frac{\partial E_z}{\partial r} \right) = -\mu \frac{\partial H_\varphi}{\partial t}, \quad (3.9)$$

$$\left(\frac{\partial E_\varphi}{\partial r} - \frac{\partial E_r}{r \partial \varphi} \right) = -\mu \frac{\partial H_z}{\partial t}, \quad (3.10)$$

$$\left(\frac{\partial H_z}{r \partial \varphi} - \frac{\partial H_\varphi}{\partial z} \right) = \varepsilon \frac{\partial E_r}{\partial t}, \quad (3.11)$$

$$\left(\frac{\partial H_r}{\partial z} - \frac{\partial H_z}{\partial r} \right) = \varepsilon \frac{\partial E_\varphi}{\partial t}, \quad (3.12)$$

$$\frac{\partial H_\varphi}{\partial r} - \frac{\partial H_r}{r \partial \varphi} = \varepsilon \frac{\partial E_z}{\partial t}. \quad (3.13)$$

For the 2D TM fields the principal field components are E_z , H_x and H_y and there is no field change in the z -direction, thus, $\partial/\partial z=0$. Under such assumption Equations (3.8)-(3.13) reduce to

$$\frac{\partial E_z}{r \partial \varphi} = -\mu \frac{\partial H_r}{\partial t}, \quad (3.14)$$

$$-\frac{\partial E_z}{\partial r} = -\mu \frac{\partial H_\varphi}{\partial t}, \quad (3.15)$$

$$\frac{\partial H_\varphi}{\partial r} - \frac{\partial H_r}{r \partial \varphi} = \varepsilon \frac{\partial E_z}{\partial t}. \quad (3.16)$$

which leads to the 2D wave equation in cylindrical coordinates,

$$\frac{\partial^2 E_z}{\partial r^2} + \frac{1}{r} \frac{\partial^2 E_z}{\partial \varphi^2} = \mu \varepsilon \frac{\partial^2 E_z}{\partial t^2}. \quad (3.17)$$

This field E_z in the vicinity of the node can be expressed as the superposition of the local solutions of the 2D wave equation expressed by Equation (3.17). Due to the fact that node dimensions are smaller than the wavelength of interest only first three modes can be used for a good field approximation [23] which means that E_z field component can be approximated as.

$$E_z(r, \varphi) = J_0(kr)X_{c0} + \cos(\varphi)J_1(kr)\frac{X_{c1}}{k} + \sin(\varphi)J_1(kr)\frac{2X_{s1}}{k}. \quad (3.18)$$

where J_i are the Bessel functions of the order i , X are modal amplitudes and k is the wavenumber $k=2\pi/\lambda$, where λ is the wavelength of the interests.

Using Equation (3.18), the field at port 1 ($\varphi=0$, $r=\Delta_1$) is,

$$E_{z1} = J_0(k\Delta_1)X_{c0} + \cos(0)J_1(k\Delta_1)\frac{X_{c1}}{k} + \sin(0)J_1(k\Delta_1)\frac{2X_{s1}}{k}. \quad (3.19)$$

Using the assumption that the argument of the Bessel function $k\Delta_1$ is small ($k\Delta_1 \ll 1$), the Bessel functions can be approximated as [45]

$$J_0(k\Delta_1) \cong 1 - \frac{(k\Delta_1)^2}{4}. \quad (3.20)$$

$$J_1(k\Delta_1) \cong \frac{k\Delta_1}{2}. \quad (3.21)$$

resulting in

$$E_{z1} \cong \left[1 - \frac{(k\Delta_1)^2}{4}\right] X_{c0} + \frac{k\Delta_1}{2} \frac{2X_{c1}}{k}, \quad (3.22)$$

Neglecting the small terms $(k\Delta_1)^2$ gives

$$E_{z1} \cong X_{c0} + \Delta_1 X_{c1}. \quad (3.23)$$

Following the same procedure for port 2, the field is expressed as,

$$\begin{aligned} E_{z2} = & J_0(k\Delta_2)X_{c0} + \cos(\varphi_0)J_1(k\Delta_2)\frac{2X_{c1}}{k} \\ & + \sin(\varphi_0)J_1(k\Delta_2)\frac{2X_{s1}}{k}, \end{aligned} \quad (3.24)$$

and is approximated with

$$E_{z2} \cong X_{c0} + \cos(\varphi_0)\Delta_2 X_{c1} + \sin(\varphi_0)\Delta_2 X_{s1}. \quad (3.25)$$

And finally for the port 0, the field is approximated by,

$$\begin{aligned} E_{z0} = & J_0(k\Delta_0)X_{c0} + \cos(\varphi_0 + \varphi_1)J_1(k\Delta_0)\frac{2X_{c1}}{k} \\ & + \sin(\varphi_0 + \varphi_1)J_1(k\Delta_0)\frac{2X_{s1}}{k}, \end{aligned} \quad (3.26)$$

$$E_{z0} \cong X_{c0} + \cos(\varphi_0 + \varphi_1)\Delta_0 X_{c1} + \sin(\varphi_0 + \varphi_1)\Delta_0 X_{s1}. \quad (3.27)$$

Equations (3.23), (3.25) and (3.27) can be expressed in a matrix form

$$\begin{bmatrix} E_{z1} \\ E_{z2} \\ E_{z0} \end{bmatrix} = \begin{bmatrix} 1 & \Delta_1 & 0 \\ 1 & \Delta_2 \cos(\varphi_0) & \Delta_2 \sin(\varphi_0) \\ 1 & \Delta_0 \cos(\varphi_0 + \varphi_1) & \Delta_0 \sin(\varphi_0 + \varphi_1) \end{bmatrix} \begin{bmatrix} X_{c0} \\ X_{c1} \\ X_{s1} \end{bmatrix}. \quad (3.28)$$

This matrix can be expressed compactly as,

$$[E_z] = [T_e][X] \quad (3.29)$$

where T_e is a matrix relating the electric field to the modal components X ,

The magnetic field H_φ component can be expressed using Equation (3.15) which results in,

$$-j\omega\mu_o H_\varphi(r, \varphi) = \frac{\partial J_o(kr)}{\partial r} X_{c0} + \frac{\partial J_1(kr)}{\partial r} \cos(\varphi) \frac{X_{c1}}{k} + \frac{\partial J_1(kr)}{\partial r} \sin(\varphi) \frac{2X_{s1}}{k}. \quad (3.30)$$

Under a small argument, the derivatives of Bessel functions can be approximated as [45]

$$\frac{\partial J_o(kr)}{\partial r} \cong -\frac{k^2 r}{2}, \quad (3.31)$$

$$\frac{\partial J_1(kr)}{\partial r} \cong \frac{1}{2}. \quad (3.32)$$

and the magnetic field at ports 1, 2 and 0 can be expressed as

$$-j\omega\mu_o \Delta_1 H_{\varphi 1} = -\frac{k^2 \Delta_1^2}{2} X_{c0} + \Delta_1 X_{c1}, \quad (3.33)$$

$$-j\omega\mu_o \Delta_2 H_{\varphi 2} = -\frac{k^2 \Delta_2^2}{2} X_{c0} + \Delta_2 \cos(\varphi_o) X_{c1} + \Delta_2 \sin(\varphi_o) X_{s1}, \quad (3.34)$$

$$\begin{aligned} -j\omega\mu_o \Delta_0 H_{\varphi 0} = & -\frac{k^2 \Delta_0^2}{2} X_{c0} + \Delta_0 \cos(\varphi_o + \varphi_1) X_{c1} \\ & + \Delta_0 \sin(\varphi_o + \varphi_1) X_{s1}. \end{aligned} \quad (3.35)$$

Equations (3.33)-(3.35) can be expressed in matrix form as,

$$\begin{bmatrix} j\omega\mu_o \Delta_1 H_{\varphi 1} \\ j\omega\mu_o \Delta_2 H_{\varphi 2} \\ j\omega\mu_o \Delta_0 H_{\varphi 0} \end{bmatrix} = \begin{bmatrix} -\frac{(k\Delta_1)^2}{2} & \Delta_1 & 0 \\ -\frac{(k\Delta_2)^2}{2} & \Delta_2 \cos(\varphi_o) & \Delta_2 \sin(\varphi_o) \\ -\frac{(k\Delta_0)^2}{2} & \Delta_0 \cos(\varphi_o + \varphi_1) & \Delta_0 \sin(\varphi_o + \varphi_1) \end{bmatrix} \begin{bmatrix} X_{c0} \\ X_{c1} \\ X_{s1} \end{bmatrix}. \quad (3.36)$$

This matrix is expressed compactly as,

$$[j\omega\mu_o\Delta^D H_\theta] = [T_h][X]. \quad (3.37)$$

where T_h is a matrix relating the magnetic field to the modal components X .

From Equation (3.29), the modal components can be obtained in term of the electric field

$$X = T_e^{-1}E_z. \quad (3.38)$$

Substituting Equations (3.38) into Equation (3.37), we get

$$j\omega\mu_o\Delta^D H_\varphi = T_h T_e^{-1} E_z. \quad (3.39)$$

Inverting the matrix $[T_e]$ and after mathematical manipulations an expression relating the magnetic field in the three transmission lines the electric field is obtained as [23, 117].

$$\begin{aligned} & \begin{bmatrix} H_{\varphi 1} \\ H_{\varphi 2} \\ H_{\varphi 0} \end{bmatrix} \\ &= \frac{j\omega\epsilon_o}{2} \frac{\begin{bmatrix} \Delta_2\Delta_0\Delta_1s_1 & \Delta_1\Delta_0\Delta_1s_2 & \Delta_2\Delta_1\Delta_1s_0 \\ \Delta_2\Delta_0\Delta_2s_1 & \Delta_2\Delta_0\Delta_1s_2 & \Delta_2\Delta_2\Delta_1s_0 \\ \Delta_2\Delta_0\Delta_0s_1 & \Delta_0\Delta_0\Delta_1s_2 & \Delta_2\Delta_0\Delta_1s_0 \end{bmatrix}}{\Delta_2\Delta_0s_1 + \Delta_1\Delta_0s_2 + \Delta_2\Delta_1s_0} \begin{bmatrix} E_{z1} \\ E_{z2} \\ E_{z0} \end{bmatrix} \\ &+ \frac{1}{j\omega\mu_o} \frac{\begin{bmatrix} \Delta_0s_2 + \Delta_2s_0 & -\Delta_0s_1 & -\Delta_2s_0 \\ -\Delta_0s_1 & \Delta_0s_1 + \Delta_1s_0 & -\Delta_1s_0 \\ -\Delta_2s_1 & -\Delta_1s_2 & \Delta_1s_2 + \Delta_2s_1 \end{bmatrix}}{\Delta_2\Delta_0s_1 + \Delta_1\Delta_0s_2 + \Delta_2\Delta_1s_0} \begin{bmatrix} E_{z1} \\ E_{z2} \\ E_{z0} \end{bmatrix}. \end{aligned} \quad (3.40)$$

where $s_i = \sin(\varphi_i)$. Equation (3.40) shows that the magnetic field is related to the electric field through an admittance matrix, where the first term on the RHS of Equation (3.40) is capacitive and the second term is inductive. As electric field is proportional to the voltage and magnetic field is proportional to the current, the following mapping can be applied [23]

$$\begin{bmatrix} E_{z1} \\ E_{z2} \\ E_{z0} \end{bmatrix} \rightarrow \begin{bmatrix} V_1 \\ V_2 \\ V_0 \end{bmatrix}, \quad \begin{bmatrix} \alpha_{s1} & 0 & 0 \\ 0 & \alpha_{s2} & 0 \\ 0 & 0 & \alpha_{s0} \end{bmatrix} \begin{bmatrix} H_{\varphi 1} \\ H_{\varphi 2} \\ H_{\varphi 0} \end{bmatrix} \rightarrow \begin{bmatrix} I_1 \\ I_2 \\ I_0 \end{bmatrix} \quad (3.41)$$

where α is a mapping constant. Mapping Equation (3.40) in Equation (3.41) leads to [23]

$$\begin{bmatrix} I_1 \\ I_2 \\ I_0 \end{bmatrix} = \frac{j\omega\alpha\epsilon_0}{2} \frac{\begin{bmatrix} \Delta_2\Delta_0\Delta_1s_1 & \Delta_1\Delta_0\Delta_1s_2 & \Delta_2\Delta_1\Delta_1s_0 \\ \Delta_2\Delta_0\Delta_2s_1 & \Delta_2\Delta_0\Delta_1s_2 & \Delta_2\Delta_2\Delta_1s_0 \\ \Delta_2\Delta_0\Delta_0s_1 & \Delta_0\Delta_0\Delta_1s_2 & \Delta_2\Delta_0\Delta_1s_0 \end{bmatrix}}{\Delta_2\Delta_0s_1 + \Delta_1\Delta_0s_2 + \Delta_2\Delta_1s_0} \begin{bmatrix} V_1 \\ V_2 \\ V_0 \end{bmatrix} + \frac{\alpha}{j\omega\mu_0} \frac{\begin{bmatrix} \Delta_0s_2 + \Delta_2s_0 & -\Delta_0s_1 & -\Delta_2s_0 \\ -\Delta_0s_1 & \Delta_0s_1 + \Delta_1s_0 & -\Delta_1s_0 \\ -\Delta_2s_1 & -\Delta_1s_2 & \Delta_1s_2 + \Delta_2s_1 \end{bmatrix}}{\Delta_2\Delta_0s_1 + \Delta_1\Delta_0s_2 + \Delta_2\Delta_1s_0} \begin{bmatrix} V_1 \\ V_2 \\ V_0 \end{bmatrix}. \quad (3.42)$$

In order to get a physical circuit representation of the previous expression, both the capacitive and inductive matrices should be reciprocal. This inductive matrix is reciprocal but the capacitive one is not. The inductive term dominates at low frequencies but when all three port voltages are identical, the resulting current is given by a capacitive matrix [117]

$$\begin{bmatrix} I_1 \\ I_2 \\ I_0 \end{bmatrix} = \frac{j\omega\alpha\epsilon_0}{2} \begin{bmatrix} \Delta_1s_1 & 0 & 0 \\ 0 & \Delta_2s_2 & 0 \\ 0 & 0 & \Delta_0s_0 \end{bmatrix} \begin{bmatrix} V_1 \\ V_2 \\ V_0 \end{bmatrix}. \quad (3.43)$$

It is then correct to approximate the capacitive matrix with the one given in Equation (3.43) so that Equation (3.42) reduces to

$$\begin{bmatrix} I_1 \\ I_2 \\ I_0 \end{bmatrix} \cong \frac{j\omega\alpha\epsilon_0}{2} \begin{bmatrix} \Delta_1s_1 & 0 & 0 \\ 0 & \Delta_2s_2 & 0 \\ 0 & 0 & \Delta_0s_0 \end{bmatrix} \begin{bmatrix} V_1 \\ V_2 \\ V_0 \end{bmatrix} + \frac{\alpha}{j\omega\mu_0} \frac{\begin{bmatrix} \Delta_0s_2 + \Delta_2s_0 & -\Delta_0s_1 & -\Delta_2s_0 \\ -\Delta_0s_1 & \Delta_0s_1 + \Delta_1s_0 & -\Delta_1s_0 \\ -\Delta_2s_1 & -\Delta_1s_2 & \Delta_1s_2 + \Delta_2s_1 \end{bmatrix}}{\Delta_2\Delta_0s_1 + \Delta_1\Delta_0s_2 + \Delta_2\Delta_1s_0} \begin{bmatrix} V_1 \\ V_2 \\ V_0 \end{bmatrix}. \quad (3.44)$$

This expression will enable representation of the node using LC equivalent network as shown in Figure 3.11, where the voltage and the current through each link are used to define E_z , H_ϕ .

The circuit parameters are given as follows [23],

$$L_i = \frac{\mu_0\Delta_i}{\alpha s_i}. \quad (3.45)$$

$$C_i = \frac{\alpha \varepsilon_0 s_i \Delta_i}{2}. \quad (3.46)$$

where ε_0 and μ_0 are the material permittivity and permeability respectively. Δ_i is the link line length, $s_i = \sin(\varphi_i)$ and α is a mapping constant.

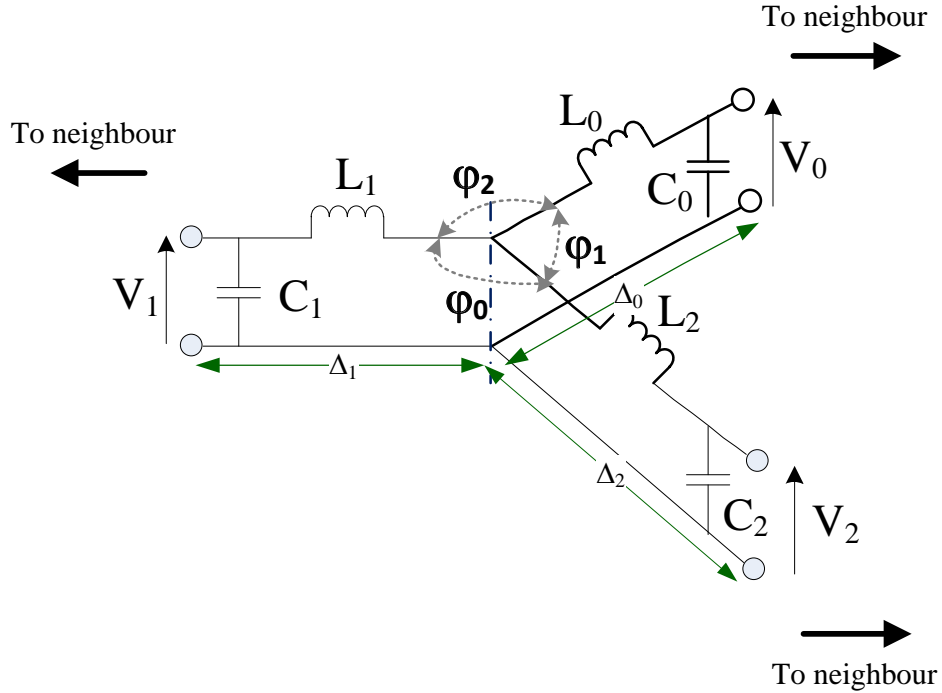


Figure 3.11: Transmission Line model of TLM node.

For L_i and C_i components to be positive $s_i = \sin(\varphi_i)$ must be positive, which can be achieved if the angle φ_i is less than π . Using Delaunay triangulations ensures that this condition is achieved. Delaunay condition states that for any two adjacent triangles the sum of the two angles facing the side shared between those triangles should be equal or less than π . Therefore, if the Delaunay condition is achieved the stability of the UTLM node approximation is ensured.

Also, the continuity of electric and magnetic fields should be investigated through the node boundaries. The continuity of the voltage across the node boundaries ensures the continuity of electric field. But since $I_i = \alpha s_i H_i$, the continuity of magnetic field is not achieved unless αs_i is the same across the adjacent nodes. This can be achieved if the circumcentre of the Delaunay triangle [23] is chosen to be the centre of the node as shown in Figure 3.12 and R is the radius of the circle that encloses the triangle.

The continuity of magnetic field is enforced on the ports which lie on the straight line that is normal to the interface between two triangles, as shown in Figure 3.12. Note that triangle circumcentre is the intersection of the three normal bisectors.

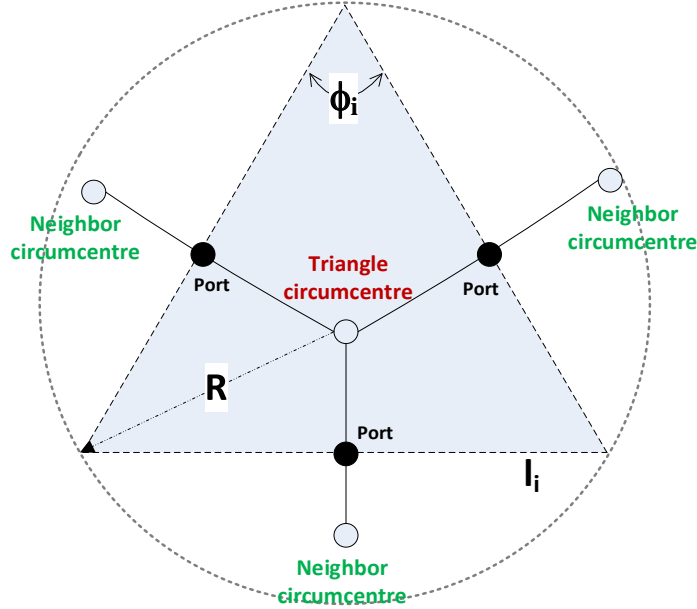


Figure 3.12: Delaunay Triangle where its circumcentre coincides with the TLM node.

In this case the length of the shared interface between the two triangles is $l_i = 2RS_i$ where l_i is also the length of the triangle side opposite to the angle ϕ_i as shown in Figure 3.12, so that $l_i = \alpha s_i H_i = 2R s_i H_i = l_i H_i$. This enables the current continuity to be enforced across the nodes.

To summarise, this section mapped the 2D Maxwell equations for the TM modes onto the triangular Delaunay node. It is shown that node centre coincides with the circumcentre of Delaunay triangle and that transmission lines follow the Voronoi mesh. The LC parameters of the equivalent transmission lines are also derived.

3.4 Circuit analysis of shunt TLM node

3.4.1 Stub model of inductor and capacitor

In this section the equivalent transmission line parameters are defined. The TLM node should coincide with the triangle circumcentre. Each node is connected to the adjacent

nodes through transmission lines. Each transmission line is modelled using a stub model, so that inductor is modelled with short circuited stub model and capacitor with an open-circuited stub model as shown in Figure 3.13 [7].

Signal travel between two adjacent nodes through transmission line with time step Δt , so it takes the signal time $\Delta t/2$ to travel from the node to the port. Time step is calculated based on the shortest transmission line in the problem region and it is given by [23]

$$\Delta t_{max} = \Delta_{min} \sqrt{2\varepsilon\mu}. \quad (3.47)$$

where Δ_{min} is the shortest transmission line in the entire region, ε is the material permittivity and μ is the material permeability.

Capacitive stubs enable synchronization of the voltage propagation along different lengths of transmission line in the unstructured mesh so that they all reach the nodal interfaces (ports) at the same time. The stubs are inserted to slow down the pulse in all lines that are greater than minimum link line [23].

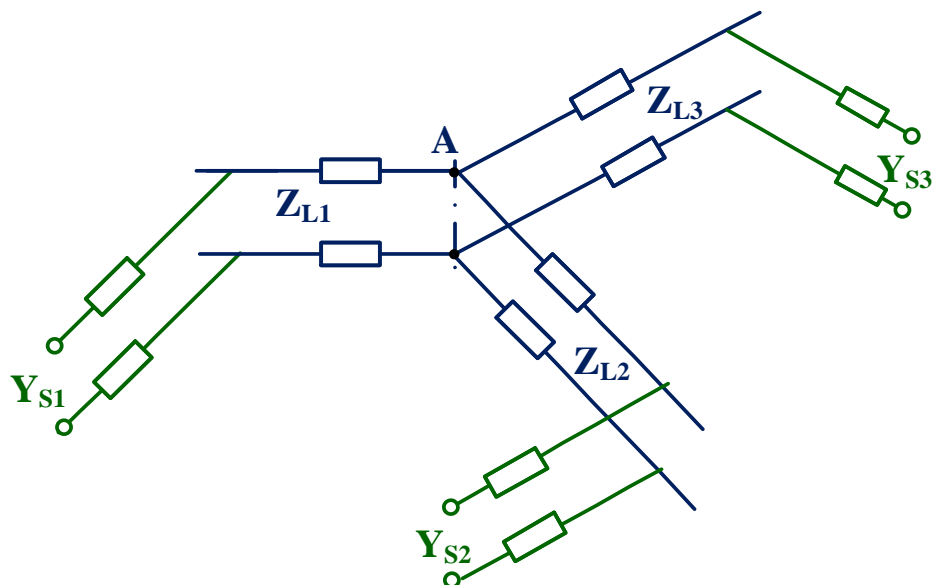


Figure 3.13: Stub model of the TLM shunt node.

The stub model of the inductor has parameters L_l , C_l , a length Δl and a round trip Δt and it is terminated with a short circuit. The propagation velocity along the line is [7]

$$u_l = \frac{\Delta l}{\Delta t/2} = \frac{1}{\sqrt{L_l C_l}} \quad (3.48)$$

Then the capacitance is calculated as follows

$$C_l = \frac{1}{u_l^2 L_l} = \frac{(\Delta t)^2}{4(\Delta l)^2 L_l} \quad (3.49)$$

The characteristic impedance of transmission line is

$$Z_L = \sqrt{\frac{L_l}{C_l}} = \sqrt{\frac{4(\Delta l)^2 L_l^2}{(\Delta t)^2}} = \frac{2L_l \Delta l}{\Delta t} = \frac{2L}{\Delta t} \quad (3.50)$$

From Equation (3.45) and Equation (3.50) the characteristic impedance of the transmission line can be calculated as,

$$Z_{Li} = \frac{2L}{\Delta t} = \frac{2\mu\Delta_i}{2R\sin\phi_i\Delta t} = \frac{2\mu\Delta_i}{l_i\Delta_t} \quad (3.51)$$

where μ is the material permeability ($\mu = \mu_0\mu_r$), Δ_i is the length of the link line ($i=0,1,2$), l_i is the triangle side and Δt is time step at which the signal travels between nodes.

The stub model of a capacitor has parameters C_s , L_s a length Δl and a round trip Δt . It is terminated with an open-circuit. The velocity of propagation is

$$u_s = \frac{\Delta l}{\Delta t/2} = \frac{1}{\sqrt{L_s C_s}} \quad (3.52)$$

Then

$$L_s = \frac{1}{u_s^2 C_s} = \frac{(\Delta t)^2}{4C_s(\Delta l)^2} \quad (3.53)$$

And the characteristic impedance of the stub will be

$$Z_C = \sqrt{\frac{L_S}{C_S}} = \sqrt{\frac{(\Delta t)^2}{4C_S^2(\Delta l)^2}} = \frac{\Delta t}{2C_S\Delta l} = \frac{\Delta t}{2C}. \quad (3.54)$$

The stub admittance Y_{si} can be calculated using the formulas in Equation (3.46) and Equation (3.54) [23],

$$Y_{si} = \frac{2C}{\Delta t} - Y_{Li} = \frac{2(2R\sin\varphi_i\varepsilon\Delta_i)}{2\Delta t} - \frac{l_i\Delta_t}{2\mu\Delta_i} = \frac{\varepsilon l_i\Delta_i}{\Delta t} - \frac{l_i\Delta_t}{2\mu\Delta_i}. \quad (3.55)$$

where ε is the material permittivity ($\varepsilon = \varepsilon_0\varepsilon_r$), Δ_i is the length of the link line ($i=0,1,2$), l_i is the triangle side and Δt is time step.

3.4.2 Thevenin equivalent circuit

In this section equivalent circuits for scatter and connect process on the UTLM node will be presented. The two Thevenin circuits are defined for the triangle node (scatter process) and for triangle ports (connect process).

The equivalent representation of the inductor and capacitor using short-circuited (SC) and open-circuited (OC) stubs and their Thevenin equivalence is schematically given in Figure 3.14.a and b respectively. The stub model of the inductor and capacitor has voltages and currents represented at discrete value of the time step $k\Delta t$. The incident voltage to the inductive stub is expressed as ${}_kV_L^i$ and the Thevenin equivalent source is twice the incident voltage $2{}_kV_L^i$ due to the round trip. The Thevenin impedance is the transmission line characteristic impedance Z_L as shown in Figure 3.14.a [7]

Similarly the Thevenin equivalent circuit for the capacitive stub is given in Figure 3.14.b and has incident voltage to the capacitive stub expressed as $2{}_kV_C^i$, and equivalent Thevenin impedance equals to the capacitive stub impedance Z_C .

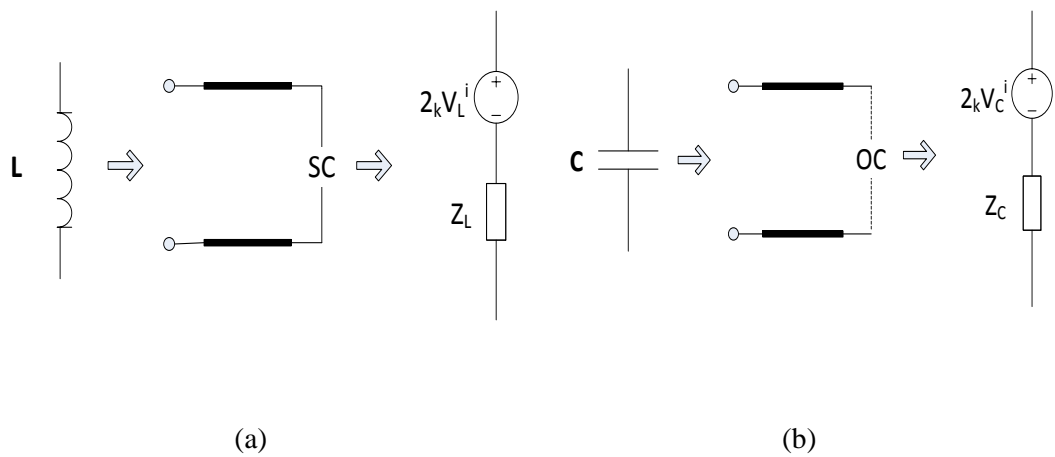


Figure 3.14: Thevenin equivalence of (a) stub inductor model, (b) stub capacitor model.

The Thevenin equivalent circuit for a UTLM shunt node A is comprised of three transmission lines as shown in Figure 3.15 where Z_{L_i} and V_{L_i} are the transmission line equivalent impedance and voltage, respectively.

The Thevenin equivalence of the port circuit can be deduced from Figure 3.16 which shows the transmission line network between two connected triangles with nodes A and B through port C defining the interface at which two neighbouring transmission lines intersect.

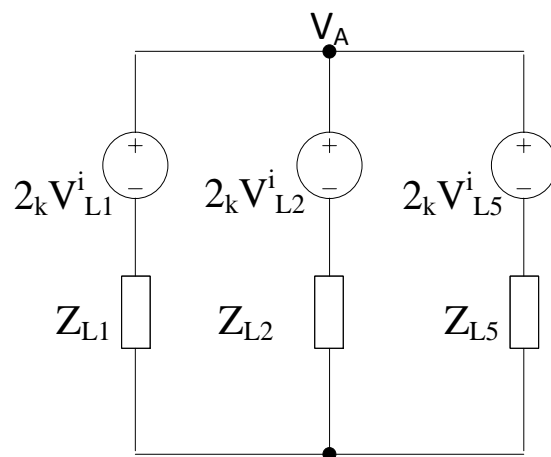


Figure 3.15: Thevenin equivalent circuit of shunt TLM node.

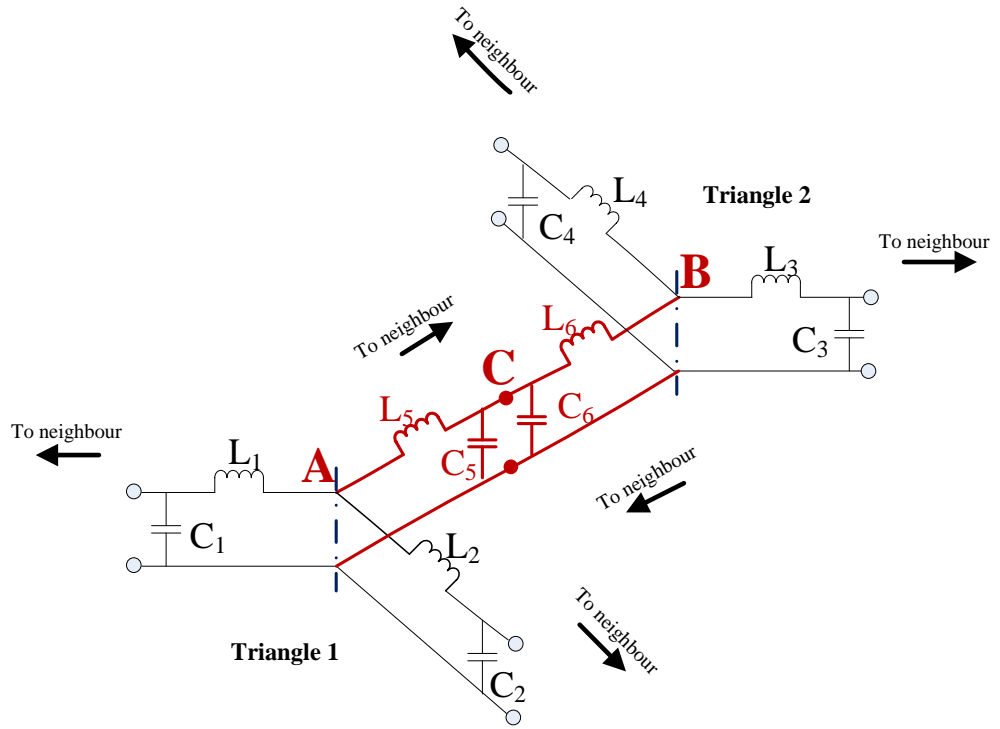


Figure 3.16: The transmission line equivalent circuit of the connected links (in red).

The equivalent admittance at the port C is expressed as

$$Y_S = Y_{S5} + Y_{S6}. \quad (3.56)$$

where Y_{S5} and Y_{S6} are the stub admittances of the two interconnected capacitive open-circuited stubs.

The Thevenin equivalent circuit for the port C is given in Figure 3.17 where Z_{L5} and Z_{L6} are the inductive impedances of the triangle A and neighbour triangle B, respectively. V_{L5}^i and V_{L6}^i are the incident voltages on the transmission lines of the triangle A and neighbour triangle B, respectively, and V_S^i and Z_S are the stub voltage and equivalent impedance of the two parallel stubs, respectively.

Since the link impedance and stub admittance formulas shown previously are associated with single triangle, the time step Δt represents the time the signal consume in travelling from circumcentre to port.

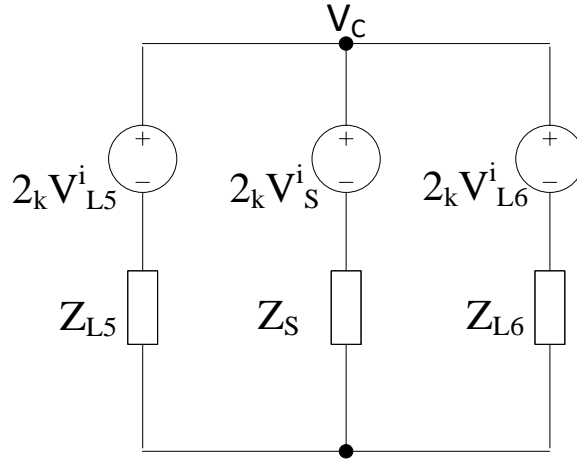


Figure 3.17: Thevenin equivalent circuit of the connection process.

3.4.3 Scatter and connect processes

The transmission line theory states that the total voltage at any point along the line consists of incident and reflected voltages. In the main TLM algorithm, at any given time step k , the voltages are incident on the nodes, from which they scatter and then connect with the neighbouring nodes at ports to define new incident voltages for the next time step, $(k+1)$.

The scattering of the incident voltages at the nodes can be analysed using the Thevenin equivalence of the node circuit in Figure 3.15. Applying Kirchhoff's current law, the node voltage is calculated as

$$V_A = \left[\frac{2_k V_{L1}^i}{Z_{L1}} + \frac{2_k V_{L2}^i}{Z_{L2}} + \frac{2_k V_{L5}^i}{Z_{L5}} \right] Z_{eq}. \quad (3.57)$$

where Z_{eq} is the equivalent impedance where $\frac{1}{Z_{eq}} = \frac{1}{Z_{L1}} + \frac{1}{Z_{L2}} + \frac{1}{Z_{L5}}$.

The reflected voltage at each link are calculated from

$$\begin{aligned} {}_k V_{L1}^r &= V_A - {}_k V_{L1}^i, \\ {}_k V_{L2}^r &= V_A - {}_k V_{L2}^i, \\ {}_k V_{L5}^r &= V_A - {}_k V_{L5}^i. \end{aligned} \quad (3.58)$$

where ${}_k V_{L1}^r$, ${}_k V_{L2}^r$ and ${}_k V_{L5}^r$ are the reflected voltages at link1, link 2 and link 3 respectively at the time step k.

The reflected voltages now propagate to neighbouring nodes and reach the node interface at which capacitive stubs are connected.

The total voltage at the interface i.e. port C, can be obtained from Kirchhoff's current law,

$$V_C = \left[\frac{2 {}_k V_{L5}^i}{Z_{L5}} + \frac{2 {}_k V_S^i}{Z_S} + \frac{2 {}_k V_{L6}^i}{Z_{L6}} \right] Z_{eq}. \quad (3.59)$$

where Z_{L5} and Z_{L6} are the link impedances, Z_S is the equivalent stub admittance, and Z_{eq} is the equivalent impedance where $\frac{1}{Z_{eq}} = \frac{1}{Z_{L5}} + \frac{1}{Z_{L6}} + \frac{1}{Z_S}$.

Then reflected voltages on transmission lines 5 and 6 and the stub are updated as follows,

$$\begin{aligned} {}_k V_{L5}^r &= V_C - {}_k V_{L5}^i, \\ {}_k V_{L6}^r &= V_C - {}_k V_{L6}^i, \\ {}_k V_S^r &= V_C - {}_k V_S^i. \end{aligned} \quad (3.60)$$

In the connect phase the voltages reflected from the port C that are expressed in Equations (3.60) are the incident voltages for the next time step k+1, i.e.

$$\begin{aligned} {}_{k+1} V_{L5}^i &= {}_k V_{L5}^r, \\ {}_{k+1} V_{L6}^i &= {}_k V_{L6}^r, \\ {}_{k+1} V_S^i &= {}_k V_S^r. \end{aligned} \quad (3.61)$$

Triangles located on boundaries have a special connection procedure. Figure 3.18 shows Thevenin equivalent circuits for different boundary types, namely short-circuited, open-circuited and matched boundary condition

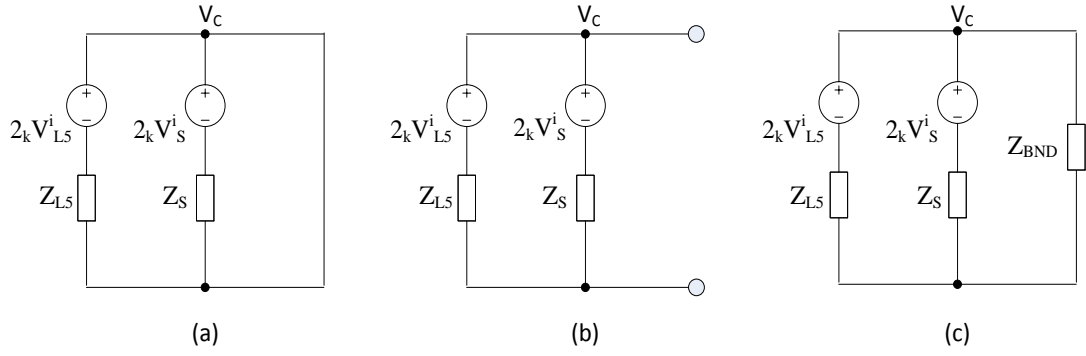


Figure 3.18: Thevenin equivalent circuit of a triangle located on (a) short circuit, (b) open circuit or (c) matching impedance boundary.

The Thevenin equivalent circuit for short circuit boundary is shown Figure 3.18(a) from where the reflected voltage is simply,

$${}_k V_{L5}^r = -{}_k V_{L5}^i. \quad (3.62)$$

If the boundary is open-circuit as in Figure 3.18(b), the port C voltage reduces to

$$V_C = \left[\frac{2{}_k V_{L5}^i}{Z_{L5}} + \frac{2{}_k V_S^i}{Z_S} \right] Z_{eq}. \quad (3.63)$$

where Z_{eq} is the equivalent impedance $\frac{1}{Z_{eq}} = \frac{1}{Z_{L5}} + \frac{1}{Z_{LS}}$

For the matched boundary shown in Figure 3.18(c), the port voltage becomes

$$V_C = \left[\frac{2{}_k V_{L5}^i}{Z_{L5}} + \frac{2{}_k V_S^i}{Z_S} \right] Z_{eq}. \quad (3.64)$$

where Z_{eq} is the equivalent impedance $\frac{1}{Z_{eq}} = \frac{1}{Z_{L5}} + \frac{1}{Z_{L3}} + \frac{1}{Z_{BND}}$

The voltage reflected from the boundaries are calculated from

$$\begin{aligned} {}_k V_{L5}^r &= V_C - {}_k V_{L5}^i, \\ {}_k V_S^r &= V_C - {}_k V_S^i. \end{aligned} \quad (3.65)$$

The scatter – connect process is repeated for a given number of timesteps or until steady state is reached.

3.5 Implementation of 2D unstructured TLM

3.5.1 Mesh geometry

Meshes are categorized according to their dimensionality. Various types of meshes are defined according to the number of elements that comprise the mesh; such as triangular mesh that comprises three sides, quadrilateral meshes of four sides, tetrahedral meshes which is composed of four triangular faces, and hexahedral meshes which is composed of six square faces. For two dimensional modelling triangles and quadrilaterals are used.

Structured mesh such as rectangular cells have identical discretisation cells, therefore the mesh dimensionality is controlled by the cell area. On the other hand, unstructured mesh, unless they are made of equilateral triangles, have greater cell variability. In the unstructured mesh, the user has two degrees of freedom when selecting or producing a mesh: the average cell size, expressed in terms of triangle area, and a measure of the shape of the triangles used. The shape of the triangle is controlled by a measure known as the mesh quality factor Q which is the ratio of the triangle circumradius to the triangle shortest edge.

A simple polygon or polyhedron is created and fed to a mesh generator. The function of the mesh generator is to triangulate the inner region into number of meshes. A polygon is known as PSLG (Planar Straight Line Graph) and it is formed by defining the outer boundaries of the intended problem; this can be achieved by setting the number of points on the boundaries and the segments connecting these points. So, by increasing the number of points, segments get smaller which lead to finer meshes. The inner space can be filled with any materials by assigning some attributes. Internal boundaries can be applied as well which makes the polygon accommodate different materials or changes in dimensions.

In this thesis the data of the polygon is fed to a mesh generator named “Triangle” created by J. Shewchuk [37].

The user controls the mesh dimensionality by applying the certain switches in “Triangle” command line to request the required mesh size and quality. The mesh size is controlled by the ‘-a’ switch which imposes the maximum area constraints in the meshed region. This is achieved by setting the required area value following this switch. For example, if the user chose the segment length L in the polygon to be 1mm, it is preferable to choose the triangles area not to exceed $(0.5L^2)$ which is 0.5mm^2 for this case, then the mesh area switch is written as ‘-a0.5’ which guarantee that the triangles produced have an area equal to or less than 0.5mm^2 . Another important switch is ‘-q’ which controls the mesh shape and consequently the mesh quality. The quality is controlled by assigning a value of the minimum angle to the -q switch. Writing -q switch in the command line with no value following it will lead to mesh generation with no angles smaller than 20 degrees. Generally, a triangle with good quality is of equilateral shape. Generally speaking, it requires good amount of trial and error working with these switches till the required mesh is achieved.

The mesh generator triangulates the region and produces four main files that contain data of the meshed area, namely:

.node file: contains the data of nodes that was provided in the original polygon in addition to new node inserted in the meshed area.

.edge file: contains the data of segments that was provided in the original polygon in addition to new segments connecting the new nodes, which forms the sides of the Delaunay triangles. Also it defines whether the segment is located on border or inside the meshed region.

.ele file: provide data about the vertices of the produced Delaunay triangles in addition to the material parameters for each triangle. And finally

.neigh file: locate the three neighbours of each triangle.

Further details of how to use “Triangle”, the usage of switches, format of input files and output files are included in Appendix A.

Meshing a space into structured meshes is created by inserting fixed equidistant points around the boundaries and inside the problem domain. The mesher then discretise the domain into structured mesh (square or rectangle) that is formed of two equal right-angled triangles as shown in Figure 3.19. Right-angled triangle has its circumcentre located on the middle of its hypotenuse. This will lead to zero link length between each two triangles forming a structured mesh as shown in Figure 3.19 circled in red, in other words the problem space will include number of zero link lines equals to the number of structured meshes. Figure 3.20 shows a rectangular space meshed into structured mesh formed of two right-angled triangles.

As the resulting meshes are of the form of equal Delaunay triangles, the UTLM algorithm laid in [23] can be applied on these structured meshes. The zero link length will lead to zero link and stub impedances upon substitution in Equations (3.51) and (3.55), then the link connecting nodes A and B is represented by a short-circuited link impedance and open-circuited stub admittance as shown in Figure 3.21.a which is reduced to the conventional shunt TLM node as shown in Figure 3.21.b.

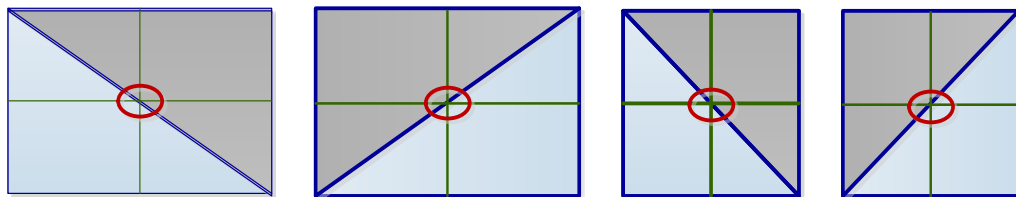


Figure 3.19: Structured mesh formed of two right-angled triangles

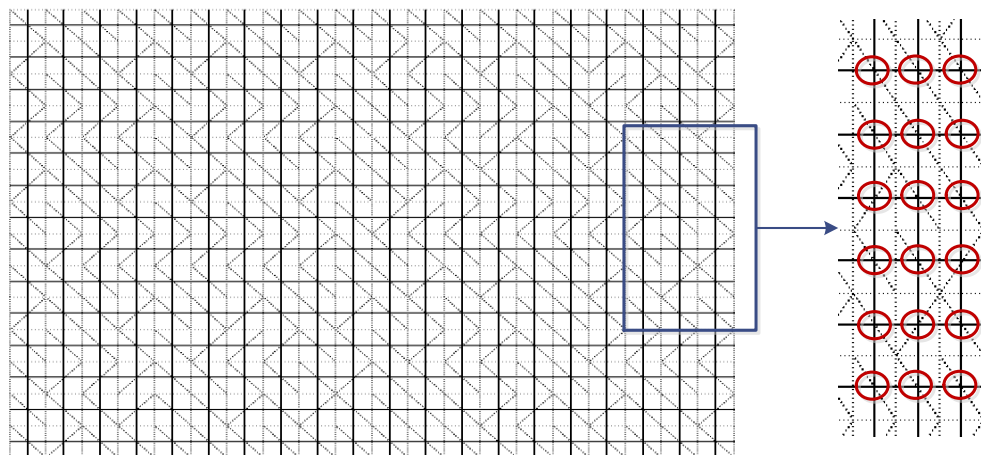


Figure 3.20: Delaunay & Voronoi mesh of PEC rectangular resonator with enlarged inset identifying presence of zero link lines in all structured meshes

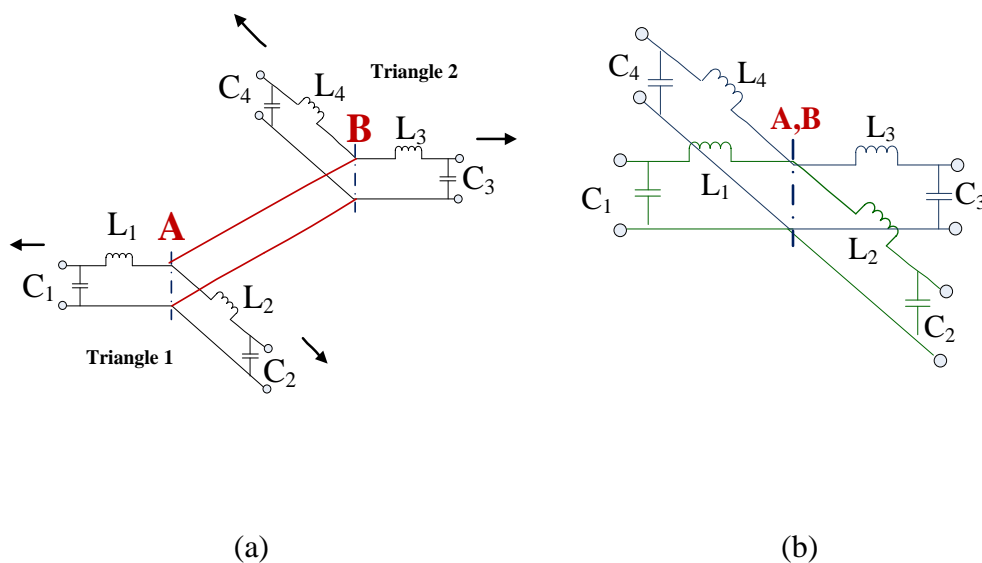


Figure 3.21: (a) short link length represented by short circuit link line and open circuit stub admittance which is equivalent to (b) the conventional structured shunt TLM node

3.5.2 Software Design

The 2D UTLM implementation is comprised basically of repetitive process of scattering and connection as mentioned in Section 3.4. Each process is repeated for all the TLM nodes within the domain of the simulated problem. Before implementing the US TLM data obtained from Shewchuk mesh generator [37] should be processed to form the complete triangulated area and identify the routes allowed for the signal to travel. This will be achieved by allocating a reference system to locate the correct neighbours and boundaries at the triangle sides. Then for the completion of the big picture some aspects should be considered, such as the excitation of the problem, the link and stub parameter calculations, the link and stub voltage calculations, followed by the calculations of the reflected voltages from the links and stubs. Generally, the software code follows the design rules laid out in [7, 23].

Figure 3.22 shows the interconnection of the modules for simulating the electromagnetic problem. The problem geometry is defined in an input file which is fed to the mesh generator, which produces meshed geometry that is defined in four main files (.node, .ele, .edge and .neigh). These files are then fed to the UTLM simulator that processes these data. According to the results produced, one can return

back to the mesh generator and modify how the problem is meshed till good accuracy is achieved.

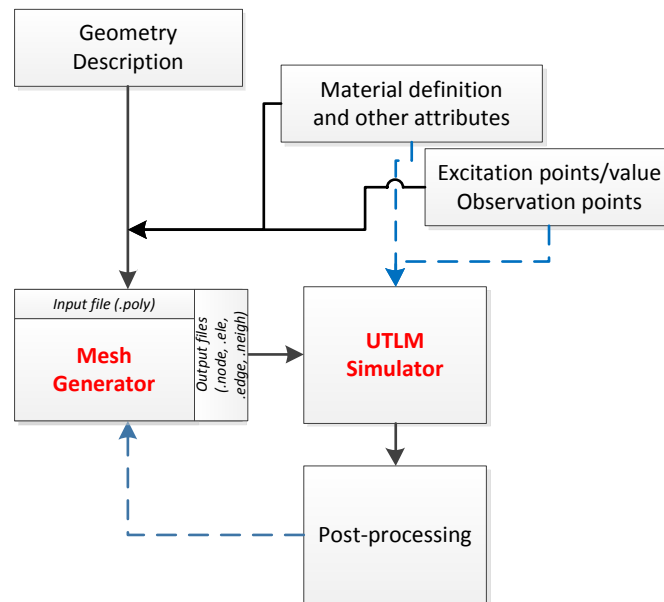


Figure 3.22: The mesh generator and UTLM simulator interrelation.

Extra attributes such as the material distribution, or the excitation and observation specifications can be either defined in the UTLM simulator or in the mesh generator stages.

Given a specific geometrical structure, a non object oriented implementation is hard to maintain since the basic mesh configuration is unique where each cell has its own parameters and attributes. This is why the high level Object Oriented Programming language C++ is used to implement the unstructured TLM (2D UTLM) tool.

The basic categories that will form the complete triangulated area are: node, edge, triangle and region. The structure is built starting from the basic element which is the nodes or triangle vertices defined by their IDs and coordinates. Each two vertices will then form a segment, segments should be marked whether they are located on borders or inside the triangulated area. Also, each segment should be allocated to the two triangles that share such segment. Triangles are then formed by segments. Triangle (or mesh) is the main element of the problem, in which each mesh should have its set of data as dimension, material, etc.

And finally, the upper category is the problem region which act as the vital part of the structure, this allow allocating meshes and their relative positions, connecting meshes and exchanging data between neighbours. Also, it contains the global parameters of the problem such as the time step, the number of iteration, source points and observation points, etc.

According to these specifications four classes are created; which are TLMnode, TLMTriangle, TLMEdge and TLMRegion. For Further detail on these classes, refer to Appendix A

3.6 General unstructured TLM algorithm

Figure 3.23 shows a general unstructured TLM algorithm. This algorithm is divided into three stages: pre-processing, main process and post-processing

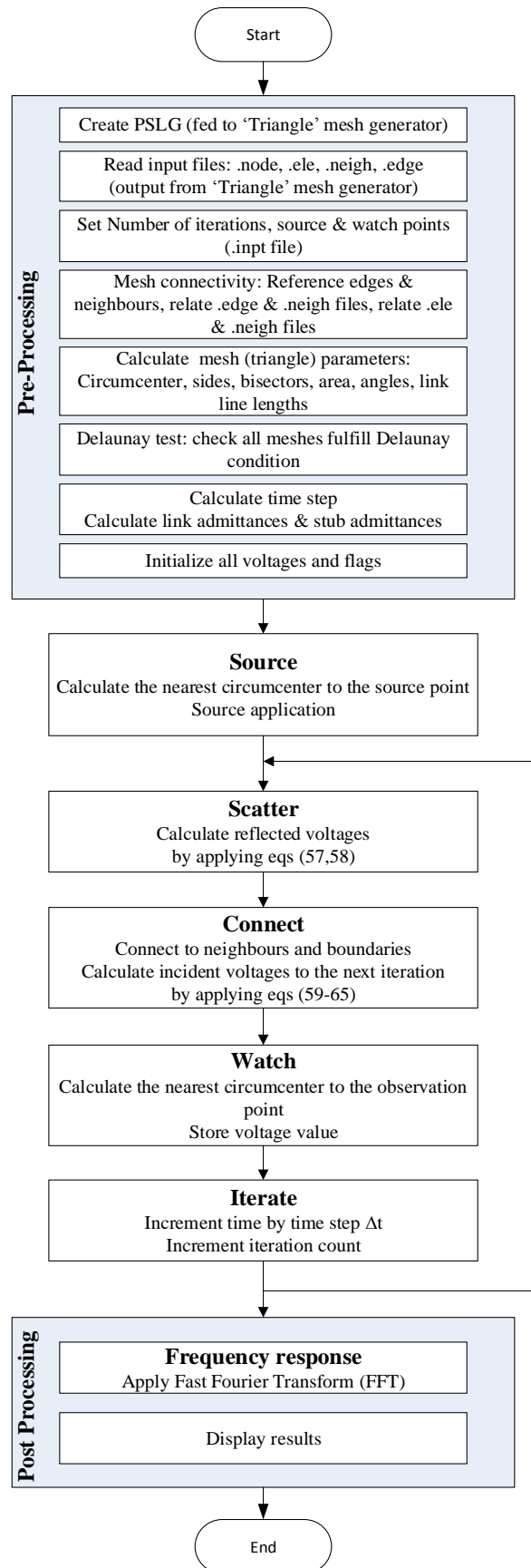


Figure 3.23: General Unstructured TLM algorithm.

3.6.1 Pre-processing

The first stage of the UTLM algorithm at which the data received from the TLM mesher is processed to define mesh connectivity. The source and excitation points are defined, the time step is set and the link and stub admittances are calculated.

Input files - In this stage the PSLG (Planar Straight Line Graph) diagram is created to define the problem shape and apply the attributes if exists (.poly file). The .poly file is fed to the mesh generator [37], and then by applying the proper switches the files .node, .ele, .edge and .neigh discussed in Appendix A are produced. In addition to the data contained in these files, an extra file is produced that contain other input parameters as the excitation and observation points and input voltage.

Mesh connectivity - Connecting triangles and defining their relative positions is one of the crucial parts in the algorithm. Proper connectivity ensures that each triangle deliver signal to the correct neighbours which consequently ensures continuous flow of the signal. The 'Triangle' [37] mesh generator provided enough data of the meshes but the three files .ele, .edge and .neigh should be linked together.

- Linking .ele and .edge files - The .ele file provides the ID of its three vertices and the .edge file contain the ID of the segment two end points. A referencing system is created for each edge which will help later on to identify the correct neighbour at each side. Note that the ID of the triangle vertices is put in an anti-clockwise manner. Starting with the first pair of vertices (V_1, V_2) of the first triangle in the .ele file and comparing them with the list of edges in the .edge file, once a match has been found the edge that has the same endpoints as V_1 and V_2 will be marked as **E12**. Then moving to the second pair of vertices for the first triangle (V_2, V_3) and applying the same criteria on the list of edges till a match is found that will be marked as **E23**, and for the third pair (V_1, V_3) the matched edge will be marked as **E13**. This will be repeated for all triangles till all edges are referenced as shown in Figure 3.24.
- Linking .edge and .neigh files - The .neigh file provides the ID of the three neighbour of each triangle. To complete the mesh connectivity calling the proper neighbour should be ensured from any side of the triangle. Since the triangle edges are marked by E12, E23 and E13, then the neighbours will take the same notations;

meaning the neighbour at the **E12** side will be marked **N12**, the neighbour at **E23** side will be marked **N23**, and that at the **E13** side is marked **N13**.

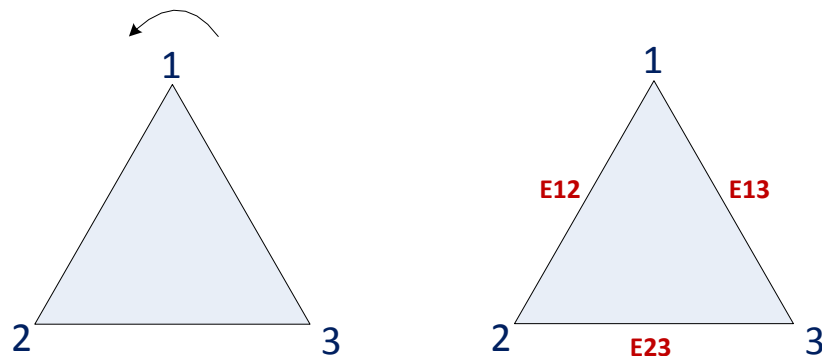


Figure 3.24: Referencing triangle edges.

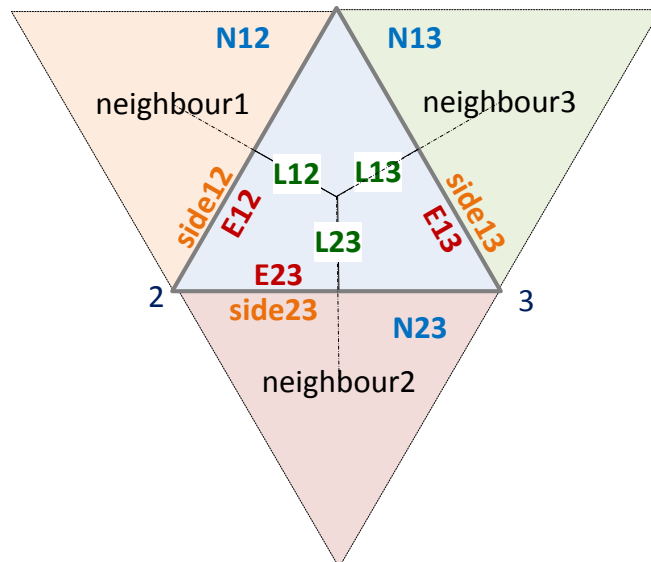


Figure 3.25: Referencing triangle neighbours.

Delaunay check - Although the mesh generator “Triangle” [37] creates Delaunay triangles, another check should be carried on to ensure that all triangles obey Delaunay condition.

Delaunay condition states that for each two adjacent triangles the sum of the angles that face the same side should be equal to or less than π .

A triangle of sides a , b and c has three angles **A** that is facing side **a**, **B** facing side **b** and **C** side **c**. The angles will be calculated according to the cosine formulae, this will ease referencing and extracting the correct angles. According to the reference system discussed earlier, **angle 1** will be the one facing **E12**, **angle 2** will be the one facing **E23** and **angle 3** is the one opposite to **E13** as shown in Figure 3.26.

The cosine formula is given generally as follows:

$$\begin{aligned}\cos A &= \frac{b^2 + c^2 - a^2}{2bc}, \\ \cos B &= \frac{c^2 + a^2 - b^2}{2ca}, \\ \cos C &= \frac{a^2 + b^2 - c^2}{2ab}.\end{aligned}\tag{3.66}$$

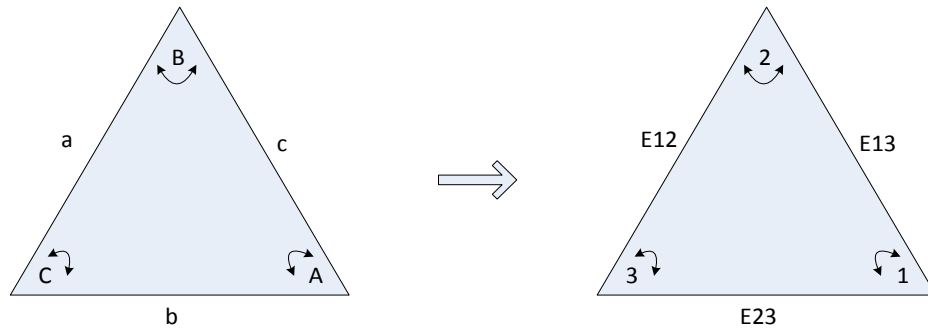


Figure 3.26: Referencing triangle angles.

Time step and admittance - Since the software design is based on the mesh as the basic element, then the transmission line lengths will be calculated and stored as the distance from triangle circumcentre to its ports, this will ensure to accommodate the change of materials when moving from a mesh to another. Special care should be taken upon substitution of Δ_{\min} in Equation (3.47). The link admittances are calculated from Equation (3.51) of which the three line admittances y_{L12} , y_{L23} and y_{L13} (shown in Figure 3.27) can be calculated,

$$y_{L12} = \frac{side_{12}\Delta t}{L_{12}\mu},$$

$$y_{L23} = \frac{side_{23}\Delta t}{L_{23}\mu},$$

$$y_{L13} = \frac{side_{13}\Delta t}{L_{13}\mu}. \quad (3.67)$$

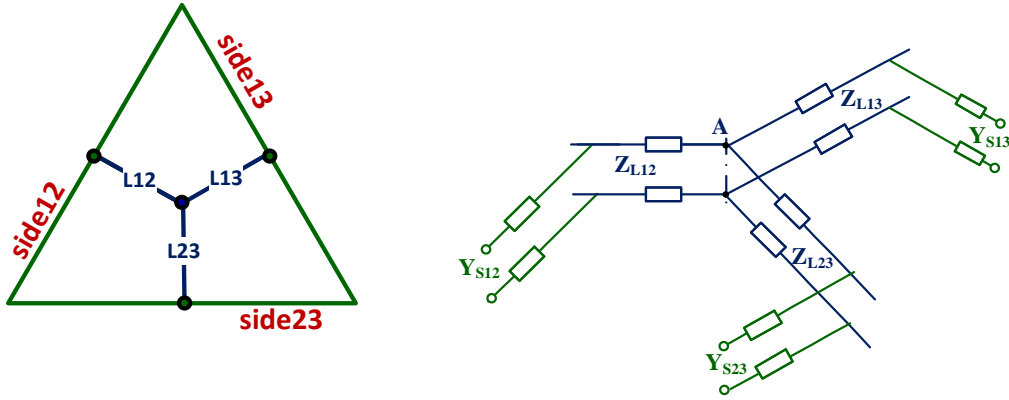


Figure 3.27: Referenced link and stub admittances.

Also, for the stub admittance Equation (3.55) will expand to express the three stub admittances y_{s12} , y_{s23} and y_{s13} as shown in Figure 3.27,

$$y_{s12} = \frac{side_{12}L_{12}\varepsilon}{\Delta t} - y_{l12},$$

$$y_{s23} = \frac{side_{23}L_{23}\varepsilon}{\Delta t} - y_{l23},$$

$$y_{s13} = \frac{side_{13}L_{13}\varepsilon}{\Delta t} - y_{l23}. \quad (3.68)$$

3.6.2 Main process

The main body of the structure involves the definition of the source function, the scatter-connect process is applied, then the UTLM simulator output is extracted for post-processing.

Source - Excitation point(s) is chosen and the coordinates are set in input file. This point is selected to be away from the boundaries or the centre of the region. Since the source should be applied at the circumcentre of the mesh, the unstructured TLM simulator calculates the distance between the provided input point and all circumcentres till a minimum distance is achieved. Then the source will be applied at the circumcentre of the nearest triangle to the given source point.

Normally a Dirac signal is inserted at the beginning of simulation at single point to provide a wide spectrum range. This is performed by setting a constant value of V at the input point at $t=0$. But a discrete sine, cosine or Gaussian pulse can be fed at the source point(s) according to the problem requirements.

Scatter - Both incident and reflected voltages are calculated according to Equations (3.57) and (3.58)

Connect - At which the presence of neighbours will be taken into account according to Equations (3.59) and (3.60). Or a connection with boundaries is performed for a triangle containing sides that falls on the outer boundaries. The voltage calculated at the scatter part is transmitted to the neighbours. Then the voltage reflected back from neighbours is calculated. This voltage will be the incident voltage at the scatter part in the next time step. Both the neighbour ID and the edge type are checked to define which connection process will be performed.

Figure 3.28 shows a basic flow chart of the connection process. If a triangle is located on a boundary from one or two sides, the side is checked to identify whether it is short-circuited, open-circuited or impedance matched, in other words the application of Equations (3.62) - (3.65).

Watch - As in the source part, the observation point(s) is set in the input file, for which the nearest circumcentre is found and the voltage value is stored in the output file at each individual time step.

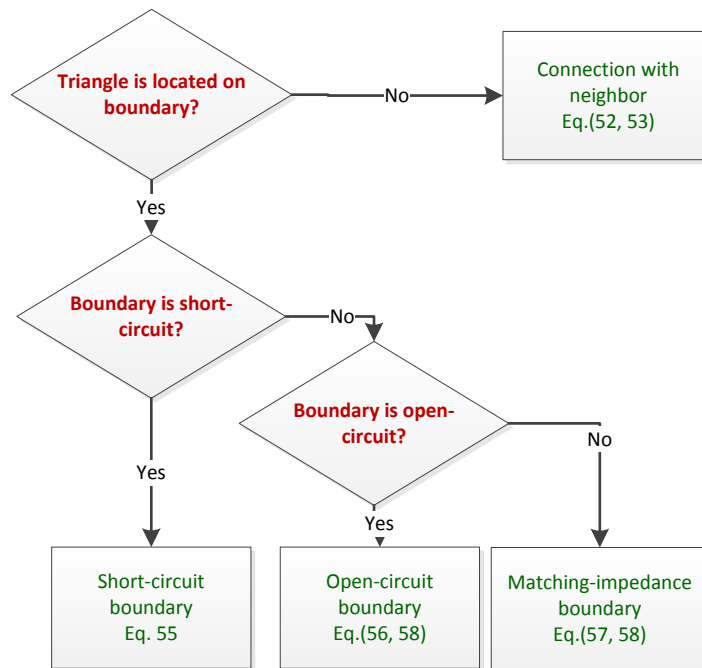


Figure 3.28: Basic flowchart for 'connect' process.

3.7 Results

This section analyses the accuracy and efficiency of the Unstructured TLM method. For this purpose several canonical problems of different shapes and materials are considered, namely air and dielectric filled metallic cylindrical and rectangular resonators. Resonators are meshed using a variety of triangular and structured meshes. The resonant frequencies are extracted from simulations and compared against the known analytical results. Results obtained using unstructured and structured TLM methods are also compared in terms of accuracy and efficiency.

3.7.1 Effect of number and type of meshes on an air-filled cylindrical PEC Resonator

First example considered is an air filled cylindrical PEC resonator of 1cm radius. The resonator is approximated by a sequence of polygonal approximations to generate a triangular mesh of Delaunay type and using readily available software provided in [37]. The outer boundary is subdivided by allocating 40, 60, 70, 80, 120 points on the resonator circumference. This produces different meshes from coarse as low as 104 triangles for the entire region as shown in Figure 3.29(a) to fine mesh containing 1498

triangles as shown in Figure 3.29(b). The resonator is excited with a Dirac function, in which a voltage of 10V is inserted at single input point at the beginning of simulation.

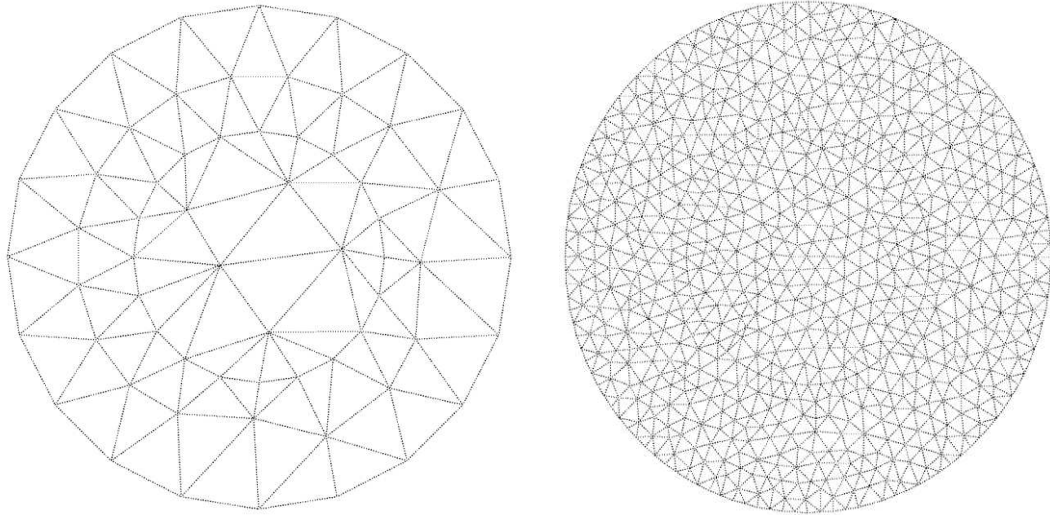


Figure 3.29: Air-filled cylindrical PEC resonator triangulated to a (a) coarse and (b) fine unstructured meshes.

The triangular meshes are then processed to obtain the Voronoi mesh of transmission lines. An example of Delaunay and Voronoi mesh for the case of 70 points along the resonator circumference is shown Figure 3.30 that contains 768 triangles, 2304 link lines and has a shortest link length of 15.96mm thus requiring time step of 37.63ps.

The time step is 58.79ps, 44.34ps, 37.63ps, 25.27ps and 22.98ps for 104, 504, 768, 1026 and 1498 triangles, respectively. This leads to execution time of 6s, 17s, 24s, 37s, and 42s, respectively.

The resonance frequencies are extracted from the time domain signal using Fast Fourier Transform (FFT) and their accuracy is compared with analytical results.

The analytical results of resonant frequencies f_c^{mn} for a circular resonator are calculated from [140]

$$f_c^{mn} = \frac{\chi_{mn}}{2\pi a \sqrt{\mu\epsilon}} \quad (3.69)$$

where χ_{mn} are the zeros of Bessel functions for $n=1,2,3,\dots$ and are given in Table 3.1

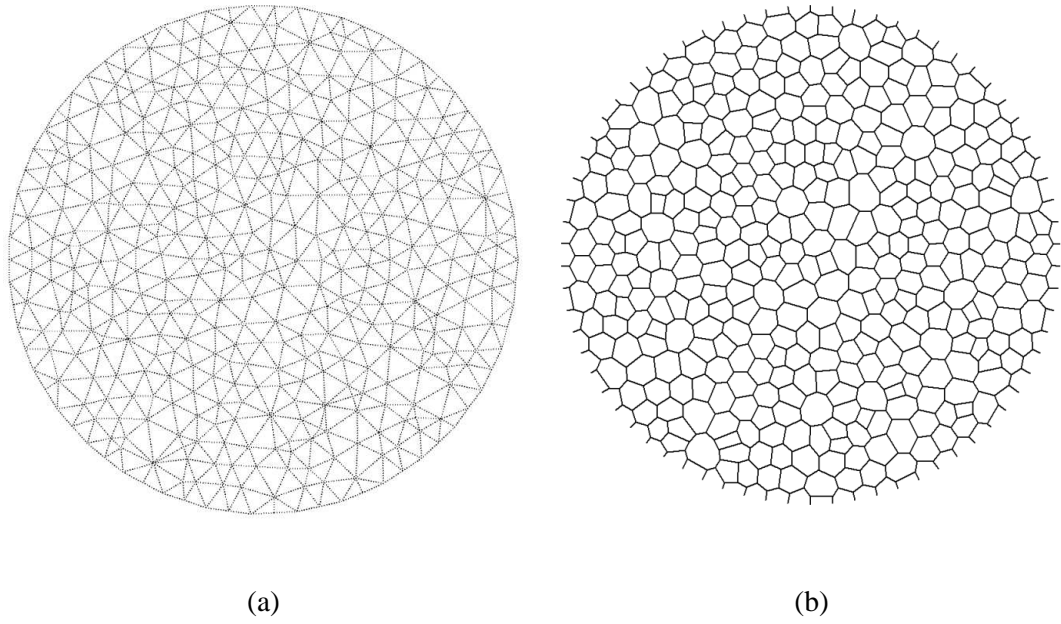


Figure 3.30: (a) Delaunay and (b) Voronoi diagram of an air-filled cylindrical PEC.

Table 3.1: Zeros χ_{mn} of Bessel functions $J_m(\chi_{mn})=0$ for $n=1, 2, 3$

	m=0	m=1	m=2	m=3
n=1	2.4049	3.8318	5.135	6.3802
n=2	5.5201	7.0156	8.4173	9.7610
n=3	8.6537	10.1735	11.6199	13.0152

Figure 3.31 shows the percentage relative error in the first five resonance modes for varieties of meshes. The relative error is calculated as $|(f_{TLM} - f_c^{mn})/f_c^{mn}|$. The coarse mesh shows the highest error which was slightly above 7% for the fundamental mode TM01 and decreased to lower than 0.05% for the fine mesh. For higher order modes, the error ranged from 5.64% to 0.06% for TM11, 2.28% to 0.21% for TM21, 1.95% to 0.21% for TM02 and finally from 2.85% to 0.24% for TM31.

Table 3.2 shows the percentage relative error for the first five resonance modes as a function of number of triangles in the mesh. Generally, for a resonator triangulated into 768 meshes and above the error for all modes is lower than 0.5%.

Figure 3.32 shows resonance curves for a coarse and fine unstructured mesh, namely, for 104 triangles and 1498 triangles. Notice that the coarse triangulation of 104 meshes

shows unwanted resonance frequencies in some of the resonance modes. Also, Figure 3.32.a shows that resonance mode TM21 splits which make it difficult to extract the correct resonance frequency. As the triangulated area becomes finer the resonance frequencies become shaper and shift to the correct places.

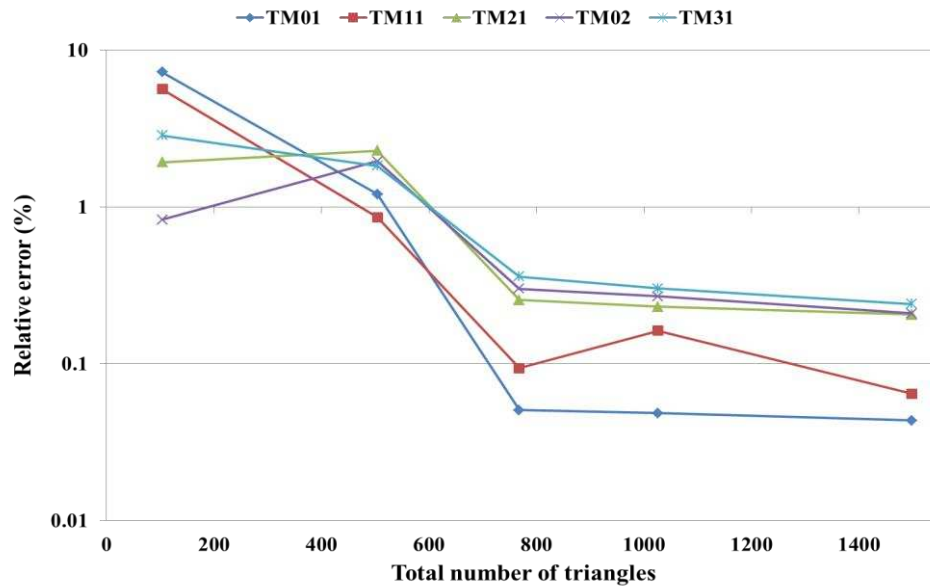


Figure 3.31: Relative error for different resonant modes of an air-filled PEC cylindrical resonator as a function of number of triangles in the UTLM mesh.

Table 3.2: Analytical and numerical resonant frequencies and relative error for a number of structured meshes of an air-filled PEC cylindrical resonator.

Number of meshes		TM01	TM11	TM21	TM02	TM31
104	f_a (GHz)	11.46769	18.27182	24.48942	26.32242	30.42378
	f_{TLM} (GHz)	10.63798	19.30189	24.01770	26.54010	29.55602
	Relative error %	7.23523	5.63752	1.92624	0.82699	2.85223
504	f_a (GHz)	11.46769	18.27182	24.48942	26.32242	30.42378
	f_{TLM} (GHz)	11.32924	18.11467	23.93075	25.80886	29.86800
	Relative error %	1.20727	0.86004	2.28127	1.95103	1.82679
768	f_a (GHz)	11.46769	18.27182	24.48942	26.32242	30.42378
	f_{TLM} (GHz)	11.46189	18.28892	24.42699	26.24335	30.31452
	Relative error %	0.05053	0.09363	0.25494	0.30038	0.35914
1026	f_a (GHz)	11.46769	18.27182	24.48942	26.32242	30.42378
	f_{TLM} (GHz)	11.47325	18.30145	24.43290	26.25157	30.33210
	Relative error %	0.04845	0.16219	0.23079	0.26916	0.30134
1498	f_a (GHz)	11.46769	18.27182	24.48942	26.32242	30.42378
	f_{TLM} (GHz)	11.46271	18.28358	24.43905	26.26741	30.35074
	Relative error %	0.04343	0.06436	0.20568	0.20898	0.24008

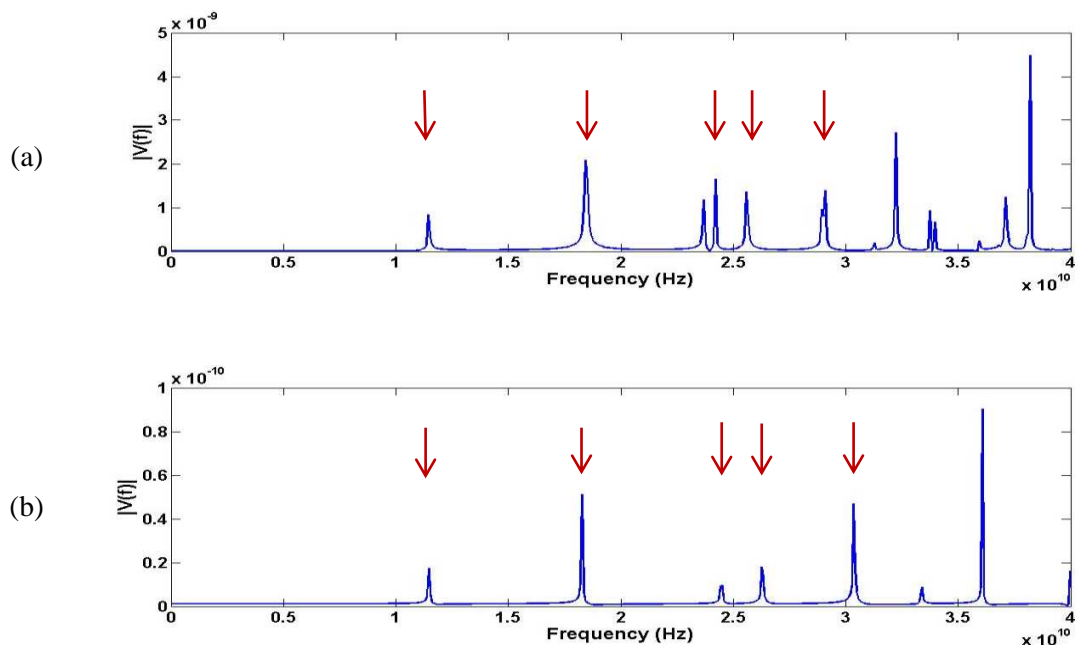


Figure 3.32: Resonant frequencies for an air-filled cylindrical PEC resonator triangulated into (a) 104 and (b) 1498 unstructured meshes, with red arrows pointing TM01, TM11, TM21, TM02 and TM31 mode positions.

In the next step the air-filled PEC cylindrical resonator is meshed using a range of structured meshes. This can be achieved by creating an input file that contains the coordinates of equidistant fixed points inside the cavity space. These points are then connected to form squares or rectangles. The mesh generator then divides each square or rectangle into two equal right-angled triangles. Although the mesh contains right-angled triangles it numerically reduces to a structured TLM mesh.

The cylindrical resonator is discretized into equivalent structured meshes of 52, 554, 392, 530 and 742. The time step for each mesh is 117.85ps, 78.57ps, 62.85ps, 47.14ps and 39.28ps, respectively, with an execution time of 4s, 9s, 13s, 19s and 24s.

Figure 3.33 shows structured meshes for the case of resonator meshed into 104 and 1484 regular meshes. Coarse mesh introduces crude staircase approximation for the resonator approximation for the resonator circumference. In the case of fine mesh the staircase approximation of the resonator shape becomes better.

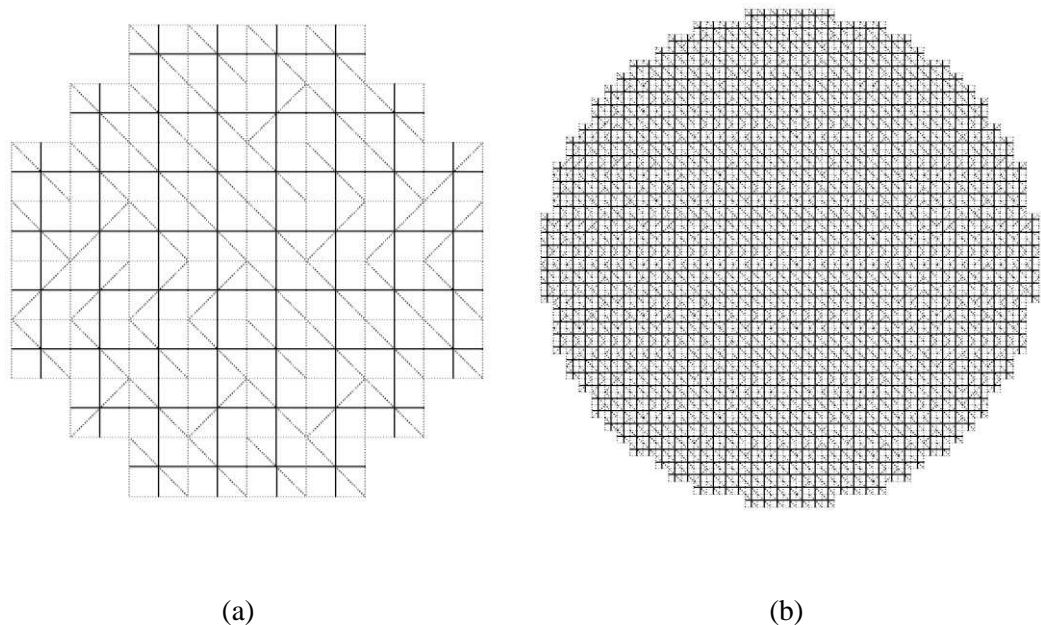


Figure 3.33: Delaunay (light) and Voronoi (dark) diagram of an air-filled cylindrical PEC resonator triangulated from a (a) coarse to (b) fine structured meshes.

Figure 3.34 shows the percentage relative error for the first five resonant frequencies as a function in different meshes. The coarse mesh with 104 meshes shows the worst error which was above 17% for the fundamental mode and decreased to 1.75% in the

case of fine structured mesh. For higher modes, the error ranged from 18.4% to 1.67% for TM11, 13.48% to 1.77% for TM21, and it fluctuates between 7.85% and 0.25% for TM02 and between 6.93% and 1.35% for TM31. Generally, there is a tendency of decrease in relative error of resonance frequencies as the number of meshes increases.

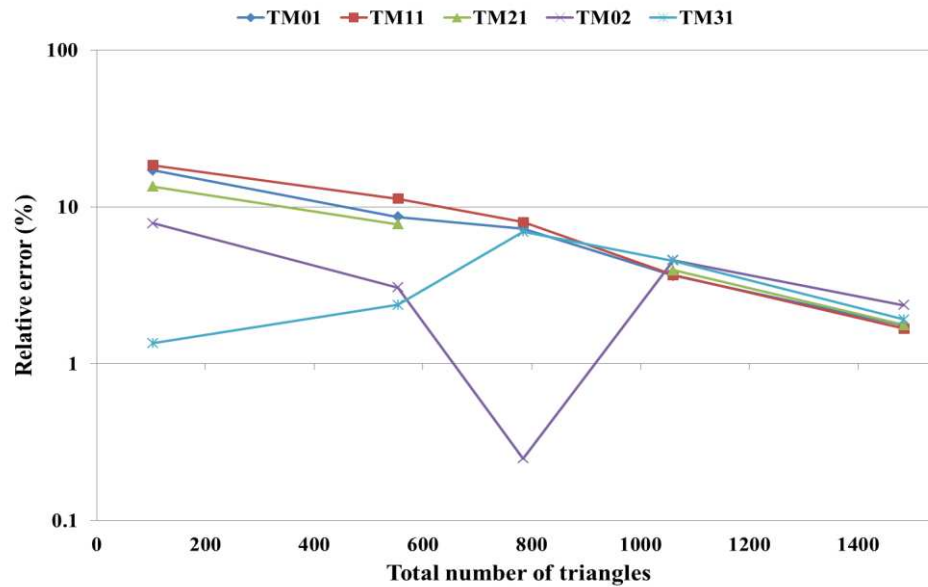


Figure 3.34: Relative error for different resonant modes of an air-filled PEC cylindrical resonator as a function of number of squares in the structured TLM mesh.

Table 3.3 shows the percentage relative error for the first five resonance modes for structured meshes with 104, 554, 784, 1060 and 1484 structured meshes.

Figure 3.35 shows resonance curves for a coarse and fine unstructured mesh, namely, for 104 triangles and 1484 triangles. Notice that the coarse triangulation of 104 meshes shows unwanted resonance frequencies and large deviation from the analytical resonant frequencies. As the triangulated area becomes finer the resonance frequencies become shaper and shift to the correct places.

Table 3.3: Analytical and numerical resonant frequencies and relative error for a number of structured meshes of an air-filled PEC cylindrical resonator.

Number of meshes		TM01	TM11	TM21	TM02	TM31
104	f_a (GHz)	11.46769	18.27182	24.48942	26.32242	30.42378
	f_{TLM} (GHz)	13.42479	21.63358	27.79017	28.38873	30.01338
	Relative error %	17.06621	18.39861	13.47827	7.85000	1.34894
554	f_a (GHz)	11.46769	18.27182	24.48942	26.32242	30.42378
	f_{TLM} (GHz)	12.45813	16.21057	22.58973	25.51664	31.14531
	Relative error %	8.63675	11.28103	7.75719	3.06119	2.37160
784	f_a (GHz)	11.46769	18.27182	24.48942	26.32242	30.42378
	f_{TLM} (GHz)	12.30277	19.73398	26.09178	26.25692	32.53216
	Relative error %	7.28202	8.00227	6.54307	0.24884	6.93004
1060	f_a (GHz)	11.46769	18.27182	24.48942	26.32242	30.42378
	f_{TLM} (GHz)	11.04926	17.59907	23.52238	25.11712	29.04701
	Relative error %	3.64882	3.68190	3.94879	4.57899	4.52530
1484	f_a (GHz)	11.46769	18.27182	24.48942	26.32242	30.42378
	f_{TLM} (GHz)	11.26693	17.96619	24.05642	25.70078	29.84214
	Relative error %	1.75066	1.67269	1.76811	2.36164	1.91179

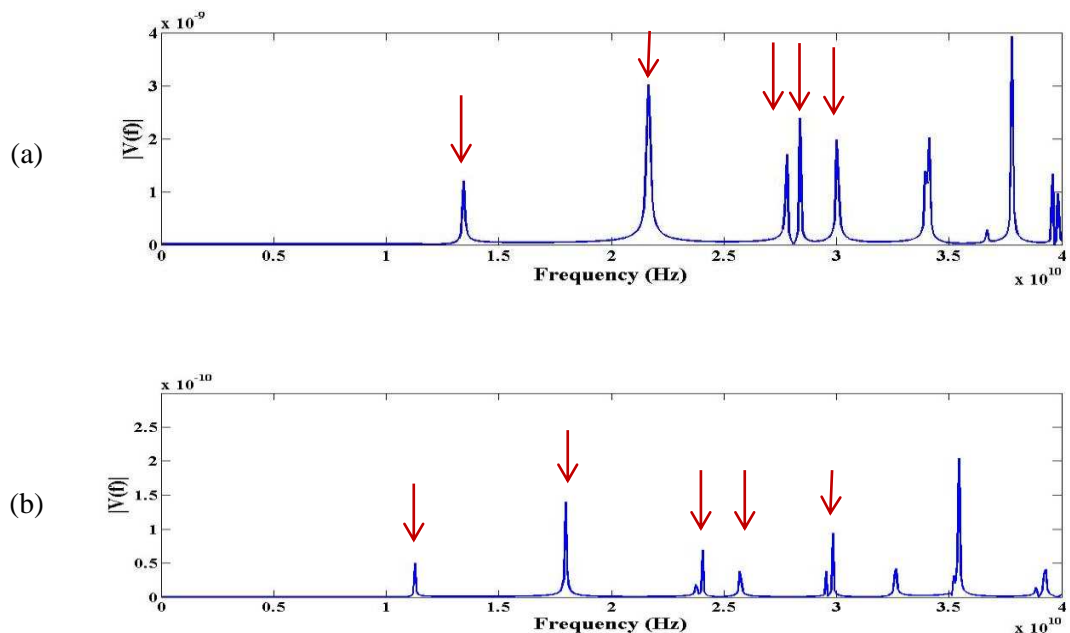


Figure 3.35: Resonant frequencies for an air-filled cylindrical PEC resonator triangulated into (a) 104 and (b) 1484 structured meshes, with red arrows pointing TM01, TM11, TM21, TM02 and TM31 mode positions.

The discretization length is extracted for unstructured and structured meshes for the sake of better comparison of the relative error in resonant frequencies. As the unstructured mesh is not uniform the discretization length is chosen to be equal to the square root of the average area $\sqrt{A_{av}}$ all over the meshed domain. The structured mesh is uniform with equal squares or rectangles filling the meshed domain but the discretization length is calculated in the same manner above. The normalized discretization length is calculated with respect to the wavelength of interest. The maximum intended frequency is chosen to be 100GHz which corresponds to a minimum wavelength of 0.003m. Figure 3.36 shows the relative error in modes TM01 for both structured and unstructured meshes. For Air-filled PEC resonator the unstructured meshes have introduced significantly lower relative error as compared to those with structured meshes. For example a resonator discretized into 59135 unstructured cells of $\sqrt{A_{av}}/\lambda_0=0.05$ achieved percentage relative error of 0.00081%, whilst when discretized into 96520 structured cells of $\sqrt{A_{av}}/\lambda_0=0.009$, the percentage relative error is 0.00806%. This is expected since the unstructured mesh offers better boundary approximation for the curved boundaries of the circular resonator as shown in Figure 3.37.

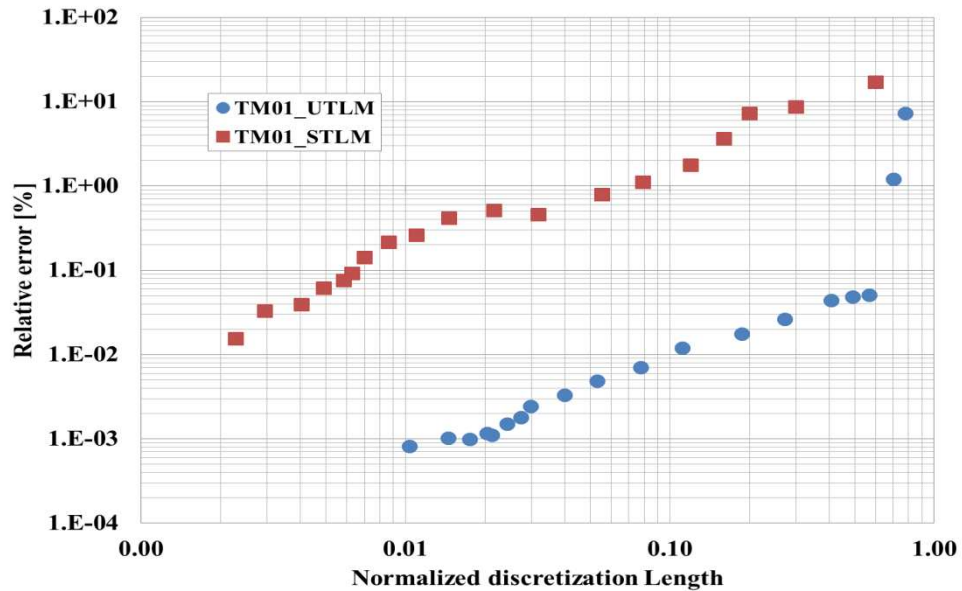


Figure 3.36: Relative error in TM01 for an air-filled PEC cylindrical resonator as a function of the normalized discretization length $\sqrt{A_{av}}/\lambda_0$ for both unstructured and structured meshes.

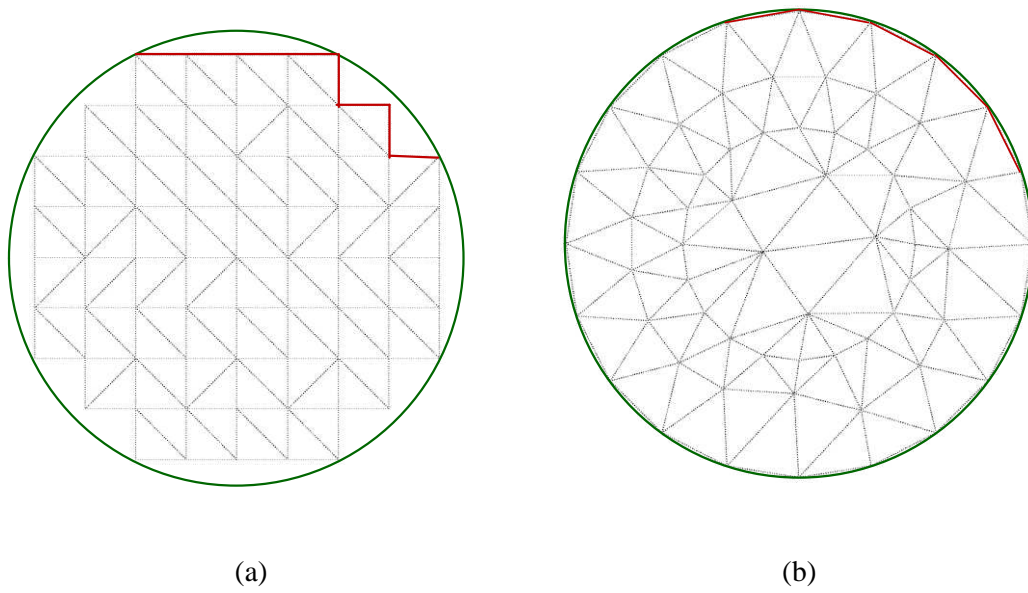


Figure 3.37: Approximation of the PEC resonator circumference (green) using (a) structured, (b) unstructured meshes.

Figure 3.38 shows the runtime as a function of the normalized discretization length for both for unstructured and structured.

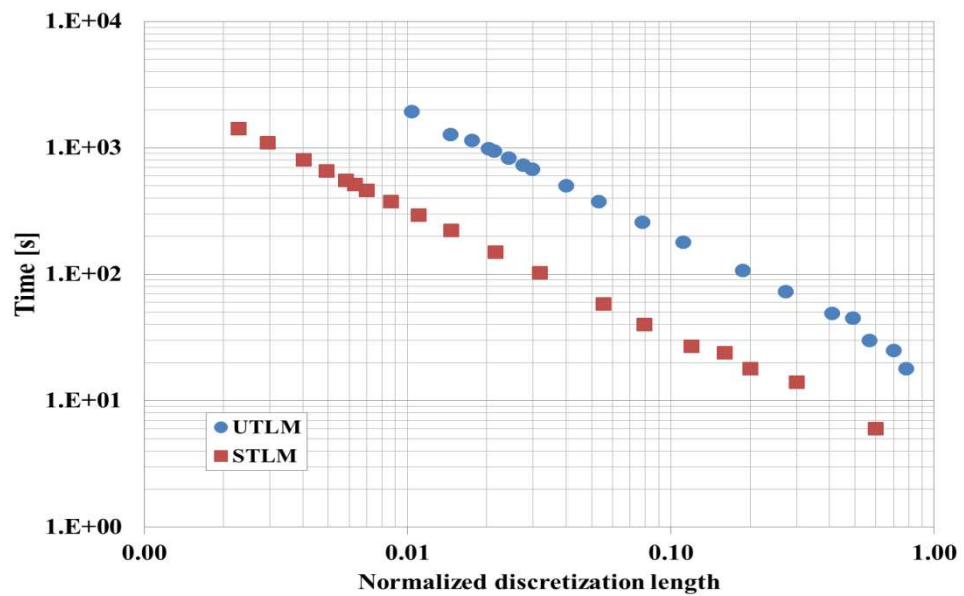


Figure 3.38: Total run time for an air-filled PEC cylindrical resonator as a function of the normalized discretization length $\sqrt{A_{av}}/\lambda_0$ for both unstructured and structured meshes.

Although unstructured mesh showed significantly better relative errors this came on the expense of longer total run time. This is attributed to the presence of short link lines that minimize the timestep and long pre-processing time which both lead to longer execution time. On the other hand, the structured mesh is uniform with fixed discretization length and bigger timestep as compared to the unstructured mesh.

3.7.2 Effect of number and type of meshes on dielectric-filled cylindrical resonator

In the previous subsection testing has been carried out for air-filled cavities. In this part the presence of dielectric materials will be investigated. Consider a PEC cylindrical resonator of radius 1cm concentrically loaded with a dielectric cylinder of relative permittivity $\epsilon_r=2.1$ and 0.5cm radius as shown in Figure 3.39. Upon creating the polygon for such resonator an internal boundary is enforced within the problem space to distinguish different regions. A closed loop of finite segments is created which has a radius of 0.5cm. Two regions (0-0.5cm and 0.5-1cm) will be defined for which all meshes inside the inner circle will be assigned a dielectric permittivity of 2.1 and the rest of meshes will be air-filled.

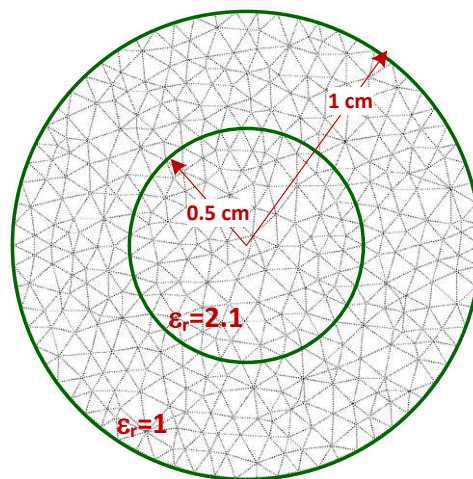


Figure 3.39: PEC cylindrical resonator of radius 1cm concentrically loaded with a dielectric cylinder of $\epsilon_r=2.1$ and 0.5cm radius.

The cylindrical resonator is triangulated by introducing 40, 60, 70, 80, 120 points on the resonator circumference. This produces different meshes of 104, 504, 768, 1026 and 1498 respectively. The time step is 85.20ps, 64.25ps, 54.53ps, 36.61ps and

33.29ps and the execution time was 18s, 25s, 30s, 45s, and 49s for 104, 504, 768, 1026 and 1498 meshes, respectively.

Figure 3.40 shows the percentage relative error in the first five resonance modes for varieties of meshes. The coarse mesh shows the highest error in fundamental mode which was slightly above 3% for the fundamental mode and decreased to 0.07% for the fine mesh. For higher order modes, the error ranged from 7.91% to 0.35% for TM11, 7.34% to 0.44% for TM21, 3.42% to 0.99% for TM02 and finally from 4.8% to 2.28% for TM31.

Table 3.4 shows the percentage relative error for the first five resonance modes as a function of number of triangles in the mesh.

Figure 3.41 shows resonance curves for a coarse and fine unstructured mesh, namely, for 104 triangles and 1498 triangles. Coarse meshes show unwanted resonance frequencies for which it make it difficult to extract the correct resonance modes. It also shows large deviation from the correct place. This is overcome by using fine meshes. As the triangulated area becomes finer the resonance frequencies become shaper and shift to the correct places.

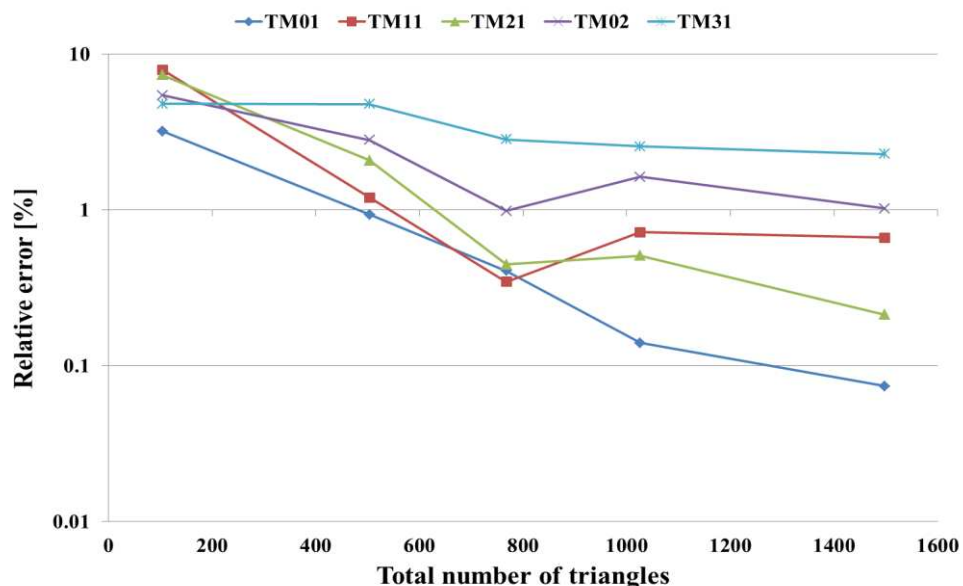


Figure 3.40: Percentage Relative error in different propagation modes of an air-filled PEC cylindrical resonator concentrically loaded with a dielectric cylinder of $\epsilon_r=2.1$ as a function of number of triangles.

Table 3.4: Analytical and numerical resonant frequencies and relative error for a number of unstructured meshes of an air-filled PEC cylindrical resonator concentrically loaded with a dielectric cylinder of $\epsilon_r=2.1$.

Number of meshes		TM01	TM11	TM21	TM02	TM31
104	f_a (GHz)	8.70157	15.02629	21.43714	22.14911	27.91078
	f_{TLM} (GHz)	8.42384	13.83698	19.86316	20.94762	26.57091
	Relative error %	3.19168	7.91488	7.34232	5.42454	4.80054
504	f_a (GHz)	8.70157	15.02629	21.43714	22.14911	27.91078
	f_{TLM} (GHz)	8.62022	14.84560	20.99117	21.52721	26.58185
	Relative error %	0.93486	1.20248	2.08034	2.80778	4.76136
768	f_a (GHz)	8.70157	15.02629	21.43714	22.14911	27.91078
	f_{TLM} (GHz)	8.66622	14.97428	21.34130	21.93084	27.11878
	Relative error %	0.40621	0.34613	0.44707	0.98546	2.83761
1026	f_a (GHz)	8.70157	15.02629	21.43714	22.14911	27.91078
	f_{TLM} (GHz)	8.68939	14.91827	21.25103	21.78810	27.19649
	Relative error %	0.14002	0.718852	0.508166	1.62992	2.5592
1498	f_a (GHz)	8.70157	15.02629	21.43714	22.14911	27.91078
	f_{TLM} (GHz)	8.69514	14.92684	21.39155	21.87827	27.27437
	Relative error %	0.07384	0.66186	0.21265	1.02280	2.28016

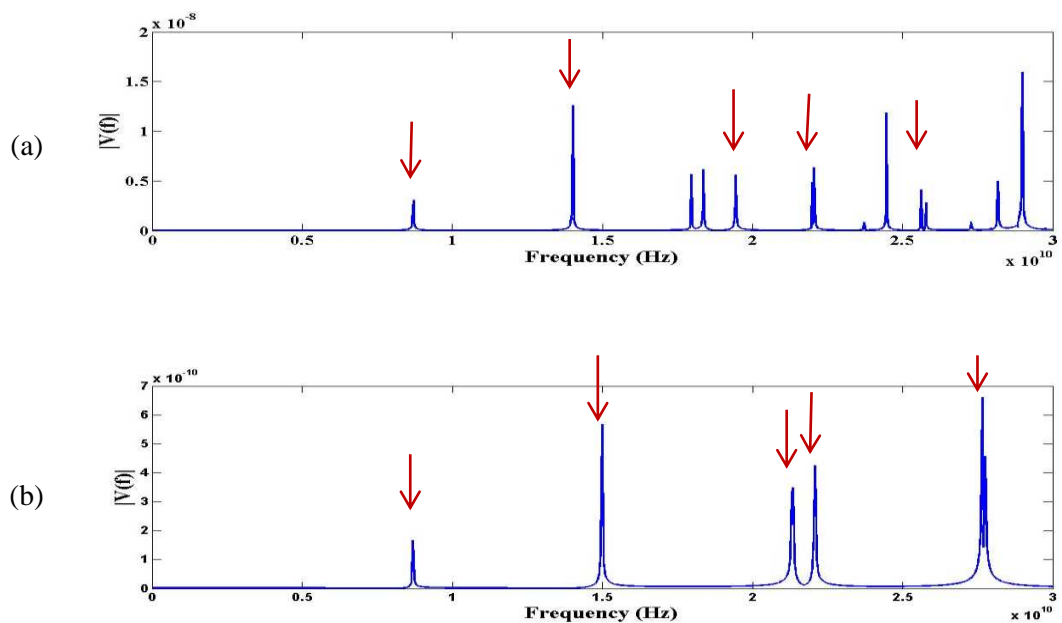


Figure 3.41: Resonant frequencies for an air-filled PEC cylindrical resonator concentrically loaded with a dielectric cylinder of $\epsilon_r=2.1$ triangulated into (a) 104 and (b) 1498 unstructured meshes, with red arrows pointing TM01, TM11, TM21, TM02 and TM31 mode positions..

Next step is to triangulate a PEC cylindrical resonator of radius 1cm concentrically loaded with a dielectric cylinder of $\epsilon_r=2.1$ and 0.5cm radius into a range of structured meshes.

The cylindrical resonator is triangulated into equivalent structured meshes of 104, 554, 784, 1060 and 1484. The time step for each mesh is 170.78ps, 113.86ps, 91.08ps, 68.32ps and 56.93ps and execution time of 6s, 14s, 18s, 24s, and 27s, respectively.

Figure 3.42 shows the percentage relative error in the first five resonance modes for varieties of meshes. The coarse mesh shows the highest error in fundamental mode which was slightly above 13% for the fundamental mode and decreased to 2.66% for the fine mesh. For higher order modes, the error ranged from 19.81% to 2.74% for TM11, 2.68% to 0.72% for TM21, 7.12% to 2.85% for TM02 and finally from 5.97% to 3.07% for TM31

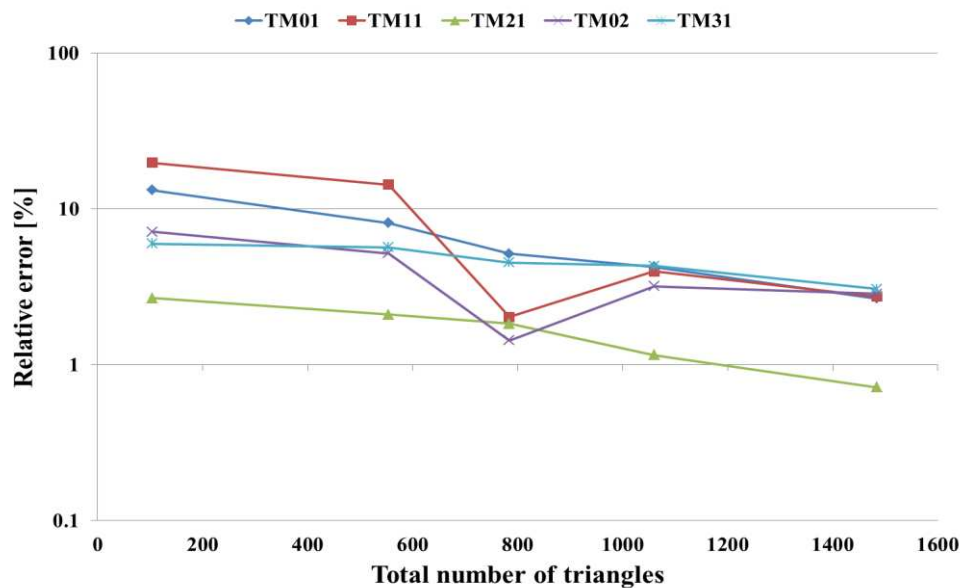


Figure 3.42: Percentage Relative error in different propagation modes of PEC cylindrical resonator concentrically loaded with a dielectric cylinder of $\epsilon_r=2.1$ as a function of number of structured meshes.

Table 3.5 shows the percentage relative error for the first five resonance modes of 104, 554, 784, 1060 and 1484 meshes. Figure 3.43 shows resonance curves for a coarse and fine unstructured mesh, namely, for 104 triangles and 1484 triangles. Notice that the coarse triangulation of 104 meshes shows unwanted resonance frequencies and large

deviation from the analytical resonant frequencies. This is overcome by using fine meshes.

Table 3.5: Analytical and numerical resonant frequencies and relative error for a number of structured meshes of an air-filled PEC cylindrical resonator concentrically loaded with a dielectric cylinder of $\epsilon_r=2.1$.

Number of meshes		TM01	TM11	TM21	TM02	TM31
104	f_a (GHz)	8.70157	15.02629	21.43714	22.14911	27.91078
	f_{TLM} (GHz)	7.55118	12.04888	22.01081	23.72640	26.24346
	Relative error %	13.22049	19.81467	2.67606	7.12123	5.97375
554	f_a (GHz)	8.70157	15.02629	21.43714	22.14911	27.91078
	f_{TLM} (GHz)	7.99343	12.87532	20.98751	21.00078	26.32710
	Relative error %	8.13811	14.31471	2.09743	5.18454	5.67408
784	f_a (GHz)	8.70157	15.02629	21.43714	22.14911	27.91078
	f_{TLM} (GHz)	8.25325	14.72146	21.04353	22.46653	26.64483
	Relative error %	5.15217	2.02864	1.83611	1.43310	4.53570
1060	f_a (GHz)	8.70157	15.02629	21.43714	22.14911	27.91078
	f_{TLM} (GHz)	8.33117	15.62465	21.18981	21.44389	26.70936
	Relative error %	4.25670	3.98211	1.15375	3.18397	4.30450
1484	f_a (GHz)	8.70157	15.02629	21.43714	22.14911	27.91078
	f_{TLM} (GHz)	8.47025	14.61434	21.28372	21.51697	27.05423
	Relative error %	2.65837	2.74153	0.71567	2.85402	3.06889

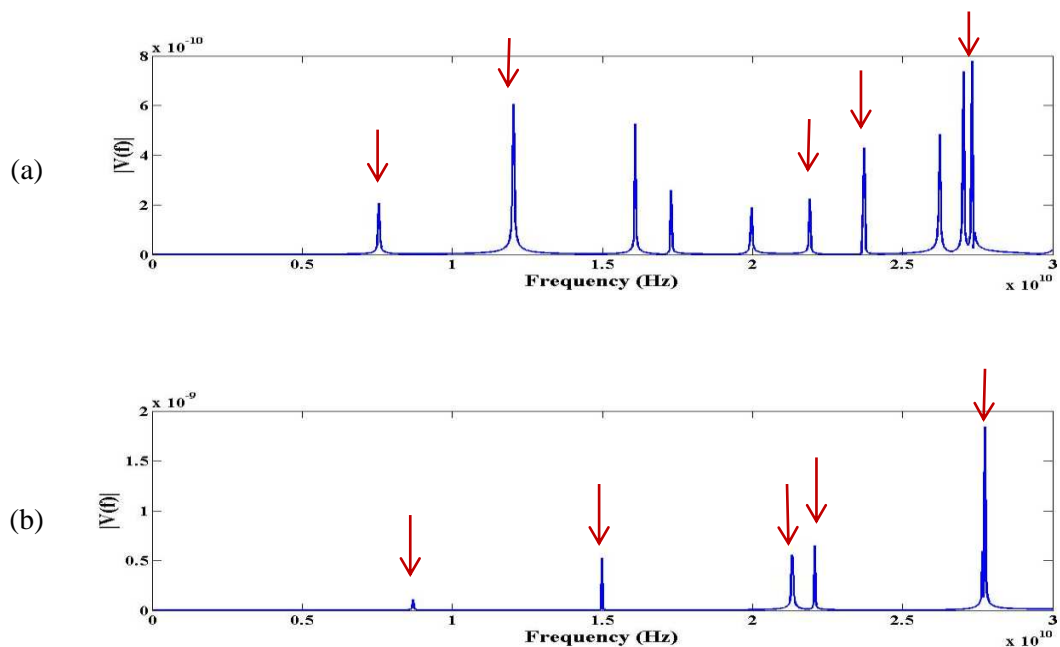


Figure 3.43: Resonant frequencies for an air-filled PEC cylindrical resonator concentrically loaded with a dielectric cylinder of $\epsilon_r=2.1$ triangulated into (a) 104 and (b) 1484 structured meshes, with red arrows pointing TM01, TM11, TM21, TM02 and TM31 mode positions.

Figure 3.44 shows the relative error in modes for both structured and unstructured meshes as a function of the normalized discretization length.

As in the case of the air-filled cylindrical resonator, the PEC resonator filled with mixed materials introduced significantly lower relative error using unstructured meshes as oppose to structured meshes. This is due to better boundary approximation using unstructured meshes.

On the other hand, unstructured meshes are executed in longer run time compared to the structured meshes due to the presence of very short link lines, which affect the time step and consequently increases the total run time. Figure 3.45 shows the runtime for different unstructured meshes and the equivalent structured meshes.

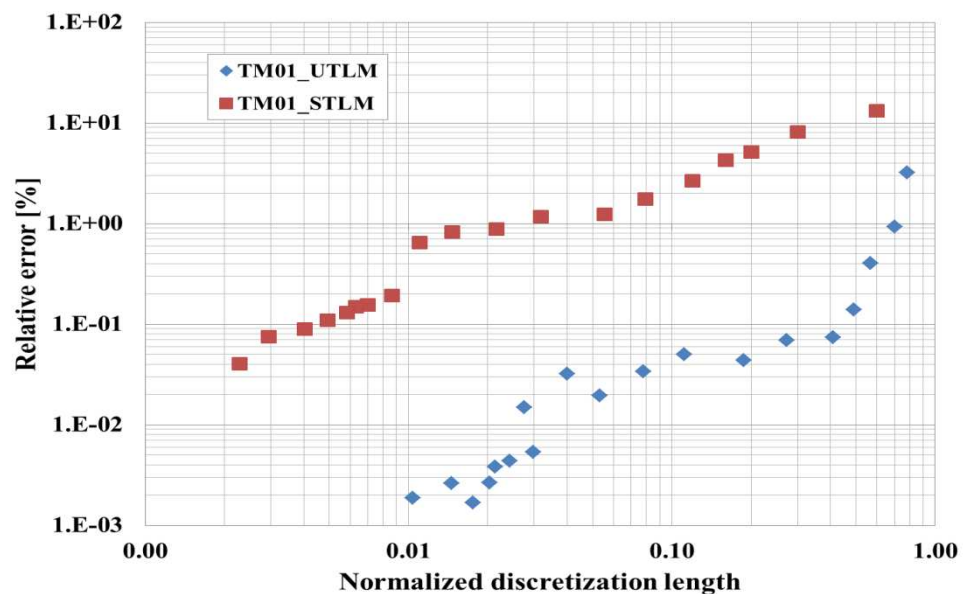


Figure 3.44: Relative error in TM01 for an air-filled PEC cylindrical resonator concentrically loaded with a dielectric cylinder of $\epsilon_r=2.1$ as a function of the normalized discretization

length $\sqrt{A_{av}}/\lambda_0$ for both unstructured and structured.

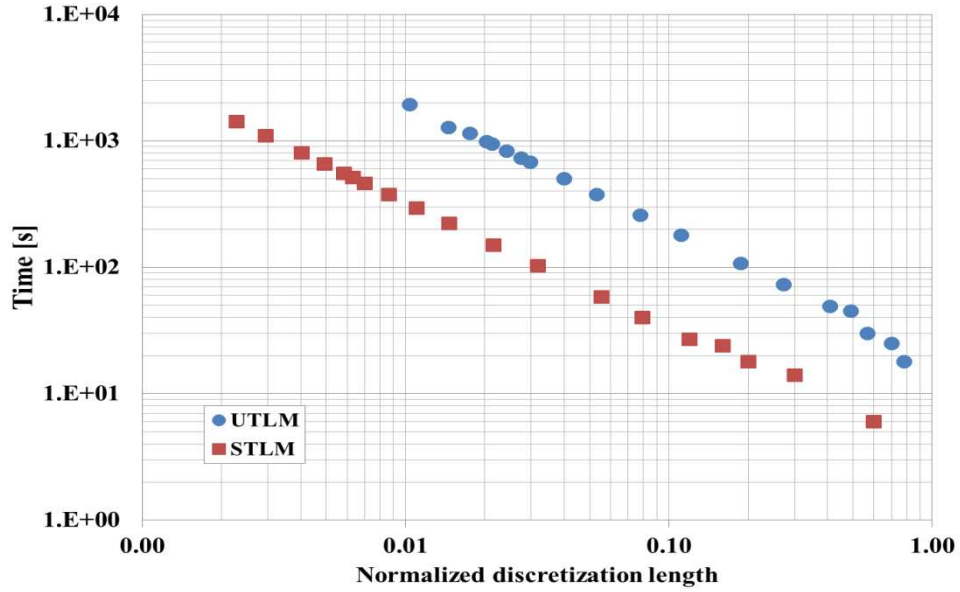


Figure 3.45: Total run time for an air-filled PEC cylindrical resonator concentrically loaded with a dielectric cylinder of $\epsilon_r=2.1$ as a function of the normalized discretization length $\sqrt{A_{av}}/\lambda_0$ for both unstructured and structured meshes.

3.7.3 Effect of number and type of meshes on an air-filled rectangular resonator

In this section, the last case to be studied is for an air-filled rectangular resonator. The effect of number and shape of the meshes will be investigated. The resonator dimensions are 10mm width by 7mm height and the rectangle boundaries are short-circuited. Figure 3.46 shows example of rectangular resonator meshed by introducing 68 points around the boundaries so that it is divided into segments of 1mm length each. The region is then triangulated into 440 triangles, with 1320 link lines. The shortest link length is 36.61mm and time step of 86.27ps.

The analytical resonant mode TM_{mn} of the rectangular resonator are calculated from the formula [45]

$$f_c^{mn} = \frac{1}{2\sqrt{\epsilon\mu}} \sqrt{\left(\frac{m}{a}\right)^2 + \left(\frac{n}{b}\right)^2}. \quad (3.70)$$

where a and b are the resonator width and height, ε is the material permittivity and μ is the material permeability. Note also that $m \neq 0$ and $n \neq 0$ for TM modes.

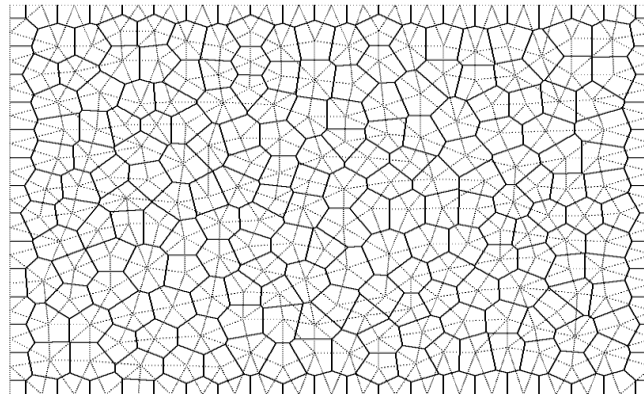


Figure 3.46: Delaunay (light) and Voronoi (dark) unstructured diagram of an air-filled rectangular waveguide of dimensions 10mm by 7mm

The rectangular resonator is triangulated into 158, 220, 440, 858 and 1806 meshes. This was achieved by introducing 40, 48, 68, 96 and 136 segments around the boundaries, respectively. The time step is 170.55ps, 88.79ps, 86.27ps, 20.06ps and 14.20ps and the execution time is 29s, 56s, 61s, 260s, and 371s for 158, 220, 440, 858 and 1806 meshes respectively.

Figure 3.47 shows the percentage relative error in the first five resonance modes for varieties of meshes. The relative error in the fundamental mode is 1.67% for the coarse mesh which reduces to 0.06% for the finest mesh. For the higher modes the relative error ranged from 2.33% to 0.75% for TM₂₁, 6.85% to 1.42% for TM₁₂, 6.03% to 1.49% for TM₃₁, and finally 5.92% to 0.63% for TM₂₂.

Table 3.6 shows the percentage relative error for the first five resonance modes of 158, 220, 440, 858 and 1806 meshes.

Figure 3.48 shows resonance curves for a coarse and fine unstructured mesh, namely, for 158 triangles and 1806 triangles. It is apparent that the coarse mesh shows large deviation of the resonance mode positions, which is improved with the finer mesh.

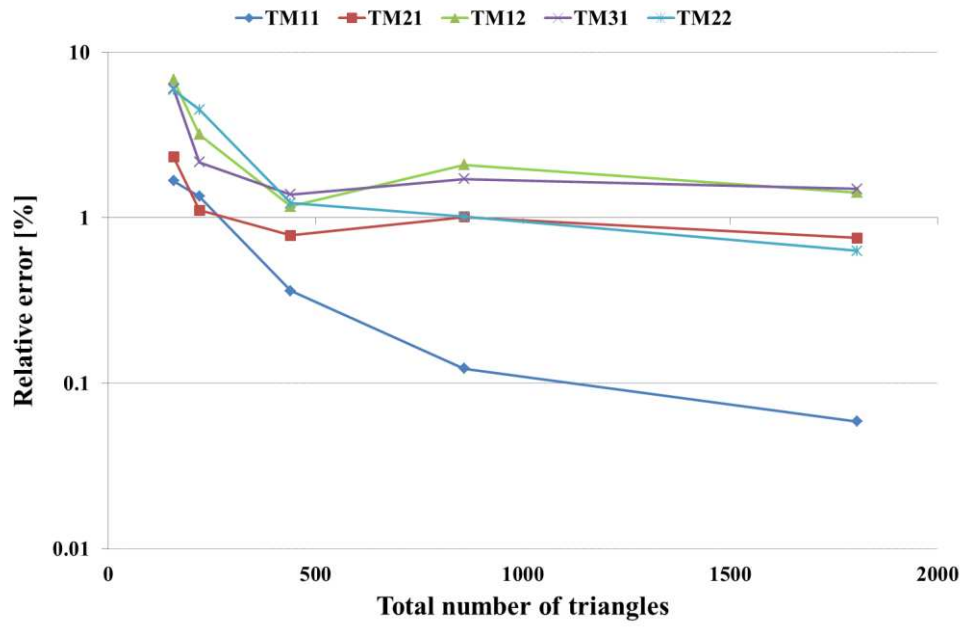


Figure 3.47: Percentage Relative error in different propagation modes of an air-filled rectangular resonator as a function of number of triangles in the UTLM mesh.

Table 3.6: Analytical and numerical resonant frequencies and relative error for a number of unstructured meshes of an air-filled rectangular resonator.

Number of meshes		TM11	TM21	TM12	TM31	TM22
158	f_a (GHz)	26.13356	36.83421	45.36581	49.79711	52.26712
	f_{TLM} (GHz)	25.69647	35.97505	42.25641	46.79294	49.17225
	Relative error %	1.67252	2.33251	6.85406	6.03282	5.92126
220	f_a (GHz)	26.13356	36.83421	45.36581	49.79711	52.26712
	f_{TLM} (GHz)	25.78214	36.42477	43.91958	48.71626	49.91543
	Relative error %	1.34469	1.11158	3.18793	2.17051	4.49937
440	f_a (GHz)	26.13356	36.83421	45.36581	49.79711	52.26712
	f_{TLM} (GHz)	26.03917	36.54614	45.89744	49.10888	52.90722
	Relative error %	0.36118	0.78207	1.17187	1.38207	1.22467
858	f_a (GHz)	26.13356	36.83421	45.36581	49.79711	52.26712
	f_{TLM} (GHz)	26.16559	37.20686	44.41647	48.94235	51.73662
	Relative error %	0.12254	1.0117	2.09263	1.71649	1.01497
1806	f_a (GHz)	26.13356	36.83421	45.36581	49.79711	52.26712
	f_{TLM} (GHz)	26.14893	37.11251	44.72137	49.05431	51.93764
	Relative error %	0.05882	0.75555	1.42054	1.49165	0.63038

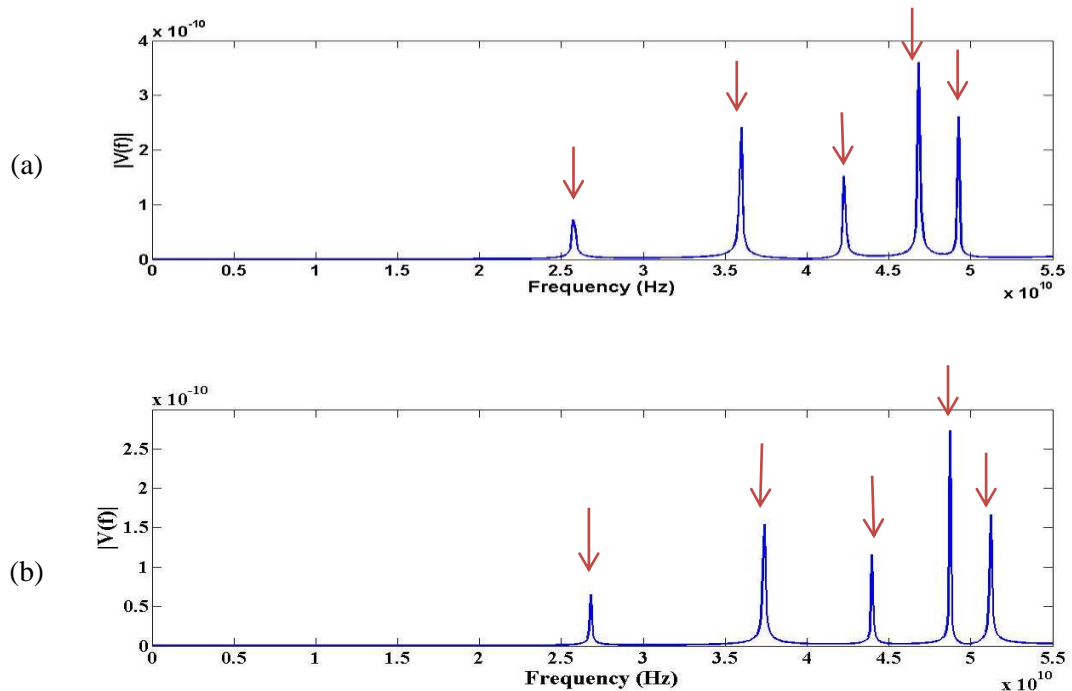


Figure 3.48: Resonant frequencies for an air-filled cylindrical PEC resonator triangulated into (a) 158 and (b) 1806 unstructured meshes, with red arrows pointing TM11, TM21, TM12, TM31 and TM22 mode positions.

In the circular resonator, the fundamental mode showed relative error of 7% for the coarse mesh, while rectangular resonator showed much better relative error, namely 1.7%. This is due to the fact that the meshes are always aligned with the rectangle borders, while there is always a resonator approximation error with respect to the circle circumference, which can be enhanced by increasing the number of segments along the circumference. On the other hand, meshing the rectangular cavities although seems simple, but special care should be considered in order not to get skinny triangles on borders, which might occur if the ratio between the segments on the length and width is much bigger or smaller than 1. Also, upon choosing the segment length, be sure that the length and width be an integer multiple of the segment length, otherwise, small or non-Delaunay triangles might be produced on corners.

Finally, the air-filled rectangular resonator is meshed using a range of structured meshes. This can be achieved by adopting the same criteria used in unstructured meshes, which is by introducing 40, 48, 68, 96 and 136 segments around the boundaries, then enforcing equidistant points within the resonator to be connected into squares (or rectangles). Then the mesher is responsible for dividing each square (or rectangle) into two equal right-handed triangles as shown in Figure 3.49. The number of the produced meshes are 200, 280, 560, 1120, and 2240 meshes, respectively. The time step is 824.95ps, 589.26ps, 589.26ps, 294.63ps and 294.63ps, and the execution time was 6s, 10s, 10s, 19s and 19s, for the 200, 280, 560, 1120, and 2240 meshes, respectively.

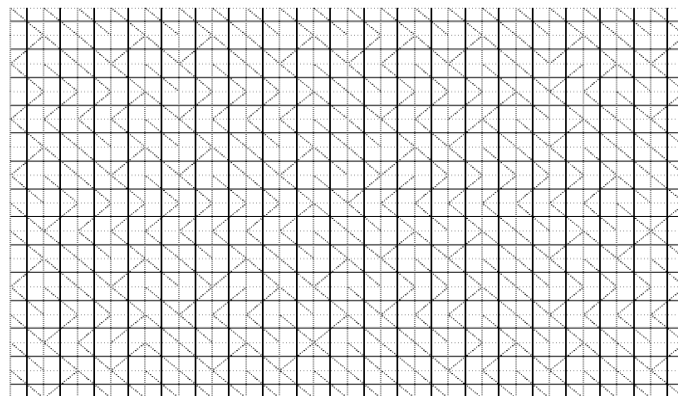


Figure 3.49: Delaunay (light) and Voronoi (dark) structured diagram of an air-filled rectangular waveguide of dimensions 10mm by 7mm

Figure 3.50 shows the percentage relative error in the first five resonance modes for varieties of meshes. The fundamental mode shows 1.5% relative error for the coarse mesh that decreases to 0.04% for the finest mesh. Higher modes introduce relative error between 3.96% and 0.33% for TM21, 3.67% and 0.81% for TM12, 1.71% and 1.27% for TM31 and 2.40% and 1.14% for TM22.

Table 3.7 shows the percentage relative error in the first five resonance modes for 200, 280, 560, 1120, and 2240 structured meshes.

Figure 3.51 shows the resonance curves for 200 and 2240 structured meshes, respectively.

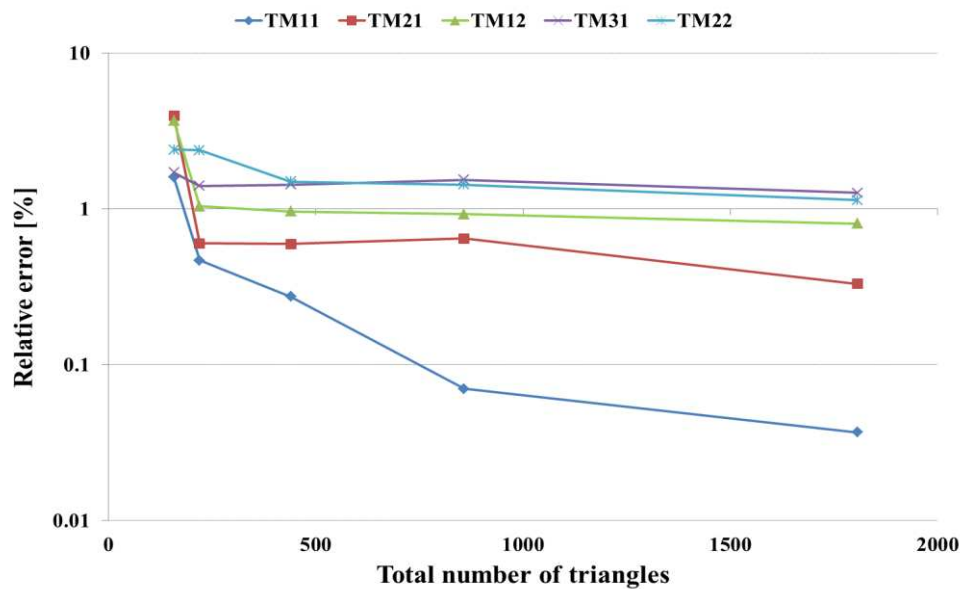


Figure 3.50: Percentage Relative error in different propagation modes of an air-filled rectangular resonator as a function of number of triangles in the structured mesh

Table 3.7: Analytical and numerical resonant frequencies and relative error for a number of structured meshes of an air-filled rectangular resonator.

Number of meshes		TM11	TM21	TM12	TM31	TM22
200	f_a (GHz)	26.13356	36.83421	45.36581	49.79711	52.26712
	f_{TLM} (GHz)	25.71651	35.37652	43.70036	50.64977	53.52167
	Relative error %	1.59584	3.95744	3.67116	1.71227	2.40027
280	f_a (GHz)	26.13356	36.83421	45.36581	49.79711	52.26712
	f_{TLM} (GHz)	26.0114	36.61275	44.89393	49.09802	51.02281
	Relative error %	0.46743	0.60124	1.04017	1.40389	2.38068
560	f_a (GHz)	26.13356	36.83421	45.36581	49.79711	52.26712
	f_{TLM} (GHz)	26.06197	36.61467	44.92892	49.08604	51.48438
	Relative error %	0.27394	0.59602	0.96304	1.42793	1.49758
1120	f_a (GHz)	26.13356	36.83421	45.36581	49.79711	52.26712
	f_{TLM} (GHz)	26.11527	36.5969	44.94668	49.03274	51.51991
	Relative error %	0.07001	0.64426	0.92389	1.53496	1.4296
2240	f_a (GHz)	26.13356	36.83421	45.36581	49.79711	52.26712
	f_{TLM} (GHz)	26.12391	36.71231	45.00012	49.16665	51.67123
	Relative error %	0.03692	0.33093	0.80609	1.26606	1.14008

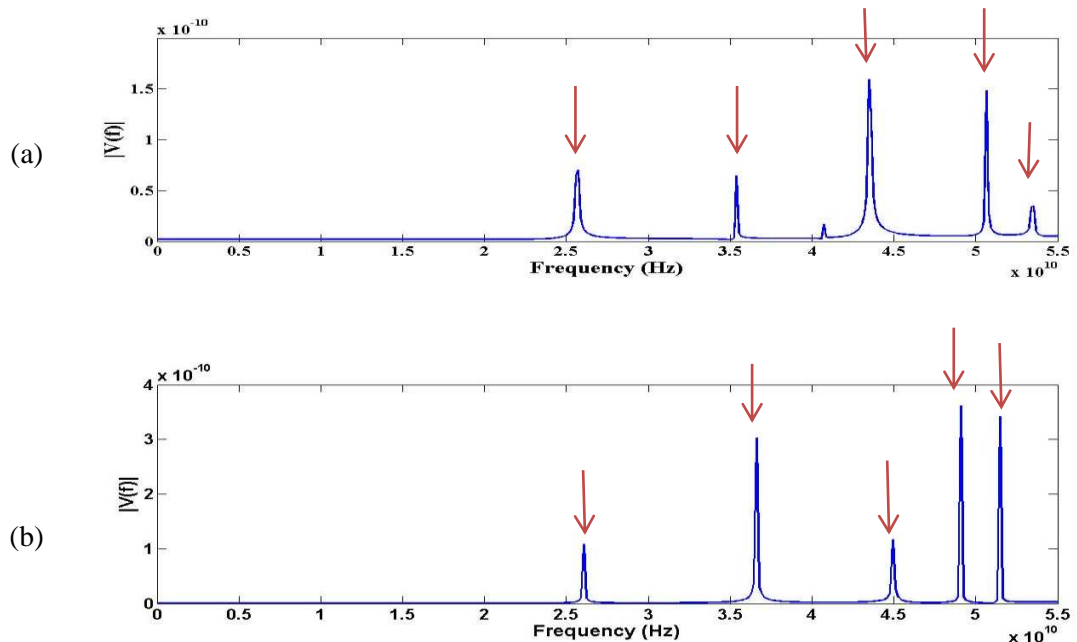


Figure 3.51: Resonant frequencies for an air-filled rectangular resonator triangulated into (a) 200 and (b) 2240 structured meshes, , with red arrows pointing TM11, TM21, TM12, TM31 and TM22 mode positions.

Figure 3.52 shows the percentage relative error in mode TM11 for both structured and unstructured meshes. Structured meshes shows slightly better relative error compared to the equivalent unstructured meshes. But generally there is no significant change in the relative error using either structured or unstructured meshes. On the other hand, the execution time for the structured meshes is much better as compared to the unstructured meshes as shown in Figure 3.53. This is due to the long processing time and the presence of much shorter link lines in the unstructured meshes which decrease the time step and consequently increases the total execution time.

Figure 3.53 shows that the execution time for the structured meshes is much better as compared to the unstructured meshes. For example, the case of $\sqrt{A_{av}}/\lambda_o = 0.65$, the unstructured meshes is executed in 12 times the execution time consumed in simulating equivalent structured meshes which on the other hand has half the relative error.

The rectangular cavities showed bigger time steps when compared with the earlier circular cavities, in both unstructured and structured meshes. Higher time steps in rectangular cavities (compared to those of the circular resonator) are supposed to lead to shorter run time (till error saturates and resonance peaks become sharp), but all meshes showed longer run time than those in circular cavities. This is assumed to be due to rectangular resonator nature that has sharp edges and corners, which lead longer time for the wave to stabilize within the resonator space.

It is better to use unstructured mesh for curved boundaries, and to use structured mesh with straight ones. So for a problem with mix of straight or curved features a hybrid usage of structured and unstructured meshes can be adopted, in that curved surfaces will be meshed with triangular cells and straight ones to be meshed with rectangular cells. This will enhance the relative error and reduce the run time. Another solution is to get benefit of low relative error achieved by the usage of unstructured meshes, but to maximize the link lengths by replacing all short link lines that fall under certain value with the model that will be presented in Chapter 4, which will increase the time step and consequently decrease the total run time.

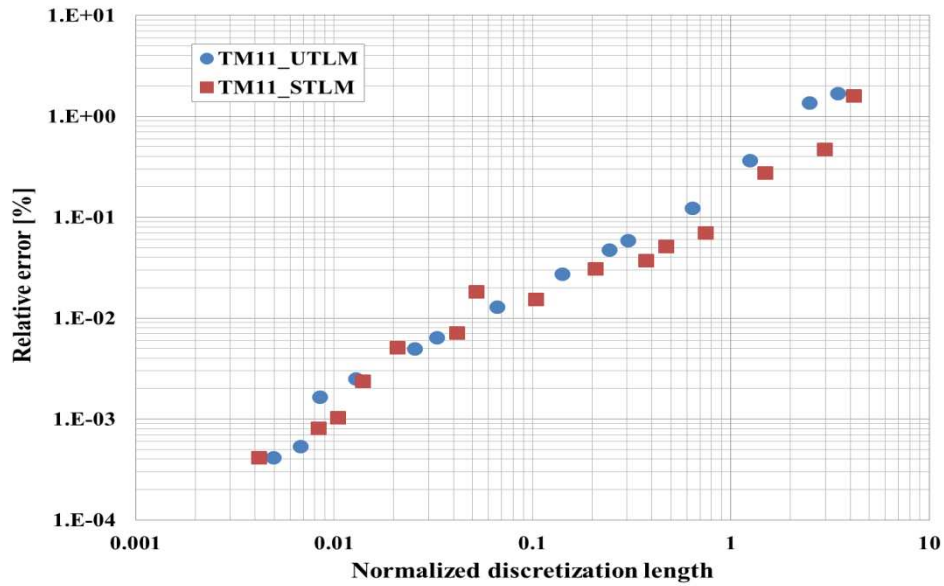


Figure 3.52: Relative error in TM11 for an air-filled PEC rectangular resonator as a function of the normalized discretization length $\sqrt{A_{av}}/\lambda_o$ for both unstructured and structured

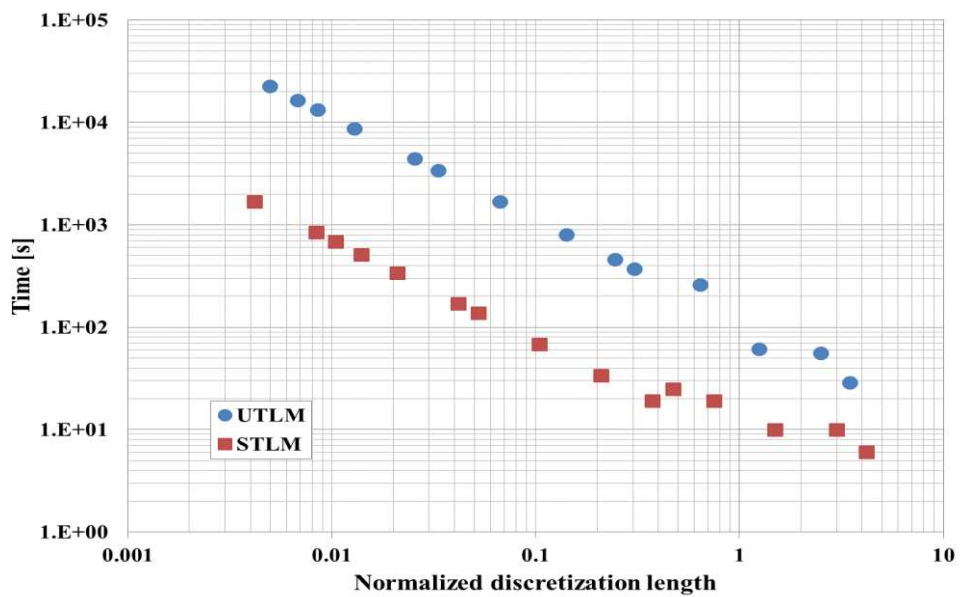


Figure 3.53: Total run time for an air-filled PEC rectangular resonator as a function of the normalized discretization length $\sqrt{A_{av}}/\lambda_o$ for both unstructured and structured meshes

3.8 Summary

In this chapter an equivalent transmission line network for 2D UTLM is derived, the implementation of the scatter-connect algorithm is presented and validation of the

algorithm has been applied on several canonical examples of cylindrical and rectangular waveguides.

Unstructured Transmission line modelling UTLM has proved that it is a versatile tool for modelling electromagnetic problems. The TLM node should coincide with the triangle circumcentres for proper implementation of Maxwell's equation. Delaunay triangles are used to produce a Voronoi diagram formed of the link lines connecting triangle circumcentres. Each triangle has three link lines which are modelled using a stub inductor model each terminated with a stub capacitor model. Time step is calculated upon the shortest link length in the simulated problem. Since the region is divided into irregular shapes proper connections and cell relative position should be taken care of. The main part of the algorithm comprises of two processes at each time step known as the 'scatter' and 'connect'. Temporal evolution of the field is done by alternative implementation of scatter and connect operations until the steady state is reached.

A computer code has been produced to simulate a region divided into Delaunay triangles. The UTLM simulator shows good results for simulating problems with different shapes and materials. It also worked well with a variety of mesh numbers. In cylindrical resonators, the percentage relative error achieved with moderate number of meshes was less than 1% for the first three resonance modes. Decreasing the discretization length leads to further reduction in relative error for both unstructured and structured meshes. UTLM showed better relative error as compared to those in STLM especially in curved boundary problems due to better boundary approximation. For rectangular resonator, both UTLM and STLM show good relative error in resonance frequencies. The total execution time for UTLM problems is longer than STLM time.

Some problems experienced a very short link lines between circumcentres that in some cases equal zero. This has severe consequences on the time step value that becomes too small and consequently it took the program huge amount of time to perform a simulation. This problem is addressed in Chapter 4 and a new model is used to replace those short link lines.

Chapter 4.

Triangle Pair Model for 2D Unstructured TLM

4.1 Introduction

In this chapter a method for relaxing the minimum link line length in the 2D unstructured TLM method is presented. As described in Chapter 3 the TLM algorithm requires that the maximum time step to be determined by the minimum link line length in the problem. Unfortunately, even Delaunay triangularization can produce very small, even approaching zero link lengths which can have severe consequences to the timestep and overall computational runtime. One such situation is shown in Figure 4.1(a) where circumcentre A lies outside the triangle boundaries and where the link length connecting centres A and B is short. Another case occurs with right-angled triangles shown in Figure 4.1(b) where the circumcentres lie on the side shared between the two triangles so point A and B coincide resulting a zero link length. The same problem is seen in the enlarged inset in Figure 4.2 of where very close to zero or very short link lines are identified.

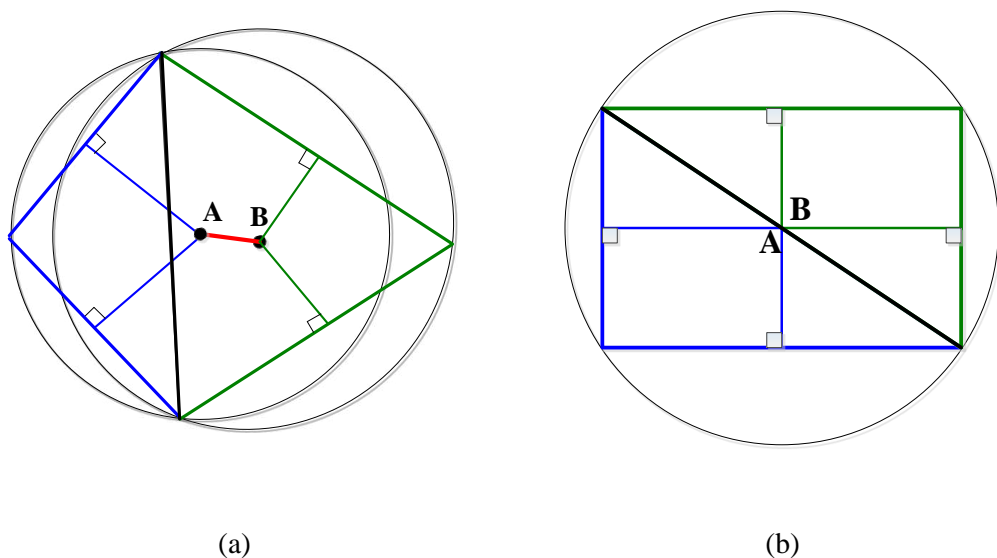


Figure 4.1: Two adjacent Delaunay triangles sharing (a) short link line, (b) zero link line

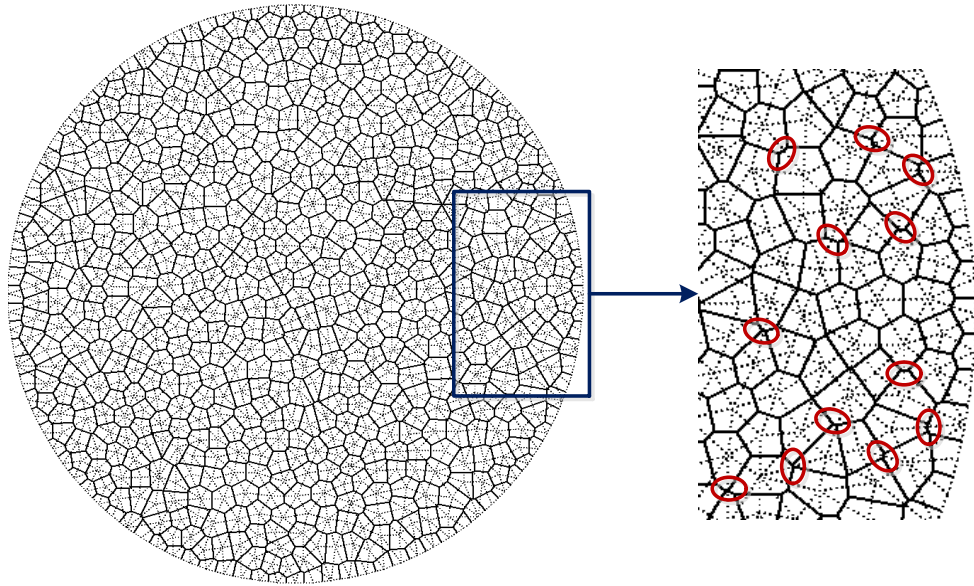


Figure 4.2: Delaunay & Voronoi mesh of PEC circular resonator with enlarged inset identifying few short link lines.

As the maximum timestep in the TLM method is determined by the minimum link length, the presence of even one short link line can have huge impact on the efficiency of TLM simulations. It is therefore important to perturb the mesh so that the very short link lengths are relaxed. Three different mesh optimisation techniques namely, centroidal Voronoi Tessellation (CVT) method, the optimal Delaunay triangulation (ODT) method and spring relaxation method have been reported and compared in [141]. Both the CVT and ODT methods are mesh smoothing techniques that seeks minimizing the interpolation error by producing similar meshes of reasonable link line lengths. On the other hand, the spring relaxation works on maximizing the minimum link length.

The CVT method involves an even spread of the triangles over the whole domain, which results similar triangles of same area and internal angles. This can be achieved by moving each triangle vertex to the centroid of its Voronoi region then calculating the new Voronoi mesh from the new vertex positions. The ODT method requires finding a node region in which a cumulative area is determined where a particular node is shared among several triangles. Calculations are then carried out to move the node region to new coordinates that will produce a smoother mesh. And in the spring relaxation, Voronoi nodes are attributed as “masses” and the link lines (connecting

masses) are treated as springs in an equivalent mechanical system. This method targets maximizing the minimum link length by bringing the systems of masses into dynamic equilibrium.

Whilst spring relaxation method performed better when boundaries are curved and stands out in terms of speed at which the relaxation occurs, CVT and ODT methods had better performance when sharp corners are introduced in the mesh [141].

The previously mentioned relaxation methods are very intensive on large meshes, and often fail with geometrically complicated problems [141]. So the bottom line is to try to get Delaunay meshes to be uniform with no presence of short link lines which is impossible to achieve, or to desensitising the algorithm to meshing artifacts by finding a solution that allows the TLM model to deal with these short link lines in a numerically robust and accurate way, a solution that does not try to fix these short links. Investigation should be carried on to find a limiting case of maximising the short link lines without compromising the accuracy of the TLM model.

In this chapter a simpler perturbation approach in which all triangle pairs that share link lines that fall below a certain threshold length are merged into an equivalent four port node. Each short link line is replaced by a capacitive and an inductive stub and the scattering at the node is done implicitly rather than explicitly thus imposing no extra burden on the runtime. Thus the problem of the short link line is solved through the TLM model rather than improving the mesh itself before applying the model.

Although the method is only briefly mentioned in [23], in this chapter we further describe its implementation and the effect it has on the efficiency and accuracy of TLM simulations. In addition to isolating short link lines that falls between adjacent triangles, a new model is presented in this chapter for short link lines that fall on problem boundaries. A mathematical approach is derived for different types of boundaries to ensure that if a short link line is located on any boundary should be isolated where a special scatter-connect process is applied.

This chapter presents the methodology and implementation for the triangle pair model. Assessment of the impact of the threshold on the accuracy and runtime of the TLM

simulations is investigated on two canonical examples, namely, air filled and partially filled cylindrical cavity for a variety of meshes.

4.2 Triangle pair model

Since the time step is calculated based on the shortest link length in the problem, the very small link length will lead to very small time step which will consequently require prohibitively long runtime.

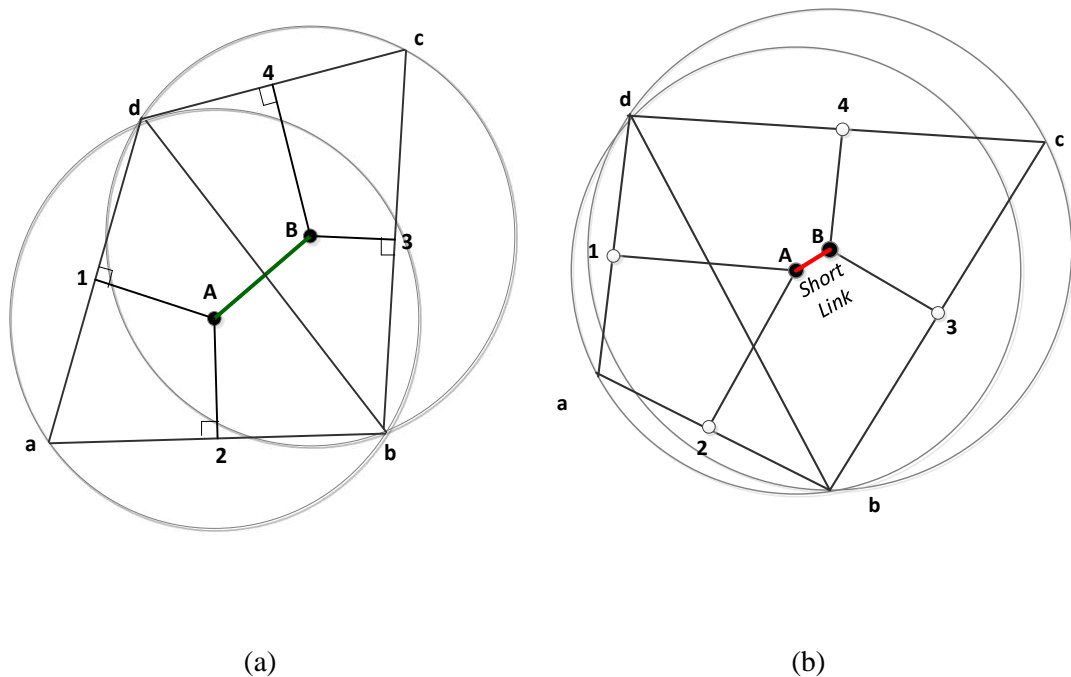


Figure 4.3: (a) Delaunay triangles with normal link lengths, (b) Delaunay triangles with a short link connecting circumcentres A and B of two adjacent nodes.

To overcome this problem, a threshold distance Δ_{thres} can be set, at which all link lengths that fall below this value are isolated in separate model. Figure 4.3(a) shows an example of two adjacent triangles sharing a normal link line and will be solved using the conventional scatter and connect process, while in Figure 4.3(b) a short link line occurs between the two triangles which will be merged into quadrilateral shape for which scatter process is done separately in a pair model.

Naturally, the choice of threshold can be such that two or all three link lines per triangle fall below threshold thus requiring a triangle to be merged with all three neighbouring

triangles. As this can result an increase in the complexity of algorithm and processing time, the threshold length is restricted so that only single pairs of triangles are formed.

Figure 4.4 shows an equivalent electrical network for the two triangles shown in Figure 4.3(b), where the red part represents the short link line shared between the two triangles.

Equivalent capacitances and inductances are given as

$$L_i = \mu \frac{\Delta_i}{l_i}, \quad (4.1)$$

$$C_i = \frac{\varepsilon \Delta_i l_i}{2}. \quad (4.2)$$

where Δ_i is the link length and l_i is the length of triangle side which link line intersects [23].

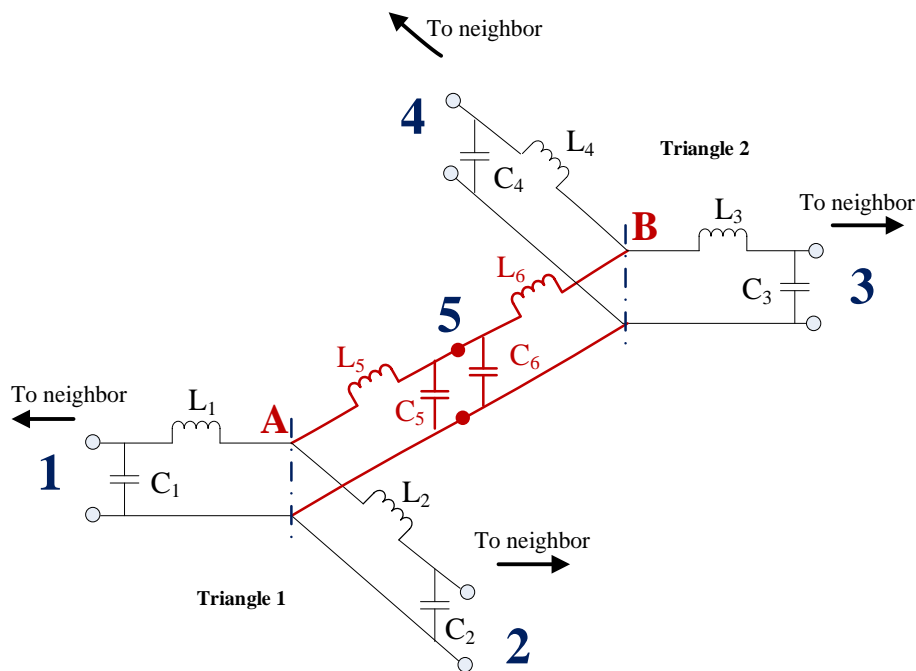


Figure 4.4: Equivalent transmission line network of two triangles in UTLM.

In the TLM method the 5-port circuit on Figure 4.4 is replaced by a transmission line network shown in Figure 4.5 whereby inductances are replaced by a transmission line of characteristic impedance,

$$Z_{Li} = \frac{2\mu_o\Delta_i}{\Delta_t l_i}. \quad (4.3)$$

and capacitances are replaced by open-circuited stubs of admittance

$$Y_{Li} = \frac{\epsilon_o l_i \Delta_i}{\Delta_t} - \frac{l_i \Delta_t}{2\mu_o \Delta_i}. \quad (4.4)$$

where $\Delta_t/2$ is the time the signal travels along the transmission lines.

In the case of short link lines that fall below certain threshold Δ_{thres} , the electrical network that represents the short link line is replaced by an inductive (short-circuited) and capacitive (open-circuited) stub as shown in Figure 4.5. The presence of the stubs eliminates physical distance between nodes A and B resulting in two triangles merging in one four port node as shown in Figure 4.5 for which scattering is done separately.

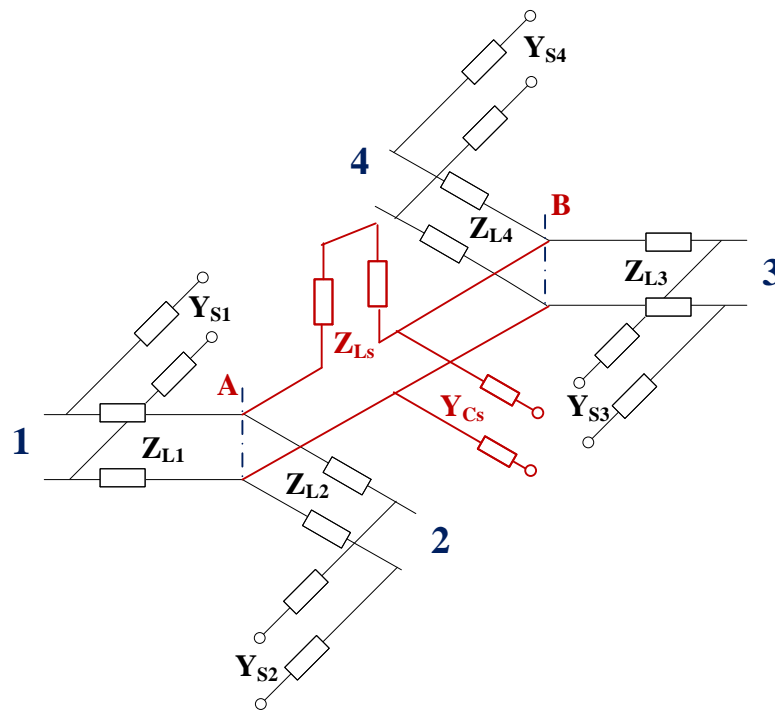


Figure 4.5: 4-port transmission line network of the triangle pair with the short link line replaced by an equivalent stub model.

The characteristic impedances of stubs are defined for the threshold length Δ_{thres} and are given as [23]

$$Z_{Ls} = \frac{2\mu_o\Delta_{thres}}{\Delta_t l_i}, \quad (4.5)$$

$$Y_{Cs} = \frac{\epsilon_o l_i \Delta_{thres}}{\Delta_t}. \quad (4.6)$$

The Thevenin equivalent circuit of Figure 4.5 is shown in Figure 4.6 where V_{Ls}^i and Z_{Ls} are the incident voltage and the characteristic impedance of the short-circuited stub, V_{Cs}^i and Z_{Cs} are the incident voltage and characteristic impedance of the open-circuited stub and V_{Lj} and Z_{Lj} ($j=1,2,3,4$) represent incident voltages and characteristic impedances of transmission lines that connect to four neighbours.

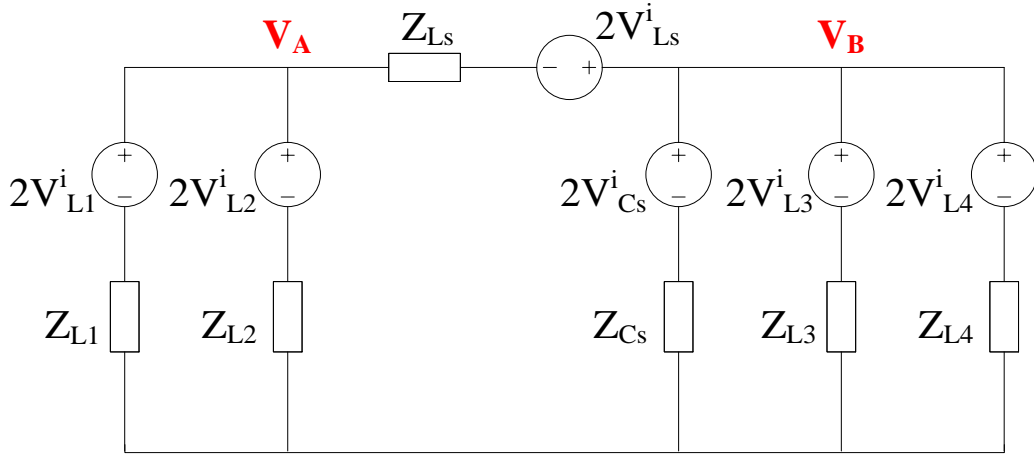


Figure 4.6: Thevenin equivalent circuit for the triangle pair.

In the scattering part of the algorithm reflected voltages are obtained from the known incident voltages. For the network in Figure 4.6 scattering is done by solving for node voltages V_A and V_B .

Applying node-voltage method at node A gives

$$\frac{V_A - 2V_{L1}^i}{Z_{L1}} + \frac{V_A - 2V_{L2}^i}{Z_{L2}} + \frac{V_A - V_B - (-2V_{Ls}^i)}{Z_{Ls}} = 0. \quad (4.7)$$

Rearranging Equation (4.7) gives the voltage V_A ,

$$V_A = \frac{1}{M} [2V_{L1}^i Y_{L1} + 2V_{L2}^i Y_{L2} + V_B Y_{Ls} - 2V_{Ls}^i Y_{Ls}], \quad (4.8)$$

where $Y_{L1,L2}$ and Y_{Ls} denote characteristic admittances of link lines and short link $Y_{L1} = \frac{1}{Z_{L1}}$, $Y_{L2} = \frac{1}{Z_{L2}}$, $Y_{Ls} = \frac{1}{Z_{Ls}}$ and $M = Y_{L1} + Y_{L2} + Y_{Ls}$

Applying node-voltage method at node B

$$\frac{V_B - V_A - 2V_{Ls}^i}{Z_{Ls}} + \frac{V_B - 2V_{Cs}^i}{Z_{Cs}} + \frac{V_B - 2V_{L3}^i}{Z_{L3}} + \frac{V_B - 2V_{L4}^i}{Z_{L4}} = 0, \quad (4.9)$$

results in,

$$V_B = \frac{1}{N} [V_A Y_{Ls} + 2V_{Ls} Y_{Ls} + 2V_{Cs} Y_{Cs} - 2V_{L3} Y_{L3} - 2V_{L4} Y_{L4}], \quad (4.10)$$

where $Y_{L3,L4}$ and $Y_{Ls,Cs}$ denote characteristic admittances of link lines and short link $Y_{L3} = \frac{1}{Z_{L3}}$, $Y_{L4} = \frac{1}{Z_{L4}}$, $Y_{Ls} = \frac{1}{Z_{Ls}}$, $Y_{Cs} = \frac{1}{Z_{Cs}}$ and $N = Y_{L3} + Y_{L4} + Y_{Ls} + Y_{Cs}$.

Solving Equations (4.8) and (4.10) for V_A and V_B gives

$$V_A = D [2AV_{L1}^i Y_{L1} + 2AV_{L2}^i Y_{L2} + 2CV_{L3}^i Y_{L3} Y_{Ls} + 2CV_{L4}^i Y_{L4} Y_{Ls} + 2CV_{Cs}^i Y_{Cs} Y_{Ls} + 2(CY_{Ls}^2 - AY_{Ls})V_{Ls}^i]. \quad (4.11)$$

and

$$V_B = D [2CY_{L1} Y_{Ls} V_{L1}^i + 2CY_{L2} Y_{Ls} V_{L2}^i + 2BY_{L3} V_{L3}^i + 2BY_{L4} V_{L4}^i + 2BY_{Cs} V_{Cs}^i + (2BY_{Ls} - 2CY_{Ls}^2) V_{Ls}^i]. \quad (4.12)$$

where $A = \frac{1}{M}$, $B = \frac{1}{N}$, $C = \frac{1}{MN}$, $D = \frac{1}{1 - CY_{Ls}^2}$, $M = Y_{L1} + Y_{L2} + Y_{Ls}$, $N = Y_{L3} + Y_{L4} + Y_{Ls} + Y_{Cs}$

Once the total voltages at ports A and B are known, the reflected voltages at all link lines are found as

$$V_m^r = V_A - V_m^i, \dots, m=1,2 \quad (4.13)$$

$$V_n^r = V_B - V_n^i, \dots, n=3,4 \quad (4.14)$$

The reflected voltages at the inductive and capacitive stubs are found as,

$$V_{LS}^r = (V_B - V_A) - V_{LS}^i, \quad (4.15)$$

$$V_{CS}^r = V_B - V_{CS}^i. \quad (4.16)$$

4.3 Short link line on the boundary plane

In some cases short link lengths can occur next the outer boundary plane as shown in Figure 4.7. Such cases need to be treated differently with equivalent Thevenin circuits which is described below for short-circuit (SC), open-boundary (OC), and boundary matched with proper impedance.

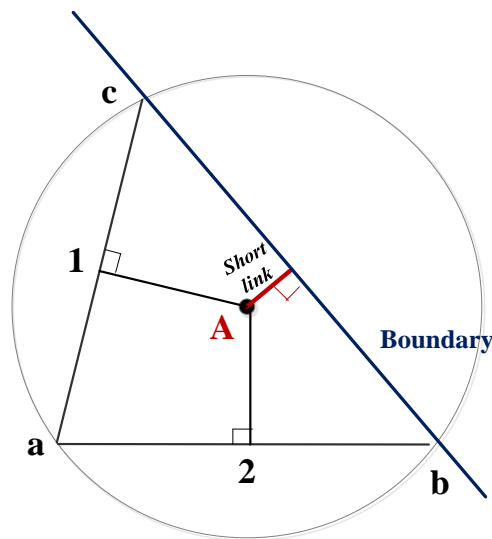


Figure 4.7: Short link located on the outer boundary plane.

4.3.1 Short-circuit boundary

If a short link line is connected on a short-circuit boundary then $V_B=0$, and the equivalent Thevenin circuit is shown in Figure 4.8

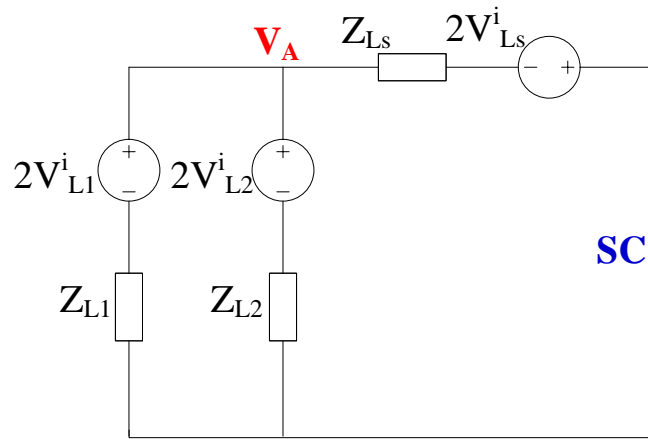


Figure 4.8: Thevenin equivalent circuit of short link line located on SC boundary.

Applying node-voltage method at node A gives

$$\frac{V_A - 2V_{L1}^i}{Z_{L1}} + \frac{V_A - 2V_{L2}^i}{Z_{L2}} + \frac{V_A - (-2V_{Ls}^i)}{Z_{Ls}} = 0. \quad (4.17)$$

The voltage V_A can be expressed as

$$V_A = \frac{1}{M} [2V_{L1}^i(Y_{L1}) + 2V_{L2}^i(Y_{L2}) - 2V_{Ls}^i(Y_{Ls})], \quad (4.18)$$

where $M = Y_{L1} + Y_{L2} + Y_{Ls}$, $Y_{L1,L2}$ and Y_{Ls} denote characteristic admittances of link lines and short link, respectively, and V_{Ls} is the short link voltage.

The reflected voltages at links lines are

$$V_{L1}^r = V_A - V_{L1}^i, \quad (4.19)$$

$$V_{L2}^r = V_A - V_{L2}^i, \quad (4.20)$$

$$V_{Ls}^r = (-V_A) - V_{Ls}^i. \quad (4.21)$$

4.3.2 Open-circuit boundary

In the case of the open-circuit boundary, Thevenin equivalent circuit is shown in Figure 4.9

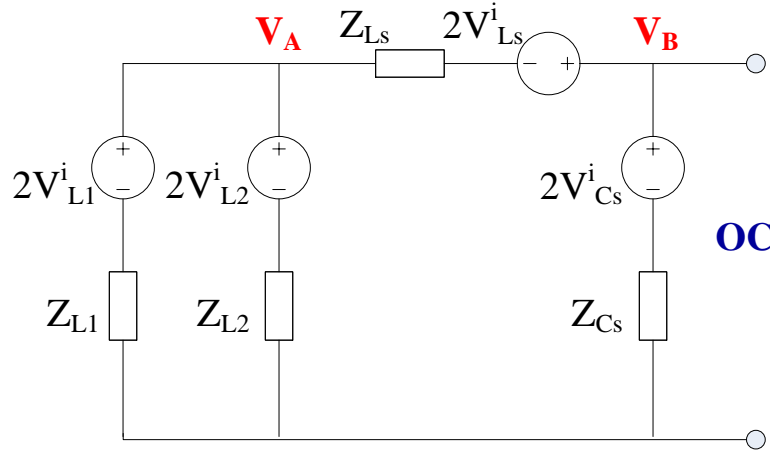


Figure 4.9: Thevenin equivalent circuit of short link line located on OC boundary.

Applying node-voltage method at nodes A & B, voltages V_A and V_B are obtained as

$$V_A = D \left[2AV_{L1}^i Y_{L1} + 2AV_{L2}^i Y_{L2} + 2CV_{Cs}^i Y_{Cs} Y_{Ls} + 2AV_{Ls} [2AV_{Ls} (BY_{Ls}^2 - Y_{Ls})] \right]. \quad (4.22)$$

$$V_B = D \left[2CY_{L1} Y_{Ls} V_{L1}^i + 2CY_{L2} Y_{Ls} V_{L2}^i + 2BY_{Cs} V_{Cs}^i + (2BY_{Ls} - 2CY_{Ls}^2) V_{Ls} \right]. \quad (4.23)$$

where $M = Y_{L1} + Y_{L2} + Y_{Ls}$, $N = Y_{Ls} + Y_{Cs}$, $A = \frac{1}{M}$, $B = \frac{1}{N}$, $C = \frac{1}{MN}$, $D = \frac{1}{1 - CY_{Ls}^2}$

And the reflected voltages at links and stub are

$$V_{L1}^r = V_A - V_{L1}^i, \quad (4.24)$$

$$V_{L2}^r = V_A - V_{L2}^i, \quad (4.25)$$

$$V_{Ls}^r = (V_B - V_A) - V_{Ls}^i, \quad (4.26)$$

$$V_{Cs}^r = V_B - V_{Cs}^i. \quad (4.27)$$

4.3.3 Impedance boundary

In some problems it is required to match the problem to certain impedance, i.e. matching the boundaries to free space or $Z_{BND} = \sqrt{\mu_o/\epsilon_o}\Omega$. Also, in some cases, a source node at the boundary is used to excite the problem (i.e. injects signals into the problem space). In the case of impedance boundary the Thevenin equivalent circuit is given generally in Figure 4.10

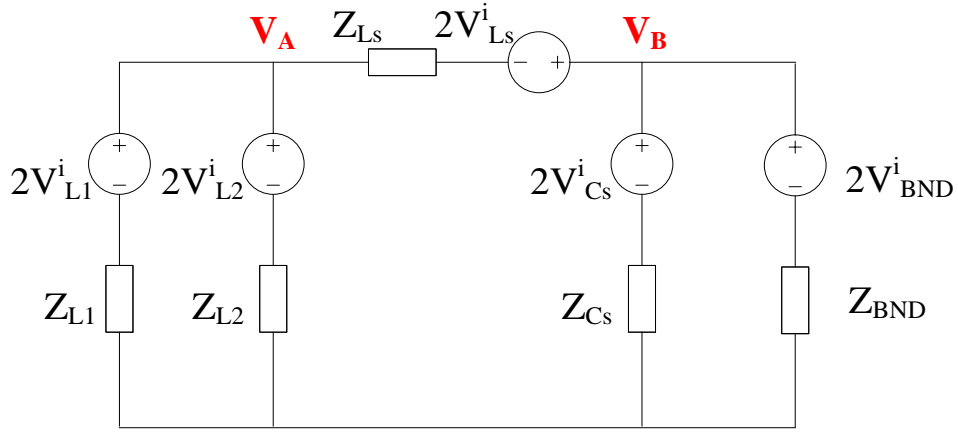


Figure 4.10: Thevenin equivalent circuit of short link line located on impedance boundary.

From Figure 4.10 and following the same approach as in Equations (4.7) and (4.9), voltages V_A and V_B are obtained as,

$$V_A = D \left[2AV_{L1}^i Y_{L1} + 2AV_{L2}^i Y_{L2} + 2CV_{BND}^i Y_{BND} Y_{Ls} + 2CV_{Cs}^i Y_{Cs} Y_{Ls} + 2AV_{Ls} [2AV_{Ls} (BY_{Ls}^2 - Y_{Ls})] \right], \quad (4.28)$$

$$V_B = D \left[2CY_{L1} Y_{Ls} V_{L1}^i + 2CY_{L2} Y_{Ls} V_{L2}^i + 2BY_{BND} V_{BND}^i + 2BY_{Cs} V_{Cs}^i + (2BY_{Ls} - 2CY_{Ls}^2) V_{Ls}^i \right], \quad (4.29)$$

where $M = Y_{L1} + Y_{L2} + Y_{Ls}$, $N = Y_{BND} + Y_{Ls} + Y_{Cs}$, $A = \frac{1}{M}$, $B = \frac{1}{N}$, $C = \frac{1}{MN}$, $D = \frac{1}{1 - CY_{Ls}^2}$

The reflected voltages are updated as follows

$$V_m^r = V_A - V_m^i, \quad m=1,2. \quad (4.30)$$

The reflected link, stub and boundary voltages are calculated from

$$V_{LS}^r = (V_B - V_A) - V_{LS}^i, \quad (4.31)$$

$$V_{CS}^r = V_B - V_{CS}^i, \quad (4.32)$$

$$V_{BND}^r = V_B - V_{BND}^i. \quad (4.33)$$

4.4 Pair model implementation

The TLM algorithm involving pair model is shown in Figure 4.11. After the initiation of incident voltages all link lengths are compared against the set threshold. If they are shorter than the given threshold length, a triangle pair is formed and the scattering is done as described in sections 4.2 and 4.3. Otherwise, the TLM algorithm follows the conventional scatter route [141] discussed in Chapter 3. This procedure is repeated for a given number of timesteps, N until a steady state is achieved.

The criteria of setting the maximum threshold length ensures that only one pair is formed for any triangle with one of its neighbours, i.e. two or more pairs are not allowed. This ensures keeping the complexity of the system to minimum. A Voronoi diagram is obtained from the Delaunay triangles that form specific shape. Voronoi diagram is formed of link lines, from which the shortest one is found and the first triangle pair is formed with the neighbour located at the short link side.

The process continues until the next formed pair would be for a triangle that is already paired, i.e. until two pairs per triangle start happening. The maximum threshold length is then set to be equal to the last value for which the criteria of ‘one link per triangle’ is not violated. In practice, the threshold length is set to be equal or smaller than the maximum threshold length. The impact of the threshold length on the accuracy of the simulations is analysed in the next section.

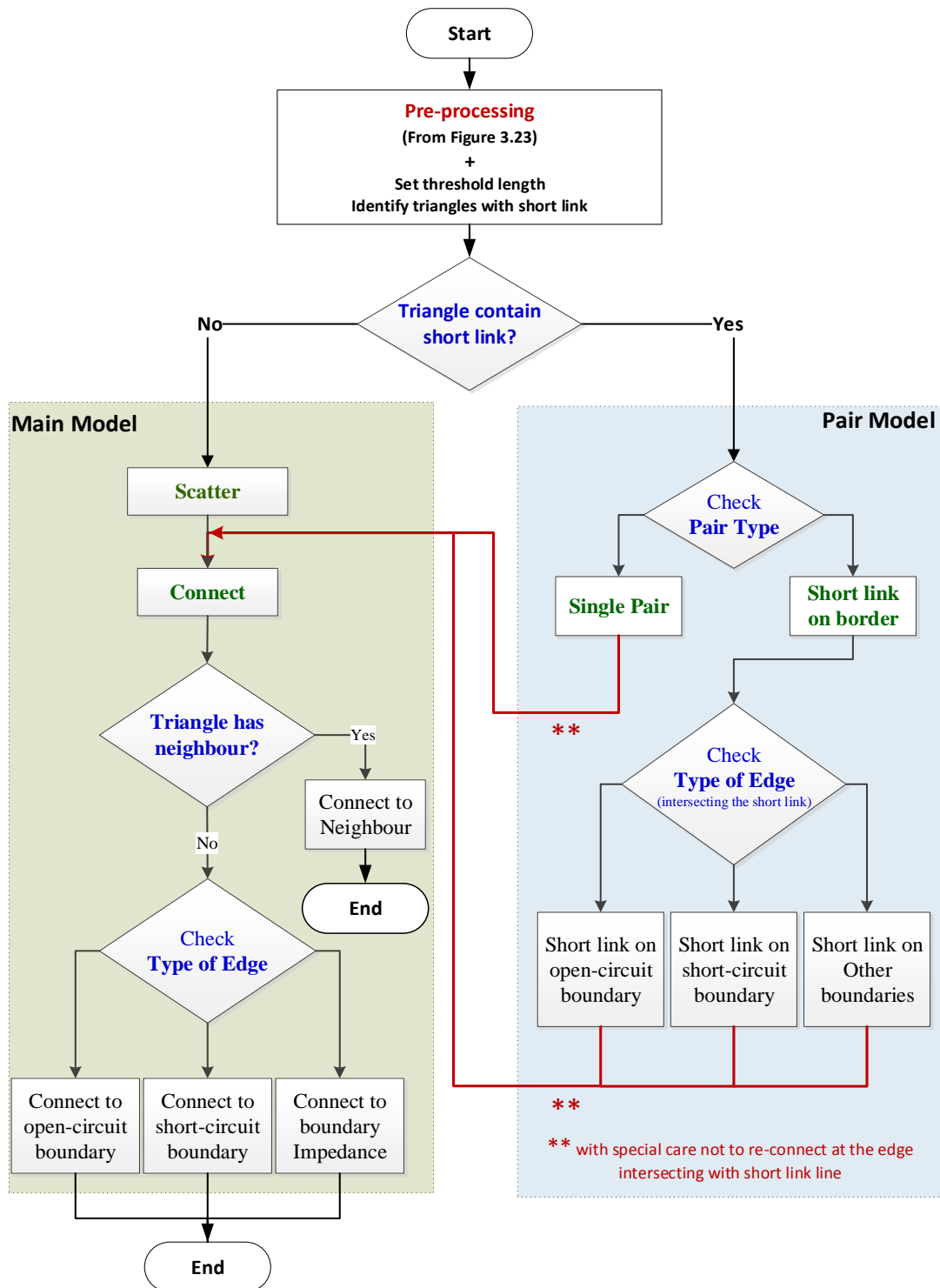


Figure 4.11: TLM algorithm containing merged triangle pairs.

For a triangle pair the scatter process is performed implicitly by applying Equations (4.11)–(4.16). Within such process connection is also performed between the triangles at the side which the short link intersects. For the rest of the pair sides the ‘connect’ process follows the same procedure applied in the main model with special care that

the connection is not performed at the side at which the triangle forms a pair. On the other hand, the model for a short link line on a border involves the scatter process for that triangle in addition to connection with the boundary, then the conventional ‘connect’ is applied to the other two sides.

Further detail of how to use and set the pair model in the unstructured TLM simulator is discussed in Appendix A

4.5 Results

This section investigates impact of the choice of threshold on the accuracy and runtime of TLM simulations. For this purpose two canonical problems are considered for which analytical results are known, namely, air-filled cylindrical PEC resonator of radius $r=1\text{cm}$ and PEC cylindrical resonator of radius 1cm concentrically loaded with a dielectric cylinder of radius 0.5cm and relative permittivity $\epsilon_r=2.1$.

4.5.1 Air filled cylindrical PEC resonator

The air filled cylindrical PEC resonator is approximated by a sequence of polygonal approximations to generate a triangular mesh of Delaunay type and using readily available software provided in [37] which also allows for implementation of boundaries and material properties. The triangular mesh is then processed to obtain the Voronoi mesh of transmission lines [23] shown in Figure 4.12. The resulting mesh contains 1261 triangles and has the shortest link line of 0.04274mm thus requiring time step of 0.1008 ps .

The mesh generated is perturbed so that all triangles that form link lengths below certain threshold are merged into four-port nodes, for which scattering is described previously. The maximum threshold length that results in only single pairs of merged triangles is found to be 0.645mm when a total of 18 pairs are formed and which results in a timestep of 4.269ps , which is more than a 40 times that of the original mesh.

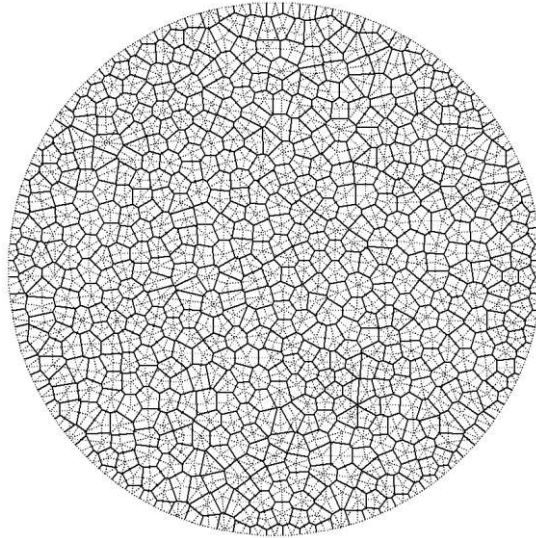


Figure 4.12: Delaunay (dotted lines) and Voronoi (thick lines) diagrams of air filled circular resonator of radius 1cm.

The fundamental mode of an air-filled circular resonator is equal to 11.46769GHz. Table 4.1 shows the relative error in the fundamental mode TM01 for the main model and then by applying different threshold lengths in which 5, 7, 14 and 18 pairs are produced.

The relative error displayed in Table 4.1 shows that the error increases with the increase of number of pairs. The relative error will be discussed in detail shortly.

Table 4.1: Relative error in fundamental mode TM01 for different number of pairs

Number of triangle pairs	0	5	7	14	18
Threshold length (mm)	0.04274	0.20000	0.30000	0.50000	0.64500
Relative error (%)	0.32116	0.90227	1.47999	2.94130	4.36548

Figure 4.13 shows the resonance frequency curves for different threshold values. The first curve represents the resonance modes for the main model only, meaning no triangles are isolated in pair model, the second and third curves represent the resonance modes for the circular resonator with the application of around 30% and 50% of the maximum threshold length, which are 0.2mm and 0.3mm that corresponds to 5 and 7 triangle pairs respectively, and the fourth curve is the resonance frequencies with the

usage of the maximum allowable threshold length which equals to 0.645mm and corresponds to 18 triangle pairs.

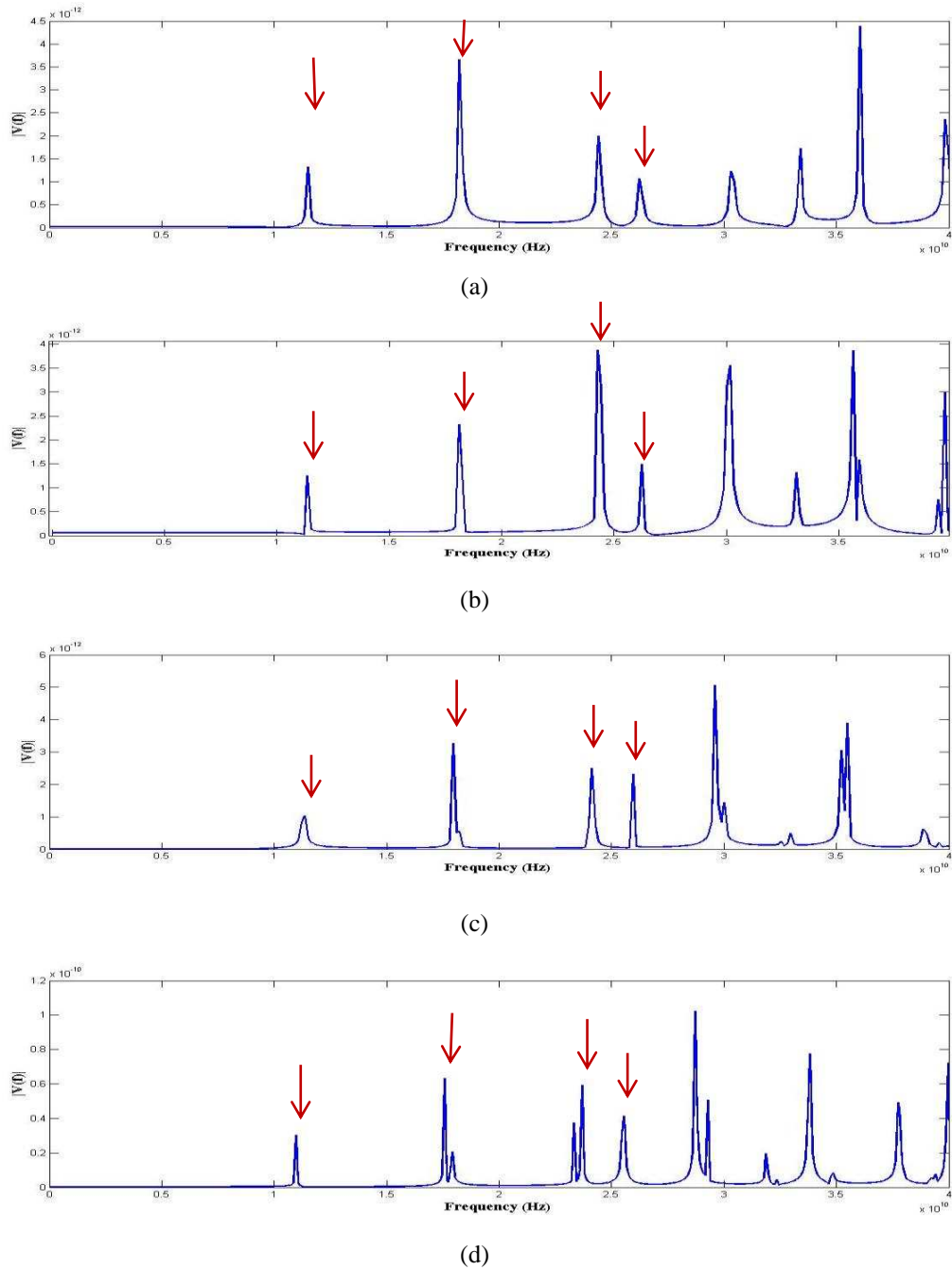


Figure 4.13: Resonance frequencies for an air-filled circular resonator of radius 1cm. (a) no pairs, (b) 30% of maximum threshold length, (c) 50% of maximum threshold length, (d) maximum allowable threshold length, with red arrows pointing modes TM01, TM11, TM21 and TM02 positions.

Note that as the threshold length increases or the more pairs are formed peaks of higher modes start to split and unwanted resonance frequencies appear on the resonance curves as shown in Figure 4.13(d).

Figure 4.14 shows the runtime and the relative error for different resonant modes namely TM01, TM11, TM21 and TM02 for different threshold lengths. For all thresholds the resonator is excited using a Dirac function and simulation is run for a total simulation time of 33min. The relative error in resonant frequency is found as $\left| \frac{f_{\text{TLM}} - f_a}{f_a} \right|$, where f_{TLM} and f_a are resonant frequencies obtained using the TLM simulator and exact analytical formula [140], respectively. The runtime is normalised with respect to the runtime achieved with no threshold applied.

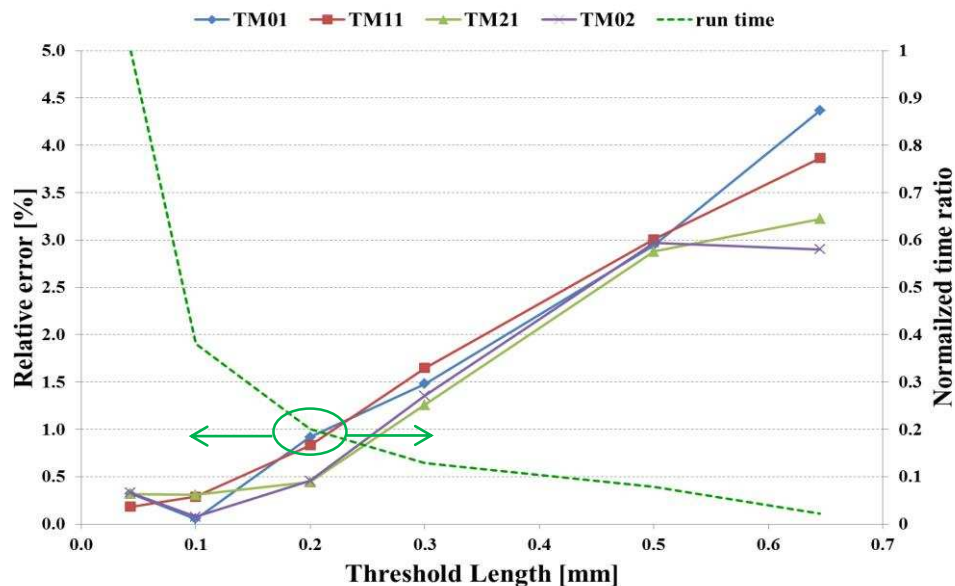


Figure 4.14: Relative error $\left| \frac{f_{\text{TLM}} - f_a}{f_a} \right|$ and the computational runtime ratio compared to the case of no threshold applied for the air-filled PEC of radius 1cm.

Table 4.2 lists the percentage relative error in the first four resonant modes for different number of pairs. For the case of no threshold the total normalised runtime is 1 and the error in resonant frequency extraction is below 1%. As the threshold is increased from 0.004mm (minimum link length) to 0.645mm the error is increasing but the total runtime is quickly reducing. The increase in error can be explained by the fact that for bigger thresholds the pair model is less accurate as the discrepancy between the actual link length and the threshold becomes greater.

However, Figure 4.14 shows that even for thresholds that are 70% below the maximum threshold of 0.645mm (threshold length=0.2mm, 5 triangle pairs), the error is kept below 1% and the runtime is reduced by 80%.

Table 4.2: Percentage relative error in the first four modes of an air-filled PEC cylindrical resonator for different number of triangle pairs

Number of triangle pairs	Threshold length (mm)	Relative error [%] in				Normalized run time
		TM01 11.46769 (GHz)	TM11 18.27182 (GHz)	TM21 24.48942 (GHz)	TM02 26.32242 (GHz)	
0	0.04274	0.32113	0.18033	0.31606	0.32867	1
2	0.10000	0.05223	0.28651	0.30764	0.07651	0.38014
5	0.20000	0.91904	0.83061	0.44312	0.45426	0.19992
7	0.30000	1.47999	1.64613	1.25689	1.35593	0.12860
14	0.50000	2.94130	3.00638	2.87814	2.97143	0.07899
18	0.64500	4.36543	3.86337	3.22338	2.90080	0.02182

Figure 4.15 shows the effect of threshold length on both the time step and total run time. Normally, within the main model the time step is calculated upon the shortest link length. In the pair model the minimum link length will be swapped with the threshold length, so as the threshold length increases the time step increases and consequently the total run time decreases. Timestep is normalised as $\Delta t_{\text{thre}}/\Delta t_{\text{min}}$ where Δt_{thre} and Δt_{min} correspond to the timestep with and without applying threshold, respectively. Notice that at a threshold length equals to 0.3mm the time step increases to approximately 7 times the original time step which is calculated based on the minimum link length (0.0045mm), whilst the run time has reduced to 0.13 of the original run time. Continuing with the increase of the threshold length till the maximum allowable limit, the time step has increased to 42 times the original time step and the run time decreased to 0.02 of the run time of the main model.

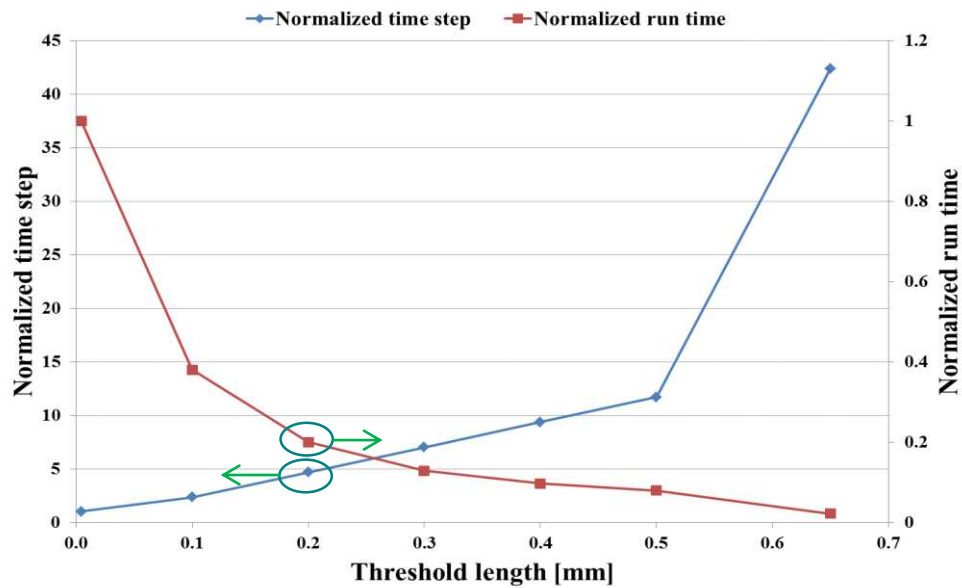


Figure 4.15: Impact of different threshold lengths on the normalized timestep and the runtime

For the same problem of air filled PEC resonator the threshold is applied to a variety of triangular meshes ranging from coarse to fine. Figure 4.16 shows the relative error in the fundamental resonant frequency TM₀₁ for the case of no threshold and the thresholds set at 30%, 50% and maximum allowable threshold so that only pairs of triangles are merged. In all cases, the relative error decreases as the number of meshes increases. Furthermore, as the value of threshold is increased the relative error also increases compared to the relative error of the mesh with no thresholds applied.

Figure 4.16 shows that in the case of coarser meshes (below 5000 triangles) certain case is noticed: these meshes tend to produce very short link lengths but also quite large maximum thresholds, so that 30% and 50% of the maximum threshold criteria results in relatively large thresholds and large numbers of paired triangles which consequently increases the error. For example, for the mesh with 3268 triangles, the minimum link length is 2.389×10^{-15} m and the maximum threshold is found to be 0.88 mm. This example shows the importance of applying the pair model, as zero link length will lead to infinitesimally small time step, and prohibitively long runtime, especially in cases of fine meshes.

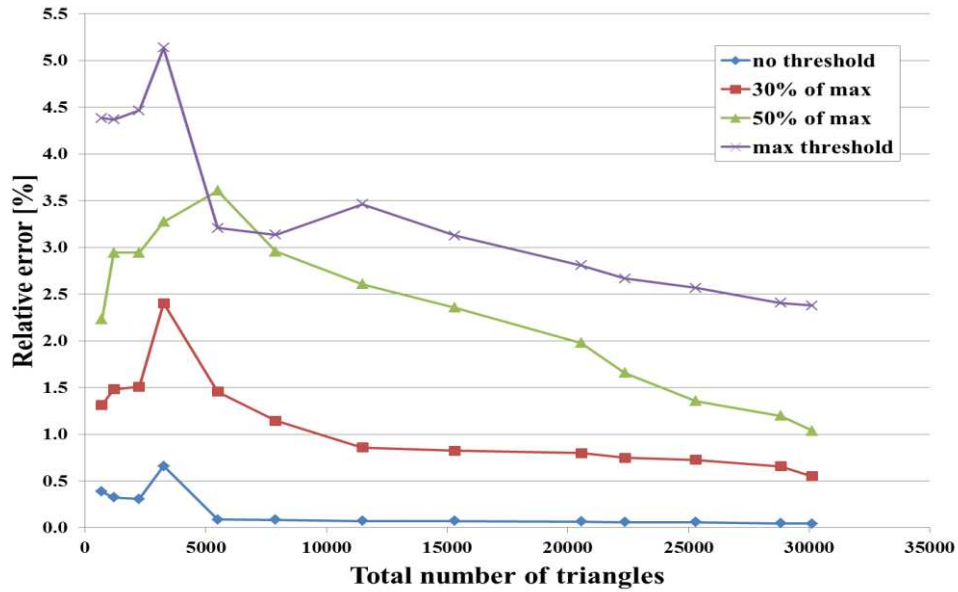


Figure 4.16: Relative error $\left| \frac{f_{\text{TLM}} - f_a}{f_a} \right|$ for the fundamental resonance TM01 of air-filled PEC of radius 1cm as a function of different mesh sizes. Different curves correspond to the cases with no threshold applied, 30% and 50% of maximum threshold and maximum threshold applied.

4.5.2 Dielectrically loaded cylindrical resonator

The second example is for the PEC cylindrical resonator of radius 1cm concentrically loaded with a dielectric cylinder of relative permittivity $\epsilon_r=2.1$ and 0.5cm radius. A closed loop of finite segments is created which has a radius of 0.5cm. Two regions (0-0.5cm and 0.5-1cm) will be defined for which all meshes inside the inner circle will be assigned a dielectric permittivity of 2.1 and the rest of meshes will be air-filled. Figure 4.17(a) shows the Delaunay mesh for the case of meshing the resonator into 1160 triangles, and Figure 4.17(d) illustrates the Voronoi diagram which is the mesh of link lines connecting the triangles circumcentres. The minimum link length of this example is 0.105mm which corresponds to the timestep of 0.36ps. The maximum threshold length is found to be 0.905mm which produces 38 paired triangles. This lead to the increase in time step value to 3.093ps.

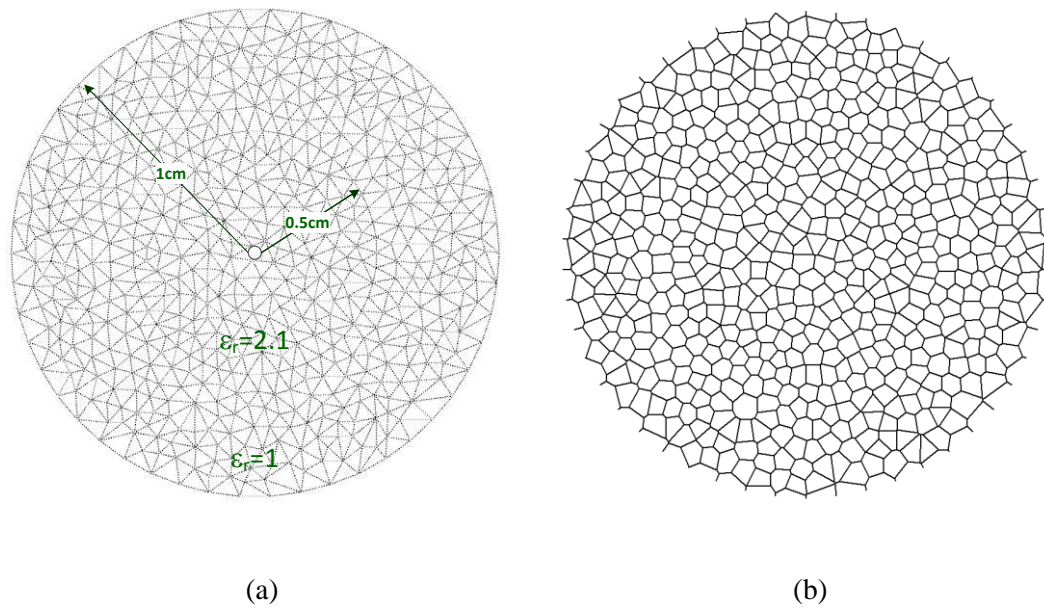


Figure 4.17: (a) Delaunay and (b) Voronoi diagrams of PEC circular resonator of radius 1cm concentrically loaded with a dielectric cylinder of relative permittivity $\epsilon_r=2.1$ and 0.5cm radius.

Figure 4.18 shows the relative error and the normalized runtime ratio compared to the case when no threshold is applied, for the first two resonant modes, TM01 and TM11, and for different threshold lengths. In all cases the problem is excited by a Dirac function and the total simulation time is kept constant at 30min. Figure 4.18 shows that as the threshold is increased the relative error increases. It is noted that for the threshold length of 0.2mm the error is kept below 0.5% whilst the runtime is reduced by more than 50% of the original run time.

Table 4.3 lists the percentage relative error in the first two resonant modes for different number of pairs. For the case of no threshold the total normalised runtime is 1 and the error in resonant frequency extraction is below 1%. Increasing the threshold length to 0.2mm the run time decreased by more than 30% and the relative error is still kept under 1%. As the threshold is increased toward the maximum allowed threshold the error is increasing but the total runtime is quickly reducing. Again, the increase in error can be explained by the fact that for bigger thresholds the pair model is less accurate as the discrepancy between the actual link length and the threshold is greater.

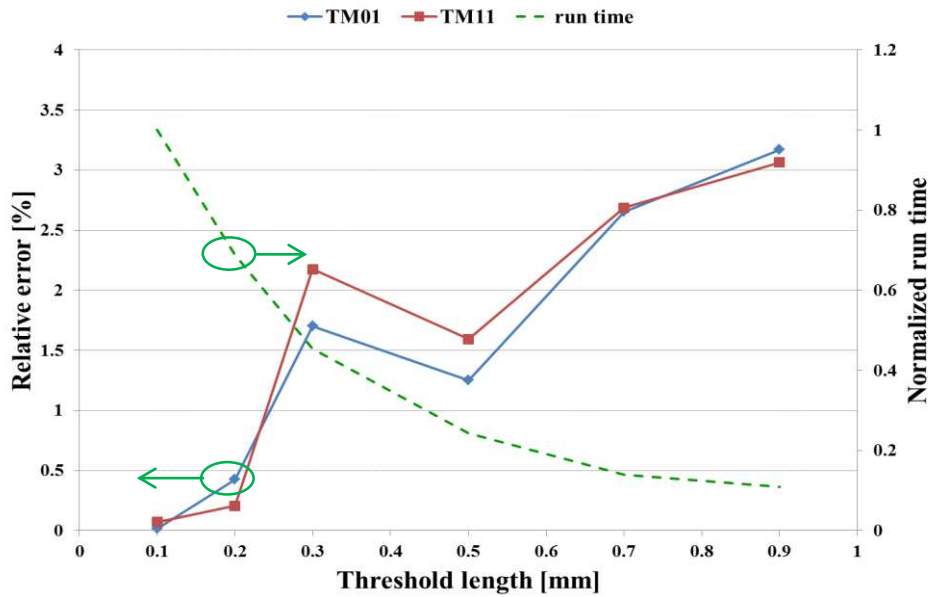


Figure 4.18: Relative error $\left| \frac{f_{\text{TLM}} - f_a}{f_a} \right|$ and the computational runtime ratio compared to no threshold applied for the PEC circular resonator of radius 1cm concentrically loaded with a dielectric cylinder of relative permittivity $\epsilon_r=2.1$ and 0.5cm radius.

Table 4.3: Percentage relative error in the first two modes of PEC circular resonator concentrically loaded with a dielectric cylinder for different number of triangle pairs

Number of triangle pairs	Threshold length (mm)	Relative error [%] in		Normalized run time
		TM01 11.50451 (GHz)	TM11 18.23887 (GHz)	
0	0.105	0.01595	0.07097	1.00000
2	0.2	0.42521	0.20657	0.68717
5	0.3	1.70221	2.17384	0.45426
7	0.5	1.25217	1.59182	0.24339
14	0.7	2.65335	2.68502	0.13901
19	0.905	3.16952	3.06336	0.10963

Figure 4.19 shows the effect the threshold length has on the timestep. Timestep is normalised as $\Delta t_{\text{thre}}/\Delta t_{\text{min}}$ where Δt_{thre} and Δt_{min} correspond to the timestep with and without applying threshold, respectively. It can be seen that threshold of 0.2mm results in doubling of the original timestep and reducing the runtime by 30%, whilst still maintaining accuracy below 0.5%, as seen in Figure 4.18.

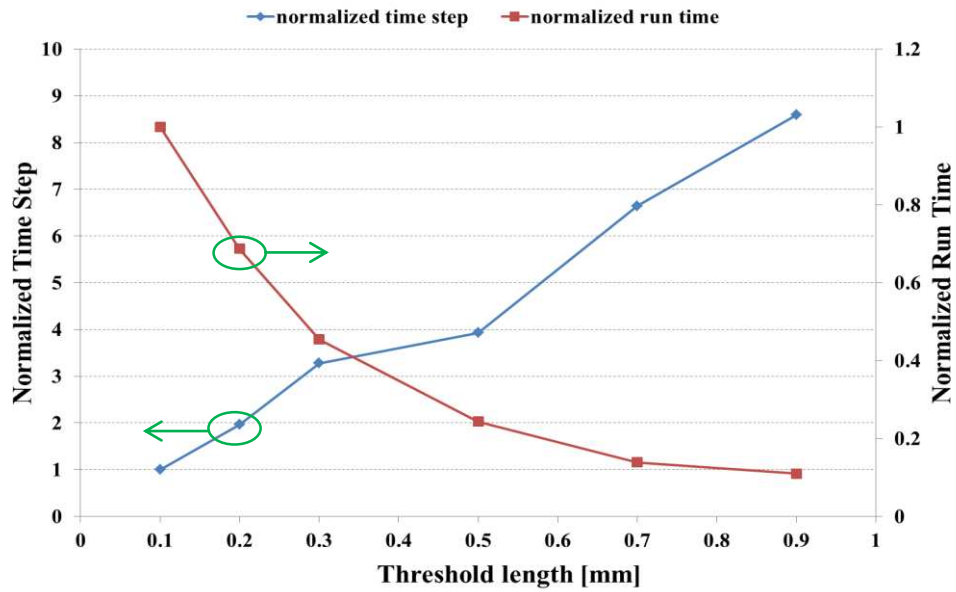


Figure 4.19: Impact of different threshold lengths on the timestep and the runtime ratio compared to the case with no threshold

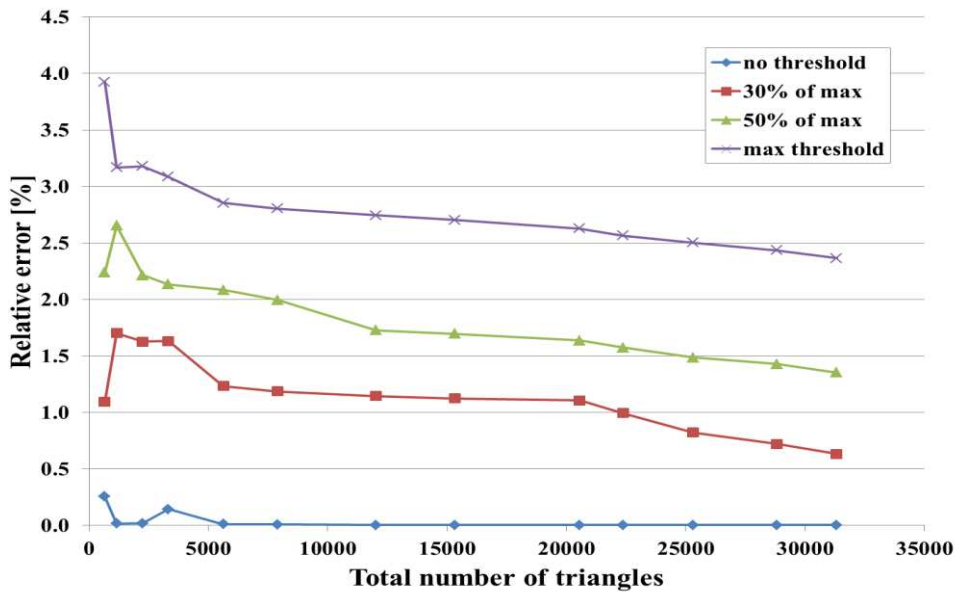


Figure 4.20: Relative error $|(f_{TLM} - f_a) / f_a|$ for the fundamental resonance TM01 of PEC cylindrical resonator of radius 1cm concentrically loaded with a dielectric cylinder of relative permittivity $\epsilon_r=2.1$ and 0.5cm radius as a function of different mesh sizes.

For the same problem of PEC cylindrical resonator of radius 1cm concentrically loaded with a dielectric cylinder of relative permittivity $\epsilon_r=2.1$ and 0.5cm radius, the threshold is applied to a variety of triangular meshes ranging from coarse to fine.

Figure 4.20 shows the relative error in the fundamental resonant frequency TM01 for the case of no threshold and the thresholds set at 30%, 50% and maximum allowable threshold. In all cases, the relative error decreases as the number of meshes increases. Furthermore, as the value of threshold is increased the relative error also increases compared to the relative error of the mesh with no thresholds applied.

4.6 Summary

This chapter shows that the automatic generation of Delaunay meshes can generate very short link lines that can negatively impact the computational runtime of TLM simulations. To alleviate this problem, a mesh perturbation method is presented whereby all short link lines that fall below a certain threshold are replaced by an inductive and capacitive stub and the triangles that contain the relevant link line are merged into a four port node (triangle pair) for which scattering is done implicitly. Short link lines that fall on any type of boundaries should be treated as special cases of pair model and solved separately. In this work the length of the threshold is limited by the criteria that only pairs of triangles are formed.

The impact of the threshold on the accuracy and computational runtime of the TLM simulations is assessed on two canonical problems of resonant mode extraction of air-filled and dielectrically loaded PEC resonators for which analytical results are known. In both cases it is shown that the threshold works effectively in reducing the overall runtime. The increase in the threshold results in the increase in the relative error as the discrepancy between the actual link length being replaced and the threshold is increased. Working with 30% of the maximum allowable threshold length will increase the time step and reduce the run time sufficiently with the advantage of keeping the error below 1%. This error can be further reduced and controlled by increasing the number of triangles in the mesh.

Introducing such model allows the simulation of different types of applications without the fear of the presence of zero link lengths, which tends to appear as the mesh sizes decrease.

Chapter 5.

Dispersion and intermodal coupling in 2D UTLM

5.1 Introduction

Simulations performed using unstructured triangular meshes have many advantages over their structured counterparts. TLM employing unstructured triangular and tetrahedral meshes offers the advantage of piecewise linear approximations to curved material boundaries as well as notably graded meshes in the proximity of physically significant fine features such as wires and apertures [19, 125]. Both of these properties can yield valuable improvements in both run time and memory consumption, albeit at the expense of algorithmic complexity. In practice, the selection of the sampling density for either a structured or an unstructured mesh is driven by both the geometry of the problem and also by the accuracy of the solutions being demanded. Therefore, it is important that the user has reference benchmarks in order to permit them to manage dispersion errors and in most cases these are expressed in terms of known results for simple geometrical scenarios such as free space.

Quantitatively, mesh induced errors can be described in terms of the phase errors of simple propagating field solutions, which are typically also anisotropic in nature or in terms of non-physical coupling between physically meaningful local fields solutions, such as waveguide modes and resonant fields.

The dispersion of the structured 2D TLM method is well documented [7] with zero and maximum dispersion observed for plane waves propagating at an angle of 45° and along the coordinate lines of a square grid, respectively [7]. Naturally, dispersion in practical problems is a complex superposition of these two extreme cases, but nevertheless, the often quoted rule of thumb for a suitable grid size in order to keep dispersion errors small, is that the distance between samples should be no larger than a tenth of the wavelength in the material concerned [7, 117]. It is noted here that whilst

the use of a finer spatial (and hence temporal) Cartesian discretisation reduces the absolute values of the dispersion, it has no impact upon its relative anisotropy.

With structured grids, the anisotropic dispersion errors are available from an analytic study of the properties of a unit grid cell, most commonly providing a quantification of the effect of mesh density upon the behaviour of plane waves propagating in unbounded free space. However, for unstructured meshes this is not possible and so benchmark data is best obtained from numerical characterisation of simple canonical cases. This chapter reports such data for the case of the 2D TLM algorithm operating upon an unstructured triangular mesh.

In this chapter the dispersion of the unstructured 2D TLM method is examined. This is done for two cases: a) by quantifying the phase error of plane wave propagation through the mesh and b) investigating the impact of unstructured mesh discretisation on the inter-modal coupling between different order spatial modes in a uniform space. The impact of the mesh on inter-modal coupling between different spatial modes is done in a statistical manner for a number of meshes. In both cases, the computational model adopted is that of a two-dimensional rectangular space with open boundary conditions on the top and bottom plate to simulate the open space. The input and output of the waveguide are matched to the free space impedance.

5.2 Mesh quality

In the unstructured case, the user has two degrees of freedom when selecting or producing a mesh: the average cell size, expressed in terms of for example triangle area, and secondly a measure of the shape of the triangles used. For example, in a triangular mesh the intuition is that use of just equilateral triangles would lead to minimal errors. However, one can neither actually tessellate a space with only equilateral triangles and in any case, the principal advantage of an unstructured mesh is being able to exploit the variety in triangular shapes to capture complex geometries with the fewest possible computational cells.

Unlike the structured mesh which has identical discretisation cells, triangular 2D meshes, unless they are made of equilateral triangles, have greater cell variability. It

must be noted that mesh generation is not a trivial exercise, especially in 3D, and that at best the user will have the ability to request that some measure of triangle quality is met, usually in an external sense. There are a number of measures of triangle quality used in mesh generation, for example, for better description of the Delaunay meshes, a widely used parameter known as mesh quality Q factor is defined as [32]

$$Q = \frac{\text{triangle circumradius}}{\text{triangle shortest edge}}. \quad (5.1)$$

In the process of triangular mesh generation the specification for the required Q factor prevents appearance of bad triangles in the mesh, such as skinny triangles [32]. The mesh of equilateral triangles has Q factor of $1/\sqrt{3}$ or 0.57735 [131]. A practical mesh of good quality of arbitrary shape would typically have Q around 0.57735 which is acceptable for EM simulations due to uniform mesh distribution.

5.3 Plane wave propagation

A plane wave is the simplest form of a propagating wave. For a wave travelling in the z direction, the plane wave has the form [45],

$$f(z, t) = A_o \cos(\omega t - kz). \quad (5.2)$$

where A_o is the amplitude, ω is the angular frequency in rad/s and k is the phase constant (or wave number) in rad/m that defines the change in the phase after the wave has travelled a distance z and is given by

$$k = \frac{\omega}{v_p} = \omega \sqrt{\mu \epsilon}. \quad (5.3)$$

The wavelength of the plane wave is defined as $\lambda = 2\pi/k$.

The phase velocity v_p is the speed at which the observer must travel to obtain the constant phase of the wave. The phase velocity of the plane wave is defined as [45],

$$v_p = \frac{\omega}{k} = \frac{1}{\sqrt{\mu\epsilon}} \quad (5.4)$$

The computational model adopted for the dispersion study is that of a two-dimensional rectangular space which resembles a parallel plate waveguide but with open boundary conditions on the top and bottom plate to simulate the open space, whilst the input and output of the waveguide are matched to the free space impedance.

Parallel plate waveguide is the simplest form of waveguide that can support Transverse Magnetic (TM), Transverse Electric (TE) and Transverse Electromagnetic (TEM) waves. Parallel plate waveguide is described by L which is the length of the waveguide and d the plate separation or width of the waveguide. In parallel plates waveguide the length is much greater than the width so the fringing effect can be neglected. The space between the plates can be filled with any material of relative permittivity ϵ_r and relative permeability μ_r . Plane wave propagation can be modelled by using a parallel plate waveguide but setting the upper and lower plates to be open-circuited as shown in Figure 5.1.

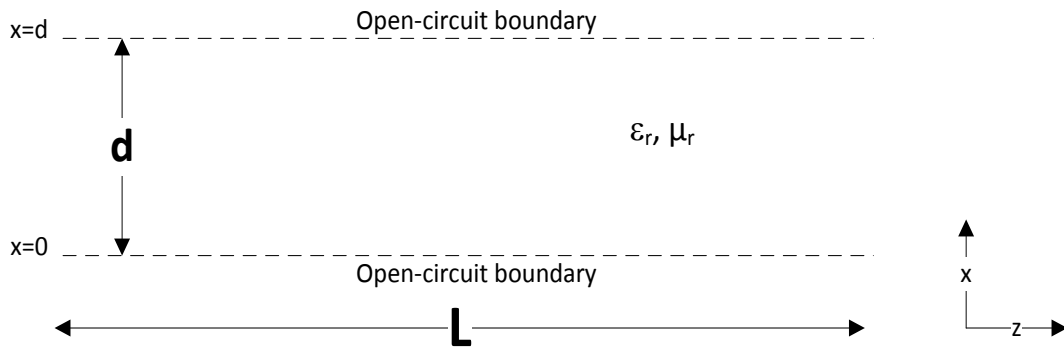


Figure 5.1: Schematic diagram of parallel plate waveguide representing plane wave propagation

Due to the fact that the unstructured TLM method is based on the shunt nodes, TM modes will be investigated. Transverse magnetic (TM) mode does not support the longitudinal component of the magnetic field ($H_z=0$) and has both transversal magnetic field components. And it has also all three electric field components. For a parallel plate waveguide of cross section in the x - y plane and wave propagation along the z -axis, the field components are E_x , H_y and E_z .

The wave equation for the electric field is expressed as [45]

$$\nabla^2 \bar{E} + \omega^2 \mu \epsilon \bar{E} = 0. \quad (5.5)$$

which can be expanded to

$$\left(\frac{\partial^2}{\partial x^2} + \frac{\partial^2}{\partial y^2} + \frac{\partial^2}{\partial z^2} + k_o^2 \right) \bar{E} = 0. \quad (5.6)$$

Since the plane wave changes only in the x-direction, then $\frac{\partial}{\partial y} = 0$, $\frac{\partial}{\partial x} \neq 0$. A plane wave propagating along the z-direction is expressed as,

$$\bar{E} = \hat{z} E_0 e^{-j\beta z}. \quad (5.7)$$

Then $\frac{\partial^2}{\partial z^2} E_z = -\beta^2 E_z$ and Equation (5.7) reduces to

$$\begin{aligned} \left(\frac{\partial^2}{\partial x^2} - \beta^2 + k_o^2 \right) \mathbf{E}_z &= 0, \\ \left(\frac{\partial^2}{\partial x^2} + k_x^2 \right) \mathbf{E}_z &= 0. \end{aligned} \quad (5.8)$$

where $k_x^2 = k_o^2 - \beta^2$ is the wave number in the x-direction

Equation (5.8) has a general solution of,

$$E_z(x, z) = e^{-j\beta z} [A \sin(k_x x) + B \cos(k_x x)]. \quad (5.9)$$

where A and B are arbitrary coefficients that can be determined by boundary conditions.

Note that for open-circuit boundary, the boundary conditions are,

$$H_y|_{x=0} = H_y|_{x=d} = 0. \quad (5.10)$$

At $x=0$ will lead to,

$$H_y(x, z) = \left(\frac{-j\omega\epsilon}{k_c^2}\right) e^{-j\beta z} [Ak_x \cos(k_x x) - Bk_x \sin(k_x x)],$$

$$0 = \left(\frac{-j\omega\epsilon}{k_c^2}\right) e^{-j\beta z} [Ak_x \cos(0) - Bk_x \sin(0)], \quad (5.11)$$

or

$$A = 0. \quad (5.12)$$

At $x=d$, and using Equation (5.12) will lead to

$$H_y(x, z) = \left(\frac{-j\omega\epsilon}{k_c^2}\right) e^{-j\beta z} [-Bk_x \sin k_x d] = 0, \quad (5.13)$$

Equation (5.13) is zero when $\sin(k_x d) = 0$, which is satisfied when,

$$k_x = \frac{n\pi}{d}. \quad (5.14)$$

where k_x is known as the transversal wavenumber.

Consequently, the H_y component of the parallel plate waveguide is defined as,

$$H_y(x, z) = H_{y0} e^{-j\beta z} \sin(k_x x). \quad (5.15)$$

Then from Equation (5.9), the E_z component is expressed as

$$E_z(x, z) = E_{z0} e^{-j\beta z} \cos(k_x x). \quad (5.16)$$

And the remaining field component E_x is obtained from Maxwell's equation,

$$E_x(x, z) = \left(\frac{-j\beta}{k_c^2}\right) \frac{\partial E_z}{\partial x} = E_{x0} e^{-j\beta z} \sin(k_x x), \quad (5.17)$$

Note that where H_{y0} , E_{z0} and E_{x0} are the fields amplitudes. From Equation (5.8) the dispersion relation is expressed as

$$k_x^2 + \beta^2 = \omega^2 \mu \epsilon. \quad (5.18)$$

from which the propagation constant in the z-direction is calculated as

$$\beta = \sqrt{\omega^2 \mu \epsilon - \left(\frac{n\pi}{d}\right)^2}. \quad (5.19)$$

For $n=0$,

$$\beta|_{n=0} = k_o = \omega \sqrt{\mu \epsilon}. \quad (5.20)$$

In order to have propagation along z-direction the condition $\beta > 0$ needs to be satisfied. This condition means that minimum frequency above which the propagation is possible [45],

$$f_c = \frac{n}{2d\sqrt{\mu \epsilon}}. \quad (5.21)$$

where f_c is the cutoff frequency. Thus the propagation in the parallel plate metal waveguide is analogous to a high-pass filter response.

The guide wavelength is the distance between planes of constant phase along the z-direction, and it is larger than the wavelength of a plane wave in the material and is given by [45]

$$\lambda_g = \frac{2\pi}{\beta} = \frac{2\pi}{\sqrt{\omega^2 \mu \epsilon - \left(\frac{n\pi}{d}\right)^2}}. \quad (5.22)$$

The waveguide characteristic impedance is given by [45],

$$Z_{TM} = \frac{E_x}{H_y} = \frac{\beta}{\omega \epsilon}. \quad (5.23)$$

The guide impedance is purely real for $f > f_c$.

The derivation for TE polarisation is similar to the TM polarisation but the wave equation is for the E_z component of the electric field.

5.4 Problem description

In this section the canonical geometry used to assess the dispersion characteristics is presented. Field propagation is simulated within a notionally homogenous free space rectangular region of length $L=100\text{m}$ and width $d=10\text{m}$ with open-circuited boundaries being placed on the top and bottom as shown in Figure 5.2. The electric field is polarised out of the plane. This configuration is chosen as it theoretically supports propagation of a dispersionless transversally uniform field along its axis which acts as a convenient reference. Both the input and output planes are terminated with the wave impedance of free space, $Z_o = \sqrt{\mu_o/\epsilon_o}$ where μ_o is magnetic permeability and ϵ_o is dielectric permittivity of the free space which theoretically impedance-match the fundamental propagating field. The structure also supports infinity of higher order waveguide modes (Equation (5.14)) each of which has a transverse (i.e. with respect to x) field distribution that is orthogonal to that of all the others. Note that each of these higher order modes can be represented as interfering waves propagating a particular angle to axis. Theoretically, there should be no inter-mode coupling between these modes along the length of the uniform cross-section structure. However, the irregular nature of an unstructured mesh will actually cause non-physical coupling to occur, analogous to propagation through a medium with small-scale variations in its material parameters. A quantification of this mesh induced coupling provides a physically meaningful measure of the consequences of local mesh irregularities.

The bulk of the problem will be meshed by many different meshes and statistically processed results presented. In order to ensure consistent reference ports for the measurements, the input and output planes are always meshed with the same number of, N , equilateral triangles as shown in Figure 5.2.

The remainder of the problem space is meshed with a Delaunay mesh, the density of which is controlled by the number of fixed vertices at the input and output planes and by demanding a required triangle quality of the mesh generation software which leads to the insertion of additional vertices. Meshes are studied based on size and quality, and this can be obtained by sitting varieties of constraints on the command line to the

‘Triangle’ software in order to get a wide span of triangle size and quality. As mentioned in Section 3.5.1, two main switches are used in the ‘Triangle’ command line; ‘-a’ switch which is concerned with mesh size limitation, and ‘-q’ switch which relates to the mesh quality. For a mesh of certain average area (fixed ‘-a’ switch) different mesh quality can be obtained by setting different angle constrains following ‘-q’ switch. Then for a mesh of certain quality (fixed ‘-q’ switch) varieties of mesh sizes from coarse to fine can be obtained by setting upper limit for triangles area following the ‘-a’ switch. Each produced mesh has a unique distribution of triangle size or shape, so for the sake of comparison and classification each mesh is expressed by a average area A_{av} and average quality factor Q , in addition to the standard deviation from the mean value.

To obtain a sequence of different meshes of the same statistical density and quality, the region is pre-seeded with a number of randomly placed vertices before meshing. Bear in mind that changing the number or the location of any of these vertices will produce different distribution of triangles, so it is almost impossible to reproduce the same mesh even by setting the same area and quality constraints.

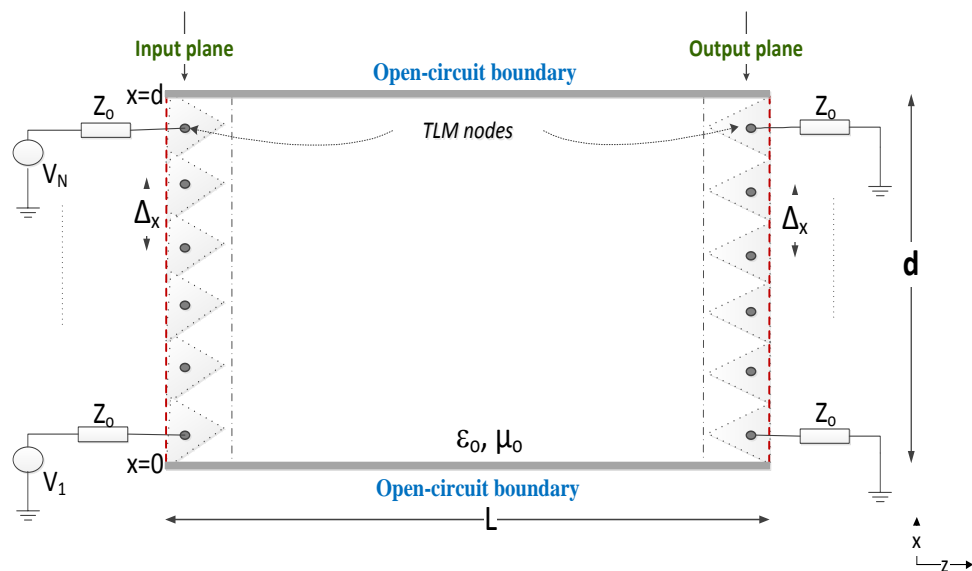


Figure 5.2: Schematic diagram of parallel plate waveguide with the enforced triangularization of the input and output planes

In this study, 2D Delaunay meshes were generated using the ‘Triangle’ mesh generator provided by Shewchuk [6]. The triangulated mesh is then processed to obtain the

Voronoi mesh of transmission lines. Figure 5.3 shows an example of the Delaunay and Voronoi meshes of a rectangular space whilst keeping the input and output planes fixed.

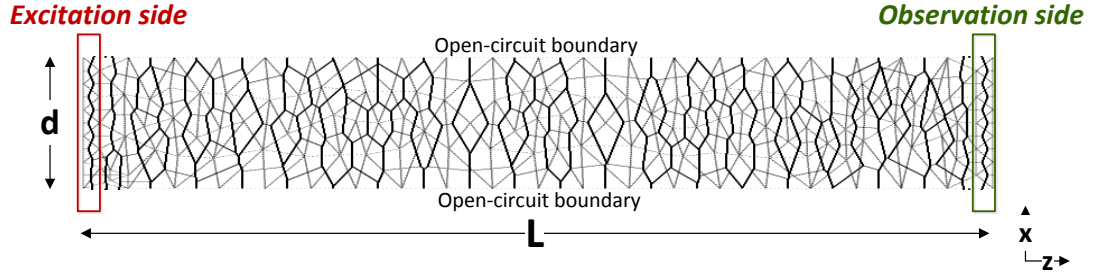


Figure 5.3: Delaunay (light) and Voronoi (dark) diagrams of a meshed rectangular space with fixed points along input and output planes.

In the simulations, the excitation to the model consists of voltage impulses on the N transmission line ports present in the input plane with a spatial distribution of

$$V_i^{in}(x) = V_o \cos\left(k_x \left(i - \frac{1}{2}\right) \Delta_x\right). \quad (5.24)$$

where i is the index of the input port, $i=1,2, \dots,N$, V_o is the input signal amplitude, k_x is the transverse wavenumber given by $k_x=n\pi/d$, and Δ_x is the distance between adjacent samples. Theoretically, after propagating along the structure length L and assuming the appropriate (frequency dependent for $n \neq 0$) source and termination impedances, the field at the output nodes has the form

$$V_i^{out}(x) = V_o \cos\left(k_x \left(i - \frac{1}{2}\right) \Delta_x\right) e^{-j\beta L}. \quad (5.25)$$

where β is the phase constant. In the TLM model the discretisation will introduce numerical dispersion, this is first assessed by extracting the phase delay β which can be obtained using the 2D discrete Fourier transform over time and x of the voltages at all UTLM nodes in the input and output planes, which for the simplest case of $n=0$, reduces to evaluating

$$e^{-j\beta L} = \lim_{\Delta_x \rightarrow 0} \frac{\sum_{i=0}^N V_i^{out}(k_x i \Delta_x, f)}{\sum_{i=0}^N V_i^{in}(k_x i \Delta_x, f)}. \quad (5.26)$$

where $V_i(k_x i \Delta_x, f)$ denotes Fourier transformed voltage at the input or output plane, i.e.,

$$V_i(k_x i \Delta_x, f) = \frac{1}{T} \sum_{m=0}^T V(k_x i \Delta_x, m \Delta_t) e^{-j2\pi \frac{f \cdot m \Delta_t}{T}}. \quad (5.27)$$

where Δ_t is the TLM time step and $T = m \Delta_t$ denotes the total simulation time.

More generally, the same approach is used to evaluate the non-physical inter-modal coupling between different spatial modes. A particular mode of transverse order n is launched into the waveguide and the coupling to each mode of order m will be assessed by a 2D Fourier transform,

$$V^{out}(k_x, f) = \frac{1}{T \cdot N} \sum_{m=0}^T \sum_{x=0}^N V^{out}(i \Delta_x, m \Delta_t) e^{-j2\pi \left(\frac{k_x \cdot i \Delta_x}{N} + \frac{f \cdot m \Delta_t}{T} \right)}. \quad (5.28)$$

The 2D FFT will exhibit peaks at values of all modes that are present in the simulation.

5.5 Study of plane wave dispersion

In this section, dispersion introduced by a triangular mesh is analysed and compared with the case where the same problem is meshed using the structured mesh.

It is well known that the ideal transmission line theory ensures the pulse shape preservation and only introduces a phase delay during propagation. In the TLM model the discretisation will introduce numerical dispersion. The estimation of dispersion is done for a case of plane wave excitation ($n=0$) for which case the phase delay is recovered at the output of the waveguide. This can be evaluated by extracting the phase delay β which can be done by first Fourier transforming voltages at all TLM nodes at the input and output planes, and then summing them and obtaining a ratio as in Equation (5.26). The analysis is done for unstructured meshes of different densities and compared against results obtained using structured meshes.

As triangular meshes have different triangle sizes, a mesh parameter is defined as $\sqrt{A_{av}}$ (m) to quantify the mesh, where A_{av} (m^2) denotes the average triangle area in the mesh. The mesh is also quantified by the mesh quality factor Q expressed in Equation (5.1) where the mean mesh quality factor is calculated for the entire mesh domain.

In the case of the structured mesh all mesh cells are of the same size and have constant area of $A=\Delta x \times \Delta z$ where Δz is the sampling width along the waveguide length.

A polygon is fed to the ‘‘Triangle’’ software that comprises the definition of the rectangular space in addition to random points inserted within the rectangle. The meshes produced are controlled by the ‘-a’ and ‘-q’ switches for mesh size and mesh quality, respectively. The rectangular space is meshed into 200 meshes of mesh parameter that ranges between 0.01 to 0.99m and with mesh quality that ranges from 0.8 to 2.3. The same space is also meshed into 10 different structured meshes that vary in size with mesh parameter that ranges from 0.1 to 1m. Keep in mind that structured meshes is formed of equilateral right-angled triangles so the mesh quality is the same for all meshes.

Table 5.1 illustrates a sample of meshes and the corresponding values following the switches ‘-a’ and ‘-q’. Note that the number assigned to the mesh parameter, mesh size and the values assigned to the ‘-q’ switch are all mean values, meaning that it rarely happened that two meshes have the exact same values, thus, meshes that falls in the same range are but into same category. The number assigned to the ‘-a switch sets an upper limit for the triangle area.

Mode $n=0$ is excited where a plane wave is discretized among N input aligned and equidistant circumcentres (left side of Figure 5.2). A constant value of 10V is inserted at each input point for duration of 1ns. At the other end of the waveguide N aligned and equidistant circumcentres forms the observation plane.

For the purpose of presenting results a ratio between the extracted phase delay β to free space wavenumber $k_o = \frac{\omega}{c}$ is calculated. In this study the phase delay β is extracted at $k_o=2$, which corresponds to the upper limit of the first 10% of the frequency spectrum obtained with FFT. Each mesh is presented by a single value of β ,

then the ratio β/k_o is calculated for each mesh. The free space wavenumber k_o corresponds to minimum wavelength $\lambda_o=3.14159\text{m}$.

Table 5.1: Sample of meshes used in the dispersion study with different mesh parameter $\sqrt{A_{av}}$ and mesh quality Q and the corresponding switches used to produce these meshes

Mesh parameter	switch	Mesh quality	switch
$\sqrt{A_{av}} \approx$	a =	Q \approx	q \approx
0.01026	0.0005	2.28	18
0.02268	0.001	2.17	20
0.05479	0.005	1.97	25
0.07277	0.007	1.83	27
0.09743	0.01	1.65	38
0.12615	0.03	1.47	44
0.15452	0.05	1.3	46
0.24859	0.1	1.16	51
0.58006	0.5	0.97	54
0.73231	0.8	0.81	60

Figure 5.4 shows the phase ratio β/k_o as function of mesh parameter $\sqrt{A_{av}}$ for selected mesh quality factor Q. For the lowest mesh quality factor Q of 0.8121 and the smallest mesh parameter $\sqrt{A_{av}} \cong 0.01\text{m}$, the mean value and standard deviation of the ratio β/k_o are 1.000789 and 0.000651, respectively which increase to 1.009846 and 0.002921 for the highest Q value of 2.28049 and the same mesh parameter. On the other hand increasing the mesh parameter $\sqrt{A_{av}}$ from 0.01m to 0.99m increased the phase ratio from 1.000789 to 1.008975 for $Q \approx 0.81219$ and from 1.009846 to 1.034653 for $Q \approx 2.28049$.

Table 5.2 shows the mean ratio β/k_o as a function of selected mesh parameters $\sqrt{A_{av}}$ for different mesh quality factor Q, as well as the standard deviation of the phase ratio.

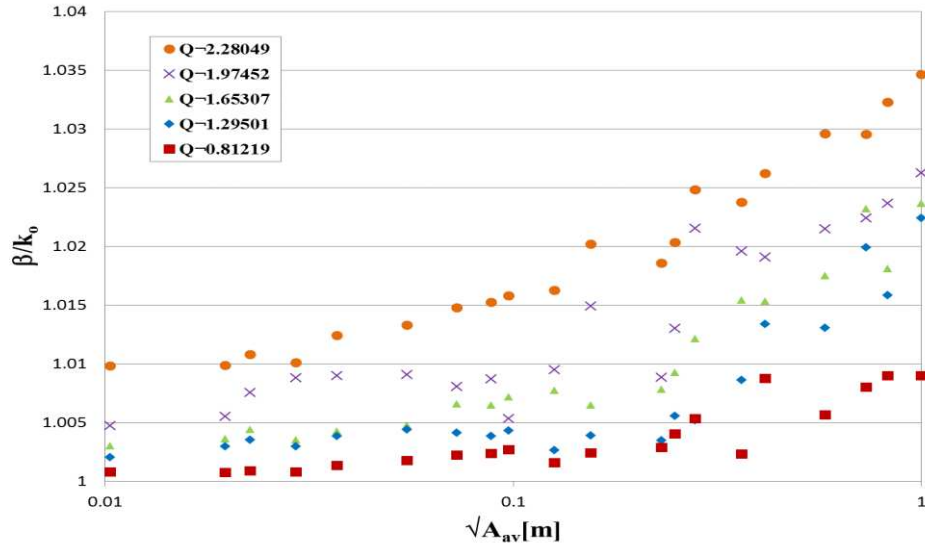


Figure 5.4: Ratio of the model phase to the free space wavenumber as a function of discretization length $\sqrt{A_{av}}$ (m) for different quality UTLM meshes ($Q \approx 0.8, 1.3, 1.7, 2.0$ and 2.3).

Table 5.2: Ratio of the model phase to the free space wavenumber β/k_0 as a function of mesh parameter $\sqrt{A_{av}}$ (m) for different mesh quality Q

$\sqrt{A_{av}}$		0.01026	0.02268	0.05479	0.07277	0.09743	0.12615	0.24859	0.58006	0.99930
Q		β/k_0								
0.81219	mean	1.00079	1.00088	1.00176	1.00225	1.00268	1.00160	1.00402	1.00566	1.00897
	StdDev	0.00065	0.00070	0.00059	0.00057	0.00063	0.00127	0.00122	0.00132	0.00019
0.97434	mean	1.00125	1.00152	1.00218	1.00229	1.00319	1.00360	1.00654	1.00885	1.01384
	StdDev	0.00063	0.00060	0.00063	0.00063	0.00064	0.00064	0.00064	0.00067	0.00260
1.156130	mean	1.00189	1.00151	1.00213	1.00220	1.00400	1.00388	1.00750	1.01038	1.01397
	StdDev	0.00054	0.00111	0.00136	0.00118	0.00129	0.00056	0.00058	0.00052	0.00095
1.29501	mean	1.00207	1.00354	1.00443	1.00414	1.00431	1.00265	1.00559	1.01309	1.02243
	StdDev	0.00094	0.00088	0.00120	0.00093	0.00083	0.00099	0.00098	0.00094	0.00172
1.46592	mean	1.00209	1.00501	1.00460	1.00466	1.00435	1.00568	1.00920	1.01600	1.02028
	StdDev	0.00133	0.00127	0.00168	0.00292	0.00293	0.00279	0.00246	0.00212	0.00218
1.65307	mean	1.00302	1.00442	1.00477	1.00659	1.00721	1.00773	1.00929	1.01750	1.02365
	StdDev	0.00193	0.00162	0.00368	0.00235	0.00426	0.00273	0.00462	0.00476	0.00173
1.84590	mean	1.00459	1.00450	1.00675	1.00704	1.00751	1.00762	1.01072	1.02109	1.02592
	StdDev	0.00237	0.00271	0.00206	0.00227	0.00231	0.00261	0.00335	0.00309	0.00381
1.97452	mean	1.00474	1.00758	1.00857	1.00768	1.00509	1.00948	1.01302	1.02108	1.02524
	StdDev	0.00294	0.00376	0.00285	0.00376	0.00221	0.00466	0.00637	0.00460	0.00156
2.17112	mean	1.00665	1.00901	1.01113	1.01272	1.01039	1.01491	1.01568	1.02478	1.02840
	StdDev	0.00253	0.00340	0.00691	0.00450	0.00446	0.00648	0.00479	0.00426	0.00343
2.28049	mean	1.00985	1.01080	1.01329	1.01480	1.01578	1.01626	1.02036	1.02960	1.03465
	StdDev	0.00292	0.00315	0.00464	0.00256	0.00548	0.00518	0.00430	0.00589	0.00477

Enforcing random points inside the problems domain produces different mesh distribution of the same mesh quality range. The variance in phase ratio due to different mesh distribution is illustrated by the vertical bars in Figure 5.5 to Figure 5.14. These figures show the ratio β/k_o as a function of the mesh parameter $\sqrt{A_{av}}$ for mesh quality Q ranging between 0.81219 and 2.28049. Generally, as the mesh parameter $\sqrt{A_{av}}$ decreases the ratio β/k_o approaches the value 1, which means that the model phase approaches the free space wavenumber. This is applicable for all values of mesh quality Q . As the value of mesh quality Q increases, the ratio β/k_o goes further away from the value 1. As mentioned previously, triangles with good quality are equilateral ones which have a Q value of 0.57735, so increasing the Q value means having triangles of bad quality which consequently increases the dispersion error. Also, for lower Q values the mesh is more uniform and shows small variance for different mesh distribution as shown by the vertical bars in Figure 5.5 through Figure 5.8. For higher values of Q the variance in the phase ratio is large as in Figure 5.9 through Figure 5.14.

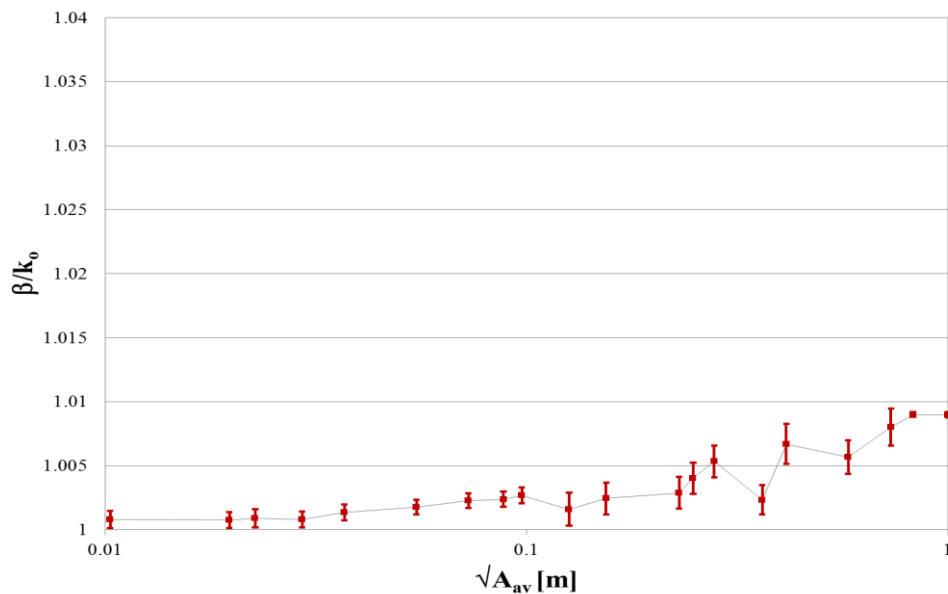


Figure 5.5: Ratio of the model phase to the free space wavenumber as a function of mesh parameter $\sqrt{A_{av}}$ (m) for mesh quality $Q \approx 0.81219$, with vertical bars depicting the variance in the phase ratio for different mesh distributions.

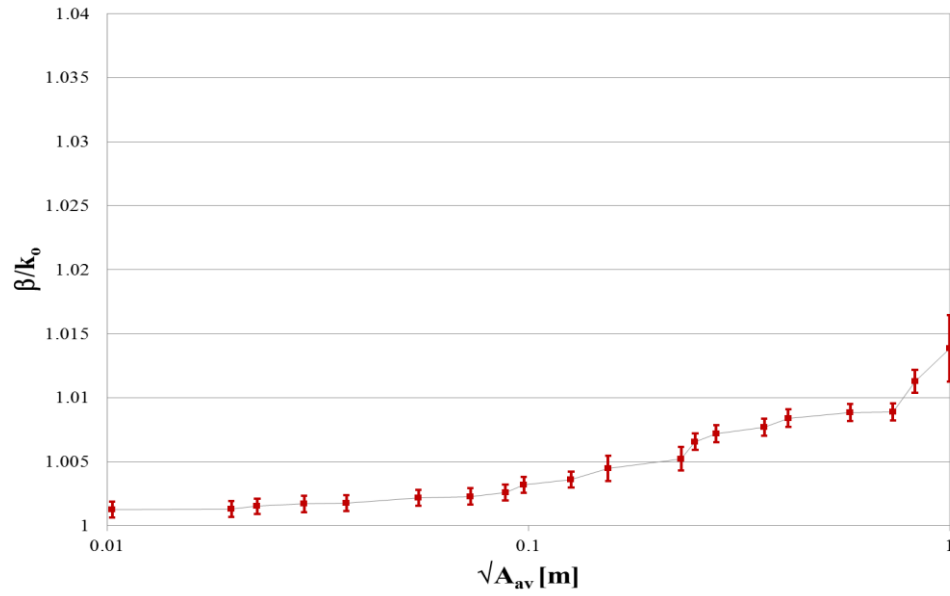


Figure 5.6: Ratio of the model phase to the free space wavenumber as a function of mesh parameter $\sqrt{A_{av}}$ (m) for mesh quality $Q \approx 0.97434$., with vertical bars depicting the variance in the phase ratio for different mesh distributions.

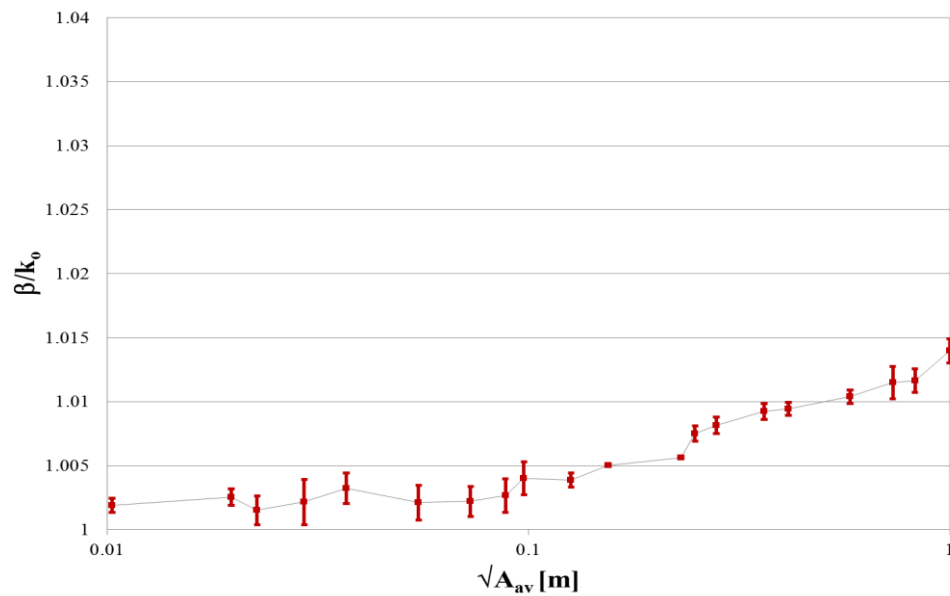


Figure 5.7: Ratio of the model phase to the free space wavenumber as a function of mesh parameter $\sqrt{A_{av}}$ (m) for mesh quality $Q \approx 1.15613$., with vertical bars depicting the variance in the phase ratio for different mesh distributions.

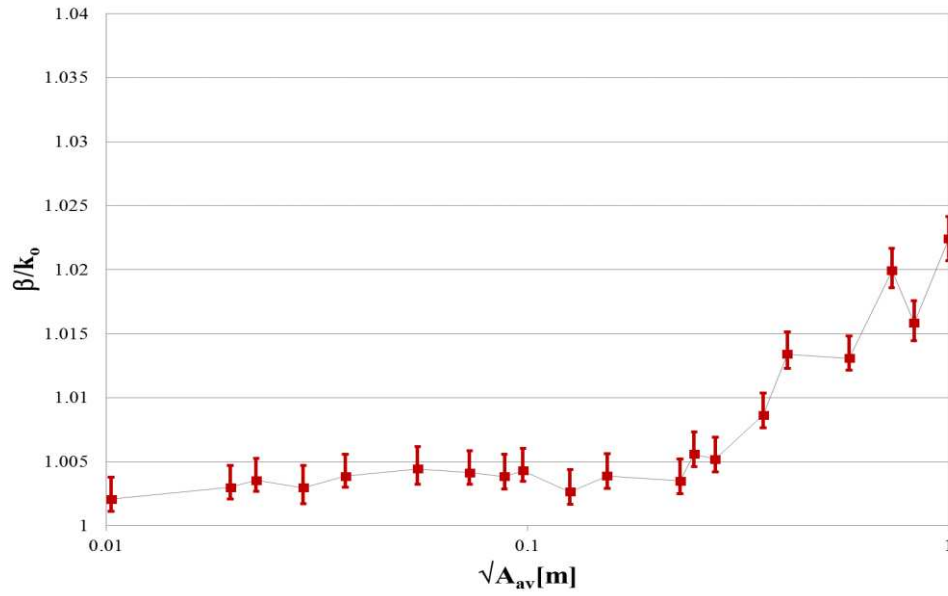


Figure 5.8: Ratio of the model phase to the free space wavenumber as a function of mesh parameter $\sqrt{A_{av}}$ (m) for mesh quality $Q \approx 1.29501$, with vertical bars depicting the variance in the phase ratio for different mesh distributions.

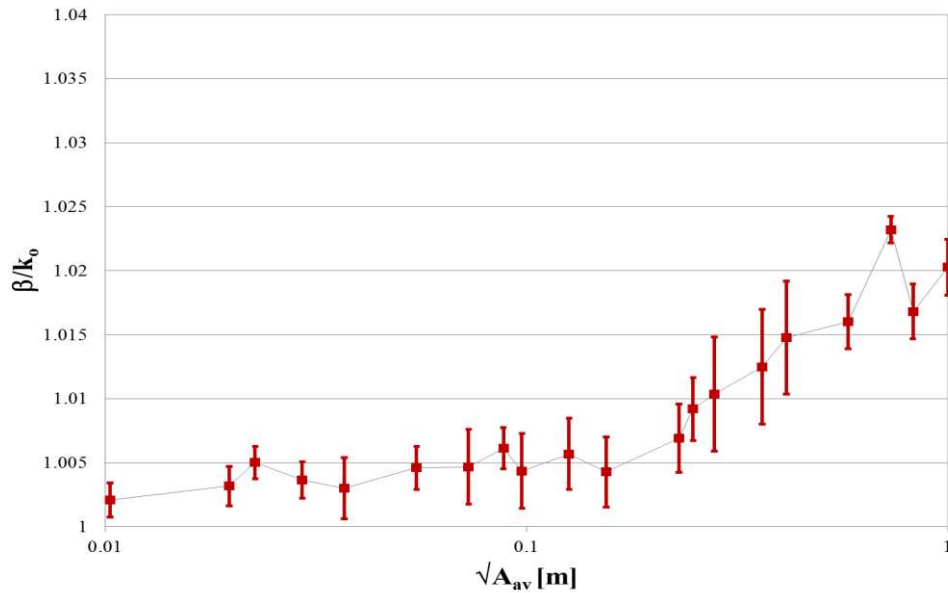


Figure 5.9: Ratio of the model phase to the free space wavenumber as a function of mesh parameter $\sqrt{A_{av}}$ (m) for mesh quality $Q \approx 1.46952$, with vertical bars depicting the variance in the phase ratio for different mesh distributions.

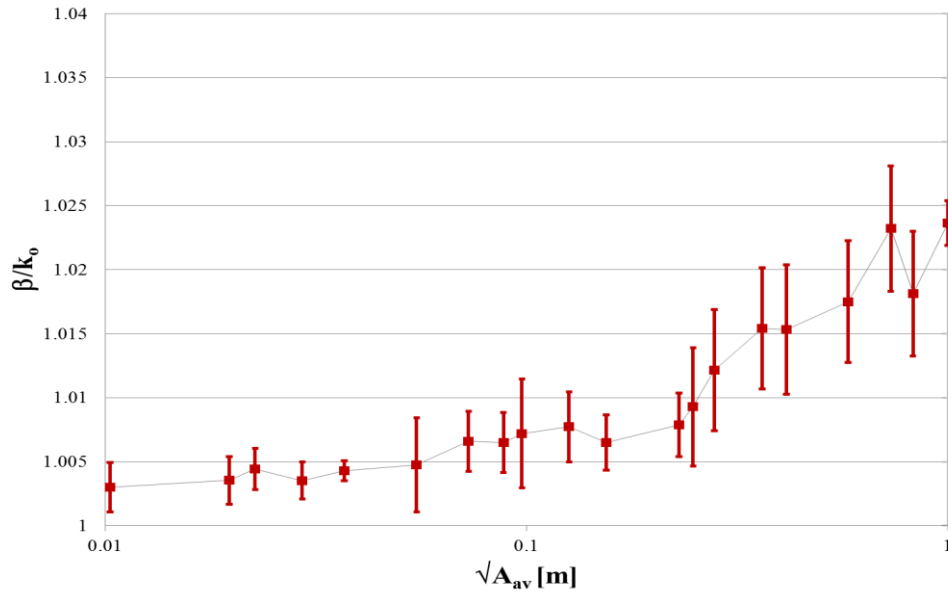


Figure 5.10: Ratio of the model phase to the free space wavenumber as a function of mesh parameter $\sqrt{A_{av}}$ (m) for mesh quality $Q \approx 1.65307$, with vertical bars depicting the variance in the phase ratio for different mesh distributions.

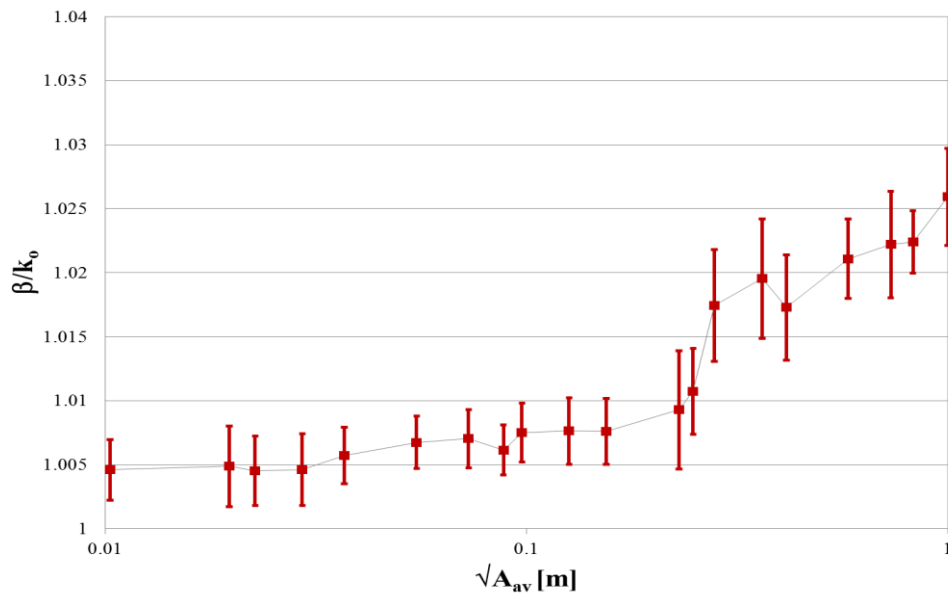


Figure 5.11: Ratio of the model phase to the free space wavenumber as a function of mesh parameter $\sqrt{A_{av}}$ (m) for mesh quality $Q \approx 1.82591$, with vertical bars depicting the variance in the phase ratio for different mesh distributions.

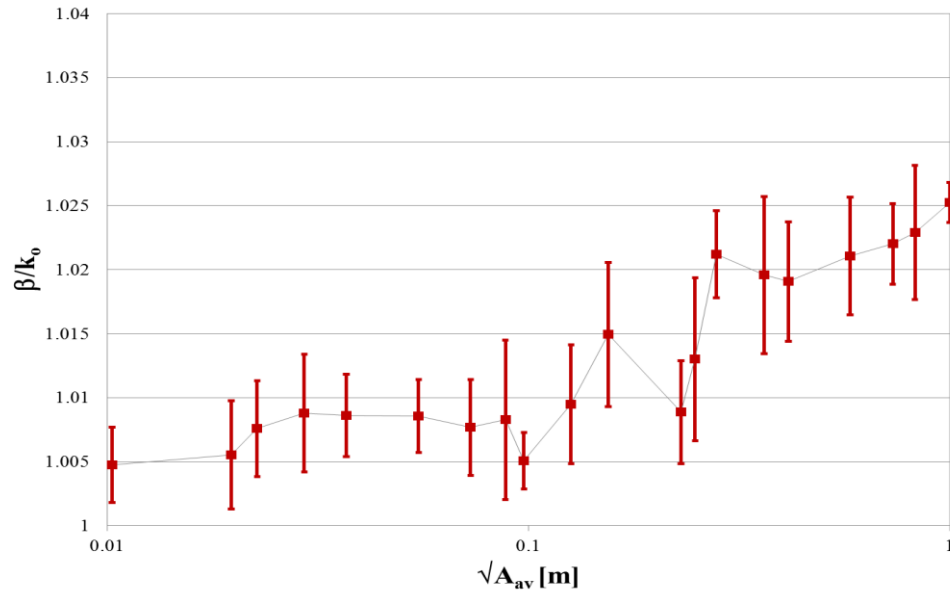


Figure 5.12: Ratio of the model phase to the free space wavenumber as a function of mesh parameter $\sqrt{A_{av}}$ (m) for mesh quality $Q \approx 1.97452$, with vertical bars depicting the variance in the phase ratio for different mesh distributions.

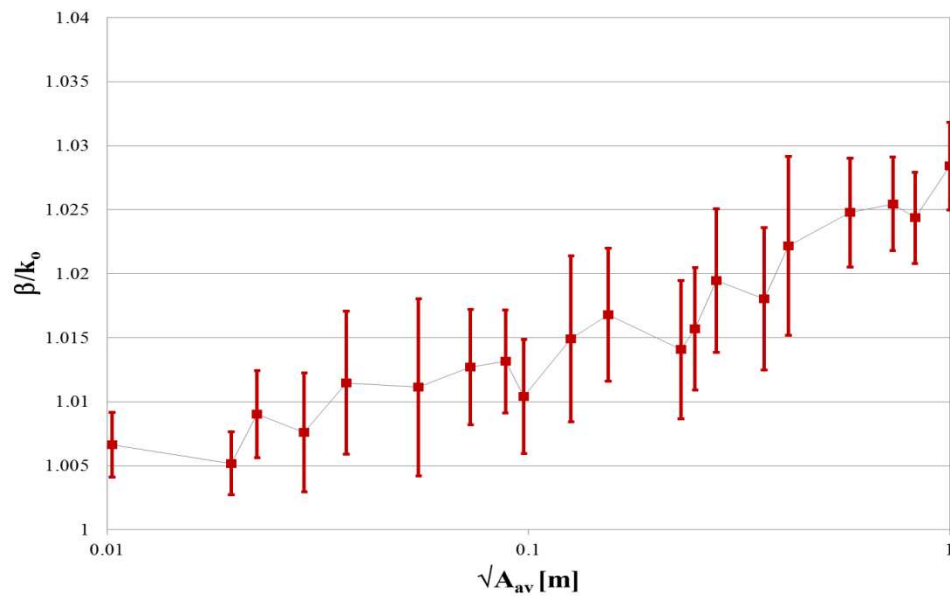


Figure 5.13: Ratio of the model phase to the free space wavenumber as a function of mesh parameter $\sqrt{A_{av}}$ (m) for mesh quality $Q \approx 2.17112$, with vertical bars depicting the variance in the phase ratio for different mesh distributions.

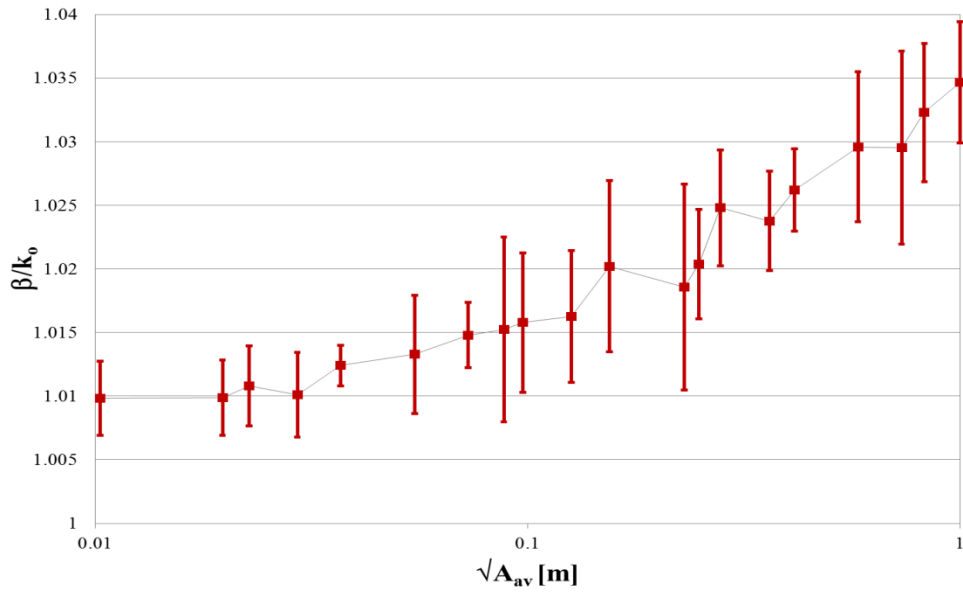


Figure 5.14: Ratio of the model phase to the free space wavenumber as a function of mesh parameter $\sqrt{A_{av}}$ (m) for mesh quality $Q \approx 2.28049$, with vertical bars depicting the variance in the phase ratio for different mesh distributions.

In order to better compare the dispersion errors of the unstructured TLM and the structured TLM meshes, Figure 5.15 shows the relative error in β for unstructured and structured meshes defined as,

$$Relative\ Error = \frac{|\beta - k_o|}{k_o} [\%]. \quad (5.29)$$

In Figure 5.15 percentage relative phase error is calculated for UTLM as a function of mesh parameter $\sqrt{A_{av}}$ for different mesh quality factor Q . In the same figure the relative phase error is calculated for structured TLM for different discretization lengths. Again, as the quality of the mesh increases or the discretization length decreases the phase relative error drops significantly. It is also noted that the mean dispersion error introduced by the unstructured TLM of different quality values is less than the error introduced by the structured TLM.

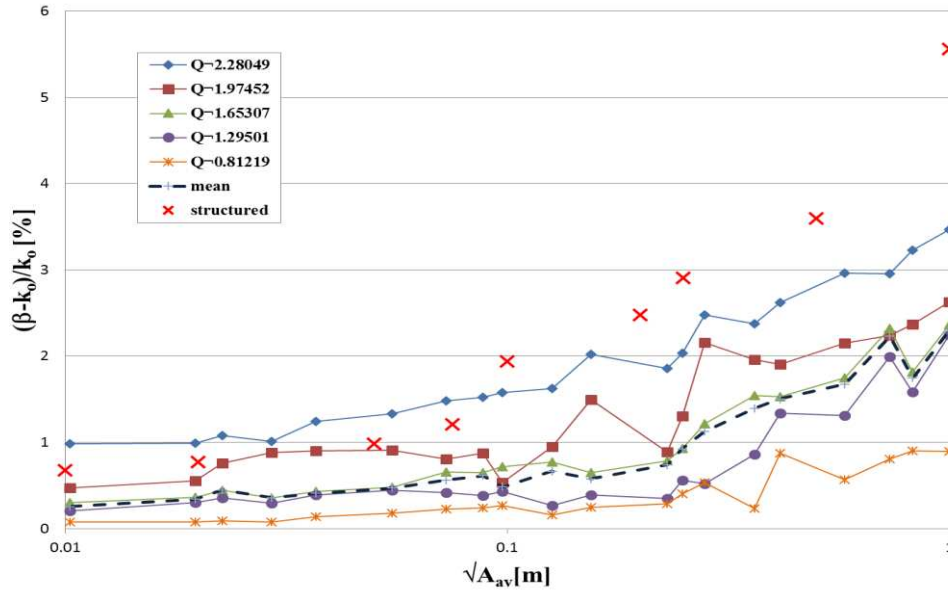


Figure 5.15: Percentage relative phase error as a function of discretization length $\sqrt{A_{av}}$ (m) for different quality UTLM meshes ($Q \approx 0.8, 1.3, 1.7, 2.0$ and 2.3) and an equivalent structured TLM mesh. The dashed line shows the mean dispersion error obtained from different quality unstructured meshes.

Table 5.3 lists the percentage phase relative error for unstructured meshes as function of selected mesh parameter $\sqrt{A_{av}}$ for selected mesh quality values Q . In the same table the percentage phase relative error for the corresponding structured mesh is displayed. For all discretization lengths, the unstructured mesh shows significant low relative phase error as compared to the equivalent structured mesh.

Figure 5.16 shows the phase ratio β/k_o as a function of mesh quality factor Q for selected mesh parameter $\sqrt{A_{av}}$, namely, 0.01, 0.1, 0.25 and 0.99m. It is shown that for fixed mesh parameter the phase ratio increases as the mesh quality Q increases. Also, as the mesh parameter $\sqrt{A_{av}}$ increases the phase ratio increases which confirms that the mesh quality affects the mesh dispersion.

Figure 5.17 shows the ratio of the TLM wave velocity, $v = \omega/\beta$ to the free space velocity, $c = 1/\sqrt{\epsilon_o\mu_o}$. In the ideal case the ratio is one, as shown in Figure 5.17 by the grey line. In all cases the dispersion error reduces as the average unit cell area reduces. Furthermore, the unstructured mesh generally has a lower dispersion error than the equivalent structured mesh.

Table 5.3: Percentage phase relative error $|\beta - k_o|/k_o$ as a function in selected $\sqrt{A_{av}}$ (m) for selected values of mesh quality factor Q

Unstructured TLM									
$\sqrt{A_{av}}$	0.01026	0.02268	0.05479	0.07277	0.09743	0.12615	0.24859	0.58006	0.99930
0.81	0.07892	0.08802	0.17627	0.22465	0.26816	0.15989	0.40227	0.56644	0.89747
1.30	0.20726	0.35413	0.44330	0.41380	0.43084	0.26462	0.55922	1.3089	2.24285
1.65	0.30162	0.44251	0.47656	0.65873	0.72073	0.77262	0.92913	1.75030	2.36464
1.97	0.47388	0.75772	0.85748	0.76759	0.50880	0.94840	1.30196	2.10778	2.52448
2.28	0.98461	1.07996	1.32864	1.47964	1.57822	1.62612	2.03556	2.95967	3.46532
mean	0.25532	0.33927	0.46844	0.56242	0.48397	0.73840	1.67531	2.30375	0.25532

Structred TLM									
\sqrt{A}	0.01000	0.02000	0.05000	0.07500	0.10000	0.20000	0.25000	0.50000	1.00000
$ \beta - k_o /k_o$									
%	0.67747	0.77183	0.98539	1.20833	1.93817	2.47827	2.90762	3.59762	5.56112

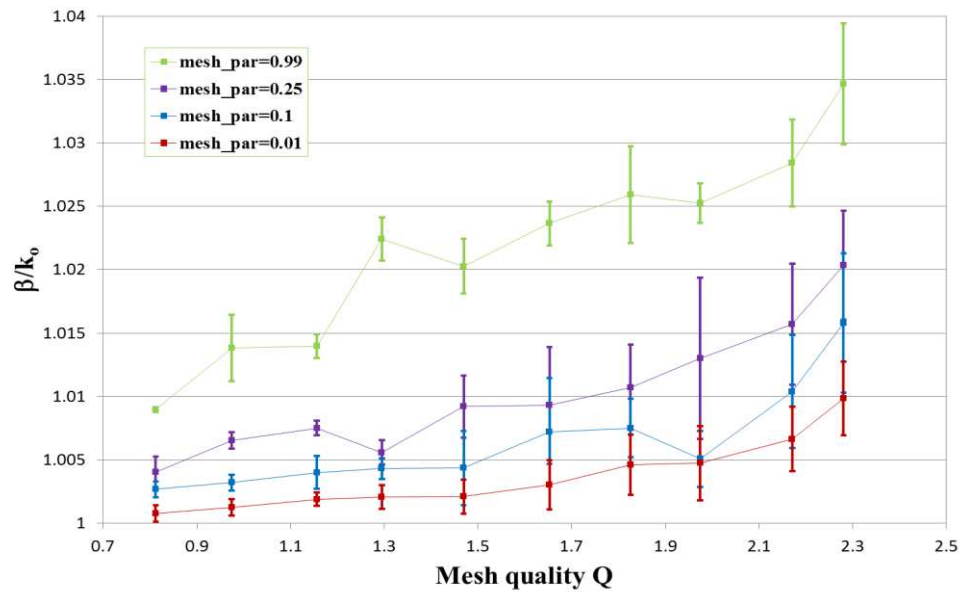


Figure 5.16: Ratio of the model phase to the free space wavenumber as a function of mesh quality Q for different mesh parameter ($\sqrt{A_{av}}=0.01, 0.1, 0.25$ and 0.99m) with vertical bars depicting the variance in the phase ratio for different mesh distributions.

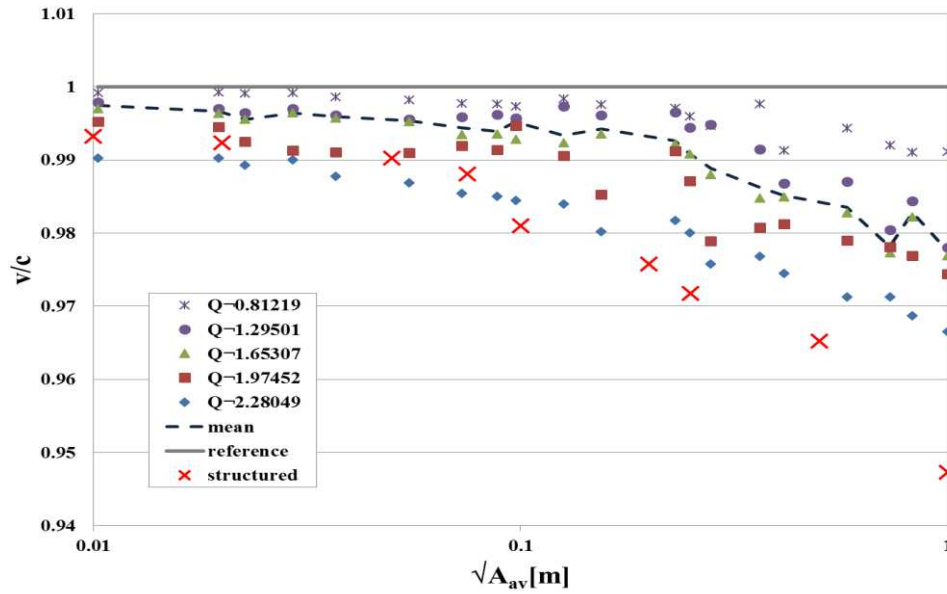


Figure 5.17: Ratio of the model wave velocity to the free space velocity (v/c) as a function of discretization length $\sqrt{A_{av}}$ (m) for different quality UTLM meshes ($Q \approx 0.8, 1.3, 1.7, 2.0$ and 2.3) and an equivalent structured TLM mesh. The dashed line shows the mean dispersion error obtained from different quality unstructured meshes.

Comparing different quality meshes, it can be seen that as the Q -factor reduces, i.e. the quality of the mesh increases, the dispersion is further reduced. This improvement is largest for coarser meshes. In fact, a coarse unstructured mesh with $\sqrt{A_{av}} = 0.99m$ but of good quality $Q \approx 0.8$ has dispersion similar to the finest TLM mesh $\sqrt{A_{av}} = 0.01m$ with $Q \approx 2.29$. It is true to say that such a good quality mesh was possible due to the simple geometry of the problem. However, all meshes with $Q \leq 2$ have also shown lower dispersion error than the equivalent structured TLM mesh. The dashed line in Figure 5.17 shows the mean dispersion error obtained from a number of different quality unstructured meshes further confirming that unstructured mesh has better dispersion properties.

An unstructured mesh is computationally more difficult to handle than a structured one and so comes with a computational runtime overhead. Figure 5.18 shows comparison of the computational run time of UTLM and STLM method having the same numerical mesh density.

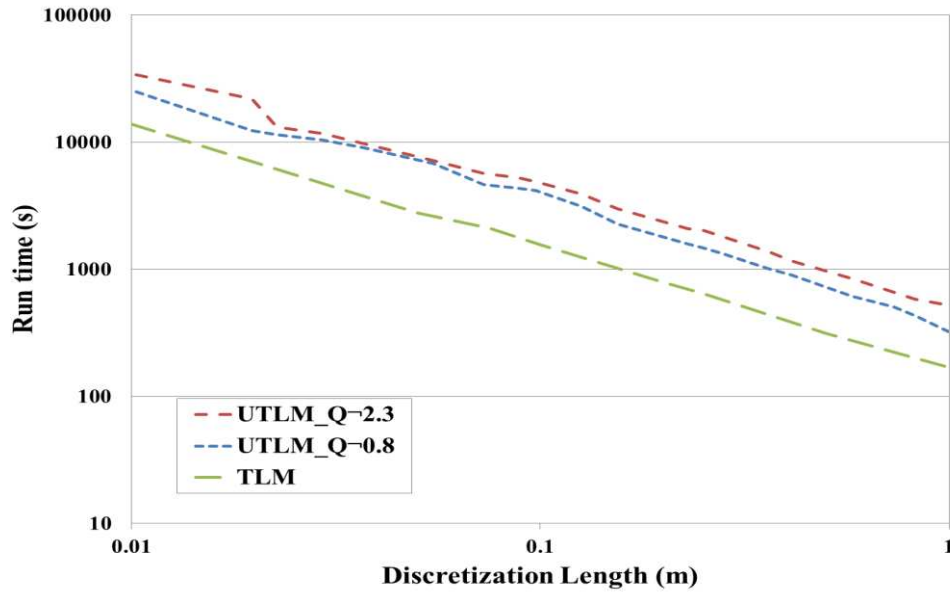


Figure 5.18: Run time for UTLM meshes of $Q \approx 0.8$ and 2.3 and equivalent STLM mesh as a function of discretization length $\sqrt{A_{av}}$.

The runtime of the UTLM mesh with $Q \approx 0.8$ and $Q \approx 2.3$ is compared against the STLM mesh for different discretization lengths $\sqrt{A_{av}}$. It is shown that both UTLM meshes have longer runtime compared to the equivalent STLM mesh. The better quality mesh ($Q \approx 0.8$) has shorter run time compared with the mesh with $Q \approx 2.3$. This can be explained by the fact good quality are more uniform which reduces the possibility of the presence of very short link lines, and consequently very small timestep.

5.6 Study of inter-modal coupling

In this section the effect of the mesh discretisation on the modal coupling between different order spatial modes is investigated on the same model outlined in Section 5.5. The intermodal coupling is investigated for different mesh discretization, mesh quality and for different mesh distributions. The different spatial mode excitations are defined by an index n in Equation (5.14). Theoretically an infinite number of spatial harmonics is supported in this waveguide but in this study excited spatial mode with $n=0, 1$ and 2 are considered, as shown schematically in Figure 5.19. In the case of the structured mesh due to its symmetry no coupling will occur between different spatial modes and at the output only excited mode will exist. However, this is not the case for the

unstructured meshes which is not symmetrical in its nature. The coupling is measured by taking a 2D FFT transform (Equation (5.28)) of the signal at the output nodes which will have peaks at all spatial modes that are in the signal.

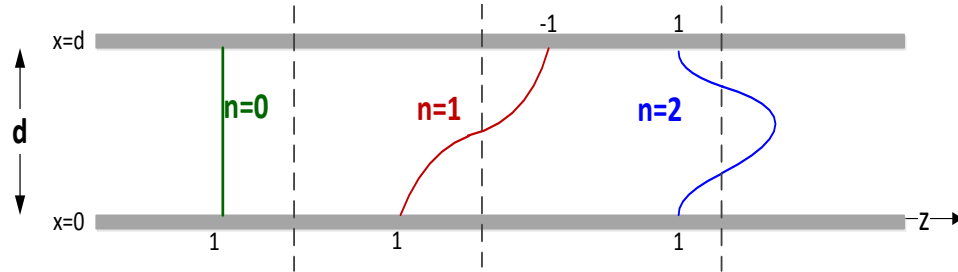


Figure 5.19: Illustrative diagram for different mode excitation in parallel plate waveguide

Figure 5.20 shows an example of a 2D FFT surface plot produced by exciting mode $n=0$ in a parallel plate waveguide of dimensions 10m by 100m. Normalized k_x is better used to illustrate the mode number (i.e. $n=0, 1, 2, 3, \dots$). This plot shows maxima at the spatial modes 0, 2 and 4.

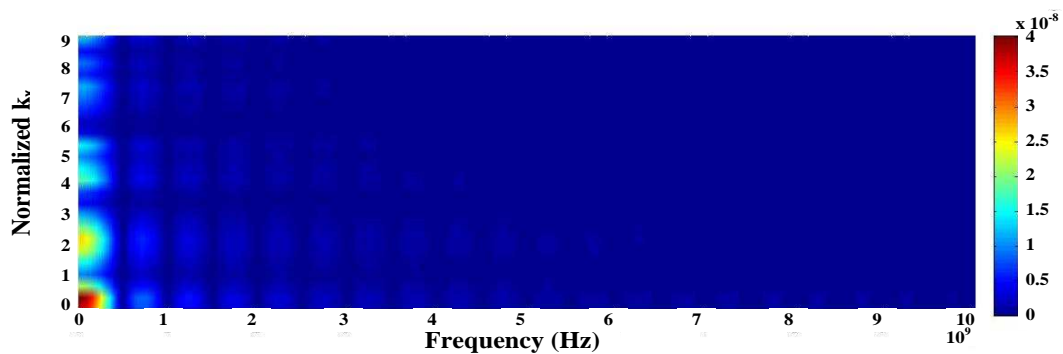


Figure 5.20: Surface plot of 2D FFT analysis of wave propagation in parallel plate waveguide

5.6.1 Mode coupling in structured meshes

In the first instance, the mode coupling is investigated using structured TLM meshes. For the parallel plate waveguide three different cases are examined of which the discretization length Δl is 0.05, 0.1 and 1.

To extract the data of modal coupling 2D data plots as shown in Figure 5.20 is extracted to illustrate the peaks at the spatial modes.

Figure 5.21 and Figure 5.22 show the normalized amplitude of the excited mode $n=0$ and $n=1$, respectively, versus the spatial mode location for the three different meshes. It is shown that maxima occur only at the excited mode, or in other words, there is no coupling with other spatial modes. This is shown for meshes of different discretization length Δl where the mode becomes more precise as the accuracy of mesh increases.

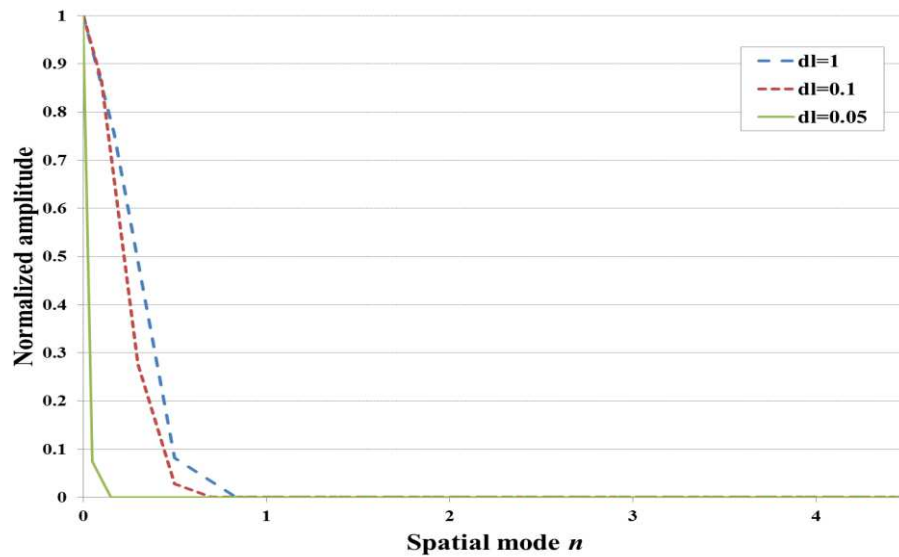


Figure 5.21: Mode coupling of the excited mode $n=0$ to other spatial modes for different discretization length Δl .

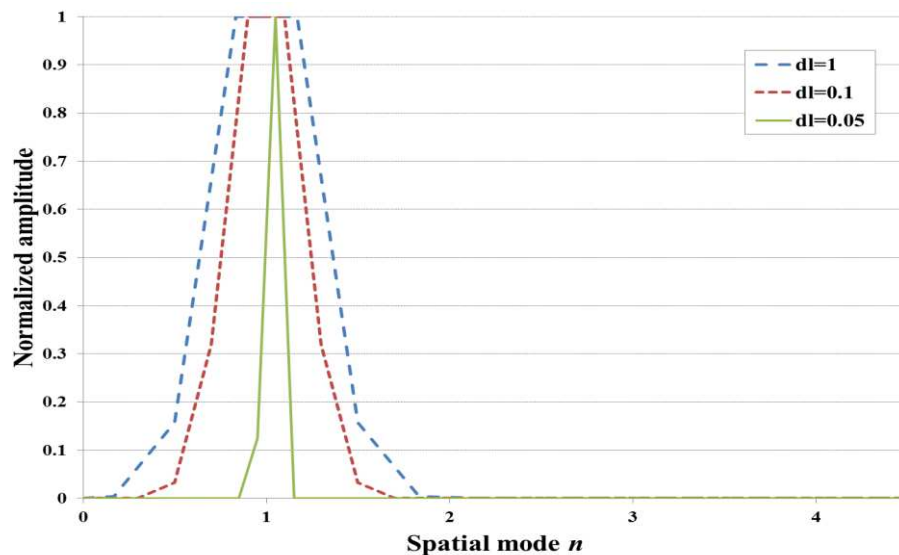


Figure 5.22: Mode coupling of the excited mode $n=1$ to other spatial modes for different discretization length Δl .

For better illustration of the effect of the unstructured mesh size and the mesh quality, the same procedure applied on structured meshes is followed and applied on 1200 different unstructured meshes.

5.6.2 Mode coupling in unstructured meshes

5.6.2.1 Excitation of mode $n=0$

In Figure 5.23 through Figure 5.27, mode $n=0$ is excited and the coupling ratio with higher spatial modes ($n=1-4$) is extracted. The curves show how the coupling ratio changes with different mesh parameters and for five different mesh quality factor Q , namely, 0.812, 1.295, 1.653, 1.974 and 2.280. Exciting mode $n=0$ lead to higher coupling ratio with the symmetrical spatial modes $n=2$ and 4. Also, it can be seen that as the mesh density is increased - expressed by the mesh parameter $\sqrt{A_{av}}$ decrease - the intermodal coupling is decreased. For example, in Figure 5.23 the mean coupling ratio with mode $n=2$ has decreased from 0.148 to 4×10^{-5} for $\sqrt{A_{av}}$ equal to 0.99 and 0.01, respectively, and a mesh quality factor equals to 0.812.

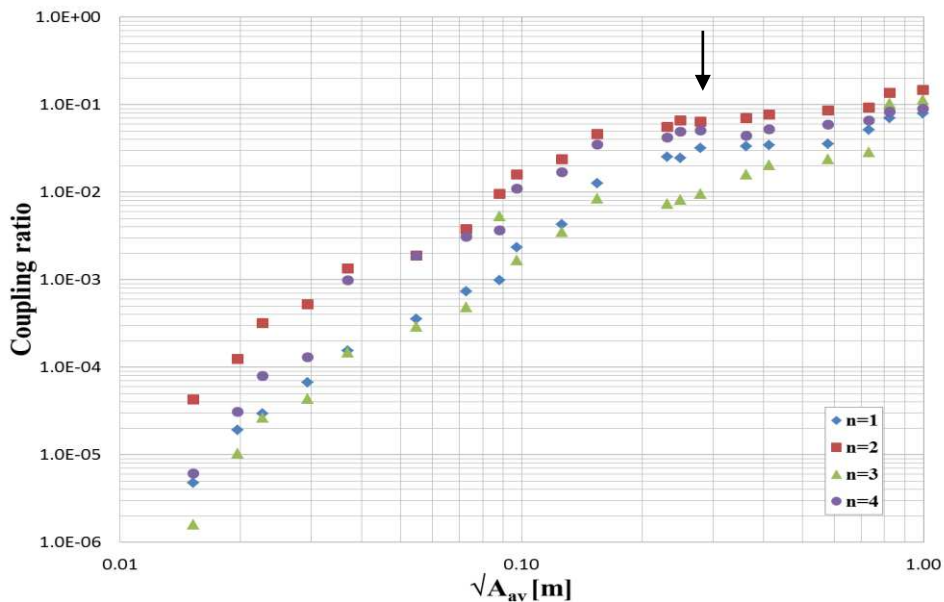


Figure 5.23: Coupling of excited mode $n=0$ to modes $n=1-4$ as a function of the mesh parameter $\sqrt{A_{av}}$ (m) for a mean mesh quality $Q \approx 0.81219$. Arrow points to mesh with

$$\sqrt{A_{av}} / \lambda_0 < 0.1 .$$

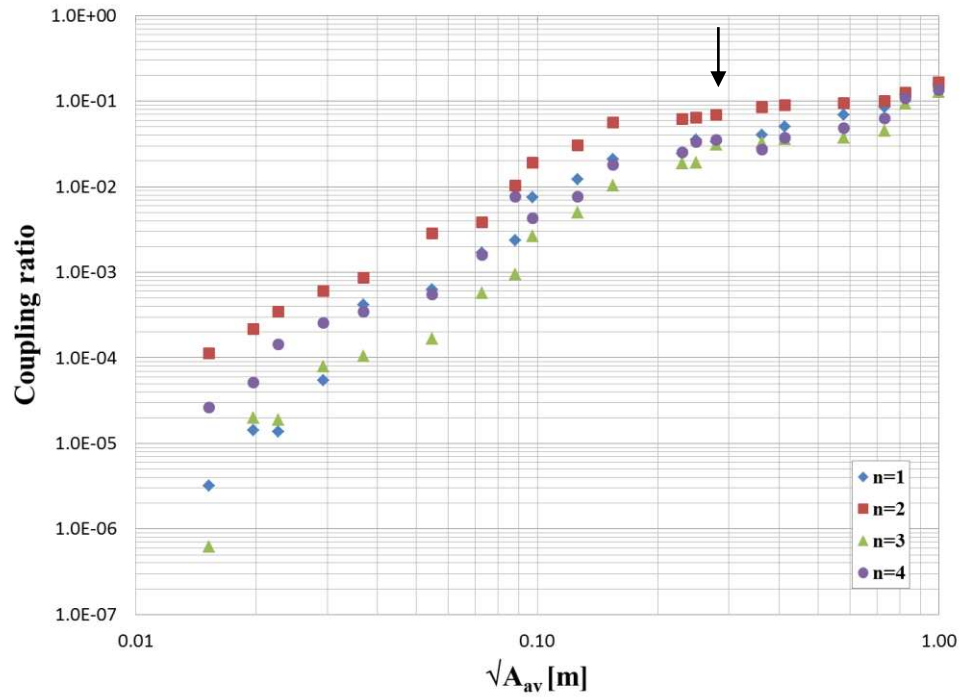


Figure 5.24: Coupling of excited mode $n=0$ to modes $n=1-4$ as a function of the mesh parameter $\sqrt{A_{av}}$ (m) for a mean mesh quality $Q \approx 1.29501$. Arrow points to mesh with

$$\sqrt{A_{av}} / \lambda_0 < 0.1 .$$

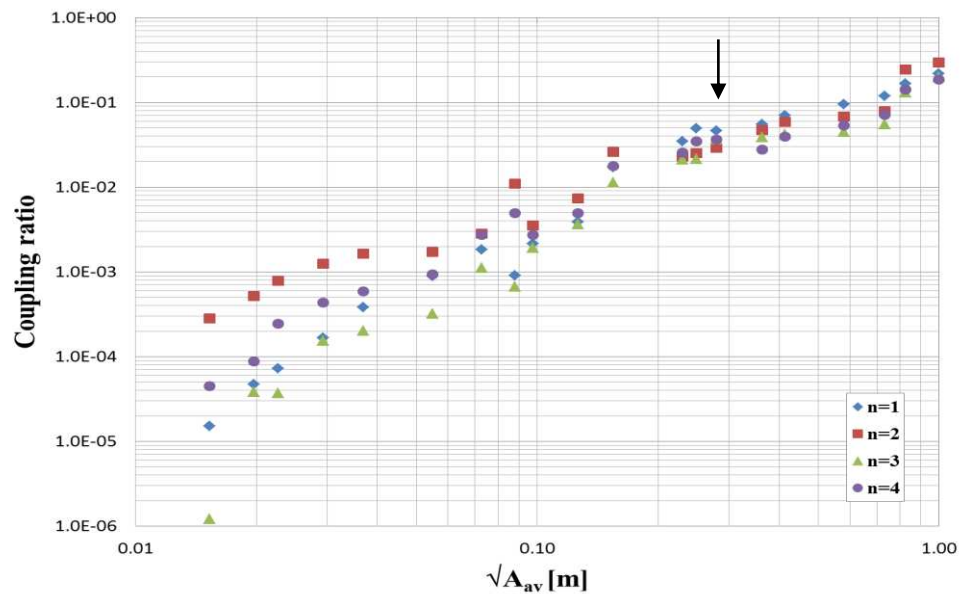


Figure 5.25: Coupling of excited mode $n=0$ to modes $n=1-4$ as a function of the mesh parameter $\sqrt{A_{av}}$ (m) for a mean mesh quality $Q \approx 1.65307$. Arrow points to mesh with

$$\sqrt{A_{av}} / \lambda_0 < 0.1 .$$

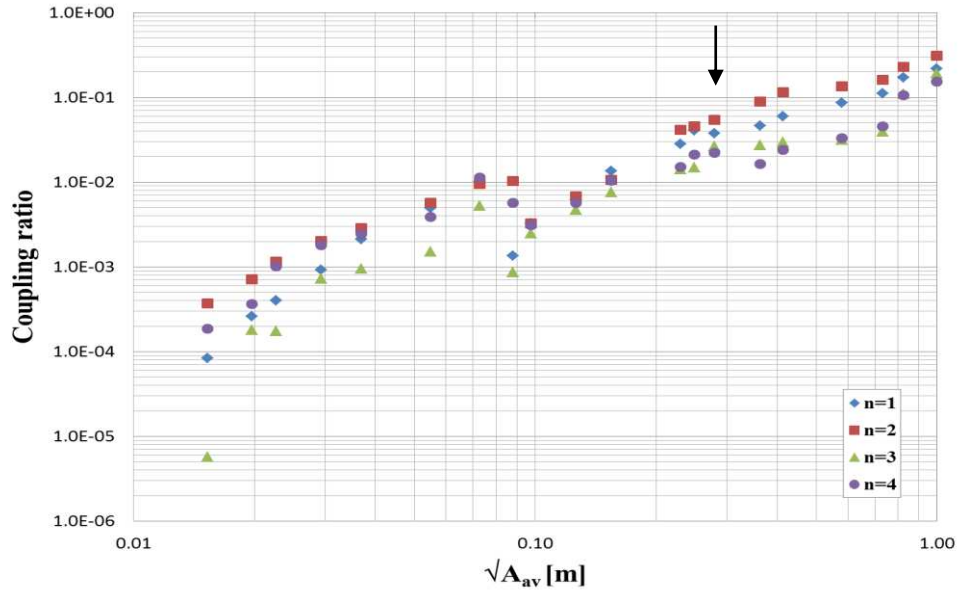


Figure 5.26: Coupling of excited mode $n=0$ to modes $n=1-4$ as a function of the mesh parameter $\sqrt{A_{av}}$ (m) for a mean mesh quality $Q \approx 1.97452$. Arrow points to mesh with $\sqrt{A_{av}} / \lambda_0 < 0.1$.

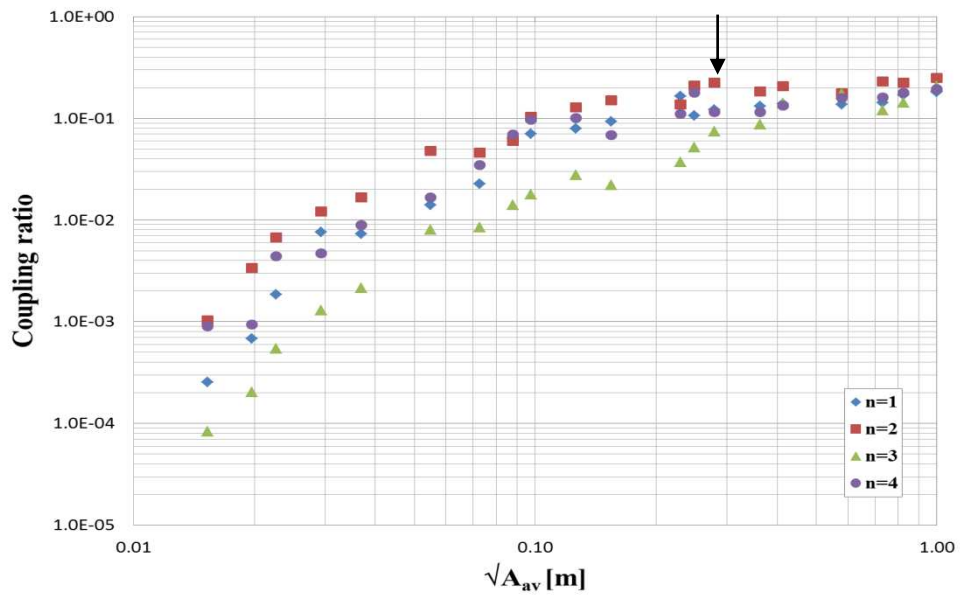


Figure 5.27: Coupling of excited mode $n=0$ to modes $n=1-4$ as a function of the mesh parameter $\sqrt{A_{av}}$ (m) for a mean mesh quality $Q \approx 2.28049$. Arrow points to mesh with $\sqrt{A_{av}} / \lambda_0 < 0.1$.

Note that in Figure 5.23 through Figure 5.27 the coupling ratio starts to decline rapidly at mesh parameter $\sqrt{A_{av}} < 0.36$ (where the black arrow points) for all values of mesh quality. This discretization length (mesh parameter) as compared to the reference wavelength $\Delta l / \lambda_o = \sqrt{A_{av}} / \lambda_o$ is less than 0.12. This means that setting the discretization length to a value less than one tenth the wavelength reduces significantly the coupling ratio of the excited mode to other modes, which agrees with the famous discretization rule of thumb [1].

Figure 5.28 and Figure 5.29 shows the coupling ratio of the excited mode $n=0$ to the spatial mode 1 and 2, respectively. As the value of the quality Q factor increases the coupling ratio increases where the worst coupling ratio is achieved with Q equals to 2.280 as shown in both figures. For example, for fixed $\sqrt{A_{av}}$ of 0.99 the mean coupling ratio with mode $n=2$ has increased from 0.148 to 0.21 for Q equals to 0.812 and 2.280, respectively. Also, for $\sqrt{A_{av}}$ of 0.01 the coupling ratio increased from 4×10^{-5} to 0.001 and Q equals to 0.812 and 2.280, respectively.

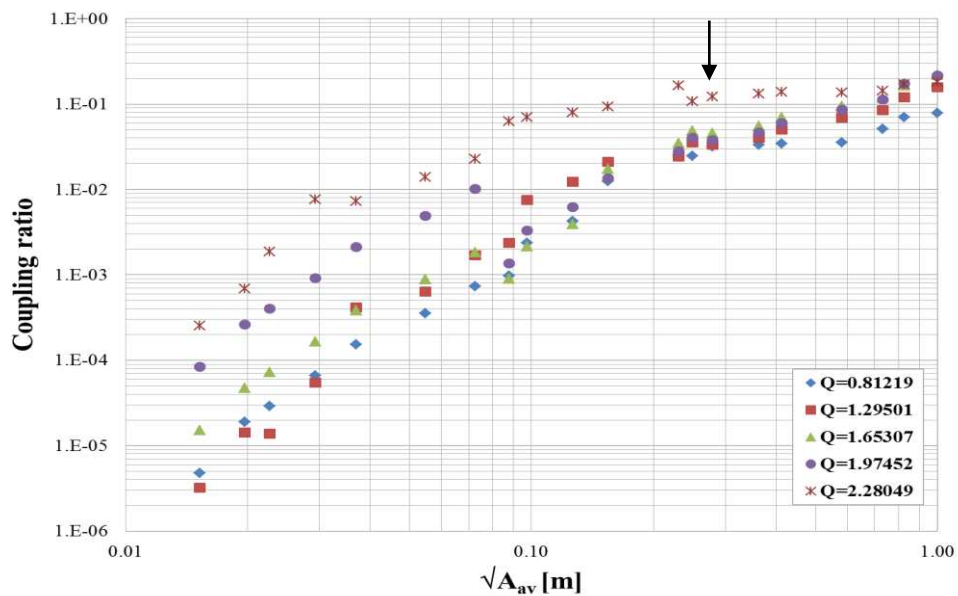


Figure 5.28: Coupling ratio of the excited mode $n=0$ with mode $n=1$ as function mesh parameter $\sqrt{A_{av}}$ (m) and for different mesh quality factor Q . Arrow points to mesh with

$$\sqrt{A_{av}} / \lambda_o < 0.1.$$

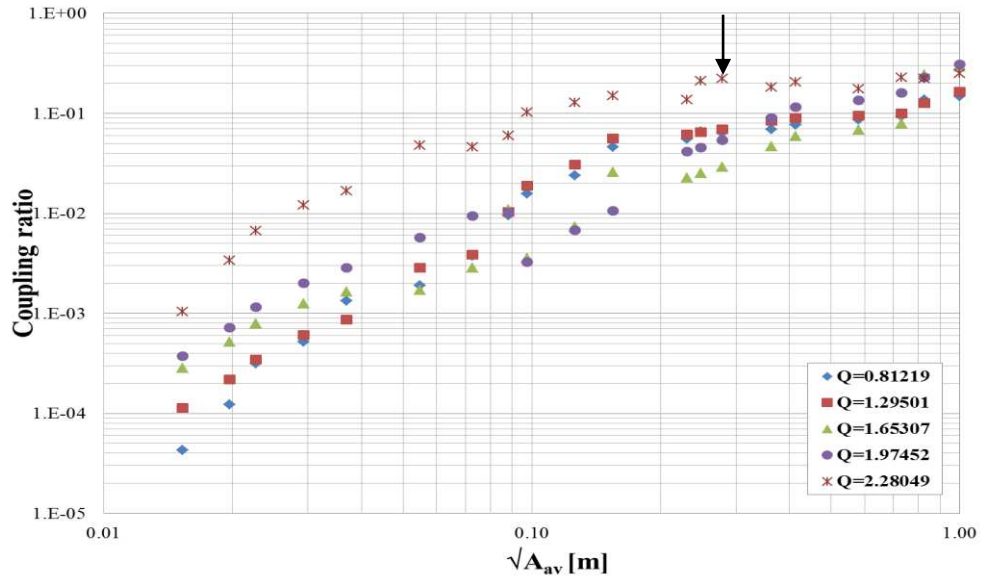


Figure 5.29: Coupling ratio of the excited mode $n=0$ with mode $n=2$ as function mesh parameter $\sqrt{A_{av}}$ (m) and for different mesh quality factor Q . Arrow points to mesh with $\sqrt{A_{av}}/\lambda_o < 0.1$.

Table 5.4 lists the coupling ratio of the excited mode $n=0$ to other spatial modes $n=1-4$ for selected mesh parameter and for mesh quality Q equal to 0.812, 1.295, 1.653, 1.975 and 2.280.

Table 5.4: Coupling ratio of the excited mode $n=0$ to spatial modes $n=1-4$ as a function of selected mesh parameter $\sqrt{A_{av}}$ (m) and for different mesh quality Q

Q	mode	$\sqrt{A_{av}}$								
		0.01026	0.02268	0.05479	0.07277	0.09743	0.12615	0.24859	0.58006	0.99930
0.81219	1	0.00000	0.00003	0.00035	0.00073	0.00235	0.00423	0.02456	0.03519	0.07883
	2	0.00004	0.00032	0.00189	0.00376	0.01577	0.02378	0.06578	0.08609	0.14752
	3	0.00000	0.00003	0.00029	0.00048	0.00166	0.00349	0.00810	0.02387	0.11236
	4	0.00001	0.00008	0.00188	0.00307	0.01094	0.01687	0.04909	0.05892	0.08922
1.29501	1	0.00000	0.00001	0.00063	0.00170	0.00751	0.01226	0.03549	0.06844	0.15785
	2	0.00011	0.00035	0.00284	0.00385	0.01900	0.03057	0.06452	0.09454	0.16509
	3	0.00000	0.00002	0.00017	0.00057	0.00265	0.00497	0.01908	0.03736	0.12698
	4	0.00003	0.00014	0.00055	0.00160	0.00433	0.00765	0.03361	0.04890	0.13414
1.65307	1	0.00002	0.00007	0.00089	0.00184	0.00216	0.00390	0.04903	0.09454	0.21807
	2	0.00028	0.00079	0.00172	0.00284	0.00356	0.00736	0.02508	0.06825	0.29494
	3	0.00000	0.00004	0.00032	0.00111	0.00191	0.00362	0.02164	0.04478	0.19928
	4	0.00004	0.00024	0.00094	0.00273	0.00275	0.00493	0.03485	0.05309	0.18648
1.97452	1	0.00008	0.00040	0.00490	0.01018	0.00327	0.00619	0.04056	0.08569	0.21690
	2	0.00037	0.00115	0.00570	0.00946	0.00325	0.00682	0.04579	0.13586	0.30825
	3	0.00001	0.00017	0.00151	0.00528	0.00248	0.00473	0.01496	0.03149	0.19112
	4	0.00019	0.00101	0.00390	0.01135	0.00313	0.00566	0.02102	0.03321	0.15408
2.28049	1	0.00025	0.00185	0.01403	0.02279	0.07035	0.07961	0.10678	0.13688	0.18070
	2	0.00104	0.00671	0.04775	0.04596	0.10318	0.12754	0.21059	0.17643	0.25017
	3	0.00008	0.00054	0.00808	0.00851	0.01789	0.02781	0.05167	0.17486	0.20763
	4	0.00090	0.00438	0.01660	0.03478	0.09646	0.10090	0.17783	0.15907	0.19240

Pre-seeding the waveguide with a number of randomly placed vertices gives a sequence of different meshes of the same statistical density and quality. The range of coupling ratio for different mesh distribution is illustrated by the vertical bars in Figure 5.30 to Figure 5.34.

Figure 5.30 through Figure 5.34 shows the variance in coupling ratio of the excited mode $n=0$ to modes 1 and 2 as function in mesh parameter $\sqrt{A_{av}}$ and for mesh quality factor Q of 0.812, 1.295, 1.653, 1.975 and 2.280, respectively. It is observed that as the mesh quality factor increases the variance in coupling ratio increases, this can be attributed to the increase of the non-uniformity of the mesh. For example, for $\sqrt{A_{av}}=0.01$ the standard deviation in coupling ratio with $n=1$ increases from 3.47×10^{-7} for $Q=0.812$ to 1.18×10^{-4} for $Q=2.280$, and for $\sqrt{A_{av}}=0.99$ the standard deviation in coupling ratio with $n=1$ increases from 0.006 for $Q=0.812$ to 0.026 for $Q=2.280$.

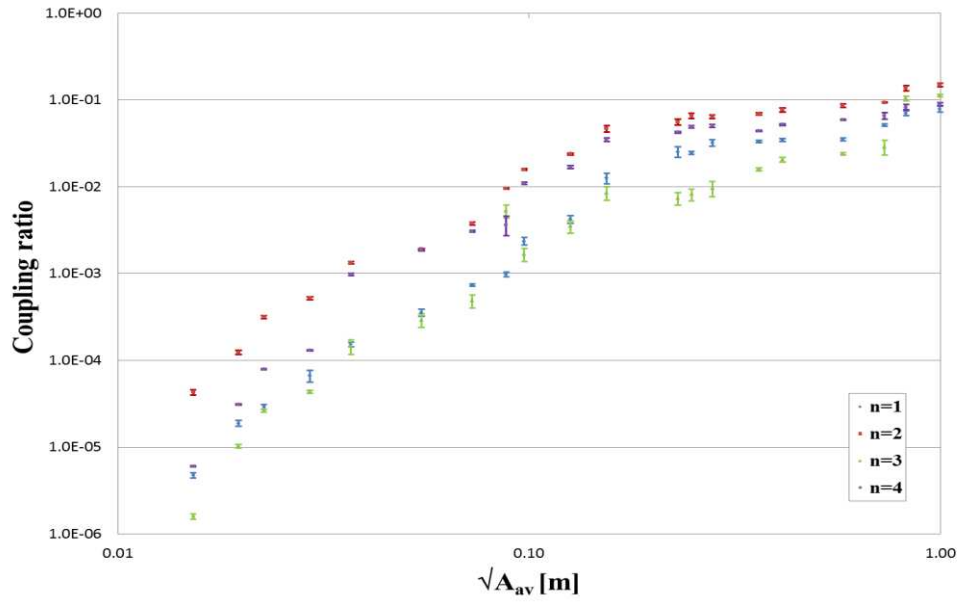


Figure 5.30: Coupling of excited mode $n=0$ to modes $n=1-4$ as a function of the mesh parameter $\sqrt{A_{av}}$ (m) for a mean mesh quality $Q \approx 0.81219$ with vertical bars depicting the coupling range for different mesh distribution.

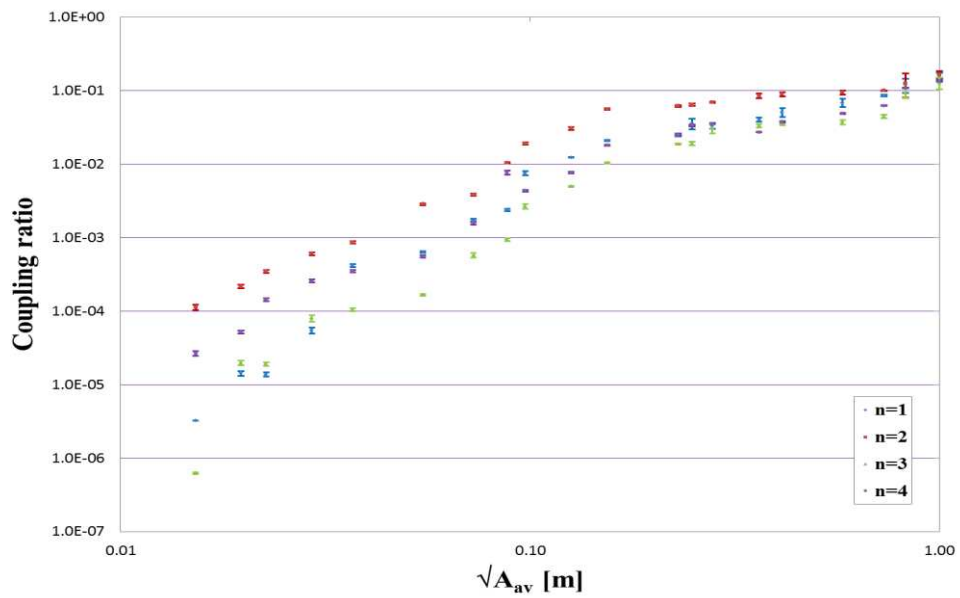


Figure 5.31: Coupling of excited mode $n=0$ to modes $n=1-4$ as a function of the mesh parameter $\sqrt{A_{av}}$ (m) for a mean mesh quality $Q \approx 1.29501$ with vertical bars depicting the coupling range for different mesh distribution.

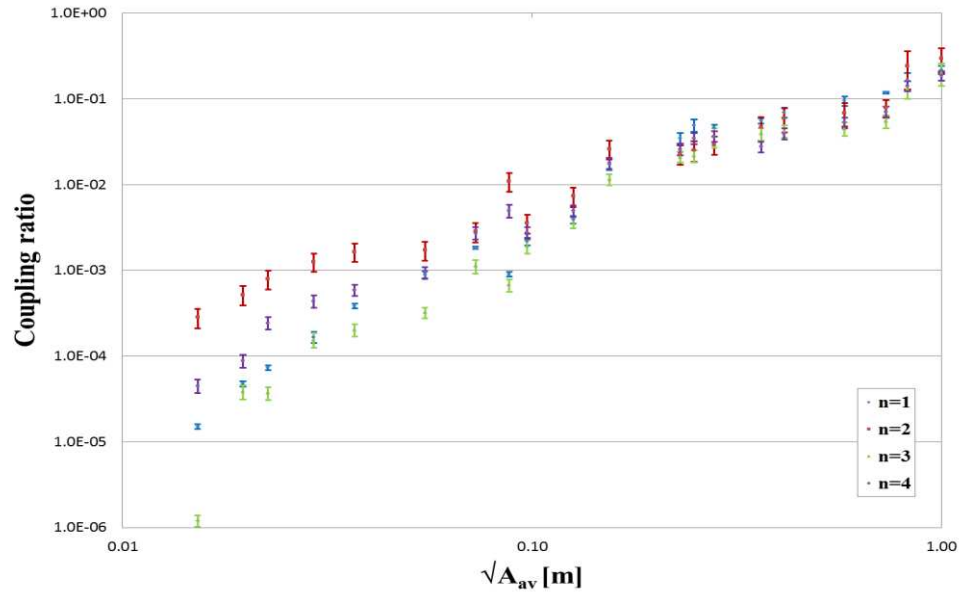


Figure 5.32: Coupling of excited mode $n=0$ to modes $n=1-4$ as a function of the mesh parameter $\sqrt{A_{av}}$ (m) for a mean mesh quality $Q \approx 1.65307$ with vertical bars depicting the coupling range for different mesh distribution.

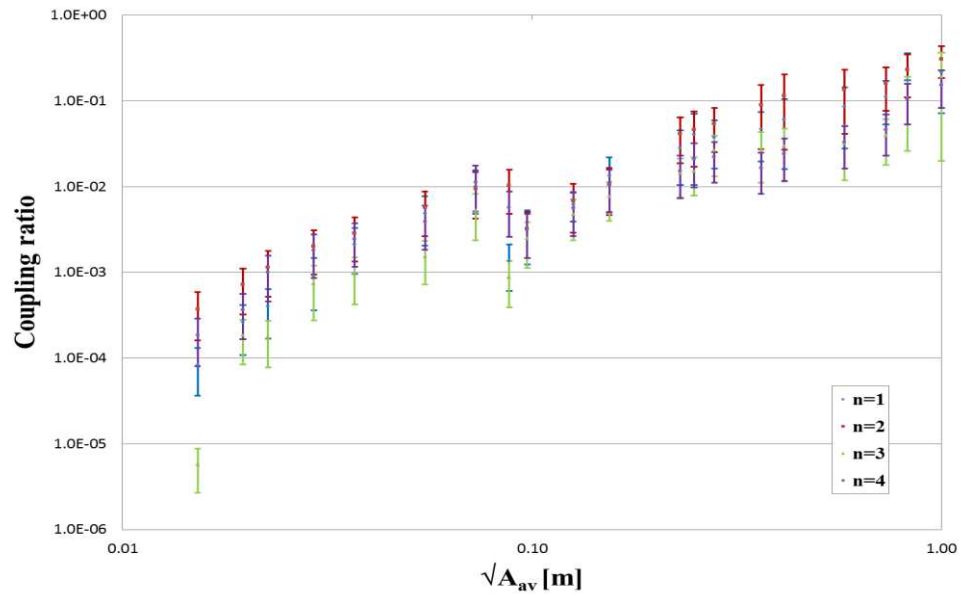


Figure 5.33: Coupling of excited mode $n=0$ to modes $n=1$ and 2 as a function of the mesh parameter $\sqrt{A_{av}}$ (m) for a mean mesh quality $Q \approx 1.97452$ with vertical bars depicting the coupling range for different mesh distribution.

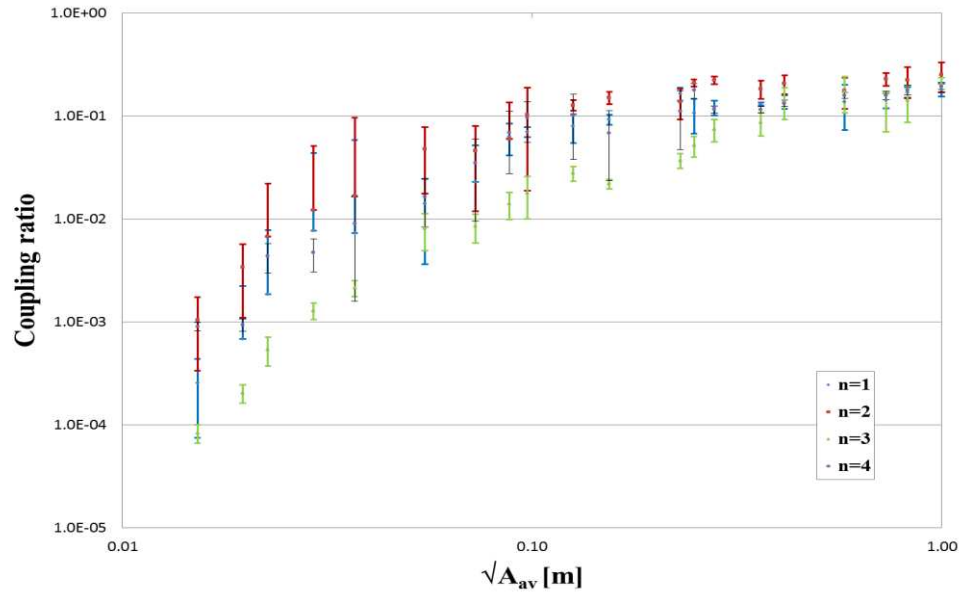


Figure 5.34: Coupling of excited mode $n=0$ to modes $n=1$ and 2 as a function of the mesh parameter $\sqrt{A_{av}}$ (m) for a mean mesh quality $Q \approx 2.28049$ with vertical bars depicting the coupling range for different mesh distribution.

5.6.2.2 Excitation of mode $n=1$

Figure 5.35 to Figure 5.39 show the coupling ratio of the excited mode $n=1$ to other spatial modes ($n=0, 2-4$) as a function of the mesh parameter and for different quality factors, namely, 0.812, 1.295, 1.653, 1.974 and 2.280. It is shown that the coupling ratio is larger with the symmetrical mode $n=3$ followed by the fundamental mode $n=0$.

As discussed previously, the coupling ratio increases with the increase of mesh parameter $\sqrt{A_{av}}$ or for less denser mesh. Also, the coupling ratio increase as the mesh quality factor Q increases as shown in Figure 5.40 and Figure 5.41. The coupling ratio of the excited mode $n=1$ with $n=3$ increased from 4×10^{-6} to 0.132 for $\sqrt{A_{av}}=0.01$ and 0.99, respectively, for $Q=0.812$. On the other hand changing the Q value from 0.812 to 2.280 increased the coupling ratio from 4×10^{-6} to 0.003 for fixed mesh parameter $\sqrt{A_{av}}=0.01$. Table 5.5 illustrates the mean coupling ratio of the excited mode $n=1$ with other spatial modes as the mesh parameter $\sqrt{A_{av}}$ changes and for different mesh quality factors Q .

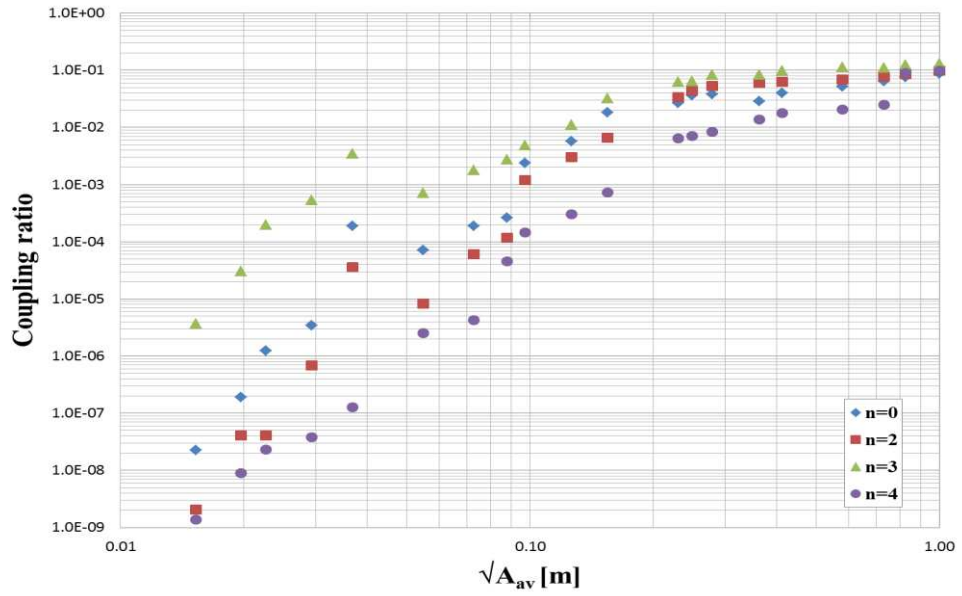


Figure 5.35: Coupling of excited mode $n=1$ to modes $n=0, 2-4$ as a function of the mesh parameter $\sqrt{A_{av}}$ (m) for a mean mesh quality $Q \approx 0.81219$.

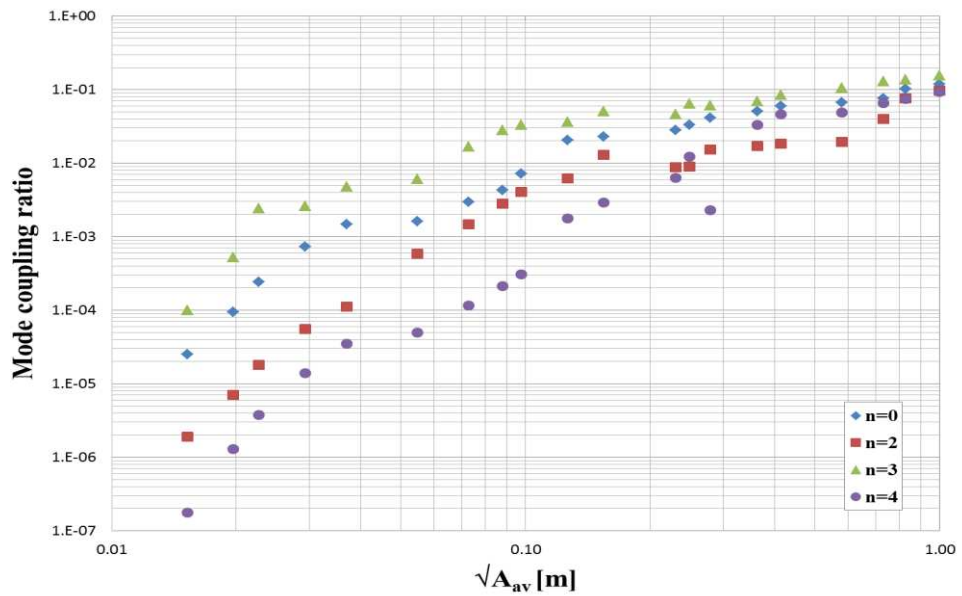


Figure 5.36: Coupling of excited mode $n=1$ to modes $n=0, 2-4$ as a function of the mesh parameter $\sqrt{A_{av}}$ (m) for a mean mesh quality $Q \approx 1.29501$.

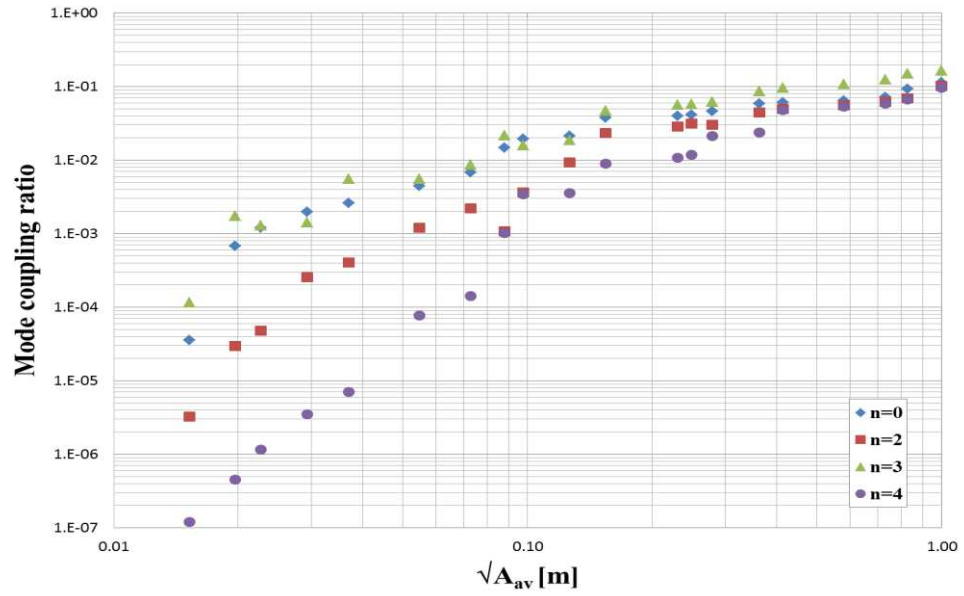


Figure 5.37: Coupling of excited mode $n=1$ to modes $n=0, 2-4$ as a function of the mesh parameter $\sqrt{A_{av}}$ (m) for a mean mesh quality $Q \approx 1.65307$.

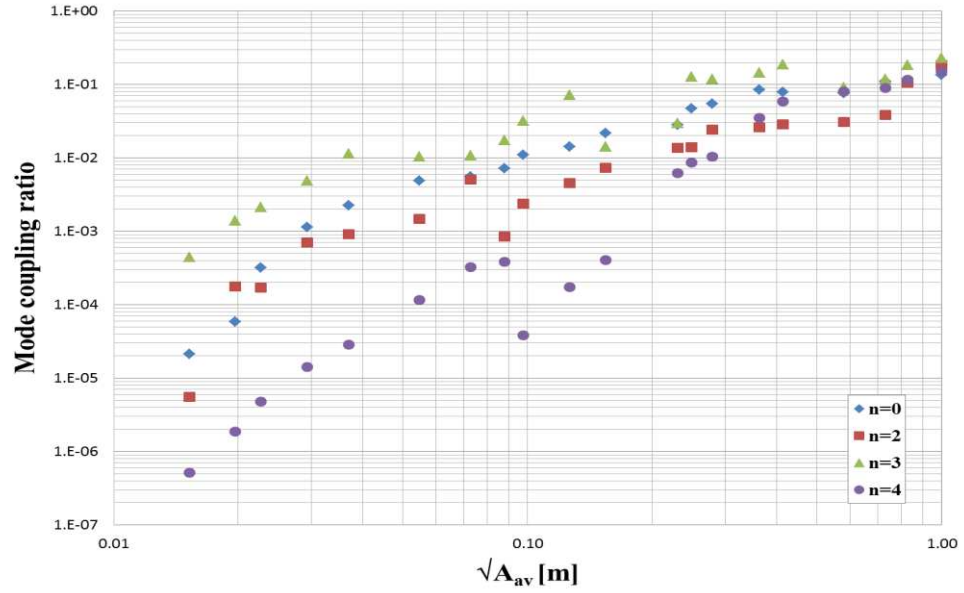


Figure 5.38: Coupling of excited mode $n=1$ to modes $n=0, 2-4$ as a function of the mesh parameter $\sqrt{A_{av}}$ (m) for a mean mesh quality $Q \approx 1.97452$.

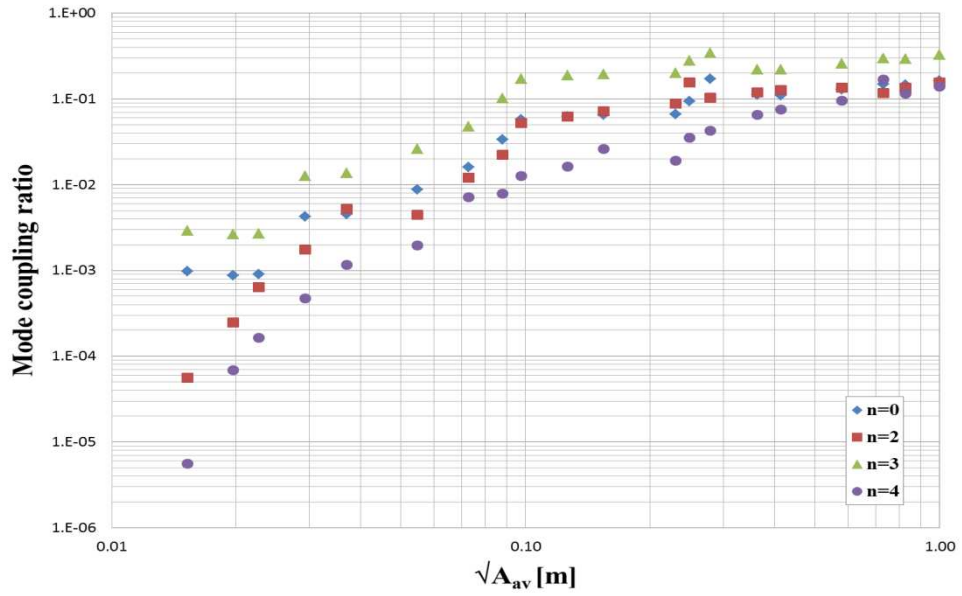


Figure 5.39: Coupling of excited mode $n=1$ to modes $n=0, 2-4$ as a function of the mesh parameter $\sqrt{A_{av}}$ (m) for a mean mesh quality $Q \approx 2.28049$.

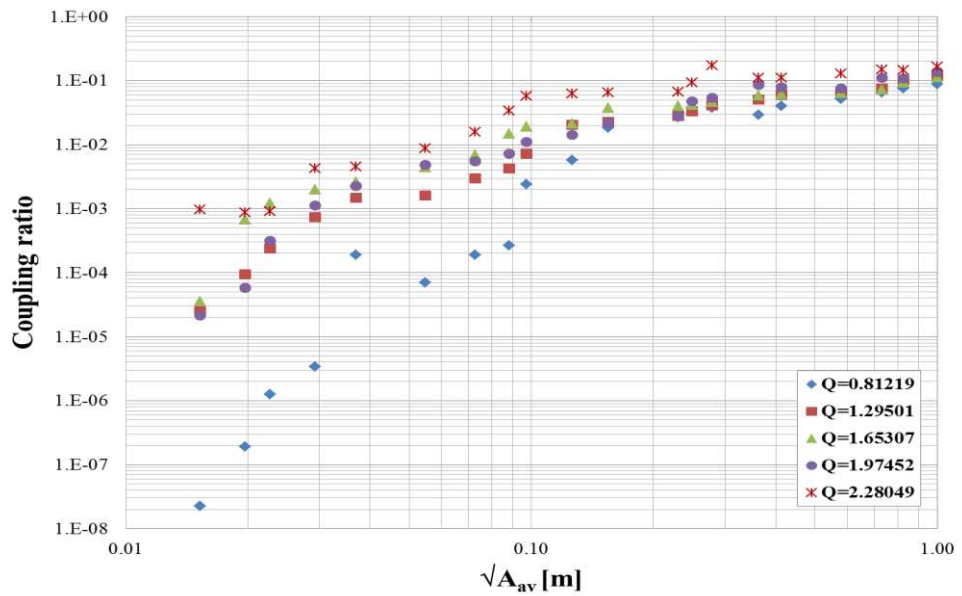


Figure 5.40: Coupling ratio of the excited mode $n=1$ with mode $n=0$ as function mesh parameter $\sqrt{A_{av}}$ (m) and for different mesh quality factor Q .

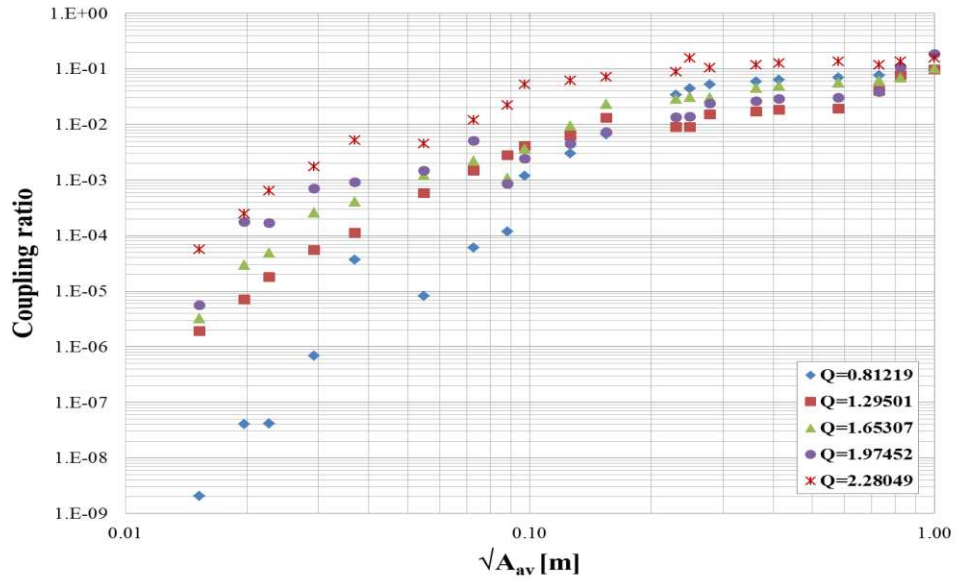


Figure 5.41: Coupling ratio of the excited mode $n=1$ with mode $n=2$ as function mesh parameter $\sqrt{A_{av}}$ (m) and for different mesh quality factor Q .

Table 5.5: Coupling ratio of the excited mode $n=1$ to spatial modes $n=0, 2-4$ as a function of selected mesh parameter $\sqrt{A_{av}}$ (m) and for different mesh quality Q

		$\sqrt{A_{av}}$								
Q	mode	0.01026	0.02268	0.05479	0.07277	0.09743	0.12615	0.24859	0.58006	0.99930
0.81219	0	0.00000	0.00000	0.00007	0.00019	0.00240	0.00570	0.03615	0.05207	0.08804
	2	0.00000	0.00000	0.00001	0.00006	0.00119	0.00301	0.04405	0.06932	0.09819
	3	0.00000	0.00020	0.00070	0.00179	0.00490	0.01122	0.06485	0.11240	0.13174
	4	0.00000	0.00000	0.00000	0.00000	0.00014	0.00030	0.00706	0.02064	0.09789
1.29501	0	0.00002	0.00024	0.00161	0.00296	0.00722	0.02056	0.03290	0.06626	0.11939
	2	0.00000	0.00002	0.00058	0.00148	0.00407	0.00625	0.00905	0.01941	0.09735
	3	0.00010	0.00243	0.00609	0.01676	0.03335	0.03639	0.06490	0.10663	0.15727
	4	0.00000	0.00000	0.00005	0.00011	0.00031	0.00177	0.01226	0.04897	0.09333
1.65307	0	0.00004	0.00121	0.00447	0.00686	0.01931	0.02129	0.04177	0.06428	0.11359
	2	0.00000	0.00005	0.00121	0.00222	0.00361	0.00935	0.03123	0.05587	0.10223
	3	0.00012	0.00130	0.00560	0.00867	0.01589	0.01869	0.05777	0.10727	0.16358
	4	0.00000	0.00000	0.00008	0.00014	0.00344	0.00356	0.01190	0.05321	0.09737
1.97452	0	0.00002	0.00032	0.00485	0.00554	0.01107	0.01413	0.04712	0.07567	0.13556
	2	0.00001	0.00017	0.00147	0.00511	0.00240	0.00455	0.01392	0.03055	0.18540
	3	0.00044	0.00215	0.01044	0.01086	0.03179	0.07158	0.12623	0.09123	0.23094
	4	0.00000	0.00000	0.00012	0.00033	0.00004	0.00017	0.00871	0.07981	0.15150
2.28049	0	0.00098	0.00090	0.00872	0.01593	0.05707	0.06218	0.09342	0.12851	0.16406
	2	0.00006	0.00063	0.00446	0.01199	0.05202	0.06223	0.15639	0.13430	0.15665
	3	0.00293	0.00270	0.02617	0.04780	0.17121	0.18655	0.28026	0.21981	0.32813
	4	0.00001	0.00016	0.00194	0.00715	0.01271	0.01633	0.03509	0.07497	0.13887

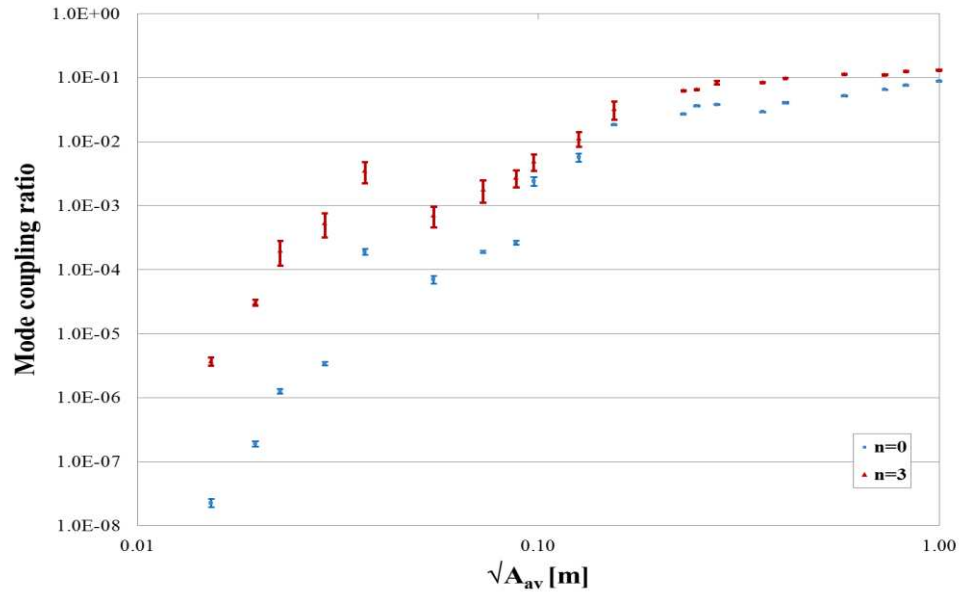


Figure 5.42: Coupling of excited mode $n=0$ to modes $n=1$ and 2 as a function of the mesh parameter $\sqrt{A_{av}}$ (m) for a mean mesh quality $Q \approx 0.81219$ with vertical bars depicting the coupling range for different mesh distribution

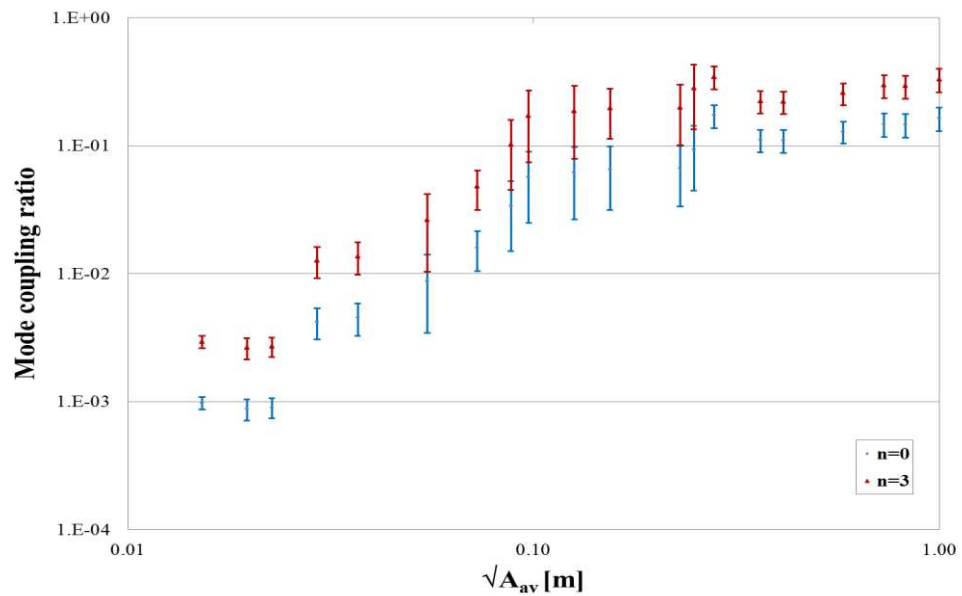


Figure 5.43: Coupling of excited mode $n=0$ to modes $n=1$ and 2 as a function of the mesh parameter $\sqrt{A_{av}}$ (m) for a mean mesh quality $Q \approx 2.28049$ with vertical bars depicting the coupling range for different mesh distribution.

5.6.2.3 Excitation of mode $n=2$

Finally exciting mode $n=2$ shows higher coupling ratio with the symmetrical modes $n=0$ and 4 as illustrated in Figure 5.44 through Figure 5.48. Coupling ratio increases with the increase of mesh parameter $\sqrt{A_{av}}$. Coupling ratio also increases with the increase of the mesh quality factor Q as shown in Figure 5.49 and Figure 5.50. The coupling ratio of $n=2$ with $n=0$ increased from 1.8×10^{-5} to 0.160 for $\sqrt{A_{av}}=0.01$ and 0.99 , respectively, for $Q=0.812$. On the other hand changing the Q value from 0.812 to 2.280 increased the coupling ratio from 1.8×10^{-5} to 0.001 for fixed mesh parameter $\sqrt{A_{av}}=0.01$. Table 5.6 illustrates the mean coupling ratio of the excited mode $n=2$ with other spatial modes as the mesh parameter $\sqrt{A_{av}}$ changes and for different quality factors Q .

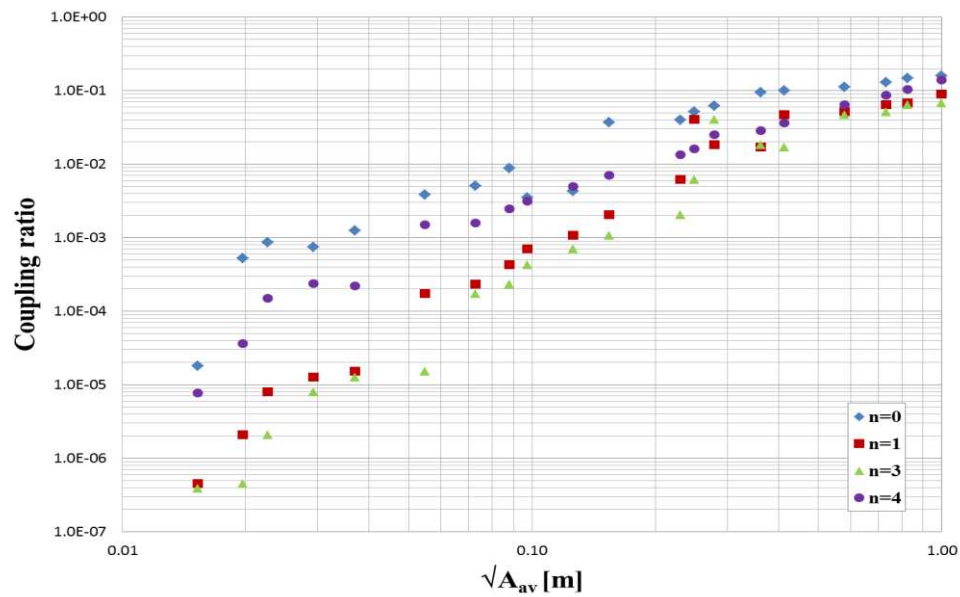


Figure 5.44: Coupling of excited mode $n=2$ to modes $n=0, 1, 3$ and 4 as a function of the mesh parameter $\sqrt{A_{av}}$ (m) for a mean mesh quality $Q \approx 0.81219$.

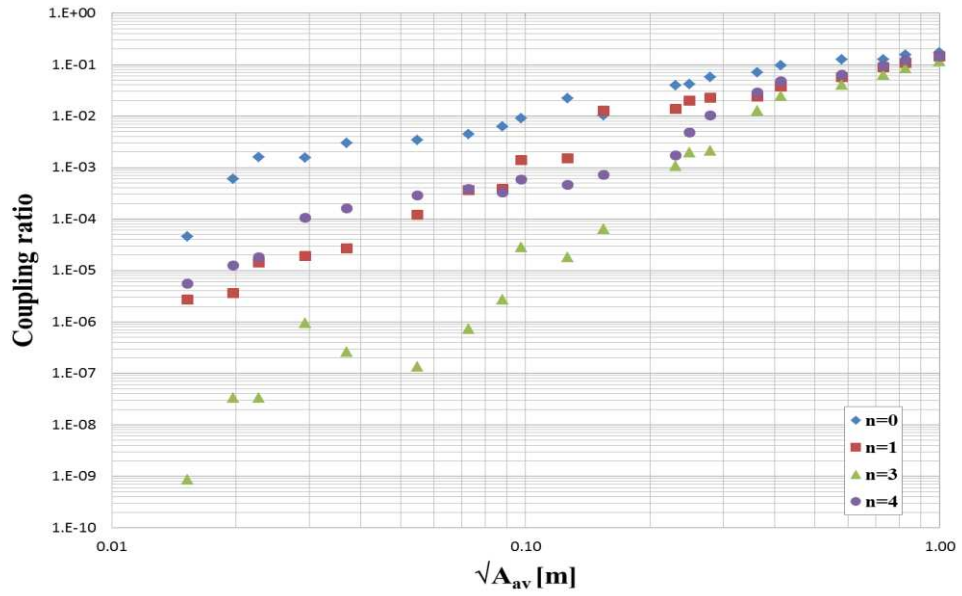


Figure 5.45: Coupling of excited mode $n=2$ to modes $n=0, 1, 3$ and 4 as a function of the mesh parameter $\sqrt{A_{av}}$ (m) for a mean mesh quality $Q \approx 1.29501$.

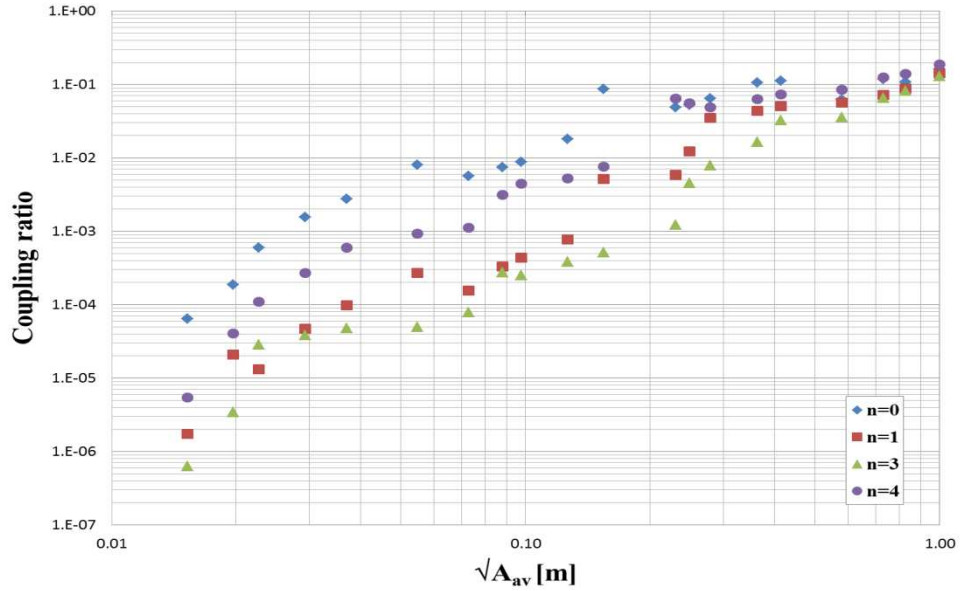


Figure 5.46: Coupling of excited mode $n=2$ to modes $n=0, 1, 3$ and 4 as a function of the mesh parameter $\sqrt{A_{av}}$ (m) for a mean mesh quality $Q \approx 1.65307$.

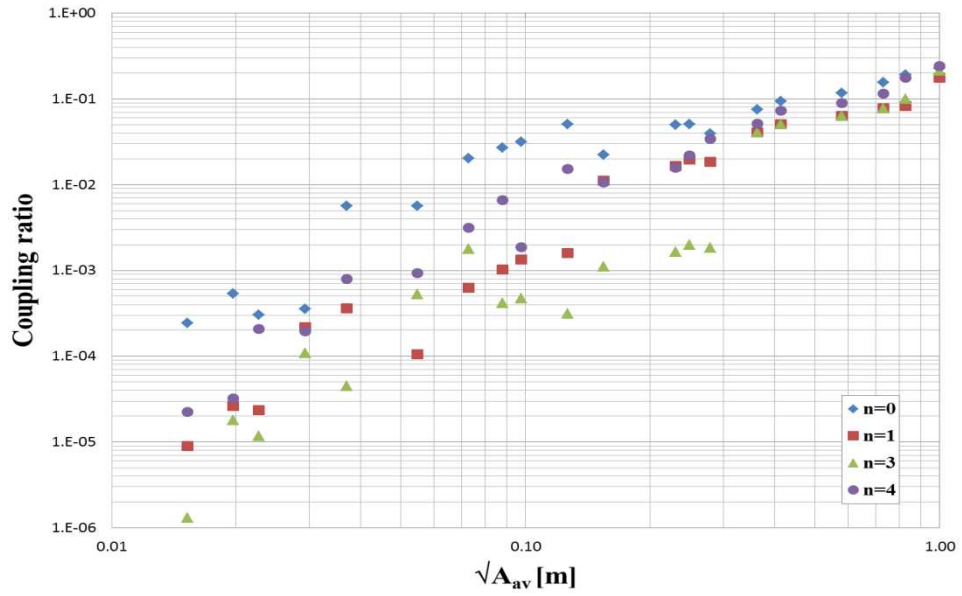


Figure 5.47: Coupling of excited mode $n=2$ to modes $n=0, 1, 3$ and 4 as a function of the mesh parameter $\sqrt{A_{av}}$ (m) for a mean mesh quality $Q \approx 1.97452$.

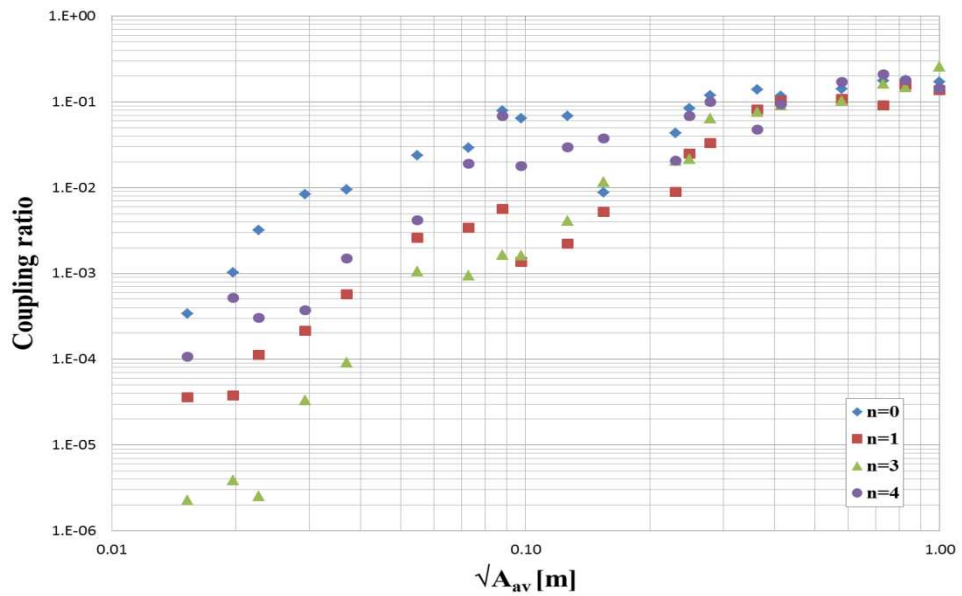


Figure 5.48: Coupling of excited mode $n=2$ to modes $n=0, 1, 3$ and 4 as a function of the mesh parameter $\sqrt{A_{av}}$ (m) for a mean mesh quality $Q \approx 2.28049$.

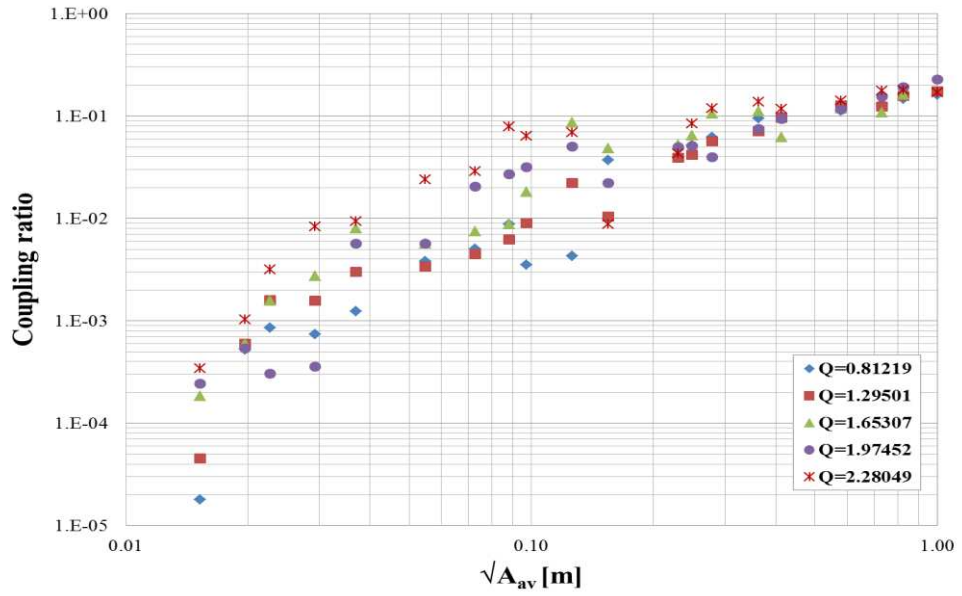


Figure 5.49: Coupling ratio of the excited mode $n=2$ with mode $n=0$ as function mesh parameter $\sqrt{A_{av}}$ (m) and for different mesh quality factor Q .

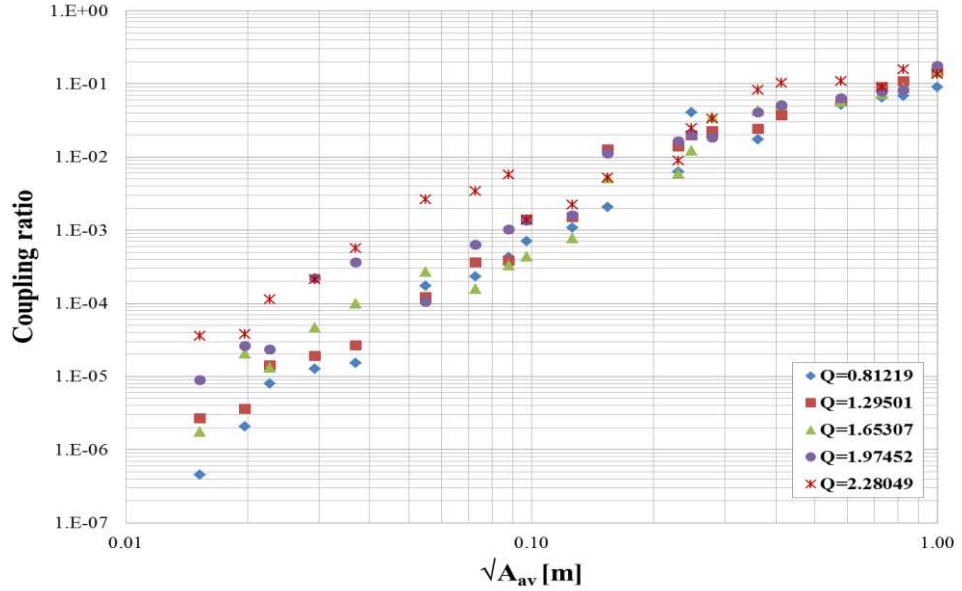


Figure 5.50: Coupling ratio of the excited mode $n=2$ with mode $n=1$ as function mesh parameter $\sqrt{A_{av}}$ (m) and for different mesh quality factor Q .

Table 5.6: Coupling ratio of the excited mode $n=2$ to spatial modes $n=0, 1, 3$ and 4 as a function of selected mesh parameter $\sqrt{A_{av}}$ (m) and for different mesh quality Q

Q	mode	$\sqrt{A_{av}}$								
		0.01026	0.02268	0.05479	0.07277	0.09743	0.12615	0.24859	0.58006	0.99930
0.81219	0	0.00002	0.00086	0.00384	0.00504	0.00351	0.00427	0.05200	0.11284	0.16035
	1	0.00000	0.00001	0.00017	0.00023	0.00070	0.00108	0.04035	0.05186	0.09021
	3	0.00000	0.00000	0.00002	0.00017	0.00043	0.00070	0.00622	0.04741	0.06833
	4	0.00001	0.00015	0.00150	0.00158	0.00312	0.00498	0.01628	0.06430	0.13984
1.29501	0	0.00005	0.00160	0.00341	0.00447	0.00897	0.02222	0.04205	0.12635	0.17356
	1	0.00000	0.00001	0.00012	0.00036	0.00141	0.00149	0.01971	0.05663	0.14462
	3	0.00000	0.00000	0.00000	0.00000	0.00003	0.00002	0.00196	0.04067	0.11627
	4	0.00001	0.00002	0.00029	0.00038	0.00058	0.00046	0.00474	0.06393	0.14374
1.65307	0	0.00006	0.00060	0.00802	0.00565	0.00879	0.01814	0.05235	0.06197	0.16145
	1	0.00000	0.00001	0.00027	0.00016	0.00044	0.00078	0.01229	0.05652	0.14218
	3	0.00000	0.00003	0.00005	0.00008	0.00025	0.00038	0.00451	0.03598	0.13066
	4	0.00001	0.00011	0.00093	0.00112	0.00445	0.00530	0.05599	0.08569	0.18606
1.97452	0	0.00024	0.00030	0.00565	0.02035	0.03165	0.05037	0.05069	0.11661	0.22598
	1	0.00001	0.00002	0.00011	0.00063	0.00134	0.00158	0.01976	0.06326	0.17655
	3	0.00000	0.00001	0.00053	0.00177	0.00047	0.00031	0.00198	0.06326	0.21186
	4	0.00002	0.00021	0.00094	0.00315	0.00188	0.01524	0.02194	0.08890	0.24056
2.28049	0	0.00034	0.00319	0.02388	0.02903	0.06398	0.06888	0.08463	0.14204	0.17007
	1	0.00004	0.00011	0.00262	0.00342	0.00137	0.00222	0.02471	0.10816	0.13614
	3	0.00000	0.00000	0.00105	0.00095	0.00161	0.00408	0.02154	0.10381	0.25596
	4	0.00011	0.00030	0.00420	0.01894	0.01797	0.02964	0.06842	0.17075	0.14285

The range of coupling ratios of the excited mode $n=2$ to spatial modes $n=0$ and 1 for different mesh distributions are illustrated by the vertical bars for $Q=0.812$ and $Q=2.280$ in Figure 5.51 and Figure 5.52, respectively. It is observed that for low mesh quality factors the variance in coupling ratio is small as compared to that produced for high quality factor. For example, for $\sqrt{A_{av}}=0.01$ the standard deviation in coupling ratio with $n=0$ increases from 3.2×10^{-9} for $Q=0.812$ to 1×10^{-6} for $Q=2.280$, and for $\sqrt{A_{av}}=0.99$ the standard deviation in coupling ratio with $n=1$ increases from 0.002 for $Q=0.812$ to 0.058 for $Q=2.280$.

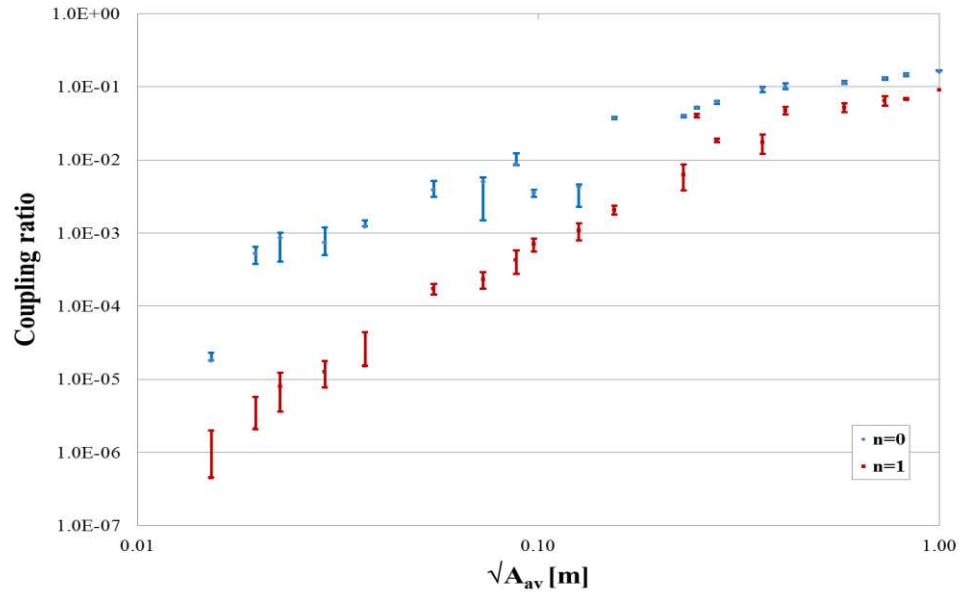


Figure 5.51: Coupling of excited mode $n=2$ to modes $n=0$ and 1 as a function of the mesh parameter $\sqrt{A_{av}}$ (m) for a mean mesh quality $Q \approx 0.81219$ with vertical bars depicting the coupling range for different mesh distribution.

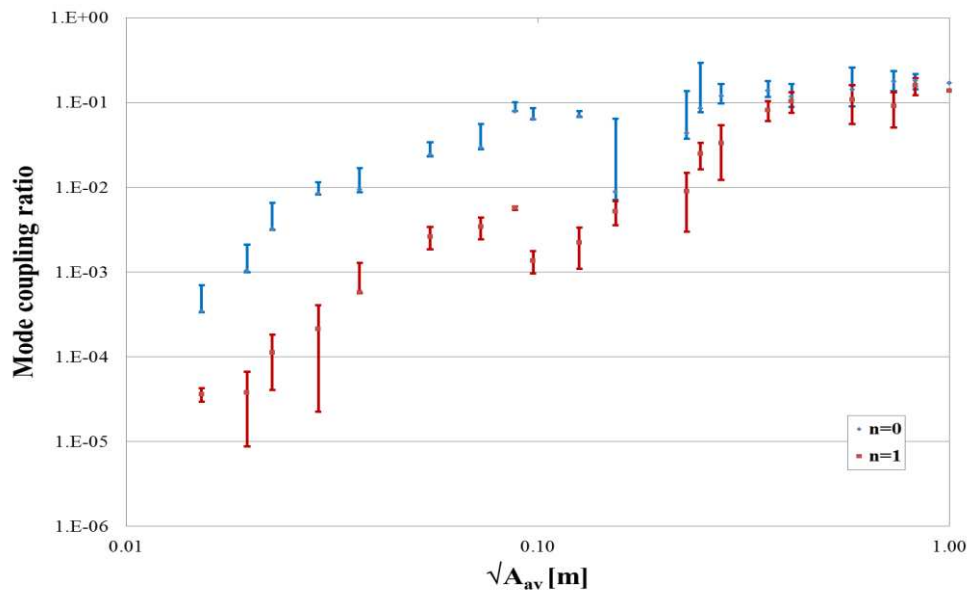


Figure 5.52: Coupling of excited mode $n=2$ to modes $n=0$ and 1 as a function of the mesh parameter $\sqrt{A_{av}}$ (m) for a mean mesh quality $Q \approx 2.28049$ with vertical bars depicting the coupling range for different mesh distribution.

To summarize, the coupling ratio of the excited mode to other spatial modes is investigated statistically for modes $n=0, 1$ and 2 . It is shown that the excited mode couples more to its symmetrical modes. Increasing the quality of the mesh (which is indicated by the decrease of the quality factor Q) leads to the decrease in the coupling ratio. Also, as the mesh becomes more dense (indicated by the decrease of the mesh parameter $\sqrt{A_{av}}$), the coupling ratio decreases. And finally different distributions of meshes of the same density and quality shows that the variance in coupling ratio increases as the mesh quality factor increases due to the non-uniformity of the mesh.

5.7 Summary

In this chapter the numerical dispersion of the unstructured 2D TLM method based on a Delaunay meshing is investigated. The dispersion is analysed by quantifying the phase error of plane wave propagation through the mesh and by investigating the impact of unstructured mesh discretisation on the coupling between different order spatial modes. The plane wave propagation is modelled using a homogeneous free space rectangular region with suitable boundary conditions.

The dispersion study showed that unstructured meshes have lower phase errors of the plane wave propagation as compared to the equivalent structured mesh. The presence of the unstructured mesh, on the other hand, causes unwanted intermodal coupling between different spatial modes due to the intrinsic mesh anisotropy. The highest coupling is recorded between symmetrical spatial modes. The intermodal coupling is analysed in a statistical manner for a range of different mesh density, mesh quality and mesh distribution. It has been shown that the quality of the mesh is an important indicator of intermodal coupling and also that intermodal coupling decreases as the mesh density and mesh quality is increased. Also, it has been shown that discretizing the problem with a discretization length less than one-tenth the reference wavelength decreases the coupling ratio significantly.

Chapter 6.

Conclusions and Future work

The main goal of the thesis was the development of a complete tool to solve 2D electromagnetic problems and solve one of the dominant problems associated with the Delaunay triangle which is the presence of short link lines. The tool was tested on both circular and rectangular configurations and it is working efficiently using unstructured and structured meshes. Also, benchmark data for dispersion error and intermodal coupling in unstructured meshes was acquired.

This chapter summarizes the main conclusions in this thesis and outlines the future work and possibilities of the research are explained.

6.1 Conclusions

Unstructured Transmission line modelling (UTLM) is a versatile tool for modelling electromagnetic problems. A simulator has been produced to simulate a region meshed into Delaunay triangles using object-oriented paradigm. As long as the TLM node coincides with the triangle circumcentres a proper implementation of Maxwell's equation is achieved.

A software package "Triangle" [37] is used to triangulate the mesh domain into number of Delaunay triangles. The problem to be simulated is defined by creating a polygon which is formed by setting number of points around the boundaries and setting the segments connecting these points. Internal boundaries can be set as well which makes the polygon accommodate different materials or changes in dimensions. In order to decrease the numerical dispersion, the sampling length is chosen to be equal to or less than one-tenth the targeted wavelength. Also, to target good triangles the area of the produced triangles should be limited to maximum of half the side squared. Care should be considered in triangulating rectangular shapes in order not to get skinny triangles on border or corners. A test on Delaunay condition should be carried out on

the produced triangles as in some case the “Triangle” has produced non-Delaunay triangles which cause instability in the UTLM simulation.

Also, a problem can be discretized into number of structured meshes by setting equidistant fixed points inside the cavity space, where these points are connected to form squares or rectangles. The mesh generator then divides each square or rectangle into two equal right-angled triangles and the algorithm reduces to the conventional TLM model. As a result the UTLM simulator is used to model both unstructured and structured meshed problem

The data of Delaunay triangles are used to produce a Voronoi diagram formed of the link lines connecting triangle circumcentres. Time step is calculated upon the shortest link length in the simulated domain. Each triangle has three link lines which are modelled using a stub inductor model each terminated with a stub capacitor model. Thevenin equivalent circuit for each link or stub is represented by a source of double the incident voltage in addition to series equivalent impedance. Since the region is divided into irregular shapes proper connections and cell relative position should be taken care of.

The main part of the algorithm comprises of two processes at each time step known as the ‘scatter’ and ‘connect’. Temporal evolution of the field is done by alternative implementation of scatter and connect operations until the steady state is reached

In Chapter 3, the UTLM simulator showed good results for simulating problems with different shapes and materials. It also worked well with a variety of mesh numbers. Three different examples have been created and tested, namely, an air-filled PEC cylindrical resonator, an air-filled PEC cylindrical resonator concentrically loaded with $\epsilon_r=2.1$ and an air-filled rectangular resonator. Each example have been simulated using different number of triangles, and also meshed into unstructured and structured meshes. The resonant frequencies are extracted by applying the FFT to the results produced from the UTLM simulator and compared against the analytical results. Meshing the problem into coarse meshes introduced unwanted resonant frequencies and shift in resonant frequencies locations, this lead to large relative error. As the

density of the mesh increased the resonance frequencies become shaper and more accurate.

For air-filled and dielectric-filled PEC cylindrical resonators, the unstructured meshes have introduced significantly lower relative error as compared to those with structured meshes; this is explained by better boundary approximations. On the other hand, unstructured meshes are executed in longer run time compared with the structured meshes due to the presence of very short link lines, which affect the time step and consequently increases the total run time. Structured meshes provided better run time due to regular formulation of the meshes which provides moderate link line length and reasonable time step and run time. For example, for air-filled cylindrical resonator, the relative error in the first five resonant modes was less than 1% using moderate number of unstructured meshes. This error increased to more than 7% using the equivalent number of structured meshes. In the case of the finest mesh the relative error in the fundamental mode with the UTLM is 40 times lower than that produced by the equivalent TLM structured mesh but former was executed in double the run time of the later.

The air-filled rectangular resonator showed better relative error range as compared to the circular resonator. This is due to the fact that the meshes are always aligned with the rectangle borders. Structured meshes showed slightly better relative error compared to the equivalent unstructured meshes and the execution time for the structured meshes is much better as compared to the unstructured meshes.

The rectangular cavities showed bigger time run times when compared with the circular cavities, in both unstructured and structured meshes. This is assumed to be due to rectangular resonator nature that has sharp edges and corners, which lead to longer time for the wave to stabilize within the resonator space.

Working on the UTLM simulator showed that the automatic generation of Delaunay meshes can generate very short link lines that can negatively impact the computational runtime of TLM simulations. To alleviate this problem, a mesh perturbation method was presented in Chapter 4 whereby all short link lines that fall below a certain threshold value are replaced by an inductive and capacitive stub and the triangles that contain the relevant link line are merged into a four port node (triangle pair) for which

scattering is done implicitly. Short link lines that fall on any type of boundaries should be treated as special cases of pair model and solved separately.

The choice of the threshold value, in this work, was limited by the criteria that only pairs of triangles are formed. The impact of the threshold on the accuracy and computational runtime of the TLM simulations was assessed on two canonical problems of resonant mode extraction of air-filled and dielectrically loaded PEC cylindrical resonators for which analytical results are known. In both cases it was shown that the threshold works effectively in reducing the overall runtime. However, the increase in the threshold length results in the increase in the relative error as the discrepancy between the actual link length being replaced and the threshold is increased. Working with 30% of the maximum allowable threshold length will increase the time step and reduce the run time sufficiently with the advantage of keeping the error below 1%. This error can be further reduced and controlled by increasing the number of triangles in the mesh.

The pair model is merged into the 2D UTLM simulator, which allowed the simulation of problems meshed into structured meshes using the 2D unstructured algorithm. Structured meshes are produced as square or rectangular meshes divided into two equal right-angled triangles. The circumcentre is located on the centre of hypotenuse of the right-angled triangle, thus leading to zero link line length between adjacent triangles forming the structured cell. The number of zero link lines is equal to the number of structured meshes filling the problem domain. Since all zero link lines are replaced by the same threshold value, the whole domain is solved in pair model which virtually appears as “pairs” free domain, and consequently the simulation will work without the error introduced by the pair model in condition to choose the threshold length smaller than one-tenth the sampling length.

In numerical simulation, free space is discretized using varieties of meshes which leads to numerical dispersion. In Chapter 5, the numerical dispersion of the unstructured 2D TLM method based on a Delaunay meshing was investigated. The dispersion is analysed by quantifying the phase error of plane wave propagation through the mesh. The plane wave propagation is modelled in rectangular homogeneous free space that

is analysed as a parallel plate waveguide with open-circuited boundary placed on the parallel plates and impedance matched input and output plane.

The dispersion due to unstructured meshes is averaged along all angles and the real dispersion falls somewhere in between the two extreme examples documented in [7] with zero dispersion for waves propagating at 45° on the mesh and the maximum dispersion for waves propagating at 0° angle in structured meshes. The dispersion study showed that unstructured meshes have lower phase errors of the plane wave propagation as compared to the equivalent structured mesh. It is also observed that the phase velocity of the signal traveling through unstructured meshes is less deviated from the free space velocity as compared to its equivalent structured meshes.

Using the same approach performed in the dispersion study, the impact of unstructured mesh discretisation on the coupling between different order spatial modes was investigated. The parallel plate waveguide was meshed into variety of meshes. The coupling was measured by taking a 2D FFT transform of the signal at the output nodes. The presence of the unstructured mesh causes unwanted intermodal coupling between different spatial modes. The highest coupling was recorded between symmetrical spatial modes, and exciting higher modes showed also large coupling with the fundamental mode. As the number of unstructured meshes increased the transfer of amplitude from the excited mode to other modes has decreased. In the case of the structured mesh, no coupling occurred between different spatial modes and at the output only excited mode existed. This is attributed to the symmetrical nature of the structured meshes.

The dispersion and intermodal coupling are analysed in a statistical manner for a range of different mesh density, quality and distribution and shows that the quality of the mesh is an important indicator of intermodal coupling. A good mesh has a mesh quality factor equals to 0.57737 which is for equilateral triangle, as meshes deviates from this value the intermodal coupling increases. Obtaining different mesh distributions for the same mesh number caused variability in the coupling ratio. This variability increases as the value of the mesh quality factor increases. The intermodal coupling decreases as the mesh density is increased. Also, a mesh with discretization length less than one-tenth the reference wavelength decreases the coupling ratio significantly.

6.2 Future work

UTLM simulator development - The simulator allowed working on both unstructured and structured meshes using the same mathematical approach of UTLM. This allows the continuity of the wave travelling along link lines which alleviate the problem that occurs at the interface between different types of meshes. A hybrid mesh of both unstructured and structured meshes will be further investigated. The UTLM simulator will be applied on practical applications of complex geometries such as microwave filters, tapers and bends.

Also, the UTLM mathematical approach will be extended to include the effect of loss and gain for modelling of different types of materials. Investigation of applying the concept of digital filters on the modelling of dispersive material will be also an extension of the UTLM work.

Pair model - The problem of short link lengths was alleviated using the pair model in which only pairs of triangles were isolated and solved separately; this model solved the problem of the presence of zero link lines, increased the time step and consequently decreased the total run time while keeping the relative error in reasonable level. The next step is to investigate clustering more than two adjacent triangles for further improvement in the total run time and study the consequences on relative error.

Transmission line modelling techniques has been applied successfully on 3D problems, but still the issue of short link lines present in tetrahedral shapes. Different approaches were investigated to solve such problem. Applying the technique of pair model in tetrahedral meshes might be an interesting point of study, where two or more tetrahedrals can be clustered and solved implicitly.

APPENDIX: UNSTRUCTURED TLM SIMULATOR

A.1. “Triangle” mesh generator

Commonly used 2D qualities mesh generator and Delaunay triangulator is known as ‘Triangle’. It is created by J. Shewchuk and is available to download from [37]. Triangle generates Delaunay Triangulations, constrained Delaunay Triangulation, conforming Delaunay Triangulation, and Voronoi diagrams.

The problem wished to be triangulated is defined using A Planar Straight Line Graph (PSLG). A PSLG is a set of points and segments that define the shape that we wish to triangulate. A polygon can be created by creating a closed loop of straight edges to introduce the problem outer boundaries. Inner boundaries also can be created by defining the proper segments to accommodate different regions or materials. Then the PSLG is fed to the mesh generator ‘Triangle’ in a file of extension .poly, which introduces additional vertices inside the polygon that are the vertices of the inner triangles. The .poly file is created according to the following layout [32]:

First section lists all vertices and defines points coordinates

First line: <# of vertices> <dimension (2 for 2D)> <# of attributes> <# of boundary markers>

Following lines: <vertex #> <x> <y>

Second section defines segments connecting points. Each segment is defined by the indices of the endpoints. Boundary markers can be associated with each segment. For open-circuit boundaries the boundary marker is set to 0, 1 for short-circuit boundaries and 2 for matching boundaries.

First line: <# of segments> <# of boundary markers (0 or 1)>

Following lines: <segment #> <endpoint> <endpoint> [boundary marker]

Third section defines holes and regions. Holes are defined by a point inside the hole, starting from this point triangles are eaten up till boundaries of the hole are reached. Be careful of the place the point is inserted as it might end up eating all triangles within the problem space. If the area doesn't contain any holes, number of holes is set to zero.

One line: <# of holes>

Following lines: <hole #> <x> <y>

The last optional part defines the regional attributes such as material parameters and regional constraints such as limits on triangle area.

Optional line: <# of regional attributes and/or area constraints>

Optional following lines: <region #> <x> <y> <attribute> <maximum area>

A.2. “Triangle” switch commands

To run ‘Triangle’, the command line syntax is

triangle -pqenILOYAa_ filename.poly

where the a switch is followed by a number in place of the underscore

The switches following the command triangle is explained as follows [32]

-p Triangulates a Planar Straight Line Graph defined in the .poly file

-q Quality mesh generation with a minimum angle constrained 20°.

-e Outputs a list of edges in a .edge file.

-n Outputs a list of neighbours of each triangle in a .neigh file.

-I Suppresses mesh iteration numbers. Suppresses the output of .node and .poly files in order that the input files not to be overwritten

-O ignores the holes in the .poly file

-A assigns regional attributes to triangles. Attributes are defined in the last section of the .poly files

-a Imposes a maximum triangle area constraint. The value of the maximum allowed area is placed after the switch. If the space after the **-a** switch a maximum area is set to one-

-h Help: Displays complete instructions/

A.3. “Triangle” output files

Triangle output four main files that are fed to the unstructured TLM simulator. These files have the extensions .node, .ele, .edge and .neigh, which contain all data required to define the triangulated area.

.node file:

First line: <# of vertices> <dimension (2 for 2D)> <# of attributes (0)> <# of boundary markers (0 or 1)>

Remaining lines: <vertex #> <x> <y> [boundary marker]

Boundary markers is set to 1 if the node is located in the outer boundary and set to 0 for internal nodes.

.ele file:

First line: <# of triangles> <nodes per triangle (always 3)> <# of attributes>

Remaining lines: <triangle #> <node> <node> <node> [attributes]

The attributes following the triangle contains material parameters, i.e. the relative permittivity in each triangle.

.neigh file:

First line: <# of triangles> <# of neighbors per triangle (always 3)>

Following lines: <triangle #> <neighbor> <neighbor> <neighbor>

If a triangle is located on a border the neighbor index is set to -1

.edge file:

First line: <# of edges> <# of boundary markers (0 or 1)>

Following lines: <edge #> <endpoint> <endpoint> [boundary marker]

The boundary marker indicates type of boundaries; 0 for open circuit boundary, 1 for short circuit boundary and 2 refers to matching boundary.

A.4. UTLM simulator input file

Another file will be created to complete the required input files that will be fed to the UTLM simulator. This fifth file has the extension .inpt which contains information about iterations, source and watch points, also it involve the Threshold value that is discussed in Chapter 4. The .inpt file has the following format

First Section:

First Line: <threshold flag (0 or 1)><threshold value (if threshold flag= 1)>

Second Line: <Run flag (0 to insert total run time, 1 to insert total number of iterations)><run time or no iteration value>

Third Line: <# of input points><# of output points>

Second section:

<x-coordinate of input point><y-coordinate of input point><voltage at input point>

Repeat for other input points

<x-coordinate of output point ><y-coordinate of output point >

Repeat for other output points

Third section:

This part of the file is written upon running the code. It is used to display the ID of the nearest triangle, and the x and y coordinates of its circumcentres for both the source points and observation points.

```
<input ID><x-coordinates of circumcentre>< y-coordinates of circumcentre  
><input voltage>
```

```
<output ID>< x-coordinates of circumcentre >< y-coordinates of circumcentre >
```

A.5. 2D ULTM classes

TLMNode: contains data associated with single node, which are the node ID and node coordinates. It also contains extra parameters to specify whether the node is located on the problem boundaries or not.

TLMEdge: defines parameters of segments, which are the segment ID, the segment endpoints, and the ID of the two triangles sharing this edge. Also an edge marker varying from 0 to 2 is specified to determine open-circuit, short-circuit or matching impedance boundaries.

TLMTriangle: holds all parameters describing the unstructured mesh such as triangle vertices, area, angles, sides, neighbours, circumcentre, link lines, admittances, voltages and material parameters, etc.

TLMRegion: contain three arrays of the previously mentioned classes. This class has a great importance of allocating meshes and their relative positions, connecting meshes and exchanging data between neighbours. Also, it contains the global parameters of the problem such as the time step, the number of iteration, source points and observation points, etc.

A.6. Identifying triangles involving short links

Starting from the minimum link length the first pair is formed and the two triangles that form this pair are flagged (flag is set to true). Note that since any of the triangle links L_{12} , L_{23} or L_{13} might be short, the pair flag take either one of three notations

pair12, **pair23** or **pair13** to identify from which side of the triangle the pair is formed. Moving to the next link length in the list the pair flag is checked; if it is set to false the second pair is formed and the triangles in the new pair are flagged and so on. If a triangle is reached where the pair flag was set to true no further pairs can be formed and the maximum allowed threshold length is set to be equal to the link length used in the last formed pair. Setting the threshold length to be equal to or less than the maximum allowed value ensures that only single pairs per triangle are formed.

The US TLM simulator allows working with or without pairs. Also, it allows working with the maximum threshold value or to set any required threshold length. Returning back to section 3.6.1, the first line in the **.inpt** file was

First Line: <threshold flag (0 or 1)><threshold value (if threshold flag= 1)>

Setting the threshold flag to zero permits the simulator to calculate and use the maximum threshold value, if it is set to 1 a threshold value should be input next to this flag. If the threshold value is set to be equal to the minimum link length then no pairs will be formed and the algorithm works as discussed in Chapter 3.

Another flag (**Pair Value**) is defined for a triangle to ensure that calculations follow the correct route. The pair value is set to zero if no pair is formed, it is set to 1 if a short link line is located on a boundary and is set to 2 if a single pair is formed.

The edge marker indicates which kind of borders is used; 0 for open-circuit boundary, 1 for short-circuit boundary and 2 for matching impedance boundary.

REFERENCES

- [1] C. Christopoulos, Principles and techniques of electromagnetic compatibility: Taylor & Francis, 2007.
- [2] J. H. Ferziger, Numerical Methods for Engineering Application. New York: John Wiley, 1981.
- [3] J. J. Leader, Numerical Analysis and Scientific Computation: Addison Wesley, 2004.
- [4] M. Sadiku, Numerical Techniques in Electromagnetic, second ed. USA: CRC press, 2001.
- [5] C. Christopoulos, An introduction to applied electromagnetism: Wiley, 1990.
- [6] A. Taflove and S. Hagness, Computational Electrodynamics: The Finite-Difference Time Domain Method, Second ed. London: Artec House, 2000.
- [7] C. Christopoulos, The Transmission-Line Modeling Method : TLM: IEEE Press, 1995.
- [8] J. Jin, The finite element method in electromagnetics. New York: John Wiley and sons, 1993.
- [9] C. Christopolous, Principles and techniques of Electromagnetic compatibility, second ed. USA: CRC press, 2007.
- [10] R. Harrington, Field Computation by Moment Methods. New York: Macmillan, 1968.
- [11] S. Heng and C. Wong, "Unstructured Mesh Generation: Theory, practice and perspectives," International Journal on Computation and Geometry Applications, vol. 10, pp. 227-266, 2000.
- [12] P. P. Marshall Bern. (2006). Lecture notes on Mesh Generation. Available: <http://persson.berkeley.edu/pub/persson06unstructured.pdf>
- [13] T. Jurgens, A. Taflove, K. Umashankar, and T. Moore, "Finite-difference time domain modeling of curved surfaces," IEEE transactions on Antenna and Wave Propagation, vol. 40, p. 10, 1992.
- [14] J. Lee, R. Palendech, and R. Mittra, "Modeling three-dimensional discontinuities in waveguides using nonorthogonal FDTD algorithm," IEEE Transactions on Microwave Theory Technology, vol. 40, p. 7, 1992.
- [15] R. Holland, "Finite-difference solution of Maxwell's equations in generalized nonorthogonal coordinates " IEEE Transactions on Nuclear Science, vol. 30, pp. 4589 - 4591, 1983.
- [16] M. Fusco, M. Smith, and L. Gordon, "FDTD algorithm in curvilinear coordinates," IEEE Transactions on Antenna and Wave propagation, vol. 38, pp. 1463 - 1471, 1991.
- [17] J. Herring and C. Christopoulos, "Multigrid transmission-line modeling method for solving electromagnetic field problems," Electronics Letters, vol. 27, pp. 1794-1795, 1991.
- [18] J. Wlodarczyk, "New multigrid interface for the TLM method," Electronics Letters, vol. 32, p. 2, 1996.

- [19] P. Sewell, T. Benson, C. Christopoulos, D. Thomas, and A. Vukovic, "Multi-grid Interface in Computational Electromagnetics," *Electronics Letters*, vol. 40, pp. 162-163, 2004.
- [20] M. Sobhy, M. Abd El-Azeem, and K. Royer, "A new multi-grid 3-D TLM algorithm for simulation of microwave FSS," *IEEE MTT-S Int. Microwave Symp. Dig.*, vol. 2, p. 4, 1996.
- [21] J. Keranen, K. J. A. Ahola, and L. Kettunen, "Implicit Yee-like Scheme on Tetrahedral Mesh," *IEEE Transactions on Magnetics*, vol. 38, pp. 717-720, 2002.
- [22] J. Gao, G. Kobidze, and B. Shanker, "Higher-Order FDTD Algorithm Using Tetrahedral Tessellation," in *IEEE AP-S International Antennas and Propagation Symposium*, Columbus, Ohio, Jun 2003, pp. 364-367.
- [23] P. Sewell, J. Wykes, T. Benson, C. Christopoulos, D. Thomas, and A. Vukovic, "Transmission-Line Modeling Using Unstructured Triangular Meshes," vol. 52, ed: *IEEE Transactions on Microwave Theory and Techniques*, 2004, pp. 1490-1497.
- [24] P. Sewell, J. Wykes, T. Benson, C. Christopoulos, D. Thomas, and A. Vukovic, "Transmission-Line Modeling (TLM) Based Upon Tetrahedral Meshes," *IEEE transactions on microwave theory and techniques*, vol. 53, pp. 1919-1928, 2005.
- [25] J. Wykes, P. Sewell, C. Christopoulos, and T. Benson, "Sub-cell models in unstructured 2D TLM," presented at the IET 7th International Conference on Computation in Electromagnetics, Brighton, 2008.
- [26] P. Sewell, "Applications for the Unstructured Transmission Line Modeling (TLM) Method in Optoelectronics," presented at the Integrated Photonics Research and Applications, San Diego, California, 2005.
- [27] T. Benson, A. Vukovic, J. Wykes, and A. Al-Jarro, "Numerical simulations of 3D micro-resonators," presented at the 10th Anniversary International Conference on Transparent Optical Networks, Athens, 2008.
- [28] T. Benson, S. Boriskina, P. Sewell, and A. Vukovic, "Micro-resonators: simulation and application," presented at the Second International Conference on Advanced Optoelectronics and Lasers.
- [29] S. Gedney, F. Lansing, and D. Rascoe, "A full-wave analysis of passive monolithic integrated circuit devices using a generalized Yee algorithm," *IEEE Transactions on Microwave Theory Technology*, vol. 44, p. 8, 1996.
- [30] D. Mavriplis, "Unstructured Grid Techniques," *Annual review fluid mechanics*, vol. 29, pp. 473-514, 1997.
- [31] P. Sewell, T. M. Benson, C. Christopoulos, and D. Thomas, "Desensitization of unstructured transmission line modelling simulations to mesh characteristics," presented at the 12th International Conference on Mathematical Methods in Electromagnetic Theory, Odesa, 2008.
- [32] J. Shewchuk. (1999). Lecture notes on Delaunay Mesh Generation. Available: <http://www.cs.berkeley.edu/~jrs/meshpapers/delnotes.pdf>
- [33] R. Dyer, H. Zhang, and T. Moller. Voronoi-Delaunay Duality and Delaunay Meshes. Available: https://www.cs.sfu.ca/~haoz/pubs/dyer_spm07.pdf
- [34] Z. Xie, O. Hassan, and K. Morgan, "The Voronoi-Delaunay Dual Diagram : Mesh Generation and Cosmetics," presented at the IET 8th International Conference on Computation in Electromagnetics (CEM 2011), Wroclaw, 2011.

- [35] G. Voronoy, "Nouvelles Applications des Paramètres Continus à la Théorie de Formes Quadratiques," *Journal für die Reine und Angewandte Mathematik*, vol. 134, pp. 198-287, 1908.
- [36] P. Sewell, T. Benson, C. Christopoulos, T. Thomas, A. Vukovic, and J. Wykes, "Implicit Element Clustering for Tetrahedral Transmission Line Modelling (TLM)," *IEEE Transactions on Microwave Theory and Techniques*, vol. 57, pp. 2005-2013, 2009.
- [37] J. Shewchuk. (2005, July 28). Triangle: A Two-Dimensional Quality Mesh Generator and Delaunay Triangulator. Available: <http://www.cs.cmu.edu/~quake/triangle.html>
- [38] H. Si and TetGen, "A Quality Tetrahedral Mesh Generator and a 3D Delaunay Triangulator," ed. Berlin, Germany: Research Group: Numerical Mathematics and Scientific Computing Weierstrass Institute for Applied Analysis and Stochastics (WIAS), 2005.
- [39] M. Krumpholz and P. Russer, "On the dispersion in TLM and FDTD," *IEEE Transactions on Microwave Theory and Techniques*, vol. 42, pp. 1275 - 1279, 1994.
- [40] A. Centeno, "A Comparison of Numerical Dispersion in FDTD and TLM Algorithms," presented at the Asia-Pacific Conference on Applied Electromagnetics. APACE 2003., 2003.
- [41] V. Trenkic, C. Christopoulos, and T. M. Benson, "Analytical Expansion of the Dispersion Relation for TLM Condensed Nodes" *IEEE Transactions on Microwave Theory and Techniques*, vol. 44, pp. 2223 - 2230, 1996.
- [42] J. Nielsen and W. Hoefler, "A complete dispersion analysis of the condensed node TLM mesh," *IEEE Transactions on Magnetics*, vol. 27, pp. 3982 - 3983, 1991.
- [43] P. Russer, "A generalized method for the calculations of the TLM dispersive relations," presented at the 23rd European Microwave Conference, Madrid, Spain, 1993.
- [44] L. R. A. X. de Menezes and W. J. R. Hoefler, "Modelling Nonlinear Dispersive Media in 2D TLM," presented at the 24th European Microwave Conference, Cannes, France, 5-9 Sept. 1994.
- [45] D. Pozar, *Microwave Engineering*, fourth ed.: John Wiley & Sons, 2011.
- [46] M. Haldar, "Introducing the finite element method in electromagnetics to undergraduates using Matlab," *International Journal of electrical engineering education* vol. 43.
- [47] A. Peterson, "Finite element solution of the vector wave equation using divergenceless basis functions," presented at the Antennas and Propagation Society International Symposium, San Jose, USA, 1989.
- [48] P. Johns, "On the relationship between TLM and finite difference methods for Maxwell's equations," *IEEE Transactions on Microwave Theory Technology*, vol. MTT-35, 1987.
- [49] Z. Chen, M. Ney, and W. Hoefler, "A new finite difference time-domain formulation and its equivalence with the TLM symmetrical condensed node," *IEEE Transactions on Microwave Theory Technology*, vol. MTT-39, 1991.
- [50] H. Jin and R. Vahldieck, "Direct derivations of TLM symmetrical condensed Node and hybrid symmetrical condensed node from Maxwell's equations using centred differencing and averaging," *IEEE Transactions on Microwave Theory and Techniques*, vol. 42, pp. 2554-2561, 1994.
- [51] M. Krumpholz and P. Russer, "A field theoretical derivation of TLM," *IEEE Transaction on Microwave Theory and Techniques*, vol. 42, pp. 1660-1668, 1994.

- [52] M. Krumpholz, C. Huber, and P. Russer, "A Field Theoretical Comparison of FDTD and TLM," *IEEE Transactions on Antenna and Wave Propagation*, vol. 43, pp. 1935-1950, 1995.
- [53] C. Eswarappa and W. Hoefer, "Bridging the gap between TLM and FDTD," *IEEE Microwave and Guided Wave Letters*, vol. 43, pp. 4-6, 1996.
- [54] W. J. R. Hoefer, "Some Thoughts on the Relationship between Finite Elements, Finite Differences and TLM," presented at the Antennas and Propagation Society International Symposium, Montreal, Quebec, Canada, 1997.
- [55] P. Silvester and R. Ferrari, *Finite Elements for electrical engineers*. Cambridge: Cambridge university press, 1990.
- [56] J. N. Reddy, *An Introduction to the Finite Element Method*, 2nd ed. New York: McGraw-Hill 1993.
- [57] D. Baumann, C. Fumeaux, P. Leuchtman, and R. Vahldieck, "Finite-volume time-domain (FVTD) modelling of a broadband double-ridged horn antenna," *International Journal of Numerical Modelling: Electronic Networks, Devices and Fields*, vol. 17, pp. 285-298, 2004.
- [58] S. Ahmed and P. Daly, "Finite-element methods for inhomogeneous waveguides," *Proc. IEEE*, vol. 116, pp. 1661-1664, 1969.
- [59] Z. J. Csendes and P. Silvester, "Numerical solution of dielectric loaded waveguides: I—Finite-element analysis " *IEEE Trans. Micro. Theo. Tech.*, vol. MTT-18, pp. 1124-1131, 1970.
- [60] Z. J. Csendes and P. Silvester, "Numerical solution of dielectric loaded waveguides:II—Modal approximation technique," *IEEE Trans. Micro. Theo. Tech.*, vol. MTT-19, pp. 504-509, 1971.
- [61] M. Hano, "Finite-element analysis of dielectric-loaded waveguides," *IEEE Trans. Micro. Theo. Tech.*, vol. MTT-32, pp. 1275-1279, 1984.
- [62] A. Bossavit and L. Kettunen, "Yee-like schemes on a tetrahedral mesh, with diagonal lumping " *International Journal of Numerical Modelling: Electronic Networks, Devices and Fields*, vol. 12, pp. 129-142, 1999.
- [63] J.-Y. Wu and R. Lee, "The advantages of triangular and tetrahedral edge elements for electromagnetic modeling with the finite-element method," *IEEE Transactions on Antennas and Propagation*, vol. 45, pp. 1431;- 1437, 1997.
- [64] S. G. Mikhlin, *Variational Methods in Mathematical Physics*. New York: Macmillan, 1964.
- [65] S. Gedney and U. Navsariwala, "An unconditionally stable finite element time-domain solution of the vector wave equation," *IEEE Microwave and Guided Wave Letters*, vol. 5, pp. 332 - 334, 1995.
- [66] G. D. Smith, *Numerical Solution of Partial Differential Equations: Finite Difference Methods* 3rd ed. New York: Oxford Univ. Press, 1985.
- [67] L. Lapidus and G. Pinder, *Numerical Solution of Partial Differential Equations in Science and Engineering*. New York: John Wiley, 1982.
- [68] W. Buchanan, "Analysis of the Electromagnetic Wave Propagation Using the 3D Finite Difference Time Domain Using Parallel Processing," PhD, Napier, UK, 1996.
- [69] D. Sullivan, *Electromagnetic Simulation Using the FDTD Method*. USA: IEEE Press on the RF and Microwave Technology, 2000.

- [70] M. De Pourceq, "Field and power-density calculations in closed microwave systems by three-dimensional finite differences" *IEEE Proc.*, vol. 132, pp. 360–368, 1985.
- [71] A. Taflove and K. R. Umashankar "Solution of complex electromagnetic penetration and scattering problems in unbounded regions" in *Computational Methods for Infinite Domain Media-structure Interaction*. vol. 46, Washington, DC: ASME, 1981, pp. 83-113.
- [72] A. Taflove, "Application of the finite-difference time-domain method to sinusoidal steady-state electromagnetic-penetration problems " *IEEE Trans. EM. Comp.* , vol. EMC-22, pp. 191-202, 1980.
- [73] K. Umashankar and A. Taflove, "A novel method to analyze electromagnetic scattering of complex objects " *IEEE Trans. EM Comp.*, vol. EMC-24, pp. 870-894, 1982.
- [74] A. Taflove and M. E. Brodwin, "Numerical Solution of Steady-State Electromagnetic Scattering Problems Using the Time-Dependent Maxwell's Equations," *IEEE Transactions on Microwave Theory and Techniques*, vol. 23, pp. 623 - 630, 1975.
- [75] X. Zhang, J. F., K. Mei, and Y. Liu, "Calculations of the dispersive characteristics of microstrips by the time-domain finite difference method," *IEEE Transactions on Microwave Theory and Techniques*, vol. 36, pp. 263 - 267, 1988.
- [76] J. S. Hornsby and A. Gopinath, "Numerical analysis of a dielectric-loaded waveguide with a microstrip line—finite-difference methods" *IEEE Trans. Micro. Theo. Tech.*, vol. MTT-17, pp. 684–690, 1969.
- [77] W. K. Gwarek "Analysis of an arbitrarily-shaped planar circuit—a time domain approach" *IEEE Trans. Micro. Theo. Tech.*, vol. MTT-33, pp. 1067–1072, 1985.
- [78] M. J. Beubien and A. Wexler, "An accurate finite-difference method for higher order waveguide modes" *IEEE Trans. Micro. Theo. Tech.*, vol. MTT-16, pp. 1007-1017, 1968.
- [79] C. A. Muilwyk and J. B. Davies, "The numerical solution of rectangular waveguide junctions and discontinuities of arbitrary cross section " *IEEE Trans. Micro. Theo. Tech.*, vol. MTT-15, pp. 450–455, 1967.
- [80] J. H. Collins and P. Daly, "Calculations for guided electromagnetic waves using finite-difference methods" *J. Electronics & Control*, vol. 14, pp. 361-380, 1963.
- [81] J. Maloney, G. Smith, and W. Scott, "Accurate computation of the radiation from simple antennas using the finite-difference time-domain method," *IEEE Transactions on Antennas and Propagation*, vol. 38, pp. 1059 - 1068, 1990.
- [82] E. Sano and T. Shibata, "Fullwave analysis of picosecond photoconductive switches," *IEEE Journal of Quantum Electronics*, vol. 26, pp. 372 - 377, 1990.
- [83] S. Hagness, A. Taflove, and J. Bridges, "Two-dimensional FDTD analysis of a pulsed microwave confocal system for breast cancer detection: fixed-focus and antenna array sensors," *IEEE Transactions on Biomedical Engineering*, vol. 45, pp. 1470–1479, 1998.
- [84] R. W. M. Lau and R. J. Sheppard, "The modelling of biological systems in three dimensions using the time domain finite-difference method" *Phys. Med. Biol.*, vol. 31, pp. 1247–1266, 1986.
- [85] G. A. Kriegsmann, A. Taflove, and K. R. Umashankar, "A new formulation of electromagnetic wave scattering using an on-surface radiation boundary condition approach " *IEEE Trans. Ant. Prop.*, vol. 35, pp. 153–161, 1987.
- [86] B. Zhiqiang, "A new finite-difference time-domain algorithm for solving Maxwell's equation " *IEEE Micro. Guided Wave Lett.*, vol. 1, pp. 382–384, 1991.

- [87] S. X. R. Vahldieck and H. Jin "Full-wave analysis of guided wave structures using a novel 2-D FDTD " *IEEE Micro. Guided Wave Lett.*, vol. 2, pp. 165-167, 1992.
- [88] R. Mittra and P. H. Harms "A new finite-difference time-domain (FDTD) algorithm for efficient field computation in resonator narrow-band structures " *IEEE Micro. Guided Wave Lett.*, vol. 3, pp. 336-318, 1997.
- [89] J. Cole, "A high accuracy realization of the Yee algorithm using non-standard finite differences " *IEEE Trans. Micro. Theo. Tech.*, vol. 45, pp. 991-996, 1997.
- [90] I. J. Craddock and C. J. Railton, "A new technique for the stable incorporation of static field solutions in the FDTD method for the analysis of thin wires and narrow strips " *IEEE Trans. Micro. Theo. Tech.*, vol. 46, pp. 1091-1096, 1998.
- [91] P. H. Harms, J. F. Lee, and R. Mittra "A study of the nonorthogonal FDTD method versus the conventional FDTD technique for computing resonant frequency of cylindrical cavities " *IEEE Trans. Micro. Theo. Tech.*, vol. 40, pp. 741-746, 1992.
- [92] Y. Chen, R. Mittra, and P. Harms, "Finite-difference time-domain algorithm for solving Maxwell's equations in rotationally symmetric geometries" *IEEE Trans. Micro. Theo. Tech.*, vol. 44, pp. 832-839, 1996.
- [93] M. Cinalli and A. Schiavoni, "A stable and consistent generalization of the FDTD technique to nonorthogonal unstructured grids," *IEEE Transactions on Antennas and Propagation*, vol. 54, pp. 1503;- 1512, 2006.
- [94] S. Hein, "Finite difference time-domain approximation of Maxwell's equations with non-orthogonal condensed TLM mesh" *International Journal of Numerical Modelling: Electronic Networks, Devices and Fields*, vol. 7, pp. 179-188, 1994.
- [95] C. Wang, B. Q. Gao, and C. P. Deng, "Q factor of a resonator by the finite difference time-domain method incorporating perturbation techniques " *Elect. Lett.*, vol. 29, pp. 1866-1867, 1993.
- [96] Wikipedia, "Finite-difference time-domain method," ed, 2014.
- [97] G. Mur, "Absorbing boundary conditions for the finite difference approximation of the time-domain electromagnetic field equations," *IEEE transactions on Electromagnetic Compatibility*, vol. 23, p. 7, 1981.
- [98] J. Berenger, "A perfectly matched layer for the absorption of electromagnetic waves," *Journal of Computational Physics*, vol. 114, p. 16, 1994.
- [99] D. Katz, T. Thiele, and A. Taflove, "Validation and extension to three dimensions of the Berenger PML absorbing boundary condition for FDTD meshes," *IEEE Microwave guided Wave Letter*, vol. 4, p. 3, 1994.
- [100] Z. Liao, H. Wong, B. Yang, and Y. Yuan, "A transmitting boundary for transient wave analysis," *Scientia Sinica (Series A)*, p. 5, 1984.
- [101] S. Gedney, "An anisotropic perfectly matched layer-absorbing medium for the truncation of FDTD lattices," *IEEE Transactions on Antennas & Propagation*, vol. 44, p. 10, 1996.
- [102] W. Hofer, *The transmission line matrix (TLM) method*. New York, USA: John Wiley, 1989.
- [103] W. J. R. Hofer, "The transmission-line matrix method—theory and applications," *IEEE Trans. Microwave Theory Tech.*, vol. MTT-33, pp. 882-893, 1985.
- [104] M. N. O. Sadiku and L. C. Agba, "A simple introduction to the transmission-line modeling " *IEEE Trans. Cir. Sys.*, vol. CAS-37, pp. 991-999, 1990.

- [105] P. B. Johns and R. L. Beurle, "Numerical solution of 2-dimensional scattering problems using a transmission-line matrix," *Proceedings of the Institution of Electrical Engineers*, vol. 118, pp. 1203 - 1208, 1971.
- [106] C. C. Wong and W. S. Wong, "Multigrid TLM for diffusion problems," *Int. J. Num. Model.*, vol. 2, pp. 103-111, 1989.
- [107] P. B. Johns, "Applications of the transmission-line matrix method to homogeneous waveguides of arbitrary cross-section" *Proc. IEEE*, vol. 119, pp. 1086–1091, 1972.
- [108] C. Christopoulos and J. L. Herring, "The application of the transmission-line modeling (TLM) to electromagnetic compatibility problems " *IEEE Trans. Elect. Magn. Comp.*, vol. 35, pp. 185–191, 1993.
- [109] L. C. Agba, "Transmission-line-matrix modeling of inhomogeneous rectangular waveguides and cavities" MSc, Department of Electrical and Computer Engineering Florida Atlantic University, Boca Raton, 1987.
- [110] P. B. Johns, "The solution of inhomogeneous waveguide problems using a transmission-line matrix," *IEEE Transactions on Microwave Theory and Techniques*, vol. MTT-22, pp. 209-215, 1974.
- [111] S. Akhtarzad and P. B. Johns, "Numerical solution of lossy waveguides: TLM computer programs " *Elec. Lett.*, vol. 10, pp. 309–311, 1974.
- [112] Y. C. Shih and W. J. R. Hofer "The accuracy of TLM analysis of finned rectangular waveguides " *IEEE Trans. Micro. Theo. Tech.*, vol. MTT28, pp. 743–746, 1980.
- [113] S. Akhtarzad and P. B. Johns, "Transmission line matrix solution of waveguides with wall losses " *Elec. Lett.*, vol. 9, pp. 335–336, 1973.
- [114] Y. C. Shih and W. J. R. Hofer, "Dominant and second-order mode cutoff frequencies in fin lines calculated with a two-dimensional TLM program " *IEEE Trans. Micro. Theo. Tech* vol. MTT-28, pp. 1443–1448, 1980.
- [115] S. Weight, "The applications of transmission line modelling implicit and hybrid algorithm to electromagnetic problems," PhD, Nottingham, 1988.
- [116] F. J. German, G. K. Gothard, and L. S. Riggs, "Modelling of materials with electric and magnetic losses with the symmetrical condensed TLM method," *Electronics letters*, vol. 26, pp. 1307 - 1308 1990.
- [117] C. Christopoulos, *The transmission-line modeling (TLM) method in electromagnetics: Morgan & Claypool*, 2006.
- [118] S. Lindenmeier, C. Christopoulos, and P. Russer, "Methods for the modeling of thin wire structures with the TLM method," presented at the IEEE MTT-S International Microwave Symposium Digest, Boston, MA, USA, 2000.
- [119] A. Ruddle, D. Ward, R. Scaramuzza, and V. Trenkic, "Development of thin wire models in TLM," presented at the IEEE International Symposium on Electromagnetic Compatibility, Denver, CO, 1998.
- [120] P. Sewell, Y. K. Choong, and C. Christopoulos, "An accurate thin-wire model for 3-D TLM simulations," *IEEE Transactions on Electromagnetic Compatibility*, vol. 45, pp. 207 - 217, 2003.
- [121] Y. K. Choong, P. Sewell, and C. Christopoulos, "Accurate wire representation in numerical models for high-frequency simulation," *37*, vol. 5, pp. 280;- 282, 2001.

- [122] P. Sewell, Y. Choong, and C. Christopoulos, "An accurate thin-wire model for 3-D TLM simulations," *IEEE Transactions on Electromagnetic Compatibility*, vol. 45, pp. 207 - 217, 2003.
- [123] A. J. Wlodarczyk and D. P. Johns, "New wire interface for graded 3-D TLM," *Electronics Letters*, vol. 28, pp. 728-729 1992.
- [124] A. Ruddle and D. Ward, "Modelling wire antennas in wider simulations," presented at the IEE Colloquium on High Frequency Simulation in Practice, London, 1997.
- [125] G. Verissimo, R. Cuggia, J. Dubard, and M. Ney, "Multi-scale modeling of antennas with TLM method," presented at the 2010 Proceedings of the Fourth European Conference on Antennas and Propagation (EuCAP), Barcelona, Spain, 2010.
- [126] J. L. Herring and C. Christopoulos, "Multigrid transmission-line modelling method for solving electromagnetic field problems," *Electronics Letter*, vol. 27, p. 2, 1991.
- [127] M. Sobhy, M. Abd El-Azeem, and K. Royer, "A new multi-grid 3-D TLM algorithm for simulation of microwave FSS " *IEEE MTT-S Int. Microwave Symp. Dig.*, vol. 2, p. 4, 1996.
- [128] S. Gedney and J. Roden, "Numerical stability of nonorthogonal FDTD methods," *IEEE Transactions on Antennas & Wave Propagation*, vol. 48, p. 9, 2000.
- [129] D. Mavriplis. An advancing front Delaunay triangulation algorithm designed for robustness.
Available: <http://ntrs.nasa.gov/archive/nasa/casi.ntrs.nasa.gov/19930003212.pdf>
- [130] P.-O. Persson. (2006). Lecture 2: Unstructured Mesh Generation.
Available: <http://persson.berkeley.edu/pub/persson06unstructured.pdf>
- [131] P. Sewell, "Lecture notes on practical discretization", unpublished|.
- [132] J. Bukardt. (2011). Meshing for the finite element method. Available: http://people.sc.fsu.edu/~jbukardt/classes/fem_2011/fem_meshing.pdf
- [133] R. Dyer, H. Zhang, and T. Moller, "Gabriel meshes and Delaunay edge flips," in *Proc. Joint Conf. Geom. Phys. Modeling*, San Francisco, CA, USA, 2009, pp. 295-300.
- [134] M. Bern and D. Eppstein, *Mesh Generation and optimal triangulation: Computing in Euclidean Geometry*. Singapore: World Sci., 1992.
- [135] L. Chen, "Meshing smoothing schemes based on optimal Deluanay triangulations " in *13th Int. Meshing Roundtable*, Williamsburg, VA, USA, 2004, pp. 109-120.
- [136] L. Chen and J. Xu, "Optimal Delaunay Triangulations," *J. Comput. Math.*, vol. 22, pp. 299-308, 2004.
- [137] Q. Du and M. Gunzburger, "Grid generation and optimization based on centroidal Voronoi tessellations," *Appl. Math. Comput.*, vol. 133, pp. 591-607, 2002.
- [138] L. Ju, "Conforming CVDT for qulaity mesh generation," *Int. J. Numer. Anal. Methods*, vol. 4, pp. 531-547, 2007.
- [139] Wikipedia. (2008, June). Delaunay triangulation.
Available: http://en.wikipedia.org/wiki/Delaunay_triangulation
- [140] R. Colin, *Foundations for Microwave Engineering*: McGraw-Hill Inc.,US, 1992.
- [141] P. Sewell, T. Benson, A. Vukovic, and S. Cole, "Mesh Optimisation Methods for Unstructured Transmission-Line Modelling," *IET Science Measurement & Technology*, pp. 1-9, 2013.